

# Topological Transport and Quantum Estimation Theory in Optomechanical Systems

**Claudio Massimiliano Sanavio**

Supervised by Prof A. Xuereb

Department of Physics  
Faculty of Science  
University of Malta

**August, 2020**

*A dissertation submitted in partial fulfilment of the requirements for the  
degree of Doctor of Philosophy.*

## Declaration by Postgraduate Students

### (a) Authenticity of Dissertation

I hereby declare that I am the legitimate author of this Dissertation and that it is my original work.

No portion of this work has been submitted in support of an application for another degree or qualification of this or any other university or institution of higher education.

I hold the University of Malta harmless against any third party claims with regard to copyright violation, breach of confidentiality, defamation and any other third party right infringement.


### (b) Research Code of Practice and Ethics Review Procedures

I declare that I have abided by the University's Research Ethics Review Procedures.

As a Master's student, as per Regulation 58 of the General Regulations for University Postgraduate Awards, I accept that should my dissertation be awarded a Grade A, it will be made publicly available on the University of Malta Institutional Repository.

<b>Faculty/Institute/Centre/School</b>	Faculty of Science
<b>Degree</b>	Doctor of Philosophy
<b>Title</b>	Topological Transport and Quantum Estimation Theory in Optomechanical Systems
<b>Candidate (Id.)</b>	Claudio Massimiliano Sanavio (1609641)

Signature of Student



Date

August 13, 2020



L-Universit`  
ta' Malta

## **University of Malta Library – Electronic Thesis & Dissertations (ETD) Repository**

The copyright of this thesis/dissertation belongs to the author. The author's rights in respect of this work are as defined by the Copyright Act (Chapter 415) of the Laws of Malta or as modified by any successive legislation.

Users may access this full-text thesis/dissertation and can make use of the information contained in accordance with the Copyright Act provided that the author must be properly acknowledged. Further distribution or reproduction in any format is prohibited without the prior permission of the copyright holder.





**L-Università  
ta' Malta**

Copyright ©2020 University of Malta

[WWW.UM.EDU.MT](http://WWW.UM.EDU.MT)

*First edition, August 13, 2020*





## Abstract

This thesis focuses on optomechanics, which is the physical description of the force that the electromagnetic radiation exerts on a reflective object. The particles involved are so tiny that a quantum mechanical description is needed. Optomechanics is the median force between a quantum mechanical oscillator and a quanta of light. Hence, it has the potential to assume a major role in future technologies.

Quantum transport has been extensively studied in the last few decades, and still offer an important substrate for emerging technologies. In this thesis we studied quantum transport and applied it to a one dimensional system of both bosonic and fermionic particles. We obtained quasi perfect many body transfer. One hurdle from obtaining perfect transfer is due to the opposite possible directions of propagation inside the system. A way to overcome this issue is offered by means of topological insulators, materials which allow unidirectional propagation.

We aim to exploit optomechanics in order to transport excitations in a robust way. We engineered an array of microresonators which has the property of a topological insulator and where the mechanical motion spreads into the material in one way only. From an experimental point of view, the realization of this kind of mechanical topological insulator requires a good knowledge of the optomechanical coupling strength.

Therefore we used quantum estimation theory to understand which is the best measurement that will lead to an optimal estimation of the optomechanical coupling constant. This will play an important role for cutting-edge technology and applications in communication, phonon-based information storage and signal-processing devices.



---

# Contents

<b>1</b>	<b>Introduction</b>	<b>3</b>
<b>2</b>	<b>Optomechanics</b>	<b>9</b>
2.1	Introduction . . . . .	9
2.2	The Hamiltonian . . . . .	10
2.2.1	Temporal evolution of the optomechanical system . . . . .	14
2.3	The driving and the linearisation procedure . . . . .	20
2.3.1	Optomechanical equations of motion . . . . .	21
2.4	Gaussian steady state . . . . .	24
2.5	Stability of the Hamiltonian . . . . .	27
2.6	Optomechanical array . . . . .	29
2.7	Summary . . . . .	31
<b>3</b>	<b>Open quantum dynamics</b>	<b>33</b>
3.1	Introduction . . . . .	33
3.2	The classical Langevin equation . . . . .	34
3.3	The quantum Langevin equation . . . . .	37
3.3.1	First Markov approximation . . . . .	40
3.3.2	The input-output formalism . . . . .	41
3.4	Application to optomechanics . . . . .	42
3.5	Summary . . . . .	47
<b>4</b>	<b>Quantum Transport</b>	<b>49</b>
4.1	Introduction . . . . .	49
4.2	The Green's function . . . . .	51

4.3	The weak-coupling chain model . . . . .	53
4.3.1	Many-body dynamics . . . . .	54
4.3.2	Perturbative transfer . . . . .	57
4.3.3	Resonances in sender-wire-receiver system . . . . .	59
4.4	Many-body dynamics . . . . .	61
4.4.1	Equivalence between bosonic and fermionic perturbative excita- tions transfer . . . . .	62
4.4.2	Heuristic approach to PP transfer . . . . .	63
4.4.3	3- and 4-excitation perturbative transfer . . . . .	64
4.5	Applications of many-body perturbative transfer . . . . .	68
4.5.1	Equivalence of fermionic and bosonic observable's dynamics . . .	69
4.5.2	Magnetisation transport . . . . .	70
4.5.3	Energy transport . . . . .	72
4.6	Three qubit entanglement . . . . .	75
4.6.1	Entanglement transfer . . . . .	78
4.7	Summary . . . . .	81
<b>5</b>	<b>Topological insulators in Optomechanics</b>	<b>83</b>
5.1	Introduction . . . . .	83
5.2	The classical Hall effect . . . . .	85
5.3	The Quantum Hall effect . . . . .	86
5.3.1	The Landau problem . . . . .	86
5.3.2	The Symmetric Gauge . . . . .	89
5.4	The adiabatic theorem . . . . .	90
5.5	The geometric phase . . . . .	92
5.5.1	A geometric approach to the Berry phase . . . . .	94
5.5.2	Relation with the Abelian Gauge theory of Electromagnetism . . .	99
5.6	2D Chern insulators . . . . .	100
5.6.1	The Harper-Hofstadter model . . . . .	103
5.6.2	Application to optics . . . . .	105
5.7	Nonreciprocal topological phononics in optomechanical arrays . . . . .	106
5.7.1	The model . . . . .	106
5.7.2	Mechanical edge states . . . . .	108
5.7.3	Topologically protected transport . . . . .	110
5.8	Summary . . . . .	113
<b>6</b>	<b>Estimation theory and application in optomechanics</b>	<b>115</b>

6.1	Classical estimation theory . . . . .	116
6.1.1	Bayesian approach . . . . .	117
6.1.2	Classical Fisher information approach . . . . .	118
6.1.3	Comparison between the approaches . . . . .	120
6.2	Quantum estimation theory . . . . .	122
6.2.1	Quantum Bayesian strategy . . . . .	123
6.2.2	Quantum Fisher information approach . . . . .	126
6.2.3	Comparison between Quantum Fisher and Bayes approaches. . . . .	128
6.3	Bayesian estimation of the optomechanical coupling strength . . . . .	129
6.4	Quantum Cramér–Rao-type inequality . . . . .	137
6.5	Optimal estimation of matter–field coupling strength in the dipole approximation . . . . .	143
6.5.1	The Jaynes-Cumming model . . . . .	145
6.5.2	Maximum-likelihood estimator . . . . .	162
6.5.3	Remarks . . . . .	171
6.6	Application of Fisher information approach to optomechanics . . . . .	174
6.6.1	Phase space quantum and classical Fisher Information . . . . .	176
6.6.2	Results . . . . .	179
6.7	Summary . . . . .	184
<b>7</b>	<b>Conclusion and outlooks</b>	<b>185</b>
	<b>References</b>	<b>189</b>

## List of Figures

2.1 The simplest optomechanical model. An optical cavity with a oscillating moving end-mirror . . . . .	10
4.1 Schematic of quantum transport . . . . .	50
4.2 Setup of the excitation transfer protocol . . . . .	54
4.3 Single-particle energy spectrum of the chain, composed by one sender, one receiver, and a wire of even and odd length $n_w$ , respectively, left and right panel . . . . .	58
4.4 Table showing the number of resonances between the sender and the wire $n_{res}$ for $n_s$ senders up to 4 and a wire of length $n_w$ , with $l = 0, 1, 2, \dots$ . . . . .	61
4.5 The transition probability of two excitations from sender sites $\{n_s\} = 1, 2$ to receiver sites $\{n_r\} = N - 1, N$ for fermions and bosons, respectively . . . . .	62
4.6 Transition probability for the transfer of three excitations from sites 1, 2, 3 to sites $N - 2, N - 1, N$ for a chain length of $N = 47$ in a time interval of $t \in (0, 160000/J)$ . . . . .	67
4.7 Transfer times $\tau$ for $n_s = 1, 2, 3, 4$ excitations in wires of different length $n_w$ fulfilling the (quasi) perturbative condition for all considered $n_s$ . . . . .	69
4.8 Average magnetisation of the receiver block, Eq. 4.62, for $n_s = 3$ in a chain of $N = 47$ . . . . .	71
4.9 Energy and charging power for a battery made out of 4 qubits $n_B = 4$ , left and right panel, respectively . . . . .	74
4.10 Schematic diagram of the classification of three qubit states: $S$ fully separable, $B$ bi-separable, $W$ and $GHZ$ non-separable. . . . .	76
4.11 Entanglement witness, tripartite negativity and concurrence on a time scale of the transfer . . . . .	79

4.12	(left panel) Maximum tripartite negativity and witness as a function of the coupling $J_0$ for a chain of length $N = 23$ and (right panel) time $\tau$ at which the maximum are achieved vs $J_0$ . . . . .	80
4.13	(left panel) Short-time behaviour of the concurrence $C^{(13)}$ and (right panel) of the tripartite negativity $N^{(3)}$ . . . . .	80
5.1	Dispersion relations of (left panel) reciprocal and (right panel) non reciprocal for a surface plasmon polariton . . . . .	84
5.2	The Hall conductivities $\sigma_{xx}, \sigma_{xy}$ in direction $x$ and $y$ respectively . . . . .	87
5.3	The bulk dispersion relation of the QWZ model . . . . .	102
5.4	The Hofstadter's Butterfly . . . . .	105
5.5	(left panel)The optomechanical array in the shape of an hexagonal Kagome lattice. (center panel) The driving field applied on the lattice and (right panel) the resulting steady state of the optical field. . . . .	107
5.6	(left panel)Band structure and (right panel) edge state of the optomechanical Kagome lattice . . . . .	109
5.7	Topological transport in the optomechanical lattice and effects of disorder . .	111
6.1	The average minimum cost of error $\bar{C}_{\min}/\omega_m^2$ , as a function of $\omega_m t$ for an initial optical coherent state with real $\alpha$ . . . . .	131
6.2	The two eigenvalues of the operator $\hat{M}_{\min}$ to be measured as a function of $\omega_m t$	132
6.3	The average minimum cost of error $\bar{C}_{\min}/\omega_m^2$ , as a function of $\omega_m t$ for different initial optical coherent state . . . . .	133
6.4	The average estimator $h(g)/\omega_m$ as a function of $g/\omega_m$ . . . . .	134
6.5	(left panel) The average minimum cost of error $\bar{C}_{\min}/\omega_m^2$ as a function of $\omega_m t$ and (right panel) the average estimator $h(g)/\omega_m$ as a function of $g/\omega_m$ , for different thermal state . . . . .	135
6.6	(left panel) The average minimum cost of error $\bar{C}_{\min}/\omega_m^2$ as a function of $\omega_m t$ and (right panel) the average estimator $h(g)/\omega_m$ as a function of $g/\omega_m$ , for different squeezed state . . . . .	135
6.7	The average minimum cost of error $\bar{C}_{\min}/\omega_m^2$ as a function of $\omega_m t$ for different initial states of the optical field . . . . .	136
6.8	The average estimator $h(g)/\omega_m$ as a function of $g/\omega_m$ . . . . .	137
6.9	The lower bound of the mean-squared error as a function of $g/\omega_m$ . . . . .	139
6.10	The lower bound of the mean-squared error as a function of $g/\omega_m$ for thermal state . . . . .	140

6.11	The lower bound of the mean-squared error as a function of $g/\omega_m$ for squeezed state . . . . .	141
6.12	The lower bound of the mean-squared error as a function of $g/\omega_m$ for different initial optical state . . . . .	141
6.13	Schematic representation of a quantum estimation scenario based on cavity QED . . . . .	146
6.14	The eigenvalues of $\hat{M}_{\min}/g_0$ as a function of $g_0\tau_c$ in the case of the Gaussian prior p.d.f. . . . .	156
6.15	The average minimum cost of error $\bar{C}_{\min}/g_0^2$ as a function of $g_0\tau_c$ in the case of the Gaussian prior p.d.f., with mean $g_0$ and variance $\sigma^2/g_0^2 = 1$ . We set $\gamma\tau_f = 0$ , such that no spontaneous decay occurs. Each curve has a global minimum that decreases and shifts to larger values of $g_0\tau_c$ with increasing $ \alpha $ . . . . .	156
6.16	The average estimator $E(\tilde{g} g)/g_0$ as a function of $g/g_0$ for the Gaussian prior p.d.f. . . . .	157
6.17	The lower bound of the mean-squared error as a function of $g/g_0$ for the Gaussian prior p.d.f. . . . .	158
6.18	The eigenvalues of $\hat{M}_{\min}/g_0$ as a function of $g_0\tau_c$ in the case of the uniform prior p.d.f. . . . .	158
6.19	The average minimum cost of error $\bar{C}_{\min}/g_0^2$ as a function of $g_0\tau_c$ in the case of the uniform prior p.d.f. . . . .	159
6.20	The average estimator $E(\tilde{g} g)/g_0$ as a function of $g/g_0$ for the uniform prior p.d.f. . . . .	159
6.21	The lower bound of the mean-squared error as a function of $g/g_0$ for the uniform prior p.d.f. . . . .	160
6.22	The average minimum cost of error $\bar{C}_{\min}/g_0^2$ reached at $\tau_c = \tau_c^*$ as a function of the detuning $\Delta$ . . . . .	161
6.23	The average minimum cost of error $\bar{C}_{\min}/g_0^2$ reached at $\tau_c = \tau_c^*$ as a function of $\gamma\tau_f$ . . . . .	161
6.24	The average maximum cost function $\bar{C}_{\max}g_0$ as a function of $g_0\tau_c$ in the case of the Gaussian prior p.d.f. . . . .	170
6.25	The average estimator $E(\tilde{g} g_0)/g_0$ as a function of $g_0\tau_c$ in the case of the Gaussian prior p.d.f. . . . .	171
6.26	The lower bound of the mean-squared error as a function of $g/g_0$ for the Gaussian prior p.d.f. . . . .	172
6.27	Quantum Fisher information (QFI) as a function of the filter function's center frequency $\Omega_k$ . . . . .	180

6.28	(left panel) Classical Fisher information (CFI) as a function of the quadrature phase $\theta$ for different values of $\eta$ . (right panel) CFI as a function of $\eta$ for two different choices of $\theta$ . . . . .	181
6.29	(left panel) The quadrature phase $\theta_{\max}$ as a function of the filter function's center frequency $\Omega_k$ and for different values of the detuning $\Delta_0$ . (right panel) $\theta_{\max}$ as a function of the detuning $\Delta_0$ for $\Omega_k = 0$ . . . . .	182
6.30	Classical Fisher information (CFI) as the function of the parameters $\kappa$ , $\gamma$ , $P$ and $g$ . . . . .	182
6.31	Semilogarithmic plot of the quantum Fisher Information (QFI) as a function of the mechanical bath temperature $T$ for different values of the mechanical decay rate $\gamma$ . . . . .	183

## Publications

The following publications have been produced during the completion of the Doctoral studies

- [1] Bernád, J.Z. and Sanavio, C. and Xuereb, A., Optimal estimation of the optomechanical coupling strength, *Phys. Rev. A*, 97, 6, 063821, (2018).
- [2] Bernád, J.Z. and Sanavio, C. and Xuereb, A., Optimal estimation of matter-field coupling strength in the dipole approximation, *Phys. Rev. A*, 99, 6, 062106, (2019).
- [3] Sanavio, C. and Bernád, J.Z. and Xuereb, A. Fisher information based estimation of optomechanical coupling strengths, *arXiv e-prints* 2002.03249, (2020).
- [4] Chetcuti, W.J. and Sanavio, C. and Lorenzo, S. and Apollaro, T.J.G., Perturbative many-body transfer, *New Journal of Physics*, 22, 3, 033030, (2020).
- [5] Apollaro, T. J. G. and Sanavio, C. and Chetcuti, W. J. and Lorenzo, S., Multipartite entanglement transfer in spin chains, *Physics Letters A*, 126306, (2020).
- [6] Sanavio, C. and Peano, V. and Xuereb, A., Nonreciprocal topological phononics in optomechanical arrays, *Phys. Rev. B*, 101, 8, 085108, (2020).



## Preface

During the completion of the Doctoral studies I have pursued many lines of research which ultimately have given me a deep understanding of the main topic expressed in the title. In this dissertation I summarize the main results obtained during these three years of doctorate and published in a total of six papers.

My journey in applying quantum estimation theory in optomechanical systems started under the supervision of Prof. A. Xuereb and Dr. J. Z. Bernád in 2017. After getting acquaintance with the topic of optomechanics and estimation theory, my role was to perform the numerical calculations and check the novel analytical results, which have been published in [1]. The year after we applied the same techniques on the estimation of the matter-field coupling strength in what is known as the Jaynes-Cummings model. I studied the system and computed the numerical results eventually published in [2]. Finally the year after, I published my first first-name paper [3], where I led the research and calculated both analytically and numerically the results.

In the meantime, I got also to better understand quantum transport and topological insulators in 1D and 2D systems. In fact, my Ph.D. project consists in a hybrid analysis of transport in optomechanical systems and inference of the Hamiltonian parameters which ultimately affect the transport. I exploited my knowledge in quantum transport in a collaboration with Prof. T. Apollaro, where we analyzed transport of excitation in a 1D-chain. In this occasion I assisted and co-supervised the master student W.J. Chetcuti and performed the calculations for the bosonic case, comparing them with the results obtained for the fermionic case. Furthermore, I performed the calculations for the transfer of entanglement and numerically computed the several entanglement witnesses and measurements. These results are published in [4] and [5]. The works have been done in collaboration with the University of Palermo and Dr. S. Lorenzo.

Finally, under the supervision of Dr. V. Peano, now at the university of Erlanghen, and Prof. A. Xuereb, I analyzed the case of a 2D optomechanical Chern insulator and performed the numerical and analytical calculations, which are published in [6].

# Introduction

Precise measurement plays an important role in science. One hundred years ago, in 1920, C. E. Guillaume was awarded to the Nobel Prize "in recognition of the service he has rendered to precision measurements in Physics" [7]. Although in the last century physics has passed through important changes, breakthrough discoveries and different perspectives on science and Nature, precise measurement will always have the important role they had. Quantum physics focuses mainly on mesoscopic and microscopic systems, which can be analyzed only with an extreme precision of the instruments. Furthermore surprising physics arises from the discovery and the measurement of minuscule forces. Optomechanics is one example of it. In everyday life we never experience the radiation pressure force, which light exerts on a surface, transferring momentum onto it. However it exists, and nowadays it can be measured and observed with powerful lasers that hit microscopic membranes, which start to oscillate. Yet, technology comes from the control of physical phenomena. Hence, the most common optomechanical set up involves a movable membrane in an optical Fabri-Pérot cavity, which provides a controlled environment for experiments. Tremendous progress in the control of radiation pressure in optomechanical systems has led to an impressive series of milestones including cooling of nanomechanical resonators to their quantum ground state, quantum-limited position measurements, and squeezing of quantum fluctuations [8]. In Chap. 2 we will introduce the basic model of the cavity-optomechanical system, a single-mode of the electromagnetic radiation field coupled via radiation pressure to a vibrational mode of a mechanical oscillator, subject to adiabatically slow motion of the mirror [9]. The analytical solutions to this simple model results in a density matrix, which describes the joint state of the field and the mechanical oscillator. Measurement on this system are performed on the optical field. Therefore we will also find an explicit solution of the dynamics of the electromagnetic field tracing out the mechanical degrees

of freedom. The single mode assumption can be experimentally obtained when the cavity is driven by an external laser with a bandwidth narrower than the separation among the different electromagnetic modes. The laser amplifies the population of only one mode, allowing us to neglect the others.

The resulting system requires the introduction of an environment which provides the external source of light. Hence, the system is better described by open quantum theory, which is the subject of Chap. 3. The equations of motion of the field operators show gains and losses due to the external noise. In fact, the intracavity field is amplified by the laser, whereas the mechanical motion is usually subject to Brownian noise for a non perfect isolation to the rest of the world. In classical mechanics this is dealt with using the classical Langevin equations. We will introduce them and their quantum counterparts, the quantum Langevin equations. Finally in Sec. 3.4 we will apply these concepts to optomechanics.

While the tunable interaction between a single optical and a single mechanical mode underlies most of the early breakthroughs, a new trend is emerging that exploits several optical and mechanical modes to perform more complex tasks. For instance, they include frequency conversion [10] or robust synchronization [11]. Furthermore, different modes can be localized in different single cavities which are connected together with optical and mechanical coupling. This defines an array of cavities that can be used for quantum transport of excitations, the subject of Chap. 4. Significant attention has been devoted to the transport of excitations along one-dimensional quantum systems [12–15]. Beside optomechanics, the transfer of excitations between edges of a spin chain, which can be mapped to a quadratic Hamiltonian, has been addressed in several works, with particular emphasis given to the quantum state transfer of a single qubit in quantum information processing. Fully engineered wires are able to achieve this goal with unit fidelity in a ballistic time [16–19]. Nevertheless, a precise control over each coupling constant is experimentally demanding, especially in solid state systems. Alternative methods have been proposed where only a few couplings are required to be addressed, generally being that between the sender (receiver) site and the quantum channel [20–25]. The case of a higher number of excitations, or the transfer of an arbitrary two-qubit state, has received less attention [26–28], whereas the transfer of a state of more than two qubits was not addressed in a setting where the quantum channel is made up of a chain with uniform couplings. Therefore, in Sec. 4.3 we address the problem of the transfer of  $n > 1$  excitations between the edges of a system described by a 1D quadratic many-body Hamiltonian. Due to the Hamiltonian's non-interacting nature, we are able to express the many-body dynamics in terms of one-body transition amplitudes. Exploiting this property, we identify the equivalence classes for the length of the 1D system for which

the transfer for up to four excitations occurs, regardless of their bosonic or fermionic nature. The transfer happens, for specific lengths of the chain, via Rabi-like dynamics in the weak-coupling regime, which we consequently dub as PP (perturbatively perfect) excitation transfer. In the case of three excitations transfer on the chain is effectively, provided that its length fulfills  $N = 4n + 7$ , with  $n$  being a non-negative integer. The excitation transfer occurs in the weak-coupling regime, of the sender and receiver block to the wire, and it approaches unity in the limit of vanishing coupling, although at a price of transfer time going to infinity. In Sec. 4.6 we focus our attention on the transfer of entanglement. Indeed we study whether the same model can be used to efficiently transfer entangled states made by three particles. The motivations are that entanglement has become in the last few decades a central topic of many applications of quantum mechanics, ranging from quantum information [29] to quantum thermodynamics [30].

Even though the weak coupling regime allows PP transfer, the dynamics follows a Rabi-like cycle, which means it is intended to come back to its original state. Moreover the chain could be subject to imperfections and fabrication defects which largely compromise the transfer. Quantum transport is more effective if it is non reciprocal, i.e. if the transport can happen in one direction only. This phenomenon can happen in topological insulators which are the subject of Chap. 5. Here we introduce them and the mathematics behind this particular behavior, which allows back-scattering immune transport and topological protection against disorder. In fact, the unidirectionality is a property of the topology of the system and small adiabatic changes are not able to affect it. In Sec. 5.7 we show how to implement topologically robust nonreciprocal phonon transport in an array of optomechanical microtoroids. This is a tunable platform that has already been used to successfully demonstrate optically mediated mechanical synchronization [11]. In each microtoroid, a mechanical breathing mode is naturally coupled to whispering gallery optical modes of both clockwise and anticlockwise chirality. The bare nonlinear optomechanical coupling typically is very small; adding a laser drive leads to a much stronger and tuneable linear coupling [8]. Following the approach of Ref. [31], we use this optomechanical tunability to select the chirality of the optical modes that are strongly coupled to the mechanical modes. Inspired by present-day implementations of optomechanical microtoroid arrays [11], we assume that the optical driving is applied only at the edge of the device. The photons hopping between neighboring toroids experience an effective spin-orbit coupling. This can be implemented following a well-tested approach based on asymmetric couplers [32, 33]. The interplay of the optical spin-orbit coupling and the laser driving induces a breaking of the time-reversal symmetry and leads to a mechanical Chern insulator supporting chiral phononic edge states. In stark contrast to geometry-based proposals [34–36] and experiments [37, 38]

for on-chip topological phononics, our setup is truly nonreciprocal, and the topological protection extends to any arbitrary fabrication imperfection. Our approach differs from earlier proposals for on-chip mechanical Chern insulators [39, 40], in that it does not require a direct mechanical coupling between the microtoroids and the driving field need not be applied to the bulk of the array.

Once again, precise measurement plays an important role. The mechanical chiral states are to be found in a narrow band gap created through avoided crossing between the mechanical and the optical band. Thus, this band gap is proportional to the strength of the optomechanical interaction, which is usually very small. How we can infer the true value of the coupling constant is the subject of Chap. 6. Inverse problems play an important role in science because they are able to inform us about relevant parameter values of a dynamical system that we cannot directly observe [41]. The objective of an inverse problem is to estimate these unknown parameters by extracting information from measurement data and assessing the uncertainty in this data, making use of all information known prior to the measurement process and a mathematical model of the dynamical system. In this approach, the parameters to be estimated are treated as random variables and they must be assigned a joint prior probability distribution function; this is the Bayesian formulation of the estimation problem and it is described in Sec. 6.1.1. The qualities of estimators acting on the space of measurement data are evaluated through cost functions or conversely by maximizing or minimizing a cost function over the set of all possible estimators leads to an optimal estimator. In this case calculus of variations is applied, which is not always an easy mathematical task, especially when the estimation problem is formulated in quantum mechanics [42–44], as reported in Sec. 6.2.1. Throughout this chapter we will see how the application of the Bayesian strategy to quantum mechanical systems does not always result in an experimentally implementable optimal estimator [1, 2, 45–47]. In particular we will focus our attention on an optomechanical cavity with quadratic coupling in Sec. 6.3 and on a two level system coupled to an optical cavity field in Sec. 6.5. In order to work with more effective models of cavity optomechanical systems [8] and to consider experimentally relevant estimation strategies [48], one has to turn the investigation on the lower bounds of some convenient measure of the estimation accuracy and this is the subject of Sec. 6.1.2 The mean squared error– the average squared difference between estimated values and true values of the unknown parameters– is usually employed as a measure of accuracy. In the case of classical systems, there are some complicated lower bounds of the mean squared error [49, 50]; however, the Cramér–Rao inequality [51, 52], reported in Sec. 6.1.2 and which defines an inferior but a simpler lower bound, can be extended to quantum systems [53], as it is shown in Sec. 6.2.2. Here, the lower bound is inversely

proportional to the quantum Fisher information (QFI) irrespective of whether the estimator is biased or unbiased; see Ref. [2]. The chosen estimation strategy, expressed as a positive-operator valued measure (POVM), provides probability distributions of the parameter to be estimated conditioned on true value of this parameter. These conditional probabilities determine the classical Fisher information (CFI), which is inversely proportional to the lower bound of the mean squared error in the classical post-processing of measurement data. As the CFI is always smaller than or equal to the QFI, which defines the smallest value of the lower bound, it is worth to investigate the circumstances where the CFI is as close as possible to the QFI [54]. In principle, given any measurement apparatus, we could fit the experimental data set with a theoretical curve and obtain a value for the estimanda. However, we may end up with an estimation characterized by very low precision, and the maximization of the CFI will help us preventing it. We apply the Fisher approach to the estimation of the nonlinear optomechanical coupling strength in Sec. 6.6. The measurement strategy involves balanced homodyne photodetection with non-ideal detectors [55] carried out on the output field. We investigate the QFI of the output field state depending on the unknown value of the optomechanical coupling and compare with CFI obtained from the data provided by the balanced homodyne photodetection. We identify those cases where CFI is as large as possible, where the lower bound of the estimation accuracy is therefore smallest.



# Optomechanics

## 2.1 | Introduction

The first time a classical optomechanical effect appeared in the scientific literature was in 1601 [56], when Kepler noticed that the tail of the comet always points outward from the sun. He argued that light could push away the comet dust. In 1873 Maxwell, and in 1876 independently Bartoli (see [57] and citations within), theorized the radiation pressure. This phenomena is the transmission of momentum from the light to an object. The light exerts a pressure on the object, which can be expressed as the quantity  $P = \frac{S}{c}$ , where  $S$  is the intensity of the Poynting vector  $S = \frac{1}{\mu_0} |\vec{E} \times \vec{B}|$  and  $c$  is the speed of light. The radiation pressure equals the energy density of the electromagnetic wave. If the light travels perpendicular to the surface of the object and it is reflected, its momentum changes from  $\vec{p}$  to  $-\vec{p}$ . For momentum conservation law the reflective object acquires a momentum  $2p$  and the total pressure experienced by the object is  $P_{tot} = 2\frac{S}{c}$ .

In the same year Maxwell conceived an experiment to demonstrate the existence of radiation pressure. He proposed a concentrated ray of an electric lamp falling on a thin metallic layer suspended in a vacuum could be used to probe the radiation of the light. However the heating caused by the electromagnetic radiation prevented radiation pressure to be effectively demonstrated. It was only after several failed attempts, among them the famous radiometer of Crookes [58], that in 1903 radiation pressure was finally proved by Lebedev [59] and independently by Nichols and Hull [57]. The latter used an apparatus, nowadays known as the Nichols radiometer, considered to be the first optomechanical instrument.

In the 30's pioneering experiments recorded the transfer of linear [60] and angular [61] momentum from light to matter, but it is only with the arrival of the laser in the 70's that light started to be used to stir and control dielectric particles [62], to cool the motion



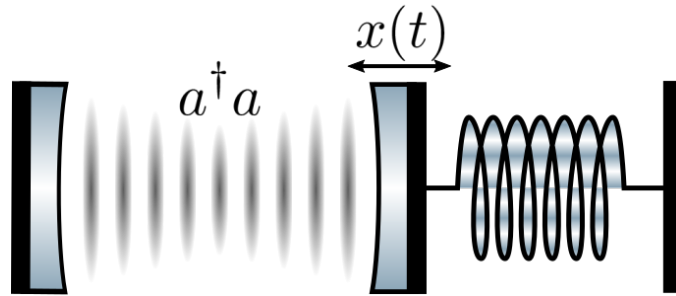


Figure 2.1: The simplest optomechanical model. An optical cavity with a oscillating moving end-mirror. The electromagnetic field is represented by the number operator  $a^\dagger a$  which accounts for the amplitude of the intracavity field.  $x(t)$  represent the displacement of the mirror induced by radiation pressure force.

of ions [63] and to trap clouds of atoms [64]. Those technological improvements find application in everyday life. To give some examples, optical tweezers are currently used to detect and analyze virus or biological cells [65], and cold atoms have application in the global positioning system (GPS), where they are used for time synchronization. Eventually in the 90's a theoretical formulation of quantum optomechanics was made. These studies include the introduction of an Hamiltonian formalism [9], the use of squeezed light for quantum noise reduction [66] and quantum non-demolition measurement [67]. Recent applications regard gravitational wave detectors and measurements below the standard quantum limit [68].

In this chapter we will approach the basics of cavity optomechanics with a particular focus on the theoretical aspects we used to accomplish our research goals. The standard set-up is an optical cavity with a moving end mirror displaced by radiation force. Optomechanics studies the oscillations of the mirror around its equilibrium point and the emergence of quantum effects.

## 2.2 | The Hamiltonian

We start our discussion by deriving the classical Hamiltonian that describes the interaction between the electromagnetic field in an optical Fabri-Pérot cavity with a moving-end mirror. The system is represented in Figure 2.1

The cavity is composed by two perfectly reflecting mirrors, one of which is movable in a potential well  $V(q)$ . We consider the movable mirror to have mass  $m$  and position  $q(t)$ . The cavity field is described by the vector potential [69]  $A(x, t)$ , where  $x$  is the

position inside the cavity with domain  $0 \leq x \leq q(t)$ . Inside the cavity, the vector potential follows the Maxwell equations in the vacuum, which can be written as the one-dimensional wave equation

$$\frac{\partial^2 A(x, t)}{\partial x^2} = \frac{\partial^2 A(x, t)}{\partial t^2}. \quad (2.1)$$

The choice of considering the one-dimensional case is supported by the fact that two different polarizations of the field don't interact with each other. Moreover, we constrain the field to be zero at the borders of the cavity,  $A(0, t) = A(q(t), t) = 0$ . On the other hand, the mechanics of the mirror is described by the Newton equation

$$m\ddot{q} = -\frac{\partial V(q)}{\partial q} + \frac{1}{2} \left( \frac{\partial A(x, t)}{\partial x} \right)^2 \Big|_{x=q(t)}, \quad (2.2)$$

where the term on the right is the radiation force in the rest frame of the moving mirror. In fact, the radiation pressure force is equal to the energy density of the field and in the rest frame it is equal to  $B'^2/2$ , where  $B'$  is the magnetic field on the surface of the mirror in this frame. The electric field  $E'$  is always zero due to the boundary conditions of  $A$ . Therefore, we can obtain Eq. (2.2) transforming back into the laboratory frame in the non-relativistic limit [9].

Let us now write the mode decomposition of the vector field  $A(x, t)$  as the set of coordinates

$$Q_k(t) = \sqrt{\frac{2}{q(t)}} \int_0^{q(t)} A(x, t) \sin\left(\frac{k\pi x}{q(t)}\right) dx, \quad (2.3)$$

which are the coefficient of a suitable Fourier series of  $A$ . Hence, we have

$$A(x, t) = \sum_{k=1}^{\infty} Q_k(t) \sqrt{\frac{2}{q(t)}} \sin\left(\frac{k\pi x}{q(t)}\right). \quad (2.4)$$

To guarantee the existence of the decomposition Eq. (2.3) we constrain  $q(t)$  to positive values, a condition achievable if we imagine an infinite barrier at  $q = 0$ , so that  $V(0) = \infty$ . Thus, the expansion allows us to write Eqs. (2.1) and (2.2) as

$$\ddot{Q}_k = -\omega_k^2 Q_k + 2\frac{\dot{q}}{q} \sum_j g_{kj} \dot{Q}_j + \frac{\ddot{q}q - \dot{q}^2}{q^2} \sum_j g_{kj} Q_j + \frac{\dot{q}^2}{q^2} \sum_{jl} g_{jk} g_{jl} Q_l \quad (2.5)$$

$$m\ddot{q} = -\frac{\partial V(q)}{\partial q} + \frac{1}{q} \sum_{kj} (-1)^k \omega_k \omega_j Q_k Q_j, \quad (2.6)$$

where  $\omega_k = \omega_k(q) = \frac{k\pi}{q}$  is the mode frequency for a specific length  $q$ . The coefficients  $g_{jk}$  are given from Eq. (2.4) as

$$g_{jk} = \begin{cases} (-1)^{k+j} \frac{2kj}{k^2-j^2}, & \text{if } k \neq j \\ 0, & \text{if } k = j, \end{cases} \quad (2.7)$$

and they account for the interaction among different modes. Alternatively, we can obtain the equations of motion (2.5) and (2.6) from the Euler-Lagrange equations of the Lagrangian

$$\mathcal{L}(q, \dot{q}, Q_k, \dot{Q}_k) = \frac{1}{2} \sum_k [\dot{Q}_k^2 - \omega_k^2(q) Q_k^2] + \frac{1}{2} m \dot{q}^2 - V(q) - \frac{\dot{q}}{q} \sum_{j,k} g_{k,j} \dot{Q}_k Q_j \quad (2.8)$$

$$+ \frac{\dot{q}^2}{2q^2} \sum_{j,k,l} g_{kj} g_{kl} Q_j Q_l. \quad (2.9)$$

Since in first quantization we deal with the Hamiltonian formalism, we can find an effective Hamiltonian that satisfies the equations of motion. Hence, we apply the canonical transformations to derive the mechanical momentum  $p$  and the momentum  $P_k$  of the  $k^{\text{th}}$  optical mode, yielding

$$p = m\dot{q} - \frac{1}{q} \sum_{j,k} g_{kj} P_k Q_j, \quad (2.10)$$

$$P_k = \dot{Q}_k - \frac{\dot{q}}{q} \sum_j g_{kj} Q_j. \quad (2.11)$$

Thus, the Hamiltonian  $H = p\dot{q} + \sum_k P_k \dot{Q}_k - \mathcal{L}$  reads

$$H(q, p, Q_k, P_k) = \frac{1}{2m} \left( p + \frac{1}{q} \sum_{j,k} g_{jk} P_k Q_j \right)^2 + V(q) + \frac{1}{2} \sum_k (P_k^2 + \omega_k^2 Q_k^2), \quad (2.12)$$

that corresponds to the total energy of the system. The first two terms are indeed the mechanical energy and the last term represents the field's energy. We note the first term corresponds to the kinetic momentum. In this Hamiltonian the canonical and kinetic momentum are different as it happens in other theories [70], p.e. electrodynamics.

We can now apply the canonical quantization, elevating the functions  $q, p, \{Q_k\}, \{P_k\}$  to operators which respect the canonical commutation relations

$$[\hat{q}, \hat{p}] = i\hbar, \quad [\hat{Q}_j, \hat{P}_k] = i\hbar \delta_{jk}, \quad (2.13)$$

$$[\hat{q}, \hat{Q}_k] = [\hat{p}, \hat{Q}_k] = [\hat{q}, \hat{P}_k] = [\hat{p}, \hat{P}_k] = 0 \quad \forall k. \quad (2.14)$$

Therefore, the corresponding quantum version of Eq. (2.12) is

$$\hat{H} = \frac{(\hat{p} + \hat{\Gamma})^2}{2m} + V(\hat{q}) + \sum_k \omega_k(\hat{q}) \left( a_k^\dagger a_k + \frac{1}{2} \right), \quad (2.15)$$

where  $a_k$  and  $a_k^\dagger$  are respectively the annihilation and creation operators for the  $k^{\text{th}}$  mode associated to each position  $q$ , defined as

$$a_k(\hat{q}) = \sqrt{\frac{1}{2\hbar\omega_k(\hat{q})}} \left( \omega_k(\hat{q}) \hat{Q}_k + i\hat{P}_k \right) \quad (2.16)$$

$$a_k^\dagger(\hat{q}) = \sqrt{\frac{1}{2\hbar\omega_k(\hat{q})}} \left( \omega_k(\hat{q}) \hat{Q}_k - i\hat{P}_k \right). \quad (2.17)$$

$\hat{\Gamma}$  is the quadratic operator

$$\hat{\Gamma} = \frac{i\hbar}{2\hat{q}} \sum_{k,j} g_{kj} \sqrt{\frac{k}{j}} \left( a_k^\dagger a_j^\dagger - a_k a_j + a_k^\dagger a_j - a_j^\dagger a_k \right), \quad (2.18)$$

that accounts for the interaction between the different modes. The Hamiltonian (2.15) is defined over the Hilbert space for which a basis is the set  $|\{n_l\}, q\rangle$  of the simultaneous eigenvectors of both the number operator and the position operator. This is somehow different to what we are used to in quantum mechanics, since both the basis and the field operators change at any time in the dynamics. Furthermore, we stress that it is only considering the field outside the boundaries of the cavity that we can rewrite the divergent part of the field energy in the Hamiltonian (2.15) as a finite term, which is known as Casimir energy [71]. However, when the intracavity field is big enough we can neglect the contribution given by the outside field and the afore written Hamiltonian becomes a very good approximation.

When a single-mode is dominant in the dynamics, we are allowed to set  $\hat{\Gamma} = 0$ , a condition that has been proven to be experimentally valid [8]. Furthermore, the radiation force produces a small displacement of the mirror, so that we can expand the potential  $V(q)$  around the equilibrium point  $q_0$ . In the neighborhood of  $q_0$  we have:

$$\begin{aligned} V(q) &\approx V(q_0) + \frac{1}{2} \frac{\partial^2 V(q)}{\partial q^2} \Big|_{q=q_0} \times (q - q_0)^2, \\ &= V(q_0) + \frac{1}{2} m\omega_m^2 (q - q_0)^2, \end{aligned}$$

where we have defined the mechanical frequency  $\omega_m = \sqrt{\frac{1}{m} \frac{\partial^2 V(q)}{\partial q^2}}$ .

The frequency  $\omega(q)$  is expanded in the same manner around  $q_0$  up to the first order and the single-mode Hamiltonian reads

$$H = \frac{p^2}{2m} + \frac{1}{2}m\omega_m^2(q - q_0)^2 + \left(\omega_0 + \frac{\partial\omega}{\partial q}(q - q_0)\right)\left(a^\dagger a + \frac{1}{2}\right), \quad (2.19)$$

where  $\omega_0 = \omega(q)|_{q=q_0}$  and we have discarded the hats on the operators for the sake of simplicity. After the shift  $q \rightarrow q + q_0$  and the introduction of the ladder mechanical operators  $b$  and  $b^\dagger$  defined analogously as in Eq. (2.16) and Eq. (2.17), we can write  $q = q_{zpf}(b^\dagger + b)$  and the optomechanical Hamiltonian as:

$$H^{\text{om}} = \omega_m^2 b^\dagger b + \left(\omega_0 - Gq_{zpf}(b^\dagger + b)\right)a^\dagger a + \dots, \quad (2.20)$$

where  $q_{zpf} = \sqrt{\frac{\hbar}{2m_{\text{eff}}\omega_m}}$  is the mechanical *zero point fluctuation*,  $G = -\frac{\partial\omega_0}{\partial q}$  is the optomechanical frequency shift for displacement and the minus sign is set by the condition that a positive displacement leads to a lower optical frequency (for example, if we think about a linear Fabri-Perot cavity one can easily find  $G = \omega_0/L$ , where  $L$  is the length of the cavity). The dots contain all the constants present in Eq. (2.19) which don't affect the dynamics.

From this Hamiltonian we can find the quantum analog of the radiation force, Eq. (2.2), is given by

$$F_{\text{rad}} = -\frac{\partial H^{\text{om}}}{\partial q} = \hbar G a^\dagger a. \quad (2.21)$$

From now on, we will use the quantity  $g_0 = Gq_{zpf}$  that describes the optomechanical interaction between a single photon and a single phonon, the latter defined as a single quanta of mechanical motion. It's worth to notice that the Hamiltonian Eq. (2.20) is already a very good approximation of many set-ups the community is using, although it is possible to create conditions for which higher orders of the interaction are needed [72]. Nevertheless in Eq. (2.20) already three operators contribute together in the optomechanical interaction  $g_0(b + b^\dagger)a^\dagger a$  and this leads to a quadratic dynamics, for which the solution of the equation of motion is not straightforward.

### 2.2.1 | Temporal evolution of the optomechanical system

Starting from a joint field–mechanics state  $|\Psi(0)\rangle$ , the time evolution of the system is given by the Schrödinger equation and can be rephrased as

$$|\Psi(t)\rangle = e^{-i\hat{H}t} |\Psi(0)\rangle. \quad (2.22)$$

We are interested in the case where there are no initial correlations between the field and the mechanical oscillator. Therefore, we choose an initial state of the form

$$|\Psi(0)\rangle = \sum_{n=0}^{\infty} a_n |n\rangle_c |\psi\rangle_m, \quad (2.23)$$

where the exact form of  $|\psi\rangle_m$  depends on the desired initial conditions. The subscripts  $c$  and  $m$  refer to the optical cavity and mechanical quantum states respectively. In the following subsections we consider initial coherent, thermal, and squeezed states.

### 2.2.1.1 | Coherent state

We start off by setting the initial mechanical oscillator to a coherent state [73]

$$|\psi\rangle_m = |\alpha\rangle_m = \sum_{n=0}^{\infty} e^{-\frac{|\alpha|^2}{2}} \frac{\alpha^n}{\sqrt{n!}} |n\rangle_m, \quad \text{with } \alpha = |\alpha| e^{i\phi}, \quad (2.24)$$

which we write in terms of the field number states  $|n\rangle_m$  ( $n \in \mathbb{N}_0$ ). Here,  $|\alpha|$  is the amplitude of the coherent state and  $\phi$  its phase. We allow the coefficients  $a_n$  of the photon-number states to be general and only impose the normalization condition  $\sum_n |a_n|^2 = 1$ . The choice of the initial state in Eq. (2.24) is our basic approach for determining the time evolution of the system, and will eventually be extended to cover initial thermal and squeezed states of the mechanical oscillator.

The interaction Hamiltonian  $g\hat{a}^\dagger\hat{a}(\hat{b}^\dagger + \hat{b})$  commutes with the free Hamiltonian of the radiation field,  $\omega_c\hat{a}^\dagger\hat{a}$ , which yields

$${}_c\langle n | \hat{H} | m \rangle_c = [n\omega_c\hat{I} + \omega_m\hat{b}^\dagger\hat{b} + ng(\hat{b}^\dagger + \hat{b})] \delta_{n,m} \quad (2.25)$$

with  $\delta_{n,m}$  being the Kronecker delta and  $\hat{I}$  the identity operator on the Hilbert space of the mechanical oscillator. Thus, the Hamiltonian (2.20) is block-diagonal with respect to photon-number states  $|n\rangle_c$ .

In order to evaluate the expression  $\exp\{-i\omega_m\hat{b}^\dagger\hat{b}t - ing(\hat{b}^\dagger + \hat{b})t\}$  we employ the Baker–Campbell–Hausdorff formula and obtain (see, for example, Ref. [74])

$$e^{-i\omega_m\hat{b}^\dagger\hat{b}t - ing(\hat{b}^\dagger + \hat{b})t} e^{i\omega_m\hat{b}^\dagger\hat{b}t} = e^{i\Phi_n(t)} e^{\alpha_n(t)\hat{b}^\dagger - \alpha_n^*(t)\hat{b}}, \quad (2.26)$$

where we have introduced the parameters

$$\alpha_n(t) = \frac{ng}{\omega_m} (e^{-i\omega_m t} - 1) \quad \text{and} \quad (2.27)$$

$$\Phi_n(t) = \frac{n^2g^2}{\omega_m^2} [\omega_m t - \sin(\omega_m t)]. \quad (2.28)$$

This implies that the full time evolution can be viewed as photon-number dependent displacements of the mechanical oscillator; with the help of Eqs. (2.25) and (2.26), we find

$$|\Psi(t)\rangle = \sum_{n=0}^{\infty} a_n e^{i\varphi_n(t)} |n\rangle_c |\beta_n(t)\rangle_m, \quad (2.29a)$$

$$\begin{aligned} \varphi_n(t) = & -n\omega_c t + \frac{n^2 g^2}{\omega_m^2} [\omega_m t - \sin(\omega_m t)] \\ & + \frac{ng}{\omega_m} \frac{\alpha^*(1 - e^{i\omega_m t}) - \alpha(1 - e^{-i\omega_m t})}{2i}, \end{aligned} \quad (2.29b)$$

$$\beta_n(t) = \frac{ng}{\omega_m} (e^{-i\omega_m t} - 1) + \alpha e^{-i\omega_m t}, \quad (2.29c)$$

where we have also used a corollary of the Baker–Campbell–Hausdorff formula, which states that the product of two displacement operators is also a displacement operator with an overall phase factor. The quantum state of Eq. (2.29) yields a complete description of the interaction between the single mode of the radiation field and the single vibration mode of the mechanical oscillator, i.e., neglecting all losses and sources of decoherence.

It may be useful to find the density operator of the optical field only. This is obtained by tracing out the mechanical system as

$$\hat{\rho}_F = \text{tr}_{\text{mech}} \{ |\Psi(t)\rangle \langle \Psi(t)| \} = \sum_{n,m=0}^{\infty} A_{n,m} |n\rangle_c \langle m| \quad (2.30)$$

with

$$\begin{aligned} A_{n,m} &= a_n a_m^* e^{i\varphi_n(t) - i\varphi_m(t) - (|\beta_n(t)|^2 + |\beta_m(t)|^2)/2 + \beta_n(t)\beta_m^*(t)} \\ &= a_n a_m^* e^{-g^2 f_{n,m}^{(2)}(t) + g f_{n,m}^{(1)}(t) - f_{n,m}^{(0)}(t)}, \end{aligned} \quad (2.31)$$

where

$$f_{n,m}^{(0)}(t) = i\omega_c t (n - m), \quad (2.32a)$$

$$f_{n,m}^{(1)}(t) = \frac{\alpha^*(1 - e^{i\omega_m t}) - \alpha(1 - e^{-i\omega_m t})}{\omega_m} (n - m), \quad (2.32b)$$

$$f_{n,m}^{(2)}(t) = \frac{1 - \cos(\omega_m t)}{\omega_m^2} (n - m)^2 - i \frac{\omega_m t - \sin(\omega_m t)}{\omega_m^2} (n^2 - m^2). \quad (2.32c)$$

### 2.2.1.2 | Thermal state

If the initial state of the mechanical oscillator is thermal, as a first step we must switch from discussing state vectors to density matrices. In this case, the uncorrelated initial state of the optomechanical system has the form

$$\hat{\rho}(t=0) = \sum_{n,m=0}^{\infty} a_n a_m^* \int \frac{e^{-|\gamma|^2/n_{\text{th}}}}{\pi n_{\text{th}}} |n\rangle_{\text{c}} |\gamma\rangle_{\text{m}} \langle m|_{\text{c}} \langle \gamma|_{\text{m}} d^2\gamma, \quad (2.33)$$

where we have used the Glauber–Sudarshan representation [75, 76] of the mechanical oscillator thermal state with the average phonon number

$$n_{\text{th}} = \left[ \exp\left(\frac{\hbar\omega_{\text{m}}}{k_{\text{B}}T}\right) - 1 \right]^{-1}, \quad (2.34)$$

where  $k_{\text{B}}$  is the Boltzmann constant and  $T$  the thermodynamic temperature of the initial state of the mechanical system. The time evolution of this system is given by

$$\hat{\rho}(t) = e^{-i\hat{H}t} \hat{\rho}(0) e^{i\hat{H}t}, \quad (2.35)$$

which yields

$$\hat{\rho}(t) = \sum_{n,m=0}^{\infty} a_n a_m^* \int \frac{e^{-|\gamma|^2/n_{\text{th}}}}{\pi n_{\text{th}}} e^{i\varphi_n(t) - i\varphi_m(t)} |n\rangle_{\text{c}} \langle m|_{\text{c}} |\beta_n(t)\rangle_{\text{m}} \langle \beta_m(t)|_{\text{m}} d^2\gamma, \quad (2.36)$$

where we have defined the phases

$$\varphi_n(t) = -n\omega_{\text{c}}t + \frac{n^2 g^2}{\omega_{\text{m}}^2} [\omega_{\text{m}}t - \sin(\omega_{\text{m}}t)] + \frac{ng}{\omega_{\text{m}}} \frac{\gamma^*(1 - e^{i\omega_{\text{m}}t}) - \gamma(1 - e^{-i\omega_{\text{m}}t})}{2i}, \quad (2.37)$$

$$\beta_n(t) = \frac{ng}{\omega_{\text{m}}} (e^{-i\omega_{\text{m}}t} - 1) + \gamma e^{-i\omega_{\text{m}}t}. \quad (2.38)$$

In the next step we trace out the mechanical degrees of freedom, as before, obtaining

$$\hat{\rho}_{\text{F}} = \text{tr}_{\text{mech}}\{\hat{\rho}(t)\} = \sum_{n,m=0}^{\infty} a_n a_m^* |n\rangle_{\text{c}} \langle m|_{\text{c}} \int \frac{e^{-|\gamma|^2/n_{\text{th}}}}{\pi n_{\text{th}}} B_{n,m}(\gamma, \gamma^*) d^2\gamma, \quad (2.39)$$

with the matrix  $B$  given by

$$B_{n,m}(\gamma, \gamma^*) = e^{-h_0 + h_1}, \quad (2.40)$$

and where the exponents are

$$h_0 = i\omega_{\text{c}}t(n - m) + \frac{g^2}{\omega_{\text{m}}^2} \left\{ [1 - \cos(\omega_{\text{m}}t)](n - m)^2 - i[\omega_{\text{m}}t - \sin(\omega_{\text{m}}t)](n^2 - m^2) \right\}, \text{ and} \quad (2.41)$$

$$h_1 = \frac{g}{\omega_{\text{m}}} [\gamma^*(1 - e^{i\omega_{\text{m}}t}) - \gamma(1 - e^{-i\omega_{\text{m}}t})](n - m). \quad (2.42)$$



Now, we perform the Gaussian integral by using  $d^2\gamma = d\text{Re}\{\gamma\} d\text{Im}\{\gamma\}$  and obtain a density matrix in the form of Eq. (2.30). Employing the notation of Eq. (2.31), we find

$$f_{n,m}^{(0)}(t) = i\omega_c t(n-m), \quad (2.43)$$

$$f_{n,m}^{(1)}(t) = 0, \quad (2.44)$$

$$f_{n,m}^{(2)}(t) = (2n_{\text{th}} + 1) \frac{1 - \cos(\omega_m t)}{\omega_m^2} (n-m)^2 - i \frac{\omega_m t - \sin(\omega_m t)}{\omega_m^2} (n^2 - m^2). \quad (2.45)$$

### 2.2.1.3 | Squeezed state

Let us now consider the case where the initial state of the mechanical system is a displaced squeezed state; we write, therefore,

$$|\Psi(0)\rangle = \sum_{n=0}^{\infty} a_n |n\rangle_c |\alpha, \zeta\rangle_m \quad (2.46)$$

with the mechanical oscillator state being defined as [77]

$$|\alpha, \zeta\rangle_m = \hat{D}(\alpha) \hat{S}(\zeta) |0\rangle_m \quad (2.47)$$

where  $\hat{D}(\alpha) = \exp(\alpha \hat{a}^\dagger - \alpha^* \hat{a})$ , with  $\alpha = |\alpha| e^{i\phi}$ , is the displacement operator, and  $\hat{S}(\zeta) = \exp[\frac{1}{2}(\zeta^* \hat{b}^2 - \zeta \hat{b}^{\dagger 2})]$ , with  $\zeta = |\zeta| e^{i\theta}$ , is the squeezing operator.

We employ the squeezed state of Eq. (2.47); in passing, however, we note that it is possible to invert the order of the displacement and squeezing operator. This results in a generalized squeezed state, which differs from the original state by the displacement parameter:

$$\hat{S}(\zeta) \hat{D}(\alpha) = \hat{D}[\alpha \cosh(|\zeta|) - \alpha^* e^{i\theta} \sinh(|\zeta|)] \hat{S}(\zeta). \quad (2.48)$$

Exploiting the block-diagonal structure of the Hamiltonian with respect to the photon-number states  $|n\rangle_c$ , and Eq. (2.26), we find

$${}_c \langle n | e^{-i\hat{H}t} |\Psi(0)\rangle = a_n e^{i\varphi_n(t)} |\beta_n(t), \zeta e^{-2i\omega_m t}\rangle_m \quad (2.49)$$

where  $\varphi_n(t)$  and  $\beta_n(t)$  are defined in Eqs. (2.29). Next, tracing out the mechanical degrees of freedom yields the state of the field in the form of Eq. (2.30), with

$$A_{n,m} = a_n a_m^* e^{i\varphi_n(t) - i\varphi_m(t)} \times \text{tr}\{|\beta_n(t), \zeta e^{-2i\omega_m t}\rangle \langle \beta_m(t), \zeta e^{-2i\omega_m t}|\}. \quad (2.50)$$

The trace in this equation can be evaluated with the help of the Glauber–Sudarshan representation, which allows us to write

$$\text{tr}\{|\beta_n(t), \zeta e^{-2i\omega_m t}\rangle \langle \beta_m(t), \zeta e^{-2i\omega_m t}|\} = \int \frac{d^2\gamma}{\pi} \langle \gamma | \beta_n(t), \zeta e^{-2i\omega_m t}\rangle \langle \beta_m(t), \zeta e^{-2i\omega_m t} | \gamma \rangle. \quad (2.51)$$

First, we note that

$$\langle \gamma | \beta_n(t), \zeta e^{-2i\omega_m t} \rangle_m = e^{-(\gamma\beta_n^*(t) - \gamma^*\beta_n(t))/2} \langle 0 | \hat{D}^\dagger(\gamma - \beta_n(t)) \hat{S}(\zeta e^{-2i\omega_m t}) | 0 \rangle, \quad (2.52)$$

where we have used the relation  $\hat{D}^\dagger(-\gamma) = \hat{D}(\gamma)$ . The overlap integral between the coherent state  $|\gamma\rangle$  and the squeezed state  $|0, \zeta\rangle$  is

$$\langle \gamma | 0, \zeta \rangle = \sqrt{\frac{e^{-|\gamma|^2}}{\cosh(|\zeta|)}} \exp\left[-\frac{1}{2}\gamma^* \zeta \tanh(|\zeta|)\right]. \quad (2.53)$$

For the purposes of Eq. (2.52) we thus obtain

$$\begin{aligned} \langle \gamma | \beta_n(t), \zeta e^{-2i\omega_m t} \rangle_m &= \sqrt{\frac{e^{-|\gamma - \beta_n(t)|^2 - \gamma\beta_n^*(t) + \gamma^*\beta_n(t)}}{\cosh(|\zeta|)}} \\ &\times \exp\left\{-\frac{1}{2}[\gamma^* - \beta_n^*(t)]^2 e^{i(\theta - 2\omega_m t)} \tanh(|\zeta|)\right\}. \end{aligned} \quad (2.54)$$

Substituting this result into Eq. (2.51) and performing the integral by using  $d^2\gamma = d\text{Re}\{\gamma\} d\text{Im}\{\gamma\}$  we obtain the coefficients in Eq. (2.31):

$$\begin{aligned} f_{n,m}^{(0)} &= i\omega_c t(n - m) + |\alpha|^2 [1 + \tanh(|\zeta|) \cos(\theta - 2\phi)] - I^{(0)} \\ &\quad + \ln\left[\cosh(|\zeta|) \sqrt{1 - \tanh^2(|\zeta|)}\right], \end{aligned} \quad (2.55a)$$

$$\begin{aligned} f_{n,m}^{(1)}(t) &= \frac{\alpha^*(1 - e^{i\omega_m t})}{\omega_m} (n - m) + \frac{I_{n,m}^{(1)}}{\omega_m} \\ &\quad + \tanh(|\zeta|) \frac{\alpha^*(1 - e^{-i\omega_m t}) e^{i\theta} n + \alpha(1 - e^{i\omega_m t}) e^{-i\theta} m}{2\omega_m} \end{aligned} \quad (2.55b)$$

$$\begin{aligned} f_{n,m}^{(2)}(t) &= -i \frac{\omega_m t - \sin(\omega_m t)}{\omega_m^2} (n^2 - m^2) \\ &\quad + \tanh(|\zeta|) \frac{(e^{-i\omega_m t} - 1)^2 e^{i\theta} n^2 + (e^{i\omega_m t} - 1)^2 e^{-i\theta} m^2}{2\omega_m^2} \\ &\quad + \frac{1 - \cos \omega_m t}{\omega_m^2} (n^2 + m^2) + \frac{I_{n,m}^{(2)}}{\omega_m^2}, \end{aligned} \quad (2.55c)$$

where, for simplicity of presentation, we collected the contributions given by the origi-

nal state in the coefficients  $I^{(0)}$ ,  $I_{n,m}^{(1)}$  and  $I_{n,m}^{(2)}$  defined as

$$I_{n,m}^{(2)} = \zeta^{(0)} [\chi_{n,m}^{(1)} + \tanh^2(|\zeta|)\chi_{n,m}^{(3)}]^2 - \zeta^{(1)} \left\{ \chi_{n,m}^{(2)} + \tanh^2(|\zeta|)\chi_{n,m}^{(4)} + \zeta^{(2)} [\chi_{n,m}^{(1)} + \tanh^2(|\zeta|)\chi_{n,m}^{(3)}] \right\}^2, \quad (2.56a)$$

$$\begin{aligned} I_{n,m}^{(1)} = & 4|\alpha| \left( \zeta^{(0)} [\chi_{n,m}^{(1)} + \tanh^2(|\zeta|)\chi_{n,m}^{(3)}] i [\sin(z_1) + \tanh(|\zeta|) \sin(z_2)] \right. \\ & + \zeta^{(1)} \{ \chi_{n,m}^{(2)} + \tanh^2(|\zeta|)\chi_{n,m}^{(4)} + \zeta^{(2)} [\chi_{n,m}^{(1)} \\ & \left. + \tanh^2(|\zeta|)\chi_{n,m}^{(3)}] \} \{ \cos(z_1) + \tanh(|\zeta|) \cos(z_2) - i\zeta^{(2)} [\sin(z_1) + \tanh(|\zeta|) \sin(z_2)] \} \right), \end{aligned} \quad (2.56b)$$

$$\begin{aligned} I^{(0)} = & 4|\alpha|^2 \left( \zeta^{(0)} [\sin(z_1) + \tanh(|\zeta|) \sin(z_2)]^2 + \zeta^{(1)} \{ [\cos(z_1) + \tanh(|\zeta|) \cos(z_2)] \right. \\ & \left. - i\zeta^{(2)} [\sin(z_1) + \tanh(|\zeta|) \sin(z_2)] \}^2 \right), \end{aligned} \quad (2.56c)$$

where  $z_1 = \omega_{\text{m}}t - \phi$ ,  $z_2 = \omega_{\text{m}}t - \phi - \theta$  and we have defined the functions

$$\chi_{n,m}^{(1)} = n(e^{-i\omega_{\text{m}}t} - 1) - m(e^{i\omega_{\text{m}}t} - 1), \quad (2.57a)$$

$$\chi_{n,m}^{(2)} = n(e^{-i\omega_{\text{m}}t} - 1) + m(e^{i\omega_{\text{m}}t} - 1), \quad (2.57b)$$

$$\chi_{n,m}^{(3)} = n(1 - e^{-i\omega_{\text{m}}t})e^{i(\theta - \omega_{\text{m}}t)} - m(1 - e^{i\omega_{\text{m}}t})e^{-i(\theta - \omega_{\text{m}}t)}, \quad (2.57c)$$

$$\chi_{n,m}^{(4)} = n(1 - e^{-i\omega_{\text{m}}t})e^{i(\theta - \omega_{\text{m}}t)} + m(1 - e^{i\omega_{\text{m}}t})e^{-i(\theta - \omega_{\text{m}}t)}, \quad (2.57d)$$

as well as the functions

$$\zeta^{(0)} = \frac{1}{4[1 - \tanh(|\zeta|) \cos(z)]}, \quad (2.58a)$$

$$\zeta^{(1)} = \frac{1 - \tanh(|\zeta|) \cos(z)}{4[1 - \tanh^2(|\zeta|)]}, \text{ and} \quad (2.58b)$$

$$\zeta^{(2)} = i \frac{\tanh(|\zeta|) \sin(z)}{1 - \tanh(|\zeta|) \cos(z)}, \quad (2.58c)$$

with  $z = \theta - 2\omega_{\text{m}}t$ .

## 2.3 | The driving and the linearisation procedure

As mentioned above, the Hamiltonian (2.15) is valid when the amplitude of the intracavity field is large enough that we can ignore the Casimir contribution to the radiation pressure force. However, in a realistic experimental set-up, many mechanical and optical modes contribute to the dynamics, making very inaccurate the approximation

in Eq. (2.19). We can overcome this issue applying an external laser with a spectral linewidth smaller than the spacing between two optical modes. In this way the driving laser populates only one optical mode of the cavity. Therefore, we can use the single-mode approximation under the assumption that only one cavity mode gives a relevant contribution to the dynamics. With this condition, we can represent the laser as a monochromatic field with frequency  $\omega_L$ . This adds to the Hamiltonian the term

$$H^d = i\hbar \left( \varepsilon \hat{a}^\dagger e^{-i\omega_L t} - \varepsilon^* \hat{a} e^{i\omega_L t} \right), \quad (2.59)$$

where  $|\varepsilon| = \sqrt{\frac{P k_{\text{ex}}}{\hbar \omega_L}}$  is the laser intensity inside the cavity,  $P$  is the laser power and  $k_{\text{ex}}$  the cavity loss rate. Equation (2.59) has been derived with the input-output formalism [78] which is extensively described in the next chapter.

It is convenient to perform an unitary transformation  $U$  on the full Hamiltonian  $H = H^{\text{om}} + H^d$  to switch to a rotating frame at frequency  $\omega_L$

$$H \longrightarrow H' = U H U^\dagger - i\hbar U \frac{\partial U^\dagger}{\partial t}, \quad U(t) = \exp\{-i\omega_L \hat{a}^\dagger \hat{a} t\}. \quad (2.60)$$

Using the commutation relations

$$[\hat{a}, \hat{a}^\dagger] = 1, \quad [\hat{a}, \hat{a}^\dagger \hat{a}] = \hat{a}, \quad e^{i\omega_L \hat{a}^\dagger \hat{a} t} \hat{a} e^{-i\omega_L \hat{a}^\dagger \hat{a} t} = \hat{a} e^{-i\omega_L t} \quad (2.61)$$

and Eq. (2.60), the Hamiltonian can be written as

$$H' = -\hbar \Delta \hat{a}^\dagger \hat{a} + \hbar \omega_m \hat{b}^\dagger \hat{b} + i\hbar \varepsilon (\hat{a} + \hat{a}^\dagger) - \hbar g_0 \hat{a}^\dagger \hat{a} (\hat{b} + \hat{b}^\dagger). \quad (2.62)$$

The parameter  $\Delta = \omega_L - \omega_0$  is called detuning and it has very important consequences in optomechanics whenever it is greater or lower than zero. In particular, if  $\Delta > 0$  we talk about blue detuning and it can lead to mechanical amplification, heating [79] and other quantum effects like squeezing[80]. Otherwise, if  $\Delta < 0$ , we are in the red detuning regime that has been used to perform cooling [81], achieve stability of the system and reach the beam splitter regime, where the number of excitons is conserved. Those effects are beyond the purpose of this thesis and we address to [8] for further explanations .

### 2.3.1 | Optomechanical equations of motion

We can finally merge together what we learned until here and write the Hamiltonian as

$$\hat{H} = \frac{\hat{p}^2}{2m} + \frac{1}{2} m \omega_m^2 \hat{q}^2 - \hbar \Delta_0 \hat{a}^\dagger \hat{a} - \hbar \frac{g_0}{x_{zpf}} \hat{a}^\dagger \hat{a} \hat{q} + i\hbar \varepsilon (\hat{a} + \hat{a}^\dagger), \quad (2.63)$$

which contains in order, the mechanical oscillator, the electromagnetic cavity field, the optomechanical interaction term and the external laser, all written in the rotating frame. Our goal of this section is to write the equations of motion for the operators involved in the dynamics. A realistic description has to consider also the contribution due to the leaking and absorption of energy toward the external world. The optical system is indeed coupled to an environment that is usually and fairly reasonably represented as a thermal bath of photons [82]. The master equation of the optical density operator  $\hat{\rho}_o$  shows a Markovian dynamics and can be easily written in Lindblad form [83]

$$\frac{d}{dt}\hat{\rho}_o = \frac{i}{\hbar}[\hat{\rho}_o, \hat{H}] + \kappa\hat{a}\hat{\rho}_o\hat{a}^\dagger - \frac{\kappa}{2}\{\hat{a}^\dagger\hat{a}, \hat{\rho}_o\}. \quad (2.64)$$

Moreover, the mechanics is subjected to Brownian noise coming from the physical support of the mirror. Here the Markovian dynamics takes place only in the high temperature limit [84] whereas the Caldeira-Leggett master equation offers a more suitable description for low temperature cases:

$$\frac{d}{dt}\hat{\rho}_m = \frac{i}{\hbar}[\hat{\rho}_m, \hat{H}] + \frac{i}{\hbar}\gamma[\{\hat{p}, \hat{\rho}_m\}, \hat{q}] - \frac{2m\gamma k_B T}{\hbar^2}[\hat{q}, [\hat{q}, \hat{\rho}_m]], \quad (2.65)$$

where  $\gamma$  is the mechanical dissipation coefficient,  $k_B$  is the Boltzmann constant,  $T$  is the temperature of the mechanical environment and  $\hat{\rho}_m$  is the mechanical density operator. Hence the whole system is described by the combination of the two master equations (2.64) and (2.65) applied on the global density operator  $\hat{\rho}$ . Following Ref. [85], from the master equation we can find the corresponding quantum Langevin equation for the optical and mechanical fields operators  $\hat{a}$  and  $\hat{b}$  respectively

$$\frac{d\hat{a}}{dt} = (i\Delta - \frac{\kappa}{2})\hat{a} + ig_0(\hat{b} + \hat{b}^\dagger)\hat{a} + \sqrt{\kappa}\hat{a}^{(in)}(t) \quad (2.66a)$$

$$\frac{d\hat{b}}{dt} = (-i\omega_m - \frac{\gamma}{2})\hat{b} + ig_0\hat{a}^\dagger\hat{a} + \sqrt{\gamma}\hat{b}^{(in)}(t), \quad (2.66b)$$

and analogously for the adjoint operators  $\hat{a}^\dagger$  and  $\hat{b}^\dagger$ . Here we stress the fact that the quantum Langevin equations are not always analytically or numerically solvable, depending on the initial conditions and on the extension of the Hilbert space. Therefore, we often need to rely on the linearisation procedure which in some cases allows us to consider the subset of the Hilbert space with fixed number of excitation. If we consider a stationary state with mean value  $\alpha = \langle \hat{a} \rangle \gg 1$  we can expand the field around this value.

This corresponds to the substitution  $\hat{a} \rightarrow \hat{a} + \alpha\mathbb{1}$ , that is the application of a displacement operator  $D_{\hat{a}}(\alpha)$  on the optical field  $\hat{a}$ . Consistently, this affects also the mechanical oscillator by shifting the minimum of the harmonic potential. This is described by the application of another displacement operator  $D_{\hat{b}}(\beta)$  on the mechanical field  $\hat{b}$ , with

$$\hat{b} = \sqrt{\frac{m\omega_m}{2\hbar}} \left( \hat{q} + \frac{i}{m\omega_m} \hat{p} \right) \quad (2.67)$$

$$\hat{b}^\dagger = \sqrt{\frac{m\omega_m}{2\hbar}} \left( \hat{q} - \frac{i}{m\omega_m} \hat{p} \right) \quad (2.68)$$

The displacement operator is defined such that

$$D_\delta^\dagger(\sigma) \delta D_\delta(\sigma) = \hat{\delta} + \sigma\mathbb{1}. \quad (2.69)$$

The above equations also define relations between  $(\beta, \beta^*)$  and  $(q_0, p_0)$ . From the physics point of view the application of the displacement operator represents the description of the dynamics of the steady state. If we suppose the system to start from a Gaussian ground state, the application of a high-intensity laser field leads the optical field to reach a steady state with amplitude  $\alpha$  and allows us to consider only the quantum fluctuations around this value. This affects also the mechanics with the optical spring effect that shifts the minimal of the mechanical harmonic potential and let us consider the quantum mechanical fluctuations of the mirror. This allows us to neglect the second order terms of the Hamiltonian, leaving to a certain extent the Gaussian nature of the state intact. In this thesis we will make use of the gaussianity of the steady state in Chapter 6.

Applying the above displacements on the full master equation obtained combining Eqs. (2.64) and (2.65) leads to a linear dynamics, for both  $\hat{a}$  and  $\hat{b}$ . Transforming back into the operators  $\hat{p}$  and  $\hat{q}$  yields to a driving free Hamiltonian

$$\hat{H}' = \hbar\Delta\hat{a}^\dagger\hat{a} + \frac{\hat{p}^2}{2m} + \frac{1}{2}m\omega_m^2\hat{q}^2 - \hbar g_0\alpha(\hat{a} + \hat{a}^\dagger)\hat{q}. \quad (2.70)$$

This Hamiltonian is the one we will consider in our further investigations since it can be used to describe most of the optomechanics experiments. It has been obtained after setting the additional conditions that

$$\Delta = -\Delta_0 - \hbar \frac{g_0^2 |\alpha|^2}{\omega_m^2 m}, \quad (2.71a)$$

$$i\varepsilon = \Delta_0\alpha + g_0\alpha q_0 - i\frac{\kappa}{2}\alpha, \quad (2.71b)$$

$$q_0 = \hbar \frac{g_0 |\alpha|^2}{\omega_m^2 m}. \quad (2.71c)$$

It can be proved that the above transformation leaves unchanged the optical and Brownian master equations (2.64)-(2.65) with the result that the new shifted operators  $\hat{a}$  and  $\hat{q}$  undergo the same optical and mechanical decay. The above conditions do not shift the momentum operator  $\hat{p}$ . It's worth to notice that the mechanical damping rate  $\gamma$  does not enter in the conditions and this is due to the form of the Caldeira-Leggett master equation.

An other interesting feature that arises from Eqs. (2.71) is the bistability. Together, they yield a third degree equation for  $|\alpha|$ . Depending on the value of the power  $P$  we may encounter a bistability of the system that will give two different solutions for the shift in the rest position of the mirror  $q_0$ . This phenomena is called bistability [86]. In quantum mechanics this can give rise to possible superposition of different equilibrium points leading to a non specified value for the the number of photons in the cavity  $|\alpha|^2 = \bar{n}_{cav}$ , in fact making impossible the linearisation. However, the bistability region can be avoided controlling the power of the driving laser  $P$ [87]. In a stable regime the intracavity number of photons  $\bar{n}_{cav}$  is well defined and we can apply the linearisation. Considering the aforementioned Hamiltonian (2.70) the quantum Langevin equations become

$$\frac{d}{dt}\hat{a}(t) = -i\Delta\hat{a}(t) + ig\alpha\hat{q}(t) - \frac{\kappa}{2}\hat{a}(t) + \sqrt{\kappa}\hat{a}^{(in)}(t), \quad (2.72a)$$

$$\frac{d}{dt}\hat{a}^\dagger(t) = i\Delta\hat{a}^\dagger(t) - ig\alpha\hat{q}(t) - \frac{\kappa}{2}\hat{a}^\dagger(t) + \sqrt{\kappa}\hat{a}^{(in)\dagger}(t), \quad (2.72b)$$

$$\frac{d}{dt}\hat{q}(t) = \frac{\hat{p}(t)}{m}, \quad (2.72c)$$

$$\frac{d}{dt}\hat{p}(t) = -m\omega_m^2\hat{q}(t) - \gamma\hat{p}(t) + g\alpha(\hat{a}(t) + \hat{a}^\dagger(t)) + \hat{\xi}(t). \quad (2.72d)$$

## 2.4 | Gaussian steady state

Optomechanics is characterized by the non-linear dynamics expressed by Eqs. (2.66). However the linearisation procedure leads us to the linear quantum Langevin equations (2.72), which depend on the Hamiltonian (2.70). It is possible, starting from the vacuum state and applying the procedure describe in the previous section, to reach a state that is Gaussian, i.e. that is completely described by its first and second moment. In fact, the vacuum state is described by a Gaussian wave-function, and we know the bilinear Hamiltonian preserves the Gaussian nature of the state [88]. For this reason in this

section we introduce the Gaussian states from the mathematical and physical point of view. In particular we will focus on the phase space description of the quantum state.

A starting point is the *characteristic function*, defined as

$$\chi[\hat{\rho}](\lambda) = \text{Tr}[\hat{\rho}\hat{D}(\lambda)], \quad (2.73)$$

where  $\hat{\rho}$  is the density operator and  $\hat{D}(\lambda)$  is the displacement operator.  $\lambda$  is a  $n$ -dimensional vector, where  $n$  is the number of modes contributing to the state. Therefore,  $\hat{D}(\lambda)$  is the generalization of the operator defined in (2.69) to all the field operators. The displacement operator forms a complete set of operators. It means that any operator  $\hat{O}$  can be written in the basis of the displacement operators as

$$\hat{O} = \int_{\mathbb{C}^n} \frac{d^{2n}\lambda}{\pi^n} \text{Tr}[\hat{O}\hat{D}(\lambda)]\hat{D}(\lambda)^\dagger, \quad (2.74)$$

where the integral is performed over the real and imaginary part of  $\lambda$ . Hence, the characteristic function has the role of the complex coefficient of this expansion, and it can be written as

$$\hat{\rho} = \int_{\mathbb{C}^n} \frac{d^{2n}\lambda}{\pi^n} \chi[\hat{\rho}](\lambda)\hat{D}(\lambda)^\dagger. \quad (2.75)$$

The phase-space description ensures a one-to-one correspondence between the  $\chi$  function and the state. Furthermore, the characteristic function generates all the symmetrically ordered moments of the state

$$\text{Tr}[\hat{\rho}(\hat{a}_k^\dagger)^p \hat{a}_l^q]_S = (-)^q \frac{\partial^{p+q}}{\partial \lambda_k^p \partial \lambda_l^{*q}} \chi[\hat{\rho}](\lambda), \quad (2.76)$$

where, for instance, the symmetric order is s.t.  $[\hat{a}^\dagger \hat{a}]_S = \frac{1}{2}(\hat{a}^\dagger \hat{a} + \hat{a} \hat{a}^\dagger)$ .

Another important quantum phase space representation is given by the *Wigner function*  $W[\hat{\rho}](\alpha, \alpha^*)$ , defined as the Fourier transform of the characteristic function

$$W[\hat{\rho}](\alpha, \alpha^*) = \int_{\mathbb{C}^n} \frac{d^{2n}\lambda}{\pi^{2n}} \exp[-i(\lambda^* \alpha + \alpha^* \lambda)] \chi[\hat{\rho}](\lambda). \quad (2.77)$$

The function  $W[\rho](\alpha, \alpha^*)$  is a quasi-probability function, meaning that it's volume is one, but it can assume negative values. It also gives the expectation value of symmetrically ordered moments

$$\text{Tr}[\rho a^{\dagger l} a^q]_S = \int d^{2n} \alpha W[\rho](\alpha) \alpha^q (\alpha^*)^l. \quad (2.78)$$

More generally the Wigner function gives the expectation values of any symmetrically ordered functions of  $\hat{a}$  and  $\hat{a}^\dagger$ . To give an example the mean value of the symmetric ordered number operator  $\hat{a}^\dagger \hat{a}$  is

$$\frac{1}{2} \langle \hat{a} \hat{a}^\dagger + \hat{a}^\dagger \hat{a} \rangle = \int W(\alpha, \alpha^*) \alpha \alpha^* d^2 \alpha. \quad (2.79)$$



Equation (2.79) can be further generalized for any operator  $\hat{O}$  leading to

$$\langle \hat{O} \rangle = \int W(\alpha, \alpha^*) O_S(\alpha, \alpha^*) d^2\alpha, \quad (2.80)$$

where the function  $O_S(\alpha, \alpha^*)$  is the symmetrically ordered form of  $\hat{O}$ . Given the operator  $\hat{O} = \sum_{j,k} c_{jk} \hat{a}^{\dagger j} \hat{a}^k$  fully expanded on the field operators, we can find the symmetric function  $O_S(\alpha, \alpha^*)$  using Eq. (2.78). This leads to a general expression for the symmetric function

$$O_S(\alpha, \alpha^*) = \sum_{jk} c_{jk} \left[ \frac{\partial}{\partial \lambda} + \frac{\lambda^*}{2i} \right]^j \left[ \frac{\partial}{\partial \lambda^*} - \frac{\lambda}{2i} \right]^k \exp[i\lambda^* \alpha + i\lambda \alpha^*] |_{\lambda=\lambda^*=0}, \quad (2.81)$$

which can be used to calculate the different expectation values. It's worth to notice that the Wigner function has an analogue position-momentum representation. This is how it was originally introduced in 1932 by Wigner

$$W[\hat{\rho}](q, p) = \frac{1}{2\pi\hbar} \int d\zeta \exp\left(-\frac{i}{\hbar} p\zeta\right) \langle q + \frac{\zeta}{2} | \hat{\rho} | q - \frac{\zeta}{2} \rangle, \quad (2.82)$$

and it has a clear interpretation in terms of position and momentum. In fact, it gives the marginal distribution of  $q$  ( $p$ ) when the integration is performed on the conjugate variable  $p$  ( $q$ ). However, we stress the fact that the Wigner function is not a probability distribution since it can assume negative values, even though for a Gaussian state (2.82) is always positive.

As mentioned before the main feature of Gaussian state is that we can reconstruct all the state just knowing the first and second moments. For a Gaussian state with density operator  $\hat{\rho}_{GS}$  and dimension  $2n$ , the Wigner function is of the form

$$W[\hat{\rho}_{GS}](\{\alpha_i, \alpha_i^*\}_i) = \frac{1}{2^n \pi^n \sqrt{\text{Det}[\mathbf{c}]}} \exp \left[ -\frac{1}{2} (A - \langle A \rangle)^T \mathbf{c}^{-1} (A - \langle A \rangle) \right], \quad (2.83)$$

where  $A = (\alpha_1, \alpha_1^*, \dots, \alpha_n, \alpha_n^*)^T$  is the variables vector,  $\langle A \rangle$  is the vector of the first moment and  $\sigma_{ij} = \langle A_i A_j \rangle - \langle A_i \rangle \langle A_j \rangle$  is the covariance matrix. The density operator  $\hat{\rho}$  can be then reconstructed and eventually written as a Gaussian exponential of the creation and annihilation operators [89].

We conclude this chapter giving the conditions for which we can actually reach the Gaussian steady state. This is a branch of mathematics that studies the stability of the dynamics. In physics this corresponds into finding the conditions for which, at  $t \rightarrow \infty$ , the mean values of the operators  $\hat{a}$ ,  $\hat{q}$  and  $\hat{p}$  is constant. We will tackle this problem in the next section.

## 2.5 | Stability of the Hamiltonian

Here we address the more general concept of stability from a mathematical point of view. We start considering a first order linear coefficient constant system. In classical physics the evolution is ruled by the equation

$$\frac{d}{dt}x = A[x(t) - x_0], \quad \text{with } x_0 \text{ being the equilibrium point.} \quad (2.84)$$

When we study the stability we ask whether  $x(t)$  converges to  $x_0$  as  $t \rightarrow \infty$  for every initial condition  $x(0)$ . The equilibrium point is called globally stable if each eigenvalue of  $A$  has negative real part. In this case  $A$  is called a stable matrix. The solution of Eq. (2.84) is

$$x(t) = e^{At}[x(0) - x_0] + x_0, \quad (2.85)$$

as it can be proved applying the derivative with respect to time.

Let us now consider a first order non-linear system. The equation describing the evolution is then

$$\frac{d}{dt}x = f(x)[x(t) - x_0], \quad \text{with } f(0) = 0, \text{ and } \lim_{x \rightarrow \infty} x(t) = x_0. \quad (2.86)$$

Since  $f$  is not linear, matrix analysis cannot give enough contribution to describe all notions of stability for  $f$ . However, we can Taylor expand  $f$  around  $x_0$ ,

$$\frac{d}{dt}x = J_f[x(t) - x_0], \quad J_f = \left. \frac{\partial f_i}{\partial x_j} \right|_{x=0}, \quad (2.87)$$

and ask whether the system is locally stable, i.e. if the Jacobian  $J_f$  has negative real part of the eigenvalues. Most of the time the calculation of the eigenvalues is not straightforward, or it's analytically impossible, since it consists in finding the zeros of a high order characteristic polynomial. In this case, to find the stability conditions, we can apply the Routh-Hurwitz criterion, for which the matrix  $A \in M_n(\mathbb{R})$  is positive stable if and only if the leading principal minors of the Routh-Hurwitz matrix  $\Omega(A)$  are positive. The construction of the matrix consists in writing the characteristic polynomial  $P_A$  of the matrix  $A$ ,

$$P_A(t) = t^n + a_{n-1}t^{n-1} + \dots + a_0. \quad (2.88)$$

The coefficients  $a_k$  are then used to define the components of  $\Omega(A)$ . Given

$$a_k = (-1)^{n-k} E_{n-k}(A), \quad \text{for } k = 0, 1, \dots, n-1, \quad (2.89)$$

we can recognize  $E_k(A)$  as the sum of the  $\binom{n}{k}$  principal minors of order  $k$ . We then build the matrix  $\Omega(A)$  as

$$\Omega(A) = \begin{pmatrix} E_1 & E_3 & E_5 & \dots & 0 \\ 1 & E_2 & E_4 & \dots & \vdots \\ 0 & E_1 & E_3 & \ddots & \vdots \\ \vdots & 0 & E_1 & \ddots & 0 \\ 0 & 0 & 0 & 0 \dots & E_n \end{pmatrix}. \quad (2.90)$$

A leading principal minor is the minor of the leading principal submatrix. The leading principal minor of order  $k$  is the submatrix composed by the first  $k$  rows and  $k$  columns. For example

$$\text{minor}_1\Omega(A) = E_1, \quad (2.91)$$

$$\text{minor}_2\Omega(A) = \begin{vmatrix} E_1 & E_3 \\ 1 & E_2 \end{vmatrix} = E_1E_2 - E_3, \quad (2.92)$$

$$\text{minor}_3\Omega(A) = \begin{vmatrix} E_1 & E_3 & E_5 \\ 1 & E_2 & E_4 \\ 0 & E_1 & E_3 \end{vmatrix} = E_1(E_2E_3 - E_4) - (E_3^2 - E_1E_5), \quad (2.93)$$

and so on and so forth. The explicit calculations of  $\Omega(A)$  if  $n = 4$  leads to the Routh-Hurwitz matrix

$$\Omega(A) = \begin{pmatrix} -a_3 & -a_1 & 0 & 0 \\ 1 & a_2 & a_0 & 0 \\ 0 & -a_3 & -a_1 & 0 \\ 0 & -a_3 & -a_1 & 0 \\ 0 & 1 & a_2 & a_0 \end{pmatrix}, \quad (2.94)$$

whose leading minors have to be positive. To make an example, and give a connection with our main topics of optomechanics, we now calculate the stability of our system. Consider indeed the Langevin equations (2.72). After defining the vector of operators  $u = (\hat{a}, \hat{a}^\dagger, \hat{q}, \hat{p})^T$  and the vector of noise operators  $\eta = (\hat{a}^{\text{in}}, \hat{a}^{\dagger\text{in}}, 0, \hat{\xi})$ , we can write the equations of motion in a compact form as

$$\dot{u}(t) = Au(t) + \eta(t), \quad (2.95)$$

where  $A$  is the dynamical matrix whose components are given by the Langevin equations. The stability of the dynamics can be tested with the Routh-Hurwitz criterion, that leads to the following set of inequalities

$$\begin{aligned} \Delta > 0 \quad \wedge \quad & 8g^2\hbar\alpha^2\Delta - (4\Delta^2 + \kappa^2)m\omega_m^2 > 0 \\ \vee \\ \Delta < 0 \quad \wedge \quad & 32g^2\hbar\alpha^2\Delta(\gamma + \kappa)^2 + m\gamma\kappa\{(4\Delta^2 + \kappa^2)[4\Delta^2 + (2\gamma + \kappa)^2]\} \\ & + 8[(2\gamma + \kappa)\kappa - 4\Delta^2]\omega_m^2 + 16\omega_m^4 > 0 \end{aligned}$$

The stability of the system is also important to find relevant features through the Lyapunov theorem. It states that given a matrix  $A \in M_n$ ,  $A$  is positive-stable if and only if  $\exists G \in M_n > 0$  s.t.  $GA + A^*G = H > 0$ , with  $H, G$  s.t.  $H = H^\dagger, G = G^\dagger, H > 0$ . Furthermore  $A$  is positive stable if and only if  $G > 0$ . This theorem gives us a condition for the stability of the dynamics that can be useful in many situations. Let us consider a practical example and take the standard solution for Eq. (2.95)

$$u(t) = \exp(At)u(0) + \int_0^t dt' \exp[A(t-t')] \eta(t'). \quad (2.96)$$

The covariance matrix is given by

$$\sigma(t, s) = \frac{\langle u(t)u(s) + u(s)u(t) \rangle}{2}. \quad (2.97)$$

Taking  $t = s$  and applying the relations between the operators we find

$$\frac{d}{dt}\sigma(t) = A\sigma(t) + \sigma(t)A^T + D(t), \quad (2.98)$$

where we have defined  $\sigma(t, t) \equiv \sigma(t)$  and  $D(t)$  is a matrix that accounts for the noise correlations. Finally if  $A$  is stable at infinite time the system reaches a steady state and Eq. (2.98) assumes the Lyapunov form  $A\sigma + \sigma A^T = -D$ . Hence, we see that using the Lyapunov theorem we know that if  $A$  gives a stable dynamics, the covariance matrix  $\sigma$  exists and it is positive.

## 2.6 | Optomechanical array

When two or more optomechanical cavities are coupled together we can talk about optomechanical arrays. Usually the radiation can leak out from one cavity and be absorbed by the adjacent one, for example with an induction process. Similarly the mechanical motion in a cavity can spread into the next ones because of a common support. We can

describe the array composed of  $N$  optomechanical cavities with a tight binding Hamiltonian of the form

$$H = \sum_{i=1}^N H_i^{\text{om}} + \sum_{\langle i,j \rangle} (J_{ij} \hat{a}_i^\dagger \hat{a}_j + K_{ij} \hat{b}_i^\dagger \hat{b}_j), \quad (2.99)$$

where  $H_i^{\text{om}}$  is the optomechanical Hamiltonian (2.63) related to the  $i^{\text{th}}$  cavity and  $J, K$  are respectively the optical and mechanical hopping constants between the two  $i^{\text{th}}$  and  $j^{\text{th}}$  adjacent cavities. Eq. (2.99) is a typical Hamiltonian that is used in transport models. We will enter in the details of this subject in Chapter 4

Here we show that for this Hamiltonian we can apply all the tools we used for the single optomechanical cavity case. Indeed Eq. (2.99) is at most quadratic in the set of operators  $\{\hat{a}_i\}_{i=1}^N, \{\hat{b}_i\}_{i=1}^N$  and from Ref. [88] we know they transform Gaussian states into Gaussian states. For this reason we know the driven system will eventually reach a steady state. We can write the quantum Langevin equation for the system operators as

$$\frac{d\hat{a}_i}{dt} = i\Delta\hat{a}_i + ig_i(\hat{b}_i + \hat{b}_i^\dagger)\hat{a}_i + i \sum_{j \in \mathcal{U}_i} J_{ij} \hat{a}_j - \frac{k}{2} \hat{a}_i + \sqrt{k} \hat{a}_i^{\text{in}}, \quad (2.100a)$$

$$\frac{d\hat{b}_i}{dt} = -i\omega_m \hat{b}_i + ig_i \hat{a}_i^\dagger \hat{a}_i + i \sum_{j \in \mathcal{U}_i} K_{ij} \hat{b}_j - \frac{\gamma}{2} \hat{b}_i + \sqrt{\gamma} \hat{b}_i^{\text{in}}, \quad (2.100b)$$

where  $\mathcal{U}_i$  is the set of the nearest neighbor sites of the cavity  $i$ . The steady state is given by the condition that the dynamical matrix  $A$ , whose components are given by Eq. (2.100a), is stable. This leads the mean values of  $\langle a \rangle, \langle b \rangle$  to be constant for each site. Hence we get an equation that can be written in a compact form as

$$\sum_j A_{ij} \langle \hat{c}_j \rangle + \sqrt{\Gamma_i} \langle \hat{c}_i^{\text{in}} \rangle = 0, \quad (2.101)$$

where  $\hat{c}$  is the vector of the all site optical and mechanical operators,  $\Gamma = \text{diag}(\kappa, \dots, \gamma, \dots)$  is the diagonal matrix of optical and mechanical decay rates.

Once we have the steady solutions for the all the operators  $\hat{a}$  and  $\hat{b}$  we can linearise the Hamiltonian with the procedure described in the previous sections, yielding  $H_1$ . Therefore the Langevin equations Eq. (2.100a) assume the form

$$\frac{d\hat{a}_i}{dt} = i[\hat{a}_i, H_1] - \frac{k}{2} \hat{a}_i + \sqrt{k} \hat{a}_i^{\text{in}}, \quad (2.102a)$$

$$\frac{d\hat{b}_i}{dt} = i[\hat{b}_i, H_1] - \frac{\gamma}{2} \hat{b}_i + \sqrt{\gamma} \hat{b}_i^{\text{in}}. \quad (2.102b)$$

We finally describe the system in the frequency domain to obtain

$$(\omega\mathbb{1} - A)\hat{c} = \Gamma\hat{c}^{\text{in}}. \quad (2.103)$$

from which we can now calculate the covariance matrix  $\sigma(t, 0)$  whose components are  $[\sigma(t, 0)]_{i,j} = \langle \hat{c}_i(t)\hat{c}_j(0) \rangle$ , that defines the correlations among the steady state operators at different times. This quantity will be useful to analyze the transport of excitation in the array (see Chapter 4) and it will be extensively used in this thesis. Using Eq. 2.103 we find in the frequency domain  $[\sigma(\omega)]_{i,j} = iG_{ij}(\omega)$ , where  $G(\omega) = (\omega\mathbb{1} - A)^{-1}$  is the Green's function matrix that gives the propagation of the state into the array. Furthermore, the equation describes the dynamics of a system subject to external noise, which is the topic of the next chapter.

## 2.7 | Summary

In this chapter we have introduced the subject of optomechanics, which is the main focus of this dissertation. We have seen in Sec. 2.2 the Hamiltonian description originally provided by C.K. Law in Ref. [9] obtained applying the canonical quantization on the Maxwell equations of the electromagnetic field inside the cavity with moving-end mirror. The resulting dynamics can be approximated to a quadratic interaction between the optical field and the position operator of the mechanical oscillator. Although description provides a simplified and realistic view of optomechanics, for in more cases the contribution given by higher-order interactions is negligible, the solution of the equations of motion can be obtained only for few cases with particular initial conditions, some of which have been investigated in 2.2.1. In general, it is possible to obtain approximated solutions for any initial condition, using numerical calculus, but we need to keep in mind that the Hilbert space of the accessible quantum states is unbounded. Therefore, we should restrict the exploration to a finite number of states which we are more interested in. In Sec. 2.3 we showed that applying a driving laser to the optical cavity we can reach a steady state and consider only the operators describing the fluctuations around the mean values. In this picture the interaction becomes linear and the equations of motion can be easily solved. Furthermore, under the right conditions, as described in Sec. 2.5, the driven optomechanical cavity reaches at equilibrium a Gaussian quantum state, for which the system is fully described by its first and second moments. This will be the prominent description used in this dissertation, which allows us to solve the dynamics of even more complicated systems, as briefly shown in Sec. 2.6. In fact, we can analyze the transfer of excitation that occurs when several optomechanical cavities are coupled

together. The study of this phenomenon enters in the more wide field of quantum transport, which finds application energy transfer and in information processing devices. We will introduce this subject in Chapter 4 and show the applications in optomechanics in Chapter 5. In order to obtain relevant informations about transport properties we need to solve Eq. (2.100a) for an array of optomechanical cavities, where the values of the mechanical and optical hopping terms give rise to different emerging properties of the physical system. But even more important, as shown in Equation (2.103) is the input term, which ultimately accounts for the interaction between the system and the external environment. It represents the noise the outer world exerts on the optomechanical cavity and it accounts for different behavior in the quantum transport as noted by the fluctuation dissipation theorem. The role of the "rest of the universe" on the dynamics of the system is the subject of the next chapter, where we introduce how the Langevin equation comes up from the concept of open quantum system.

# Open quantum dynamics

## 3.1 | Introduction

Any physical system, regardless of how much we tried and managed to isolate, is actually surrounded by an external environment with which it interacts and exchanges energy, particles, and important physical quantities. Furthermore, quantum mechanics expects a certain amount of entanglement shared by the system and the rest of the universe. It would seem impossible to deal with the quantum theory, which demand to write the wavefunction of the universe. Fortunately, the theory of open quantum system allows us to handle the interactions between the system and the environment surrounding it and have a quite good description of the system. With regards to our optomechanical cavity, we see that both the photon field and the mechanical oscillator interact extensively with the environment. For instance, a non completely reflective mirror leads the cavity field to be affected by absorption and leaking to the environment. As we described in Chapter 2, the cavity field is often driven by an external laser. It hits the external surface of the cavity and passes in, amplifying the internal electromagnetic field. At the same time, the mechanical oscillator is subjected to losses due to dispersive support and affected by noise from external sources of vibration. The general effect of losses and gains lead the dynamics of the system to be non unitary. In particular, we have a situation where the amplitude of the fields is not conserved. All those effects are treated in the open quantum system theory.

In this chapter we want to address the theoretical aspects of open quantum system with a focus on the quantum Langevin equation which we already showed in Chapter 2. The effects of the system-environment interaction ranges from thermalization to decoherence. From the quantum Langevin equation point of view we can see them as the effect of a quantum noise affecting the dynamics. Here we show a little portion of the general



theory of open quantum system and we refer to other books, such as [85] and [82], for a wider description.

We start the chapter with the description of the classical Langevin equation. We then go to quantum mechanics giving a short description of the open quantum system theory. We then give a description of the quantum Brownian dynamics and finally give the general form of the quantum Langevin equation. We will see this has a particular role in the definition of input and output fields. To conclude we will apply these concepts to the optomechanical system, recovering the results showed in Chapter 2

## 3.2 | The classical Langevin equation

The Langevin equation originally aimed to provide a description of the Brownian motion, eventually having a much broader role in physics. In this section we follow Ref. [90] for the treatment of the Brownian motion and the classical Langevin equation. Let's first consider a particle of mass  $m$  freely moving in a fluid and subject to a friction. The Newton equation is  $m \frac{dv}{dt} = -\alpha v(t)$ , where  $\alpha$  is the friction term. This law was originally used by Stokes to describe a spherical particle embedded in a fluid. For the particle was big enough to ignore the fluctuations of the fluid, the solution  $v(t) = v_0 \exp(-\frac{\alpha}{m}t)$  finely described the dynamics. When considering small particles the fluctuations arise in the equation of motion in the form

$$\frac{d}{dt}v(t) = -\eta v(t) + \zeta(t), \quad (3.1)$$

where  $\eta = \alpha/m$  and  $\zeta(t)$  is the term representing the noise. The mean value of a physical quantity here is defined as

$$\langle A(t) \rangle = \int_{t-\tau/2}^{t+\tau/2} \frac{1}{\tau} A(s) ds, \quad (3.2)$$

with  $\tau$  being the time-scale of the system. We require  $\tau$  to be long compared to individual molecular collision time, but short enough compared to the relaxation time defined as the inverse of the friction constant  $\eta^{-1}$ . We ask the mean value of the noise to be  $\langle \zeta(t) \rangle = 0$ , so that in the long period the random effects of the noise average to zero. Furthermore we ask the correlation of the noise at different times to be null,  $\langle \zeta(t)\zeta(t') \rangle = 0$  for  $|t - t'| > \tau$ . This condition reflects the absence of memory in the dynamics. If we consider a particle with initial velocity  $v_0$  the solution to the classical Langevin equation is given by

$$v(t) = v_0 e^{-\eta t} + \int_0^t ds e^{-\eta(t-s)} \zeta(s). \quad (3.3)$$

In the limit  $\tau \rightarrow 0$  the correlation assumes a Dirac delta form  $\langle \zeta(t)\zeta(t') \rangle = q\delta(t - t')$ . With this condition we can consider an ensemble of particles with initial velocity  $v_0$  and get  $\langle v(t) \rangle = v_0 e^{-\eta t}$  and for the mean of the velocity squared

$$\begin{aligned} \langle v^2(t) \rangle &= v_0^2 e^{-2\eta t} + \int_0^t \int_0^t ds ds' e^{-\eta(t-s)} e^{-\eta(t-s')} q \delta(s - s') \\ &= v_0^2 e^{-2\eta t} + \frac{q}{2\eta} (1 - e^{-2\eta t}). \end{aligned} \quad (3.4)$$

From the equipartition theorem we have at thermal equilibrium

$$\left\langle \frac{mv^2}{2} \right\rangle = \frac{k_B T}{2}. \quad (3.5)$$

The equilibrium is reached for large times  $t \rightarrow \infty$ , when the first term of the r.h.s. of Eq. (3.4) goes to zero. Comparing the two expressions we obtain

$$q = 2\eta \frac{k_B T}{m}. \quad (3.6)$$

Equation (3.6) is also known as the fluctuation-dissipation relation [91], which relates the correlation of the noise with the friction factor  $\eta$ . A more general statement of the fluctuation-dissipation theorem involves the correlation of a system variable at different times [92]. We define the time correlation functions  $C(t)$  at equilibrium as

$$C(t) = \langle v(t)v(0) \rangle = \lim_{T \rightarrow \infty} \frac{1}{T} \int_0^T v(t+s)v(s) ds. \quad (3.7)$$

From the Wiener-Khinchin theorem, the power spectrum is the Fourier transform of the correlation function and at equilibrium we get

$$C(t) = \frac{k_B T}{m} e^{-\eta|t|}, \quad (3.8)$$

Thus, the power spectrum  $P(\omega)$  assumes the Lorentzian form

$$P(\omega) = \int dt \frac{1}{\sqrt{2\pi}} C(t) e^{i\omega t} = \frac{1}{\sqrt{2\pi}} \frac{k_B T}{m} \frac{2\eta}{\omega^2 + \eta^2}. \quad (3.9)$$

If we consider the noise  $\zeta(t)$  to be delta-correlated we have its power spectrum  $P_\zeta$  to represent white noise, in fact

$$C_\zeta(t) = 2\eta \frac{k_B T}{m} \delta(t) \quad (3.10a)$$

$$P_\zeta(t) = 2\eta \frac{k_B T}{m}, \quad (3.10b)$$

which is another example of fluctuation-dissipation relation. We now take a step further and consider the case of a particle in a fluid with an external force. With respect to Eq. (3.1) we have the addition of a term  $F^{\text{ext}}$ . If the force depends on the position, for instance  $F^{\text{ext}} = -kx$  we have

$$\frac{d^2x}{dt^2} = -\eta \frac{dx}{dt} - \frac{k}{m}x + \zeta(t), \quad (3.11)$$

that, after defined the spring frequency  $\omega_0 = \sqrt{\frac{k}{m}}$ , can be Fourier transformed into

$$x(\omega) = \frac{\zeta(\omega)}{(-\omega^2 - i\eta\omega + \omega_0^2)}. \quad (3.12)$$

In this case the power spectrum of the position  $P_x(\omega)$  describes a damped harmonic oscillator, with

$$\begin{aligned} P_x(\omega) &= \lim_{T \rightarrow \infty} \frac{1}{2T} \frac{|\zeta(\omega)|^2}{|\omega_0^2 - \omega^2 - i\eta\omega|^2} \\ &= 2\eta \frac{k_B T}{m} \frac{1}{(\omega^2 - \omega_0^2)^2 + \eta^2 \omega^2}. \end{aligned} \quad (3.13)$$

We want now to apply the results of this section into optomechanics. In fact, in the regime where many photons are present in the cavity, the Hamiltonian can be linearized and the mean values of the operators follow the classical equations of motion. Let's consider the operators  $x(t)$  and  $a(t)$  of a single optomechanical cavity in the linearized regime

$$\frac{d^2x(t)}{dt^2} = -\Omega^2 x - \gamma \frac{dx}{dt} + \frac{\hbar g}{m} (\alpha^* a + \alpha a^*) + \frac{F^{\text{ext}}}{m} \quad (3.14a)$$

$$\frac{da(t)}{dt} = \left( i\Delta - \frac{\kappa}{2} \right) a + iG\alpha x \quad (3.14b)$$

The equation (3.14a) is analogue to Eq. (3.11) with the extra term given by the optomechanical interaction. Moreover, the dynamics of the mechanical oscillator is coupled with the dynamics of the cavity field described in Eq. (3.14b). Thus, the Fourier transform of the mechanical motion is

$$x(\omega) = \frac{F^{\text{ext}}}{m[\Omega^2 - \omega^2 - i\omega\gamma] + \Sigma(\omega)} \quad (3.15)$$

where the denominator is the mechanical response function for the optomechanics. Note that it contains an extra term respect to the denominator in Eq. (3.12),  $\Sigma(\omega)$ , which

is called optomechanical self-energy [93]. When we set the resonant condition  $\omega = \Omega$  the imaginary part of  $\Sigma(\omega)$  gives an additional damping term

$$\gamma_{\text{opt}} = \frac{1}{m\Omega} \text{Im}[\Sigma(\Omega)], \quad (3.16)$$

which is due to the optomechanical interaction. Once again, the optical contribution to the mechanical damping is given by the fluctuations of the external force  $F^{\text{ext}}$ .

### 3.3 | The quantum Langevin equation

Classically the problem of a system interacting with an external source of noise has been coped by Langevin with its equation for a Brownian particle moving in a viscous fluid under the influence of a potential. In the previous chapter we analyzed the effect of an external force stirring the particle in a noise environment. Here we aim to find the quantum analog of Eq. (3.11) and a reasonable description of the quantum noise. In this section we will follow Refs. [82, 85].

In order to do so in our treatment we will need to assume [82] the external environment to be a thermal bath. i.e. a sum of harmonic oscillators, with a smooth frequency spectrum. We also require the coupling between the system and the bath to be linear in the bath harmonic oscillator operators and the coupling constant to be a smooth function of the frequency. We will use these conditions to produce a theory that describes the interaction of the system in a similar manner as the Langevin equation. The noise indeed can describe either an external signal, the fluctuations of the medium or the vacuum noise itself. This latter for instance is a component of quantum mechanics that cannot be neglected, or else the intrinsic rules of quantum mechanics, such as the canonical commutation relations, are violated [94] as we will see throughout this chapter.

Let's start from a general description of an open quantum system. When we refer to the pair system-environment the dynamics is described by a unitary transformation as the global system is closed. Given the total Hamiltonian  $H_{\text{SE}}$ , the quantum state  $\rho_{\text{SE}}$  fulfills the usual Heisenberg equation

$$\frac{d}{dt}\rho_{\text{SE}} = -i[H_{\text{SE}}, \rho_{\text{SE}}]. \quad (3.17)$$

However, if we want to describe just the dynamics of the system density operator  $\rho_{\text{S}} = \text{Tr}_{\text{E}}[\rho_{\text{SE}}]$  we need to trace out the environment degrees of freedom and Eq. (3.17) assumes the more generic form

$$\frac{d}{dt}\rho_{\text{S}} = \mathcal{L}[\rho_{\text{S}}], \quad (3.18)$$

where  $\mathcal{L}[\bullet]$  is the Liouvillian super-operator that gives the dynamics of the system. The time evolution of the density operator is called master equation and the approximations mentioned at the beginning of this section are useful in order to find a solution and a way to write it down.

We start from the description of the heat bath as a collection of harmonic oscillators

$$H_{\text{bath}} = \sum_n \left( \frac{p_n^2}{2m_n} + \frac{k_n q_n^2}{2} \right), \quad (3.19)$$

where  $p_n, q_n$  are the  $n^{\text{th}}$  bath canonical operators. We can write the total Hamiltonian as  $H_{\text{SE}} = H_{\text{sys}} + H_{\text{bath}} + H_{\text{int}}$  that is a sum of the system Hamiltonian, the bath Hamiltonian and the interaction respectively. The system Hamiltonian is a function of a vector of system operators  $\mathbf{Z}$ , such that  $H_{\text{sys}} = H_{\text{sys}}(\mathbf{Z})$ . It can however remain unspecified. The interaction has the form of a linear interaction between a system operator  $X$  and the bath operators  $q_n$ , yielding

$$H = H_{\text{sys}}(\mathbf{Z}) + \sum_n \left( \frac{p_n^2}{2m_n} + \frac{k_n}{2} (q_n - X)^2 \right). \quad (3.20)$$

In some models, as in the Caldeira-Leggett model [95], the interaction is added manually through a term  $-\sum_n k_n q_n X$ , and the quadratic term proportional to  $X^2$  is omitted. However, even though this interaction appears natural, lacks in making the energy spectrum bounded and eventually leads the bath to do not reach a thermal equilibrium state, with the result that the quadratic term has to be added manually [94]. Analogously to this interaction model, called independent oscillator model, we can consider the case where the system operator  $X$  interacts with the bath through a linear coupling with the momentum operators  $p_n$  of the bath. We can see that a simple canonical transformation leads the two models to be equivalent

$$\begin{aligned} q_n &\rightarrow p_n / \sqrt{k_n} \\ p_n &\rightarrow -q_n \sqrt{k_n} \\ \sqrt{k_n} &\rightarrow k_n. \end{aligned} \quad (3.21)$$

The Heisenberg equation for the operators  $p_n, q_n$  is

$$\dot{q}_n = p_n - k_n X \quad (3.22a)$$

$$\dot{p}_n = -\omega_n^2 q_n. \quad (3.22b)$$

We can also express the operators  $p_n, q_n$  in terms of the creation annihilation operators  $b_n^\dagger, b_n$  defined as

$$b_n^\dagger = \frac{\omega_n q_n - i p_n}{\sqrt{2\hbar\omega_n}} \quad b_n = \frac{\omega_n q_n + i p_n}{\sqrt{2\hbar\omega_n}}, \quad (3.23)$$

where the oscillator frequency is defined as  $\omega_n = \sqrt{\frac{k_n}{m_n}}$ , and finally find the Heisenberg equations for the bath operators

$$\dot{b}_n(t) = -i\omega_n b_n - k_n \sqrt{\frac{\omega_n}{2\hbar}} X, \quad (3.24)$$

whose solution is

$$b_n(t) = e^{-i\omega_n(t-t_0)} b_n(t_0) - k_n \sqrt{\frac{\omega_n}{2\hbar}} \int_{t_0}^t e^{-i\omega_n(t-t')} X(t') dt'. \quad (3.25)$$

To find the quantum Langevin equation for a generic system operator  $Y \in \mathbf{Z}$  we use the Heisenberg equation

$$\begin{aligned} \dot{Y} &= \frac{i}{\hbar} [H_{sys}, Y] + \frac{i}{2\hbar} \sum_n [\{Y, p_n - k_n X\}, k_n X] \\ &= \frac{i}{\hbar} [H_{sys}, Y] + \frac{i}{2\hbar} \sum_n [\{Y, q_n\}, k_n X], \end{aligned} \quad (3.26)$$

that is, after substituting the solution Eq. (3.25) in Eq. (3.26):

$$\dot{Y} = \frac{i}{\hbar} [H_{sys}, Y] - \frac{i}{2\hbar} [X, \{Y, \xi(t) - \int_{t_0}^t f(t-t') \dot{X}(t') dt' - f(t-t_0) X(t_0)\}], \quad (3.27)$$

where we have defined the functions  $\xi(t)$  and  $f(t)$  as

$$\xi(t) = i \sum_n k_n \sqrt{\frac{\hbar\omega_n}{2}} \left( b_n^\dagger(t_0) e^{i\omega_n(t-t_0)} - b_n(t_0) e^{-i\omega_n(t-t_0)} \right) \quad (3.28a)$$

$$f(t) = \sum_n k_n^2 \cos \omega_n t. \quad (3.28b)$$

We can see from Eq. (3.27) that  $f(t)$  gives the contributions from other times in the past and for this it is called memory function.

From now on we will consider the environment to be large enough that we can approximate the sum with integrals. So we extend our previous calculations to the continuum. Therefore we can write

$$f(t) = \int_{-\infty}^{\infty} \cos(\omega t) G(\omega) d\omega, \quad (3.29)$$

where  $G(\omega)$  has the significant role in the dynamics of governing the damping features.

### 3.3.1 | First Markov approximation

In order to proceed further with the calculation we perform what is usually called the first Markov approximation [82]. We state here that the correlations timescales of the reservoir are shorter than the decay timescale of the system. Furthermore we state that the timescale of validity of Eq. (3.26) are shorter than the gross timescale over which the system evolves. With these assumptions we can set the function  $G(\omega)$  to be constant,  $G(\omega) = \gamma/\pi$ . Equation (3.29) becomes:

$$f(t) = \frac{2\gamma}{\pi} \int_{-\infty}^{\infty} \cos(\omega t) d\omega = 2\gamma\delta(t). \quad (3.30)$$

Now the function  $f(t)$  describes a no-memory situation and the form of the Langevin equation is the most similar to the classical one, with

$$\dot{q}(t) = \frac{p(t)}{m} \quad (3.31a)$$

$$\dot{p}(t) = -V'(q(t)) - \gamma\dot{q}(t) + \zeta(t), \quad (3.31b)$$

with the difference that describes the time evolution of operators. Nevertheless, another important difference lies in the correlations of the noise operators. Whereas in the classical case the correlation is a delta function in the quantum framework we get

$$[\zeta(t), \zeta(t')] = 2i\hbar\gamma \frac{d}{dt} \delta(t - t'), \quad (3.32)$$

that means that even if the system shows no memory, the noise operators commutator still depends on past times. It represents a huge but necessary difference with respect to the classical case. We can use the explicit form of the memory function to finally write Eq. (3.27) as

$$\dot{Y} = \frac{i}{\hbar} [H_{sys}, Y] - \frac{i}{2\hbar} \{ [X, Y], \zeta(t) - \gamma\dot{X} \}. \quad (3.33)$$

The calculation of the commutation relations of the noise operator with the system operators leads to

$$[Y(t), \zeta(s)] = 2\gamma \frac{d}{ds} \left( u(t-s) [Y, X(s)] \right), \quad (3.34)$$

where

$$u(x) = \begin{cases} 1 & x > 0 \\ \frac{1}{2} & x = 0 \\ 0 & x < 0 \end{cases}. \quad (3.35)$$

The last equation saves the causality stating that the behavior of the operator  $Y$  depends only on past values of the noise operator  $\xi$ .

### 3.3.2 | The input-output formalism

Let's now address the quantum Langevin equation Eq. (3.27) to a case of interest where the interaction is between the ladder operators  $b, b^\dagger$  of the bath and a single system operator  $c$  and its Hermitian conjugate  $c^\dagger$ , i.e.

$$H_{SE} = H_{sys} + H_{bath} + H_{int}, \quad (3.36a)$$

$$H_{bath} = \hbar \int d\omega \omega b^\dagger b, \quad (3.36b)$$

$$H_{int} = i\hbar \int d\omega k(\omega) \left( b^\dagger c - c^\dagger b \right). \quad (3.36c)$$

Hence, the solution of the Langevin equation for the bath operator Eq. (3.25) becomes

$$b(\omega) = b_0(\omega) e^{-i\omega(t-t_0)} + k(\omega) \int_{t_0}^t e^{-i\omega(t-t')} c(t') dt' \quad (3.37)$$

and Eq. (3.26):

$$\dot{a} = -\frac{i}{\hbar} [a, H_{sys}] + \int d\omega k(\omega) \left( b^\dagger(\omega) [a, c] - [a, c^\dagger] b(\omega) \right). \quad (3.38)$$

We substitute the solution from Eq. (3.37) in Eq. (3.38) and apply the first Markov approximation, setting  $k(\omega) = \sqrt{\frac{\gamma}{2\pi}}$ . We also define the *in* field:

$$b^{(in)}(t) = \frac{1}{\sqrt{2\pi}} \int d\omega e^{-i\omega(t-t_0)} b_0(\omega). \quad (3.39)$$

The *in* operator represents a bosonic operator that fulfills the standard commutation relation,  $[b^{(in)}(t), b^{(in)}(t')] = \delta(t - t')$ . Eq. (3.38) reads

$$\dot{a} = -\frac{i}{\hbar} [a, H_{sys}] - \left( [a, c^\dagger] \left( \frac{\gamma}{2} c + \sqrt{\gamma} b^{(in)}(t) \right) - \left( \frac{\gamma}{2} c^\dagger + \sqrt{\gamma} b^{(in)\dagger}(t) \right) [a, c] \right). \quad (3.40)$$

In the equations above the damping is included in the terms  $\frac{\gamma}{2}c$  and  $\frac{\gamma}{2}c^\dagger$ . The noise is encoded in the operators  $b^{(in)}$  and  $b^{(in)\dagger}$ .

If we consider the integral in Eq. (3.37) to have extremes  $t, t_1$ , with  $t_1 > t$  we can define the *out* operator  $b^{(out)}(t) = \frac{1}{\sqrt{2\pi}} \int d\omega e^{-i\omega(t-t_1)} b_1(\omega)$  that describes the field going out from the cavity. After simple algebra we can finally show the input-output relation [78]

$$b^{(out)} = b^{(in)} - \sqrt{\gamma} c. \quad (3.41)$$



A hand wave interpretation of this equation considers the output field as the sum of the input field and the damped field that remains in the cavity.

Let's now consider the system to be a harmonic oscillator with  $H_{\text{sys}} = \hbar\omega_0 a^\dagger a$  and the typical interaction s.t.  $c = a$ . We can write Eq. (3.40) as:

$$\dot{a} = -i\omega_0 a - \frac{\gamma}{2}a + \sqrt{\gamma}b^{(\text{in})}(t). \quad (3.42)$$

As we have seen in the Chapter 2 we calculate the stationary value  $\alpha = \langle a \rangle$  of the operator  $a$ . We can average both sides of Eq. (3.42), setting the l.h.s. to zero. Defining  $\beta^{(\text{in})} = \langle b^{(\text{in})} \rangle$ , the stationary value is then reached for:

$$\alpha = \sqrt{\gamma} \frac{\beta^{(\text{in})}}{i\omega_0 - \frac{\gamma}{2}}. \quad (3.43)$$

The solution just presented refers to the simple situation of a single oscillator coupled with an external bath of oscillators. The stationary field gives in cavity QED an important quantity that has been necessary in the previous chapter to linearize the Hamiltonian and express the system in terms of the fluctuating field around the value  $\alpha$ . However, the solution for the stationary field in the case of optomechanics is slightly more complicated and it is described in chapter 2, Eq. (2.101) for the case of an optomechanical array.

## 3.4 | Application to optomechanics

In order to describe this optomechanical system effectively, one has to consider decoherence and excitation losses, i.e., the concept of open quantum systems has to be applied. In this section we will make use of the linearization procedure described in Chapter 2 and finally find the autocorrelation matrix of the system operators, which ultimately depends on the correlation of the noise.

The single mode field is affected by a decay with rate  $\kappa = \kappa_{\text{in}} + \kappa_{\text{loss}}$ , where  $\kappa_{\text{in}}$  is the loss rate associated with the input–output fields and  $\kappa_{\text{loss}}$  is related to what are commonly called internal losses [96]. The latter quantity could, for example, originate from the fact that the cavity mirrors act to scatter photons from the cavity mode of interest to other modes or to the outside environment. The mechanical oscillator is in contact with a phonon bath at temperature  $T$  and experiences a friction or decay rate  $\gamma$ . The dynamics is given in the Heisenberg picture with the use of the quantum Langevin equations

already expressed in Chapter 2, Eqs. (2.72)

$$\hat{a} = -i\omega_c \hat{a} + ig\hat{a}\hat{q} - \frac{\kappa}{2}\hat{a} + \sqrt{\kappa_{\text{in}}}\hat{a}_{\text{in}} + \sqrt{\kappa_{\text{loss}}}\hat{a}_{\text{loss}}, \quad (3.44a)$$

$$\hat{a}^\dagger = i\omega_c \hat{a}^\dagger - ig\hat{a}^\dagger\hat{q} - \frac{\kappa}{2}\hat{a}^\dagger + \sqrt{\kappa_{\text{in}}}\hat{a}_{\text{in}}^\dagger + \sqrt{\kappa_{\text{loss}}}\hat{a}_{\text{loss}}^\dagger, \quad (3.44b)$$

$$\hat{q} = \frac{\hat{p}}{m'}, \quad (3.44c)$$

$$\hat{p} = -m\omega_m^2 \hat{q} - \gamma \hat{p} + \hbar g \hat{a}^\dagger \hat{a} + \hat{\zeta}. \quad (3.44d)$$

where  $\hat{a}_{\text{in}}$  is the input noise operator associated with the modes of the radiation field outside the cavity.  $\hat{a}_{\text{loss}}$  is the operator describing the internal losses. The cavity operates at optical frequencies, i.e.,  $\hbar\omega_c/k_B T \gg 1$  holds to a very good approximation at reasonable temperatures, and therefore the operators  $\hat{a}_{\text{in}}(t)$  and  $\hat{a}_{\text{in}}^\dagger(t')$  represent a Markovian source of noise. Thus, they commute for  $t \neq t'$ . Their correlation functions in the vacuum state  $|0\rangle$  read

$$\langle 0 | \hat{a}_{\text{in}}(t) \hat{a}_{\text{in}}^\dagger(t') | 0 \rangle = \delta(t - t'), \quad (3.45a)$$

$$\langle 0 | \hat{a}_{\text{in}}^\dagger(t') \hat{a}_{\text{in}}(t) | 0 \rangle = 0. \quad (3.45b)$$

The operators  $\hat{a}_{\text{loss}}(t)$  and  $\hat{a}_{\text{loss}}^\dagger$  have similar commutation relations and furthermore they commute at all times with  $\hat{a}_{\text{in}}(t)$  and  $\hat{a}_{\text{in}}^\dagger(t')$ .

The mechanical oscillator is coupled to a thermal bath, via the quantum Brownian noise operator  $\hat{\zeta}(t)$ , which is non-Markovian. Making use of the spectral density  $J(\omega)$  of the phonon modes in the bath and the weak coupling of the mechanical oscillator to the bath [97] one can define the following functions [98]

$$\mathcal{D}_R(\tau) = \int_0^\infty d\omega J(\omega) \cos(\omega\tau) \coth\left(\frac{\hbar\omega}{2k_B T}\right) \quad (3.46a)$$

$$\mathcal{D}_I(\tau) = \int_0^\infty d\omega J(\omega) \sin(\omega\tau). \quad (3.46b)$$

Now, we are able to calculate the two-time correlation function of  $\hat{\zeta}(t)$ :

$$\langle \hat{\zeta}(t) \hat{\zeta}(t') \rangle = \hbar [\mathcal{D}_R(t - t') - i\mathcal{D}_I(t - t')]. \quad (3.47)$$

The mean of  $\hat{\zeta}(t)$  is zero and its non-Markovian nature allows us to preserve the correct commutation relations between  $\hat{p}$  and  $\hat{q}$  during the time evolution [98]. It is worth to highlight the difference between Markovian and non-Markovian noise. The Markovian noise is characterized by having a two-time correlation function proportional to a Dirac

delta. This situation is as close as possible to the classical Markovian description, where the noise at time  $t$  has no correlations with the noise at time  $t' \neq t$ . However, quantum mechanics forbids to consider genuine Markovian noise, albeit delta-correlated noise provides a good approximation when the temperature of the bath is much higher than the energy of the system, for the correlation function goes to zero at times shorter than the typical timescale of the dynamics. Thus, Brownian noise correlation functions such as Eq. (3.47), can be approximated into delta functions in the limit  $T \rightarrow \infty$ .

An extensively studied case is the Ohmic spectral density with a Lorentz–Drude cutoff function

$$J(\omega) = \frac{2m\gamma}{\pi} \omega \frac{\Omega^2}{\omega^2 + \Omega^2},$$

where  $\Omega$  is the high-frequency cutoff. An Ohmic spectral density with exponential cut-off [99],

$$J(\omega) = \frac{2m\gamma}{\pi} \omega \exp\left(-\frac{\omega}{\Omega}\right) \quad (3.48)$$

leads to very similar behavior to one with Lorentz–Drude cutoff function, albeit with the advantage that the integrations in Eqs. (3.46a), (3.46b) have analytical solutions in closed form:

$$\begin{aligned} \mathcal{D}_R(\tau) &= \frac{2m\gamma}{\pi} \frac{\Omega^2 (\Omega^2 \tau^2 - 1)}{(\Omega^2 \tau^2 + 1)^2} + \frac{2m\gamma}{\pi \hbar^2} (k_B T)^2 \left[ \Psi^{(1)}(z) + \Psi^{(1)}(z^*) \right], \\ z &= \frac{1 - i\Omega\tau}{\hbar\Omega} k_B T, \\ \mathcal{D}_I(\tau) &= \frac{2m\gamma}{\pi} \frac{2\Omega^3 \tau}{(\Omega^2 \tau^2 + 1)^2} \end{aligned}$$

with  $\Psi^{(1)}(z)$  being the polygamma function [100].

Usually the single mode of the cavity is driven by a laser with frequency  $\omega_L$  and intensity  $\epsilon$ . This process can be modified through the addition of the following term to the Hamiltonian, see Eqs. (2.59):

$$H_L = i\hbar\epsilon \left( \hat{a}^\dagger e^{-i\omega_L t} - \hat{a} e^{i\omega_L t} \right), \quad (3.49)$$

whose phases  $\pm\omega_L t$  can be easily absorbed after going into a rotating frame, see Eq.(2.60), with a resulting detuning for the optical frequency  $\Delta_0 = \omega_c - \omega_L$ . In terms of the power  $P$  of the laser, the driving intensity is  $\epsilon = \sqrt{2\kappa_{\text{in}} P / \hbar\omega_L}$ .

Under the assumption that  $|\alpha|$  is large, we can truncate the equations of motion to first order in the fluctuation operators. Finally, the differential equations of the shifted operators can be written in the concise form

$$\dot{u}(t) = Au(t) + \eta(t), \quad (3.50)$$

where we have defined the vector of operators  $u(t) = (\delta\hat{q}(t), \delta\hat{p}(t), \delta\hat{X}(t), \delta\hat{Y}(t))^T$ , which are the fluctuations operators and we have defined the two quadratures of the single mode field  $\delta\hat{X} = (\delta\hat{a}^\dagger + \delta\hat{a})/\sqrt{2}$  and  $\delta\hat{Y} = i(\delta\hat{a}^\dagger - \delta\hat{a})/\sqrt{2}$ . We define analogously the quadratures  $\hat{X}_{\text{in}}, \hat{Y}_{\text{in}}, \hat{X}_{\text{loss}}$  and  $\hat{Y}_{\text{loss}}$ . The vector of noise operators is

$$\eta(t) = (0, \hat{\xi}(t), \sqrt{\kappa_{\text{in}}}\hat{X}_{\text{in}}(t) + \sqrt{\kappa_{\text{loss}}}\hat{X}_{\text{loss}}(t), \sqrt{\kappa_{\text{in}}}\hat{Y}_{\text{in}}(t) + \sqrt{\kappa_{\text{loss}}}\hat{Y}_{\text{loss}}(t))^T.$$

Furthermore, we have

$$A = \begin{pmatrix} 0 & \frac{1}{m} & 0 & 0 \\ -m\omega_m^2 & -\gamma & \sqrt{2}\hbar g\alpha & 0 \\ 0 & 0 & -\frac{\kappa}{2} & \Delta \\ \sqrt{2}g\alpha & 0 & -\Delta & -\frac{\kappa}{2} \end{pmatrix}. \quad (3.51)$$

The solution to (3.50) reads

$$u(t) = \exp(At)u(0) + \int_0^t dt' \exp[A(t-t')] \eta(t'). \quad (3.52)$$

The autocorrelation matrix is given by

$$R(t, s) = \langle u(t)u(s)^T \rangle.$$

Making use of the relation

$$\langle u(0)\eta(t)^T \rangle = \langle \eta(t)u(0)^T \rangle = 0, \quad t \geq 0,$$

one finds for the autocorrelation matrix the expression

$$R(t, s) = \exp(At) \langle u(0)u(0)^T \rangle \exp(A^T s) + \int_0^t \int_0^s dt' dt'' \exp[A(t-t')] M(t' - t'') \exp[A^T(s-t'')]$$

where we defined the matrix

$$M(t' - t'') = \langle \eta(t')\eta(t'')^T \rangle = \begin{pmatrix} 0 & 0 & 0 & 0 \\ 0 & \langle \hat{\xi}(t')\hat{\xi}(t'') \rangle & 0 & 0 \\ 0 & 0 & \frac{\kappa}{2}\delta(t' - t'') & i\frac{\kappa}{2}\delta(t' - t'') \\ 0 & 0 & -i\frac{\kappa}{2}\delta(t' - t'') & \frac{\kappa}{2}\delta(t' - t'') \end{pmatrix}. \quad (3.53)$$

Let us consider the symmetric autocorrelation matrix

$$\sigma(t, s) = \frac{R(t, s) + R^T(t, s)}{2}.$$

Taking  $t = s$  we obtain

$$\frac{d}{dt}\sigma(t) = A\sigma(t) + \sigma(t)A^T + D(t),$$

where  $\sigma(t) \equiv \sigma(t, t)$ , and with

$$D(t) = \int_0^t dt' \frac{M(t-t') + M^T(t-t')}{2} \exp[A^T(t-t')] + \int_0^t dt' \exp[A(t-t')] \frac{M(t'-t) + M^T(t'-t)}{2}. \quad (3.54)$$

This can be further simplified via

$$M_1(t-t') = \frac{M(t-t') + M^T(t-t')}{2} = \begin{pmatrix} 0 & 0 & 0 & 0 \\ 0 & \hbar \mathcal{D}_R(t-t') & 0 & 0 \\ 0 & 0 & \frac{\kappa}{2} \delta(t-t') & 0 \\ 0 & 0 & 0 & \frac{\kappa}{2} \delta(t-t') \end{pmatrix},$$

because  $\mathcal{D}_R(-t) = \mathcal{D}_R(t)$  and  $\mathcal{D}_I(-t) = -\mathcal{D}_I(t)$ , which follows the implication that  $M_1(t-t') = M_1(t'-t)$ . Finally, we can write

$$D(t) = \int_0^t d\tau \left[ M_1(\tau) \exp(A^T \tau) + \exp(A \tau) M_1(\tau) \right]. \quad (3.55)$$

The stability of the system,  $\lim_{t \rightarrow \infty} \exp(At) = 0$ , can be derived by applying the Routh–Hurwitz criterion [101] which has been described in Chapter 2. This has been thoroughly investigated in the last decade and the two nontrivial conditions on the parameters of  $A$  show that if the system is stable, then the bistability of the dynamics is avoided [102]. From now on we consider these conditions to be satisfied. Therefore,  $u(t)$  for  $t \rightarrow \infty$  approaches zero, which implies that the autocorrelation matrix  $\sigma(t)$  coincides with the matrix in the stationary solution. The stationary correlation matrix is defined as  $\sigma = \lim_{t \rightarrow \infty} \sigma(t, t)$  and is the solution to the following Lyapunov equation

$$A\sigma + \sigma A^T = -D, \quad (3.56)$$

where we have defined the matrix

$$D = \int_0^\infty d\tau \left[ M_1(\tau) \exp(A^T \tau) + \exp(A \tau) M_1(\tau) \right]. \quad (3.57)$$

Note that the Lyapunov equation above works for any kind of noise and any possible noise correlations, as long as the dynamics is stable. We used them in our paper [3] and in Chapter 6 where a realistic description of an optomechanical cavity allows us to find the best strategy for the estimation of the Hamiltonian parameters.

Furthermore, the input-output relations and the quantum Langevin equations will be used in the next chapters to calculate the transport of both photons and phonons in an array of optomechanical cavities. Before to go into transport in optomechanical systems, in the next chapter we will introduce quantum transport and analyze the transfer of both fermionic and bosonic particles between the two edges of a 1D chain.

## 3.5 | Summary

The open quantum theory offers a more realistic description of any physical system. After a short introduction of the main ideas, we introduced the quantum Langevin equation in Sec. 3.3. From first principles, we were able to write the effect of the external environment introducing a noise term, which enters in the time evolution of the system operators. The correlation functions of the noise provide a description of the interaction between the environment and the system. Hence, if the correlation at different times follows a Dirac delta, the system experiences no memory effects, as the noise is completely independent from the values it assumed in the past. This condition reflects in an analytically solvable set of equations, as can be easily seen substituting this condition in the integral in Eq. (3.55).

As the focus of this dissertation is optomechanics, in Sec. 3.4 we showed how the quantum Langevin equations find application in a system with an external optical and mechanical environment. The first one can be described as Markovian noise, since at room temperature the number of photons at cavity frequencies is so small they result in being highly uncorrelated. However this can be not true for the mechanical bath, for the mechanical frequency is usually much smaller, and we have to consider non vanishing correlations between different times. Furthermore, when analyzing the mechanical noise, we considered a specific system-environment coupling, provided by the independent-oscillator model in Hamiltonian (3.20), which gives a different-time correlation function written in Eq. (3.47), where the explicit form of it depends on the spectral density of the environment.

This chapter gives an important introduction to open quantum system which is ultimately connected to quantum transport and quantum estimation theory and this connection is provided mostly by the input-output relations (3.41). The connection with quantum transport is given by means of the fluctuation-dissipation theorem, which is strictly related to the transport of physical quantities in the approximated regime of linear interactions. We will go into the details of this in the next chapter. Furthermore, when considering the transport of a physical quantity in a medium, the input-output relations offer a natural way of analyzing the transfer. For example, one could have a source of light, let the photons to travel in a medium such as an optical fiber or a crystal, and finally detect the transmitted signal at the end of the medium. Thus, we use the input-output relations to connect the input and output signals. Let us notice that usually an optimal transfer considers impedance matching conditions, which guarantees the maximum amount of transmitted signal amplitude. We will see it in details in our applications in Chapter 5. Consistently, we can access the physical system only through

the output field, as this is the one we detect with an instrument. Thus, in Chapter 6 we will use them to provide a realistic description of an estimation process on an optomechanical cavity, where the detection is performed on the optical field escaping the cavity toward photodetectors.

# Quantum Transport

## 4.1 | Introduction

Quantum transport describes the motion of particles in microscopic and mesoscopic systems. Here, the difference with the macroscopic systems lies in the coherence length of a quantum particle which is considered to be larger than the size of the system. Therefore, the description can only pass through the wavefunction of the particle, for quantum phenomena cannot be neglected. The important lengths are the coherence length  $l_c$ , the elastic mean free path  $l_0$ , the Fermi wavelength of the particle  $\lambda_F$  and the size of the system,  $L$ . We need to consider the quantum effects of the transport whenever

$$\lambda_F \leq l_0 < L < l_c. \quad (4.1)$$

This condition can be found either at low temperatures, when the coherence length is increased, or in synthetic systems. When we want to calculate the transport properties of a system the simplest model considers two leads surrounded by a reservoir, and a scattering region between them, see Fig. 4.1. Consider a one dimensional system. The leads are semi-infinite regions with free particle Hamiltonian, namely

$$H_{\text{lead}} = \frac{|p_x|^2}{2m}, \text{ for } x \text{ inside the leads} \quad (4.2)$$

The reservoir instead is macroscopic, and it is such that the particle entering in the scattering region is thermalized at certain temperature and chemical potential. Furthermore, different particles entering in the sample have completely uncorrelated phases. The scattering region has a mesoscopic Hamiltonian whose form is irrelevant. The eigenstates of Eq. (4.2) are plane waves with momentum  $k = \sqrt{(2mE)/\hbar^2}$ . Hence, a generic wavefunction has the form





Figure 4.1: Two leads are connected through a scattering region. The four states represented as  $a, b, c, d$  travel in the two directions. The transport is calculated from the left to the right lead making use of the scattering matrix  $S$ .

$$\psi_E(x) = \begin{cases} \phi_{k,l}(x) = a^+ e^{ikx} + a^- e^{-ikx}, & \text{for } x < 0, \\ \phi_{k,r}(x) = b^+ e^{ikx} + b^- e^{-ikx}, & \text{for } x > L, \\ \psi_{E,S}(x), & \text{for } 0 \leq x \leq L. \end{cases} \quad (4.3)$$

The plus and minus sign give the direction of propagation of the wave. For our purposes, we do not need to solve the Schroedinger equation and find the explicit form of the wavefunction. We do know the solution requires continuity of the function and of the derivative and it is enough to see the linear dependence of coefficients  $a^\pm$  and  $b^\pm$ . Thus, we can write this dependence with the help of the linear operator  $S$ , also known as the scattering matrix, which relates the left and right coefficients

$$\begin{pmatrix} a^- \\ b^+ \end{pmatrix} = \begin{pmatrix} r & t' \\ t & r' \end{pmatrix} \begin{pmatrix} a^+ \\ b^- \end{pmatrix} = S \begin{pmatrix} a^+ \\ b^- \end{pmatrix}, \quad (4.4)$$

where  $r$  and  $t$  are the reflection and transmission amplitudes and the primed ones are the amplitudes in the opposite direction.

The scattering matrix is unitary. This property accounts for current conservation. The incoming flux  $I_{\text{in}} = |a^+ + b^-|^2$  shall be equal to the outgoing flux  $I_{\text{out}} = |a^- + b^+|^2$ , thus  $S^\dagger S = I$  and

$$I_{\text{in}} = I_{\text{out}} \iff \begin{cases} 1 = |r|^2 + |t|^2 = |r'|^2 + |t'|^2 \\ 0 = r^* t' + t^* r' = t'^* r + r'^* t. \end{cases} \quad (4.5)$$

More explicitly, we can define the current through the continuity equation

$$\partial_x I + \partial_t \rho = 0, \quad (4.6)$$

which is zero for a stationary state  $\rho$  with energy  $E$ . Furthermore

$$I = \frac{\hbar}{2mi} \psi_E^*(x) \overleftrightarrow{\partial}_x \psi_E(x), \quad (4.7)$$

where we have defined the double derivative operator  $\overleftrightarrow{\partial}_x = (\overrightarrow{\partial}_x - \overleftarrow{\partial}_x)$ . We can apply the definition on the state 4.3 and obtain

$$I_{k,l} = \frac{\hbar}{2imk} (a^{+*} e^{-ikx} + a^{-*} e^{ikx}) \overleftrightarrow{\partial}_x (a^+ e^{ikx} + a^- e^{-ikx}) \quad (4.8)$$

$$= \frac{\hbar}{m} (|a^+|^2 - |ra^+ + t'b^-|^2) \quad (4.9)$$

for the left lead and

$$I_{k,r} = \frac{\hbar}{m} (|ta^+ + r'b^-|^2 - |b^-|^2) \quad (4.10)$$

for the right lead. If we make them equal we get the unitarity of  $S$ .

If the system has also time reversal symmetry, i.e.  $H^* = H$ , we have that if  $\psi(x, t)$  is an eigenstate of the Hamiltonian, also  $\psi(x, -t)^*$  is an eigenstate. Hence, the scattering matrix acquires the extra property that  $S = S^T$ . It's worth to notice that in electromagnetism a free particle subject to a magnetic field  $\mathbf{B} = \nabla \times \mathbf{A}$  loses the time reversal symmetry. The Hamiltonian of the system is

$$-\frac{\hbar^2}{2m} \left( \nabla + i \frac{e}{\hbar} \mathbf{A} \right). \quad (4.11)$$

We have that  $H(\mathbf{B}) = H^*(-\mathbf{B})$  and it is straightforward to prove that the scattering matrix gets the property  $S(\mathbf{B}) = S(-\mathbf{B})^T$ , that is different from time-reversal symmetry. We will go more in the details of the effect of magnetic fields on transport in the next chapter.

## 4.2 | The Green's function

In this section we present a well-known method for solving differential equations which has extensive applications in physics and overall in this thesis. We first introduce a very simple example, the solution of the Poisson's equation

$$\nabla^2 \phi(\mathbf{x}) = -\frac{1}{\epsilon_0} \rho(\mathbf{x}). \quad (4.12)$$

The Green's function  $G(\mathbf{x})$  is defined such that

$$\nabla^2 G(\mathbf{x}) = \delta(\mathbf{x}), \quad (4.13)$$

therefore the solution of Eq. (4.12) can be obtained as

$$\phi(\mathbf{x}) = -\frac{1}{\epsilon_0} \int d\mathbf{x}' G(\mathbf{x} - \mathbf{x}') \rho(\mathbf{x}'). \quad (4.14)$$

We can easily find the solution for the Green's function as  $G(\mathbf{x}) = 1/(4\pi|\mathbf{x}|)$  and when we substitute it in the previous equation we find the potential made by a charge distribution

$$\phi(\mathbf{x}) = \frac{1}{4\pi|\mathbf{x}|} \int d\mathbf{x}' \frac{\rho(\mathbf{x}')}{|\mathbf{x} - \mathbf{x}'|}. \quad (4.15)$$

This pedagogical example show the power of the Green's function method in solving Hamiltonian's spectrum and Schrödinger equations. Let's consider the Schrodinger equation

$$[H_0(\mathbf{x}) + V(\mathbf{x})]\psi_E = E\psi_E, \quad (4.16)$$

where  $H_0$  is a Hamiltonian that we know the solution, and  $V$  is a perturbation. Let's also suppose the spectrum is continuous and  $E$  any value in a given range. The Green's function method leads to

$$[E - H_0(\mathbf{x})]G_0(\mathbf{x}, \mathbf{x}', E) = \delta(\mathbf{x}' - \mathbf{x}), \quad (4.17)$$

with the boundary condition that  $G_0(\mathbf{x}, \mathbf{x}') = G_0(\mathbf{x}', \mathbf{x})$ . Hence, we can find the inverse of the Green's function considering

$$\int d\mathbf{x}'' G(\mathbf{x}, \mathbf{x}'') G(\mathbf{x}'', \mathbf{x}) = \delta(\mathbf{x}' - \mathbf{x}), \quad (4.18)$$

as  $G_0^{-1}(\mathbf{x}, E) = E - H_0(\mathbf{x})$ . Thus, we have

$$[G_0^{-1}(\mathbf{x}, E) - V(\mathbf{x})]\psi_E = 0. \quad (4.19)$$

Gathering together the above equations we can find the solution of the Schrodinger equation as

$$\begin{aligned} \psi_E(\mathbf{x}) &= \psi_E^0(\mathbf{x}) + \int d\mathbf{x}' G(\mathbf{x}, \mathbf{x}', E) V(\mathbf{x}') \psi_E(\mathbf{x}') \\ &= \psi_E^0(\mathbf{x}) + \int d\mathbf{x}' G(\mathbf{x}, \mathbf{x}', E) V(\mathbf{x}') \psi_E^0(\mathbf{x}') + \mathcal{O}(V^2), \end{aligned} \quad (4.20)$$

with  $\psi_E^0(\mathbf{x})$  being the eigenfunction of  $H_0$  with energy  $E$ . Here we found the same solution obtained in perturbation theory. The full solution contains an infinite sum of

Green's function  $G_0$  and wavefunctions  $\psi_E^0$ . By comparison with the Schroedinger equation, the Green function  $G$  of the full problem satisfy the so-called Dyson equation

$$G = G_0 + G_0 V G. \quad (4.21)$$

Now we want to add the time dependence onto the solution  $\psi_E$ , yielding

$$\psi_E(\mathbf{x}, t) = \int d\mathbf{x}' \int dt' G(\mathbf{x}, t, \mathbf{x}', t') \psi(\mathbf{x}', t'). \quad (4.22)$$

Hence the Green's function can be seen as the propagator from the point  $(\mathbf{x}, t)$  to  $(\mathbf{x}', t')$ ,

$$G(\mathbf{x}, t, \mathbf{x}', t') = -i\theta(t - t') \langle \mathbf{x}, t | \exp[-iH(t - t')] | \mathbf{x}', t' \rangle. \quad (4.23)$$

with  $\theta(t - t')$  being the Heaviside step function, which has non null values only for positive time interval  $t - t'$ .

Nothing forbid us to extend the defined formalism to many-particle system. The single particle Green's function in this case corresponds to the retarded Green's function

$$F(\mathbf{x}, t, \mathbf{x}', t') = -i\theta(t - t') \langle [\psi(\mathbf{x}, t), \psi^\dagger(\mathbf{x}', t')]_{\pm} \rangle, \quad (4.24)$$

where we make use of the anticommutator  $[\cdot, \cdot]_+$  when the particles are fermions, and the commutator  $[\cdot, \cdot]_-$  when they are bosons. The state  $\psi(\mathbf{x}, t)$  can be written in the second quantization as a sum of creation and annihilation particle operators. It's worth to notice that in the framework of quantum transport Eq. (4.24) takes general name of Kubo formula [103]

## 4.3 | The weak-coupling chain model

In this section we introduce the model we analyzed in our paper [4]. We found that this model allowed quantum transport with a probability close to one. We consider a hopping Hamiltonian with nearest-neighbor interaction  $J_i$  and an on-site potential  $h_i$  on a 1D lattice

$$\hat{H} = \sum_{i=1}^N \frac{J_i}{2} (\hat{c}_{i+1}^\dagger \hat{c}_i + \hat{c}_i^\dagger c_{i+1}) + h_i \hat{c}_i^\dagger \hat{c}_i, \quad (4.25)$$

where the  $\hat{c}$ 's represent either fermions or bosons, and open boundary conditions are assumed,  $\hat{c}_{N+1} = \hat{c}_{N+1}^\dagger = 0$ . In the subsequent sections, we will assume that the couplings  $J_i$  are all uniform but for the couplings  $J_i = J_0$  between the sender (receiver) block and the wire (see Fig. 4.2). We will also set the coupling within the sender (receiver) block

and within the wire as our time and energy unit  $J_i = J = 1$ . In the present section, these assumptions are unnecessary for the diagonalisation of the model we are going to outline.

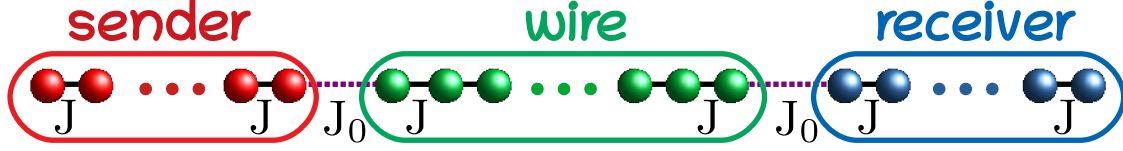


Figure 4.2: Setup of the excitation transfer protocol. Sender and receiver block, with the excitations residing in the former, are weakly coupled by  $J_0$  at both edges of a wire. Each part is made up by a 1D lattice described by the Hamiltonian in Eq. 4.25 with  $J_i = J = 1$ , but for  $J_0 \ll 1$ , and  $h_i = h$ .

As a consequence of the  $U(1)$  symmetry of the model, the number operator,  $\hat{N} = \sum_{i=1}^N \hat{c}_i^\dagger \hat{c}_i$ , commutes with the Hamiltonian in Eq. 4.25, implying conservation of the total number of excitations. This allows the dynamics to be addressed in excitation-number invariant subspaces. Moreover, due to the non-interacting, i.e., quadratic, nature of the Hamiltonian, single-particle eigenstates are sufficient to investigate the full many-body dynamics.

The hopping Hamiltonian in Eq. 4.25 in the single-particle sector is diagonalised as

$$\hat{H} = \sum_{k=1}^N \omega_k |\phi_k\rangle\langle\phi_k| \equiv \sum_{k=1}^N \omega_k \hat{c}_k^\dagger \hat{c}_k, \quad (4.26)$$

where  $\{\omega_k, |\phi_k\rangle \equiv \hat{c}_k^\dagger |0\rangle\}$  are the eigenvalues and the eigenvectors of the tridiagonal matrix,  $A \equiv \langle i | \hat{H} | j \rangle = \frac{J}{2} (\delta_{i,j+1} + \delta_{i,j-1}) + h_i \delta_{i,j}$ , describing the single-particle dynamics in the direct space basis,  $|i\rangle \equiv \hat{c}_i |0\rangle$ . Here, and in the following,  $|i\rangle \equiv |00\dots 1_i \dots 00\rangle$  represents a state with one excitation sitting on site  $i$ . The symbol  $A$  has been used to stress the equivalence between  $\hat{H}^{(1)}$  and the adjacency matrix used in graph theory [16]. From Eq. 4.26 one obtains that the eigenenergies (eigenvectors) in the  $n$ -particle subspace are given by the sum (tensor product) of the single-particle eigenenergies (eigenvectors). The fermionic or bosonic statistics of the particles determines the size of the Hilbert space, reading the binomial factor  $\binom{N}{n}$  for  $n$  fermions on a lattice with  $N$  sites and  $\binom{N+n-1}{N-1}$  for bosons. In the next Section we will write the many-body dynamics in terms of single-particle transition amplitudes.

### 4.3.1 | Many-body dynamics

Having sketched in the previous subsection the spectral decomposition of the Hamiltonian operator, one is able to express the dynamics of an arbitrary number of excitations

in the initial state in the chain in terms of single-particle dynamics [26, 28, 104]. We will however restrict in the following to initial states featuring only one excitation residing on each of the sender sites, while the wire and the receiver sites are empty. Whereas the restriction of at most one excitation per site is a necessary conditions if Eq. 4.25 models spinless fermions, for bosons multiple excitation-occupancy per site would be allowed initial states. We will not consider the latter initial state conditions also in view of comparing the role of the particle statistics in the investigated dynamics. Clearly for bosonic excitations, the dynamics brings along multiple excitation-occupancy per site.

The transition amplitude for the transfer of  $n_s$  excitations, residing on the sender sites  $\{n_s\} = \{s_1, s_2, \dots, s_{n_s}\}$ , to the receiver sites  $r$ , residing on the receiver sites  $\{n_r\} = \{r_1, r_2, \dots, r_{n_r}\}$ , can be expressed in terms of the submatrix  $F_{\{n_s\}}^{\{n_r\}}(t)$  of the transition amplitude matrix  $F(t)$ , where only the rows (columns) corresponding to the sites in the block  $\{n_s\}$  ( $\{n_r\}$ ) are taken into account. The transition matrix  $F(t)$  itself is built from single-particle transition amplitudes

$$f_i^j(t) = \langle j | e^{-it\hat{H}} | i \rangle = \sum_{k=1}^N e^{-i\omega_k t} \langle j | \phi_k \rangle \langle \phi_k | i \rangle = \sum_{k=1}^N e^{-i\omega_k t} \phi_{jk} \phi_{ki}^* \quad (4.27)$$

as follows

$$F(t) = \begin{pmatrix} f_1^1(t) & f_1^2(t) & \cdots & f_1^N(t) \\ f_2^1(t) & \cdots & \cdots & f_2^N(t) \\ \vdots & & \ddots & \vdots \\ f_N^1(t) & \cdots & \cdots & f_N^N(t) \end{pmatrix}, \quad (4.28)$$

where  $\hat{H}$  is the Hamiltonian in Eq. 4.26 and  $\phi_k$  its eigenvectors. Being  $F$  unitary,

$$\sum_{j=1}^N |f_i^j(t)|^2 = 1, \forall i \text{ and } \sum_{i=1}^N |f_i^j(t)|^2 = 1, \forall j, \quad (4.29)$$

embody the normalisation condition for the single-particle transition probability from a fixed site index  $i$ , or to a fixed site index  $j$ , as expected by excitation number conservation.

As depicted in Fig. 4.2, in the presence of the mirror symmetric Hamiltonian in Eq. 4.25, the eigenvectors of the tridiagonal matrix  $A$  are known to be either symmetric or antisymmetric [105]:  $\phi_{kn} = (-1)^{k+1} \phi_{k, N+1-n}$ , with  $J_i > 0$  and eigenvalues  $\omega_k$  listed in decreasing order. This yields  $f_i^j(t) = f_j^i(t)$  and  $f_i^j(t) = f_{N+1-i}^{N+1-j}(t)$ , resulting in both a persymmetric and centrosymmetric transition matrix  $F$ . Clearly, once sender and receiver blocks (of the same size) are chosen at each edge of the chain, the resulting submatrix will retain only its persymmetry. Furthermore, the effect of a uniform potential

$h$  on the eigenvalues  $\omega_k$  in Eq. 4.26 equals only to a uniform shift of their values at zero potential. As a result of the mirror-symmetry, the eigenvalues are symmetric around their middle value. Thus, one has  $\omega_{\frac{N}{2}+i} = -\omega_{\frac{N}{2}+1-i}$ , where  $i = 1, 2, \dots, \frac{N}{2}$  for even  $N$  and  $\omega_{\frac{N+1}{2}+i} = -\omega_{\frac{N+1}{2}-i}$ , where  $i = 0, 1, 2, \dots, \frac{N-1}{2}$  for 'odd  $N$ . All these conditions translate in having  $f_i^j(t)$  purely real (imaginary) for even (odd)  $i + j$ .

In view of the previous results, we now explicitly construct the submatrix  $F_{\{n_s\}}^{\{n_r\}}(t)$  for an arbitrary number of excitations  $n_s = n_r$ . For  $n_s \neq n_r$ , the transition amplitude is identically null because of the excitation number conserving nature of the Hamiltonian. Let us assume, without loss of generality, that each of the  $n_s$  excitations resides on each site of the lattice at both edges, i.e,  $\{n_s\} = 1, 2, \dots, n_s$  and  $\{n_r\} = N + 1 - n_r, N + 2 - n_r, \dots, N$ , see Fig. 4.2. Dropping henceforth the time-dependence, the relevant submatrix,  $F_{\{n_s\}}^{\{n_r\}}$  of  $F$ , is obtained by selecting the first  $n_s$  rows and the last  $n_r$  column,

$$F_{\{n_s\}}^{\{n_r\}} = \begin{pmatrix} f_1^{N+1-n_r}(t) & f_1^{N+2-n_r}(t) & \cdots & f_1^N(t) \\ f_2^{N+1-n_r}(t) & \cdots & \cdots & f_2^N(t) \\ \vdots & & \ddots & \vdots \\ f_{n_s}^{N+1-n_r}(t) & & \cdots & f_{n_s}^N(t) \end{pmatrix}. \quad (4.30)$$

Finally, the transition probability for  $n_s$  excitations initially on the sender block to be retrieved on the receiver block is obtained from the square modulus of the determinant and the permanent of  $F_{\{n_s\}}^{\{n_r\}}$  for fermions and bosons, respectively [106]. In the determinant (permanent) expansion, each term represents an allowed many-body transition amplitude channel - in the form of a product of one-body transition amplitudes from a sender to a receiver site. Hence, the square modulus accounts for interference among all these channels.

It is interesting to stress that, although in general  $|\det(F_{\{n_s\}}^{\{n_r\}})|^2 \neq |\text{perm}(F_{\{n_s\}}^{\{n_r\}})|^2$ , equality is retrieved whenever all non-vanishing terms in the determinant have the same signature. This results, as we will show in the following, that at specific times -including when  $\max_t [F_{\{n_s\}}^{\{n_r\}}]$  is achieved- the transition probability of  $n_s$  excitations between the edges of the chain is independent of its fermionic or bosonic nature.

In order to relax a bit the notation, hereafter we will label the  $n_r$  receiver sites starting from the edge,  $n_r = 1, 2, \dots, n_s$ . This allows to highlight the persymmetry of the submatrix  $F_{\{n_s\}}^{\{n_r\}}$

$$F_{\{n_s\}}^{\{n_r\}} = \begin{pmatrix} f_1^{n_s}(t) & f_1^{n_s-1}(t) & \cdots & f_1^1(t) \\ f_2^{n_s}(t) & \cdots & \cdots & f_2^1(t) \\ \vdots & & \ddots & \vdots \\ f_{n_s}^{n_s}(t) & & \cdots & f_{n_s}^1(t) \end{pmatrix}, \quad (4.31)$$

which now translates in  $f_i^j(t) = f_j^i(t)$ . As a consequence, there are only  $\frac{n_s(n_s+1)}{2}$  distinct transition amplitudes in the submatrix in Eq. 4.31. Still, finding the conditions by which the transition probability approaches one is a formidable task. A determinant (permanent) of a  $n_s$ -dimensional square matrix is made up of a sum of  $n_s!$  terms, each given by a product of  $n_s$  transition amplitudes, of which, at most,  $\lceil \frac{n_s}{2} \rceil$  terms are equal because of persymmetry, with  $\lceil \bullet \rceil$  being the ceiling function. Therefore, at least  $\lceil \frac{n_s}{2} \rceil$  transition amplitudes have to reach one at the same time. Notice also that both  $\det \left( F_{\{n_s\}}^{\{n_r\}} \right)$  and  $\text{perm} \left( F_{\{n_s\}}^{\{n_r\}} \right)$  are purely real (imaginary) for odd (even) lengths of the chain. Because  $F_{\{n_s\}}^{\{n_r\}}$  is a corner submatrix of Eq. 4.28, it is not unitary, but  $\left| F_{\{n_s\}}^{\{n_r\}} F_{n_s}^{n_r \dagger} \right|_{ij} \leq 1$  and

$$\sum_{j \in \{n_r\}} \left| f_i^j(t) \right|^2 \leq 1, \forall i \in \{n_s\} \text{ and } \sum_{i \in \{n_s\}} \left| f_i^j(t) \right|^2 \leq 1, \forall j \in \{n_r\}, \quad (4.32)$$

hold as a consequence of the particle-number conservation.

In this work, we derive the conditions for which the transition probability, both for fermions and bosons, approaches one by weakly coupling the sender and receiver block to the wire. We dub this dynamical regime *perturbative transfer*. Notice that the transfer becomes perfect, i.e.,  $\det \left( F_{\{n_s\}}^{\{n_r\}} \right) \left[ \text{perm} \left( F_{\{n_s\}}^{\{n_r\}} \right) \right] \rightarrow 1$  in the limit  $J_0 \rightarrow 0$ , which, however, implies also infinite transfer time. In the following we set  $J_0 = 0.01$ , although we checked that perturbative transfer does not depend on the specific value of  $J_0$  insofar the weak-coupling condition  $J_0 \ll J = 1$  is satisfied.

### 4.3.2 | Perturbative transfer

Perturbative couplings have been used in several settings, from quantum-state transfer to entanglement generation. However, previous works focused mainly on one-excitation transfer [107–109], with some exceptions dealing with two-excitation transfer [27, 28, 110]. The case of  $n > 2$  excitation transfer has not yet been addressed in the perturbative regime. Let us first recap a few results for the one- and two-excitation perturbative transfer which will be useful to describe the relevant dynamical features taking place also for  $n_s > 2$ .

For one-excitation transfer, the bosonic or fermionic nature of the particle does not play any role, as there is no statistics involved and the transfer amplitude, is given by Eq. 4.27. Because of the perturbative coupling, only the two (three) eigenvectors, lying in the middle of the single-particle spectrum, have non-negligible overlap with the initial and final state, see Fig. 4.3. This reduces the transition probability to



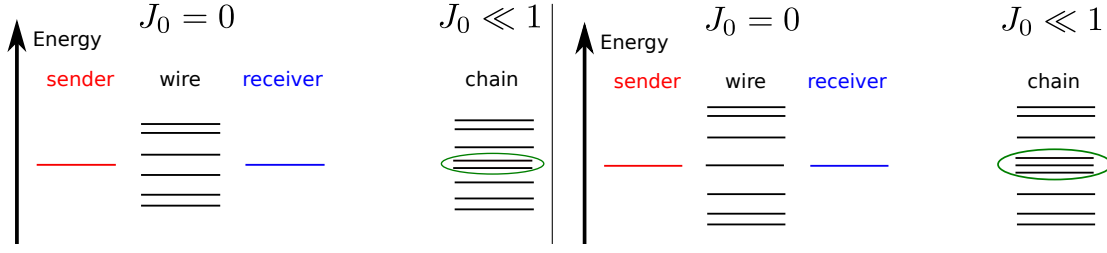


Figure 4.3: Single-particle energy spectrum of the chain, composed by one sender, one receiver, and a wire of even and odd length  $n_w$ , respectively, left and right panel. In both cases, the energy levels, before and after the coupling is switched on, are shown. Notice that, for an even length of the wire (left panel) no resonances occur between the sender (receiver) eigenenergy and the ones of the wire, at variance with the case of an odd length of the wire (right panel). As a consequence, for  $n_w$  even, two quasi-degenerate eigenenergies, whose eigenstates are localised on the sender and receiver site, enter in Eq. 4.27. For  $n_w$  odd, instead, a wire energy eigenstate is resonant with the sender (receiver) energy and three quasi-degenerate eigenstates enter the dynamics depicted by Eq. 4.27. This yields, in the latter case, a non-zero probability for the excitation to be found in the wire. The green line highlights the quasi-degenerate states.

$$|f_1^N(t)|^2 = \begin{cases} \left| \sum_{k=\frac{N}{2}}^{\frac{N}{2}+1} e^{-i\omega_k t} \phi_{Nk} \phi_{k1}^* \right|^2 = \left| \phi_{\frac{N}{2},1} \right|^2 (1 - \cos \omega_e t) \right|^2 & \text{for } N \text{ odd} \\ \left| \sum_{k=\frac{N+1}{2}-1}^{\frac{N+1}{2}+1} e^{-i\omega_k t} \phi_{Nk} \phi_{k1}^* \right|^2 = \left| 2i \phi_{\frac{N+1}{2}-1,1} \sin \omega_o t \right|^2 & \text{for } N \text{ even} \end{cases}, \quad (4.33)$$

where, for even  $N$ ,  $\omega_e = \frac{E_{\frac{N}{2}+1} - E_{\frac{N}{2}}}{2} \sim J_0^2$  and  $\phi_{\frac{N}{2},1} \simeq \frac{1}{\sqrt{2}}$ , and, for odd  $N$ ,  $\omega_e = \frac{E_{\frac{N+1}{2}} - E_{\frac{N+1}{2}-1}}{2} \sim J_0$ , and  $\left| \phi_{\frac{N+1}{2}-1,1} \right| \simeq \frac{1}{\sqrt{2}}$  only for  $N \gg 1$ . The approximate values for these coefficients can be obtained by a simple procedure, which we illustrate below for even  $N$ . When  $J_0 = 0$ , the sender and the receiver each have one eigenenergy state in the single-excitation sector with energy  $E = h$ , that  $|1\rangle$  and  $|N\rangle$ , respectively. In the presence of a perturbative coupling,  $J_0 \ll 1$ , the degeneracy between the sender and the receiver eigenstate is broken and, in the single-particle sector, the eigenstates are  $|\Psi^\pm\rangle \simeq \frac{1}{\sqrt{2}} (|1\rangle \pm |N\rangle)$ , because of mirror-symmetry. From Eqs. 4.33, we see that excitation transfer can be achieved with a probability perturbatively close to one. A similar procedure yields perturbative transfer of one excitation also for odd  $N$ . The main difference between the two cases lies in the fact that, for even  $N$ , there are no resonances between the sender (receiver) and the wire single-particle energy states, whereas, for odd

$N$  such a resonance occurs, see Fig. 4.3. Consequently, in the former case the energy splitting is a second-order perturbative effect, whereas, in the latter, it is a first-order one. This translates in shorter transfer times for the odd-length wire.

The characteristic feature of 1-excitation transfer in Eqs. 4.33 is the presence of a single frequency, which gives rise to Rabi-like oscillations of the excitation between the pair of two-level systems embodied by the sender and the receiver qubit. For  $n = 1$  excitation transfer, this is a direct consequence of the weak-coupling which couples perturbatively only two (three) single-particle levels. On the other hand, for  $n > 1$ , there will be more levels entering the dynamics (the precise number will be given in the next subsection) and, therefore, more frequencies enter the sum of the transition amplitude in Eq. 4.27. As a consequence, Rabi-like oscillations are much harder to achieve. Nevertheless, if one of the frequencies is much smaller than every other, then it will dominate the dynamics, i.e., it will form the envelop of the transition amplitude in Eq. 4.27 and, therefore, unit probability is achievable in a Rabi-like dynamical scenario. Such a scenario is here defined as perturbative transfer. Let us also specify that here we are referring to perturbative transfer of excitations, that is, having the determinant (permanent) of Eq. 4.31 equal to one. Although every physical quantity in quadratic models can be expressed in terms of single-particle amplitude, perturbative transfer of excitations does not necessarily imply perturbative transfer of, say, an arbitrary quantum state. Nevertheless, as we will see in Sec. 4.5, perturbative transfer of excitations implies perturbative transfer of energy and magnetisation, for instance.

### 4.3.3 | Resonances in sender-wire-receiver system

In order to determine the number of eigenstates giving a non-negligible contribution to the transition amplitude in Eq. 4.27, it is necessary to identify which states of the sender (receiver) block exhibit resonances with the wire's eigenstates. In the weak-coupling regime, this identifies different lengths of the wire giving rise to resonances between its eigenenergies and those of the sender (receiver) block.

As mentioned in the previous subsection, for an excitation sitting initially on the first site,  $|1\rangle$ , only two or three terms are relevant in the wave packet in Eq. 4.27, depending whether  $N$  is even or odd, respectively [107]. In the former case there are only two eigenvectors  $|\phi_k\rangle$  of the system having a non-negligible overlap with sites 1 and  $N$ , whilst in the latter they amount to three. This can be deduced by considering the number of resonant energy levels of the uncoupled system, sender, receiver, and wire. For  $J_0 = 0$ , there is only one single-particle energy eigenstate for the sender and the receiver, respectively, with energy  $E = h$ . The energy spectrum of the wire is given by  $E_k = h + \cos \frac{k\pi}{n_w+1}$  [111].

Therefore, in order to have degeneracy between the sender (receiver) and the wire,  $N$  has to be odd as the condition  $\cos \frac{k\pi}{n_w+1} = 0$  has to hold. When  $J_0$  is switched on in the weak-coupling limit,  $J_0 \ll 1$ , the degeneracy is lifted by  $\delta$ . For even  $N$ , it becomes a second-order perturbation effect, and the energy splitting is  $\mathcal{O}(J_0^2)$ , whereas, for odd  $N$ , the effect is of first order yielding an energy splitting  $\mathcal{O}(J_0)$ . Being the transfer time  $\tau \propto \delta^{-1}$ , perturbative transfer in odd-length chains is faster than in even-length ones. Now we consider the case of  $n_s = n_r > 1$ . In order to have resonant energy levels with the wire, made of  $n_w$  sites, the following condition has to hold

$$\frac{k\pi}{n_s+1} = \frac{q\pi}{n_w+1}, \quad k = 1, \dots, n_s \text{ and } q = 1, \dots, n_w. \quad (4.34)$$

which, when put in the following form

$$q = \frac{n_w+1}{n_s+1}k, \quad (4.35)$$

shows that whenever two length of wire,  $n_w$  and  $m_w$  are congruent modulo  $n_s+1$ , i.e.,  $n_w \equiv m_w \pmod{(n_s+1)}$ , the two wires share the same number of resonant modes with the sender. As a consequence, different lengths of wire  $n_w$ , but belonging to the same equivalence class, will exhibit similar dynamical behaviour, in particular, with respect to perturbative excitation transfer. To find the number of resonant modes  $n_{res}$ , one has to solve Eq. 4.35 for each integer  $p$  in the least residue system mod  $(n_s+1)$ , i.e.,  $p = 0, 1, \dots, n_s$ . It turns out that the mode  $q$  of the wire is resonant with the mode  $k$  of the sender for

$$q = \frac{m(n_s+1) + p + 1}{n_s+1}k = \left(m + \frac{p+1}{n_s+1}\right)k, \quad (4.36)$$

where  $m$  is an integer and the length of the wire is  $n_w = m(n_s+1) + p$ .

A few instances, relevant in the following, will be analysed. For  $p = 0$ , hence a wire of length  $n_w = m(n_s+1)$ , Eq. 4.36 reads

$$q = mk + \frac{1}{n_s+1}k. \quad (4.37)$$

This equation never holds as  $k < n_s+1$  and therefore no resonances are present between the wire and the sender for arbitrary  $n_s$ . For  $p = 1$  and  $n_w = m(n_s+1) + 1$ , one gets

$$q = mk + \frac{2}{n_s+1}k, \quad (4.38)$$

which is satisfied only for  $n_s$  odd and brings about resonance between the mode  $k = \frac{n_s+1}{2}$  and  $q = \frac{n_w-1}{2} + 1$  of the sender block and the wire, respectively. Furthermore,

$n_s$	1		2			3				4				
$n_w$	$2l$	$2l+1$	$3l$	$3l+1$	$3l+2$	$4l$	$4l+1$	$4l+2$	$4l+3$	$5l$	$5l+1$	$5l+2$	$5l+3$	$5l+4$
$n_{res}$	0	1	0	0	2	0	1	0	3	0	0	0	0	4

Figure 4.4: Table showing the number of resonances between the sender and the wire  $n_{res}$  for  $n_s$  senders up to 4 and a wire of length  $n_w$ , with  $l = 0, 1, 2, \dots$

because of the reflection symmetry of the energy spectrum of both systems, this is the only resonance present. Finally, we consider the case  $p = n_s$ , corresponding to  $n_w = m(n_s + 1) + n_s$ . Eq. 4.36 becomes  $q = (m + 1)k$ , meaning that each sender energy eigenstate is resonant with one eigenstate of the wire. This is the maximum number of resonances in the system as the energy levels of the uncoupled blocks in Fig. 4.2 are non-degenerate.

Following such a procedure for each  $p$  we build the table in Fig. 4.4 for an arbitrary number of senders  $n_s$ .

## 4.4 | Many-body dynamics

Now, before dealing with the case  $n_s > 2$ , we first discuss some of the results obtained in Ref. [27] for the case of two-excitation transfer. Our previous discussion about the perturbation order of the sender-wire resonances immediately explains the reason wires of length  $n_w = 3l + 2$  perform perturbative quantum-state transfer in a faster time than wires of length  $n_w \neq 3l + 2$ . Indeed, the former case exhibits first-order perturbation correction to the three-fold quasi-degenerate energy eigenstates relevant to Eq. 4.27, whereas, in the latter case, the first correction to the two-fold quasi-degenerate eigenstates is of second-order. For the details about the transfer time and the perturbative expansions we refer the reader to Ref. [27], and for the generation of entangled states between the sender and receiver block to Ref. [110].

Here we highlight the fact that the bosonic or fermionic nature of the excitations plays a key role in the dynamics because of the different dimensions of the Hilbert space of the Hamiltonian in Eq. 4.25 due to their different statistics. Indeed, as for fermions the receiver's Fock space is made up of a single state in the two-particle sector, namely  $|11\rangle$ , for bosons, in addition to the latter, also the states  $|02\rangle$  and  $|20\rangle$  build up the Fock space. Consequently, the transition probability between the states  $|12\rangle$  and  $|N-1 N\rangle$  for fermions and bosons are not equivalent at all times. Nevertheless, the fermionic transition amplitude envelops the bosonic one, with the two bosons exploring the receiver's Hilbert space on a time scale  $J$ , see Fig. 4.5. It is worthwhile to anticipate that such

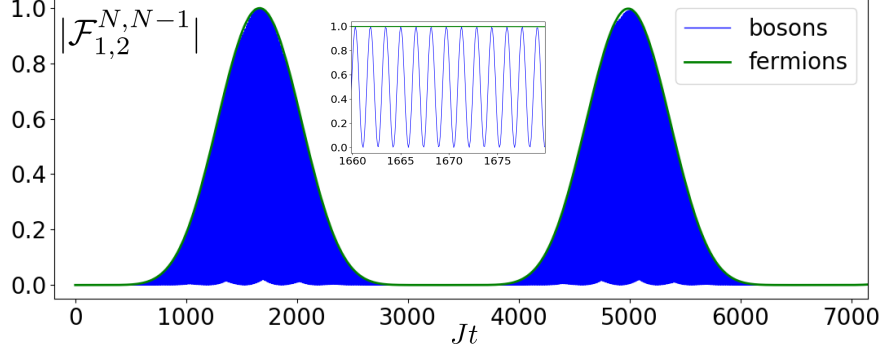


Figure 4.5: The transition probability of two excitations from sender sites  $\{n_s\} = 1, 2$  to receiver sites  $\{n_r\} = N - 1, N$  for fermions and bosons, respectively. Excitations bounce back and forth between the sender and the receiver block via a Rabi-like dynamics, where the green curve is for fermions and constitutes the envelop of the blue curve for bosons. The inset shows the dynamics in a interval of around unit transfer probability for fermions, highlighting the boson dynamics on a time scale of order of  $J$ . The length of the chain is  $N = 45$ .

a difference of their respective transition probabilities does not have consequences on several observables, such as the average excitation number on each site, as we will show in Sec. 4.5.

#### 4.4.1 | Equivalence between bosonic and fermionic perturbative excitations transfer

As can be seen from Fig 4.5, the two-fermion transition probability is the envelop for the bosonic one. As a consequence, perturbative transfer is achieved at the same time for both classes of particles. This is a general feature of the model and can be explained by means of perturbation theory.

In the weak-coupling limit, and in the absence of resonances with the wire, we can approximate the perturbed eigenstates having non-zero overlap with the sender and the receiver sites as the symmetric and antisymmetric linear combination of the degenerate single-particle eigenstates of the sender and the receiver block

$$|\Psi_k\rangle_{sr} = \frac{1}{\sqrt{2}} \left[ \sqrt{\frac{2}{n_s + 1}} \sum_{l=1}^{n_s} \sin \frac{k\pi l}{n_s + 1} |l\rangle \pm \sqrt{\frac{2}{n_s + 1}} \sum_{l=1}^{n_s} \sin \frac{k\pi l}{n_s + 1} |N + 1 - l\rangle \right]. \quad (4.39)$$

It turns out that the transition amplitude in Eq. 4.27 is bounded by

$$\max_t \left| f_i^j(t) \right| = \max_t \left| \sum_{k=1}^N e^{-i\omega_k t} \phi_{jk} \phi_{ki}^* \right| \leq \sum_{k=1}^N |\phi_{jk} \phi_{ki}^*| = \frac{2}{n_s + 1} \sum_{k \in \{n_s\}} \left| \sin \frac{k\pi j}{n_s + 1} \sin \frac{k\pi i}{n_s + 1} \right|. \quad (4.40)$$

The last term on the RHS of Eq. 4.40 is equal to one only for  $i + j = n_s + 1$  and  $i = j$ . This translates in a submatrix  $F_{\{n_s\}}^{\{n_r\}}$  (Eq. 4.31) which can, at most, have unit single-particle amplitudes either on the main diagonal or on the skew-diagonal, respectively. Although, the determinant (permanent) of  $F_{\{n_s\}}^{\{n_r\}}$  may become one also due the contribution of many terms in their respective expansion, it is highly improbable that such a fully constructive interference between wavepackets  $f_i^j(t)$ , for arbitrary  $i$  and  $j$ , will take place, especially in the presence of many frequencies entering the dynamics. As a result, also in view of the normalisation condition in Eq. 4.29, perturbative transfer is most likely to occur when all the terms either on the main, or on the skew-diagonal, will reach unit single-particle transition amplitude. It is now immediate to realise that perturbative transfer for an arbitrary number of excitations is independent from their bosonic or fermionic nature as the signature of the determinant of Eq. 4.31 does not play any role.

#### 4.4.2 | Heuristic approach to PP transfer

The result in Eq. 4.40 and the resonance conditions derived in Sec. 4.3.3 allow us also to give a rule of thumb as to whether perturbative excitation transfer is achievable for an arbitrary number of excitations  $n_s$  in a wire of given length  $n_w$  by means of the protocol of Fig. 4.2. Building on the argument for one-particle transfer the single-particle transition amplitudes entering the submatrix in Eq. 4.30 are given by Eq. 4.27, where only resonant modes have to be kept.

Let us consider the case where  $j = N + 1 - i$ , i.e., mirror-symmetric sites in the sender and receiver block, respectively, corresponding to the elements on the diagonal of the matrix in Eq. 4.31. In the absence of resonant modes with the wire, Eq. 4.27 reads

$$\begin{aligned} f_i^j(t) &= \sum_{k=1}^{2n_s} e^{-i\omega_k t} \phi_{jk} \phi_{ki}^* = \sum_{k=1}^{2n_s} \phi_{jk} \phi_{ki}^* \left( e^{-i\delta_k t} - e^{i\delta_k t} \right) e^{-i\omega_k t} \\ &= \sum_{k=1}^{n_s} \phi_{jk} \phi_{ki}^* \left( e^{-i\delta_k t} - e^{i\delta_k t} \right) \left( e^{-i\omega_k t} + e^{i\omega_k t} \right) = -i \sum_{k=1}^{n_s} \frac{\phi_{ik} \phi_{ki}^*}{4} \sin \delta_k t \cos \omega_k t, \end{aligned} \quad (4.41)$$

where in the last line, without loss of generality, we have considered an instance of even  $i + j$  and mirror-symmetry of the energy spectrum has been exploited. The transition amplitude is hence given by a wavepacket of  $n_s$  travelling waves, each given by a

product of harmonic functions, being sines or cosines depending on  $n_w$ ,  $n_s$ , and  $k$ . The specific form of the harmonic function of  $\omega_k$  not being relevant, we notice that the frequencies entering the functions satisfy  $\delta_k \ll \omega_k$ , as the energy shift of the  $k$ -th energy level is negligible with respect to its unperturbed value. As a consequence,  $\sin \delta_k t$  shapes up the envelop of  $k$ -th wave of  $f_i^j(t)$ . Therefore it is straightforward to conclude that, in order to have  $f_i^j(t) = 1$  at some specific time  $t = \tau$ , the  $\delta_k$ 's should be all commensurate, which is a hard condition to fulfill, or only one  $\delta_k^*$  should be much smaller than all the others. The latter condition defines the rule of thumb for perturbative excitation transfer:

$$\exists! \delta_k \ll \delta_q, \quad (4.42)$$

where the  $\delta$ 's are the energy shifts of the corresponding energy levels entering Eq. 4.41. Eq. 4.42 states that if in the wavepacket of Eq. 4.41 there is only one energy being corrected at a higher order in perturbation theory, perturbative excitation transfer is attainable. Indeed, being  $n$ -excitation transfer achievable by the product of the single-particle transfer on the (skew) diagonal, each evolving with the same eigenenergies as in Eq. 4.41, the transfer time is given by  $\tau \simeq \frac{\pi}{2\delta_k^*}$ .

An identical argument applies in the presence of resonances with the wire where the single-particle transition amplitude reads

$$f_i^j(t) = \sum_{k=1}^{2n_s+n_w} e^{-i\omega_k t} \phi_{jk} \phi_{ki}^* \quad (4.43)$$

and the energy shifts  $\delta_k$  are evaluated taking into account the triple quasi-degenerate nature of the energy level(s).

### 4.4.3 | 3- and 4-excitation perturbative transfer

Let us now address the case of  $n_s > 2$ . For three fermionic excitations, in order to have perturbative transfer

$$|F_s^r|^2 = \left| \begin{array}{ccc} f_1^{N-2} & f_1^{N-1} & f_1^N \\ f_2^{N-2} & f_2^{N-1} & f_1^{N-1} \\ f_3^{N-2} & f_2^{N-2} & f_1^{N-2} \end{array} \right|^2 \simeq 1, \quad (4.44)$$

where, without ambiguity, we have labeled by  $s$  and  $r$  the sender and receiver sites, respectively. According to the arguments in the previous sections, we analyze the contribution of the main diagonal to the determinant, with similar arguments holding for

the skew diagonal contribution,

$$|F_s^r|^2 = \left| \left( f_1^{N-2} \right)^2 f_2^{N-1} \right|^2. \quad (4.45)$$

For the case of  $n_w = 4n + 1$ , the single-particle transition amplitude in Eq. 4.27 now reads

$$f_i^j(t) = \sum_{k=1}^7 e^{-i\omega_k t} \phi_{jk} \phi_{ki}^*. \quad (4.46)$$

From Fig. 4.4 we notice that two double quasi-degenerate and one triple quasi-degenerate eigenstates have non-negligible overlap with the sender and receiver sites. As the former degeneracy is resolved at second-order in perturbation theory, and the latter at first-order, this implies that, for  $J_0 \rightarrow 0$ , we may expect the rule of thumb in Eq. 4.42 to hold as 2<sup>nd</sup>-order energy shifts are  $\mathcal{O}(J_0^2)$  whereas 1<sup>st</sup>-order shifts are  $\mathcal{O}(J_0)$ .

Indeed, we see that perturbative transfer is ruled by the following term

$$|F_s^r(t)| \simeq |\sin^2 \omega_{76}^- t|^2, \quad (4.47)$$

where  $\omega_{76}^- = \frac{E_7 - E_6}{2}$  is the 2<sup>nd</sup>-order perturbation energy shift of the double quasi-degenerate energy eigenstate. The positions of  $E_6$  and  $E_7$  of Eq. 4.26 in the single-particle energy spectrum of the chain, ordered in increasing values, are given by  $k = \lfloor \frac{N+1}{2} \cos^{-1} \frac{1}{\sqrt{2}} \rfloor - 1$  and  $\lfloor \frac{N+1}{2} \cos^{-1} \frac{1}{\sqrt{2}} \rfloor - 2$ , respectively.

Concerning the other lengths of wire  $n_w$  in Fig. 4.4, for  $n_s = 3$ , we notice that they all have exclusively 1<sup>st</sup>- or 2<sup>nd</sup>-order perturbation energy corrections. By the rule of thumb in Eq. 4.42, we do not expect perturbative transfer, being all the energy shifts of the same order of magnitude for a given  $n_w$ . In addition, we show that also non-perturbative transfer does not occur, being the energy shifts incommensurate.

Let us first analyse the non-resonant cases in Fig. 4.4  $n_w = 4l, 4l + 2$ . As only six eigenstates take part in the dynamics, the single particle transition amplitude between a sender and a receiver site reduces to

$$f_i^j(t) = \sum_{k=1}^6 e^{-i\omega_k t} \phi_{jk} \phi_{ki}^*. \quad (4.48)$$

From the perturbative expansion of Eq. 4.39, the envelop of the transition amplitude in Eq. 4.48 can be written as

$$|F_s^r(t)| = \left| \frac{1}{4} \left( \sin E_4 t + \sin \frac{E_6 - E_5}{2} t \right)^2 \sin \frac{E_6 - E_5}{2} t \right|, \quad (4.49)$$



where  $E_4$  is given by the energy level labeled by  $k = \frac{N}{2} + 1$ ,  $E_6$  and  $E_5$  by  $k = \lfloor \frac{N+1}{2} \cos^{-1} \frac{1}{\sqrt{2}} \rfloor$  and  $\lfloor \frac{N+1}{2} \cos^{-1} \frac{1}{\sqrt{2}} \rfloor + 1$ , respectively. From Eq. 4.49, it is evident that, in order to achieve transfer of 3 excitations,  $E_4$  and  $E_6 - E_5$  have to be commensurate. This implies that

$$\begin{cases} E_4 t &= \frac{(4n+1)\pi}{2} \\ \frac{E_6 - E_5}{2} t &= \frac{(4m+1)\pi}{2} \end{cases} \text{ and } \begin{cases} E_4 t &= \frac{(4n+3)\pi}{2} \\ \frac{E_6 - E_5}{2} t &= \frac{(4m+3)\pi}{2} \end{cases}, \quad (4.50)$$

have to hold with  $n$  and  $m$  integers, in order to have the oscillatory functions in Eq. 4.49 be 1 or -1 at the same time. Hence, one of the two following conditions has to be fulfilled

$$\frac{E_6 - E_5}{2E_4} = \frac{4m+1}{4n+1} \text{ and } \frac{E_6 - E_5}{2E_4} = \frac{4m+3}{4n+3}. \quad (4.51)$$

The impossibility of the transfer arises because, for  $J_0 \rightarrow 0$ , we find numerically that the energy ratio  $\frac{E_6 - E_5}{2E_4} \rightarrow \frac{1}{2}$ . Therefore, Eqs. 4.51 can not be fulfilled by any integer pair  $n$  and  $m$ , as can be readily seen from the fact that they can be cast into

$$8m = 4n - 1 \text{ and } 8m = 4n - 3, \quad (4.52)$$

respectively. The same argument about incommensurability of the eigenfrequencies entering Eq. 4.48 applies for wires of length  $n_w = 4n + 3$ . Notice that, in the latter case, according to Fig. 4.4 there are 3 sets of triple quasi-degenerate eigenstates, all coming from 1<sup>st</sup>-order perturbation expansion. Nevertheless the same argument applies as the ratio of the energy shifts is found numerically to be  $\frac{1}{2}$  for  $J_0 \rightarrow 0$ .

Notice that, as we are reporting a limiting procedure, there may be instances of  $J_0$  where the ratio becomes quasi-commensurate, and after a very large amount of time a transfer probability close to one may be achieved. Such fortuitous cases, however, are not the topic of our investigation, as we are considering the conditions to be fulfilled in order to achieve perturbative transfer in the generic limit of weak coupling instead of some specific values of  $J_0$ , which may eventually be a set of zero measure and hence extremely sensible to disorder.

To summarise, we have found that for  $n_s = 3$  excitations, placed at one edge of a wire of length  $n_w$  and in the weak-coupling limit  $J_0 \rightarrow 0$ , perturbative transfer is achievable only for  $n_w = 4l + 1$  where the unique 2<sup>nd</sup>-order perturbation eigenenergy correction determines the transfer time. Other equivalence classes of the wire's length do not achieve unit transfer of three excitations because all the energy shifts belong to the same perturbation order and commensurability between frequencies is not achieved. In Fig. 4.6 we depict the results only for the case of successful perturbative transfer.

Let us now address the case of  $n_s = 4$ . From Fig. 4.4 we see that all energy shifts, for a given  $n_w$ , are of the same order in perturbation theory, either 1<sup>st</sup>-order for  $n_w = 5l + 4$  or

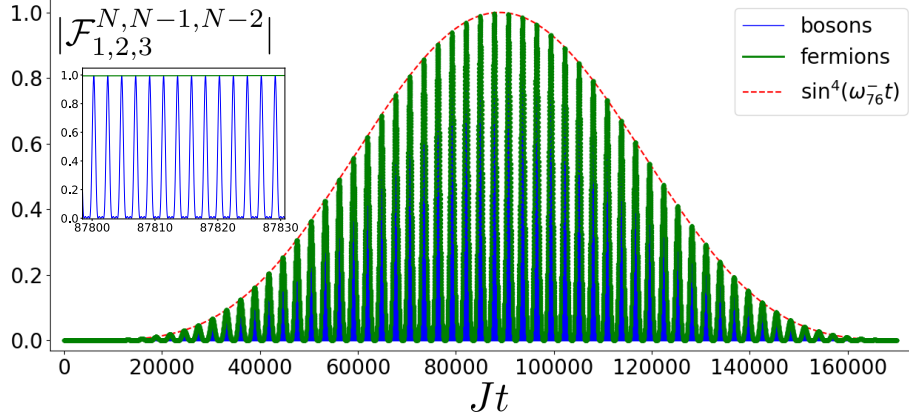


Figure 4.6: Transition probability for the transfer of three excitations from sites 1, 2, 3 to sites  $N - 2, N - 1, N$  for a chain length of  $N = 47$  in a time interval of  $t \in [0, 160000/J]$ . The blue (green) line shows the exact dynamics for bosons (fermions), whilst the red dotted line is the envelop of the three-particle transition as calculated in Equation (4.47). In the inset, a zoom around the time of perturbative transfer is shown.

$2^{\text{nd}}$ -order in all the other case. Therefore, at variance with the case  $n_s = 3$ , the condition for perturbative excitation transfer given by Eq. 4.42 is not satisfied. Nevertheless, there are lengths of the wire  $n_w$  exhibiting successful  $n_s = 4$  excitation transfer, whereas other lengths do not. The reason, as we will show, can be traced back to the fact that for some length of wires  $n_w$ , the energy splitting at  $2^{\text{nd}}$ -order in perturbation theory is almost one order of magnitude lower for some energy levels than it is for others. Let us analyse first the successful case.

For  $n_w = 5l + 2$ , the perturbed eigenstates are located at position  $k = \lfloor \frac{N+1}{\pi} \cos^{-1} \frac{\sqrt{5+1}}{4} \rfloor - 1$  and  $k = \lfloor \frac{N+1}{\pi} \cos^{-1} \frac{\sqrt{5+1}}{4} \rfloor$  for the higher energy state, and  $k = \lfloor \frac{N+1}{\pi} \cos^{-1} \left( \frac{\sqrt{5-1}}{4} \right) \rfloor$  and  $k = \lfloor \frac{N+1}{\pi} \cos^{-1} \left( \frac{\sqrt{5-1}}{4} \right) \rfloor + 1$  for the lower one. By numerical evaluation, we obtain that the ratio  $\omega_{78}^-$  to  $\omega_{56}^-$  goes to 0.14, for  $J_0 \ll 1$  and irrespective of  $l$ . The same situation occurs for  $n_w = 5l + 1$ . In these cases  $n_s = 4$  excitation transfer occurs, although it is not ruled by a single frequency and hence, according to our definition, is not perturbative excitation transfer. Indeed, in order to determine the transfer time, one has to find the maximum of two-single particle transition amplitudes entering the 4 excitation transition probability between the edges of the chain,

$$|F_s^r|^2 = \left| \left( f_1^{N-3} \right)^2 \left( f_2^{N-2} \right)^2 \right|^2. \quad (4.53)$$

The fact that one energy shift is almost one order of magnitude lower than the other

entering the dynamics allows one to determine the order of magnitude of the transfer time as given by  $\tau = \frac{\pi}{2\omega_{78}^-}$ . In Fig. 4.7 a comparison of the latter with the exact numerical result for excitation transfer is shown in panel d. On the other hand, for  $n_w = 5l, 5l + 3, 5l + 4$ , one has  $\omega_{56}^- \simeq \omega_{78}^-$ , with the ratio going to 0.38. perturbative transfer does not occur and also non-perturbative transfer has not been found for several instances within time intervals related to the inverse of the energy splits. Clearly, this does not mean that the excitations may not be transferred at a certain time, being only two frequencies involved and occasional instances of commensurability may occur between the energy shifts, but this would hardly be robust against the length of wire and perturbations of  $J_0$ .

Finally, we present an unified scenario for the shortest transfer time achievable via perturbative transfer for  $n_s = 1, 2, 3$  excitations in the sender block in Fig. 4.7. We have also added the case  $n_s = 4$  to highlight its qualitatively similar behaviour to perturbative transfer. Here we assume that the sender and receiver are connected by a wire able to transfer from one to four excitations by weakly coupling the respective blocks to the end to the wire. In order to have a wire able to perform such a task, its length  $n_w$  has to fall in all the equivalence classes allowing perturbative transfer for  $n_s = 1, 2, 3$  and quasi-perturbative transfer for  $n_s = 4$ . Whereas  $n_w$  can be arbitrary for  $n_s = 1, 2$ , for  $n_s = 3, 4$ , the length of the wire has to be  $n_w = 4l + 1$  and  $n_w = 5l + 1$  or  $n_w = 5l + 2$ , respectively. This yields to wires length of  $n_w = 20l + 1$  and  $n_w = 20l + 17$ , respectively. In Fig. 4.7, we report the transfer times for the former case, noticing its linear increase with the wire's length for  $n_s = 2, 3, 4$ . On the other hand, for  $n_s = 1$ , the increase is  $\sqrt{n_w}$  as the frequency involved in the perturbative transfer is derived from resolving the degeneracy via first-order perturbation theory, as shown for odd  $N$  in Sec. 4.3.2.

## 4.5 | Applications of many-body perturbative transfer

In the previous sections, we have shown that perturbative transfer of  $n$  excitations is possible between the edges of a quantum wire. Now we analyse some cases where perturbative transfer is applied to the transport of relevant physical quantities, such as magnetisation and energy, highlighting first the invariance with respect to the fermionic or bosonic nature of the excitations.

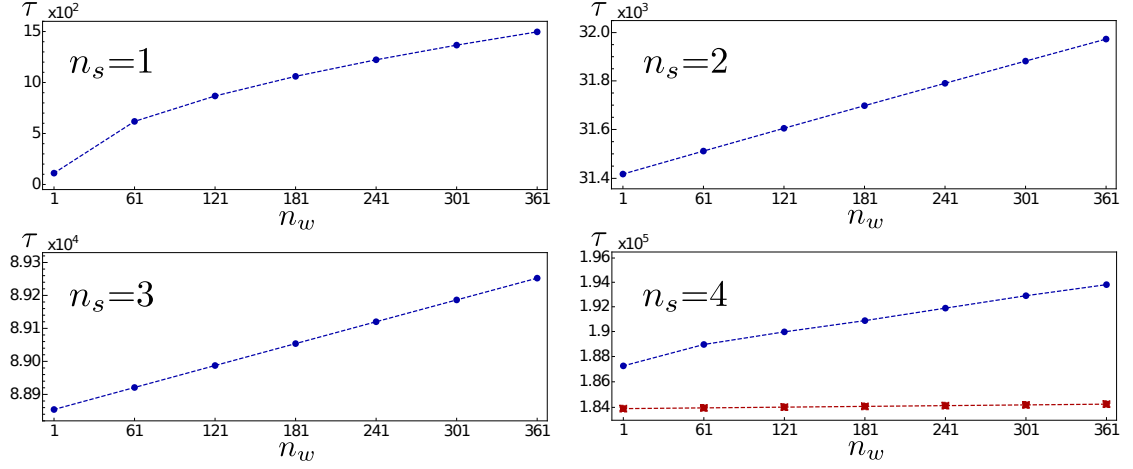


Figure 4.7: Transfer times  $\tau$  for  $n_s = 1, 2, 3, 4$  excitations in wires of different length  $n_w$  fulfilling the (quasi) perturbative condition for all considered  $n_s$ . Notice that, whilst for  $n_s = 1$  the transfer time increases as  $\sqrt{n_w}$  because the relevant frequency is obtained by first-order perturbation theory, in all other cases the slowest frequency is given by second-order perturbation theory, yielding thus a linear increase with  $n_w$ . In the lower right panel, for  $n_s = 4$ , the blue curve is the exact numeric transfer time, whereas the red one reports  $\tau = \frac{\pi}{\omega_{78}}$ . Both follow a linear increase, although with different slope.

### 4.5.1 | Equivalence of fermionic and bosonic observable's dynamics

An arbitrary one-body observable in second quantisation is given by

$$\hat{O} = \sum_{nm} a_{nm} \hat{c}_n^\dagger \hat{c}_m + h.c. , \quad (4.54)$$

where the  $\hat{c}$ 's are bosonic or fermionic operators acting on site  $n$  and  $m$ . Expressing average of the observable's dynamics in Heisenberg representation, where  $\hat{H}$  is given by Eq. 4.25 yields

$$\langle \hat{O}(t) \rangle = \sum_{nm} a_{nm} \sum_{kq} \phi_{kn} \phi_{qm}^* e^{i(E_k - E_q)t} \langle \hat{c}_k^\dagger \hat{c}_q \rangle . \quad (4.55)$$

As the single-particle spectrum of the Hamiltonian in Eq. 4.25 is identical both for fermions and bosons, the only difference between the dynamics of an observable on a fermionic or bosonic many-body system that can possibly arise has to come from the average on the initial state of the operators on the RHS of Eq. 4.55.

In our setting the initial state is given by one or zero excitations per site

$$|\Psi(0)\rangle = \prod_{i=\{n_s\}} \hat{c}_i^\dagger |0\rangle , \quad (4.56)$$

which is also the only initial state that fermions and bosons can have in common. Evaluating the average on the RHS of Eq. 4.55 on this initial state reads

$$\langle 0 | \hat{c}_1 \hat{c}_2 \dots \hat{c}_{n_s} \hat{c}_k^\dagger \hat{c}_q \hat{c}_{n_s}^\dagger \dots \hat{c}_2^\dagger \hat{c}_1^\dagger | 0 \rangle . \quad (4.57)$$

Expressing all operators in the position basis reads

$$\sum_{ij} \phi_{ki} \phi_{qj}^* \langle 0 | \hat{c}_1 \hat{c}_2 \dots \hat{c}_{n_s} \hat{c}_i^\dagger \hat{c}_j \hat{c}_{n_s}^\dagger \dots \hat{c}_2^\dagger \hat{c}_1^\dagger | 0 \rangle . \quad (4.58)$$

By using Wick's theorem, we notice that the non-zero fully-contracted terms are those having an even number of permutations. As a consequence, the dynamics of an arbitrary one-body observable, such as in Eq. 4.55, is independent of the bosonic or fermionic nature of the excitations. For instance, the average number of particles on a lattice site,  $\langle \hat{n}(t) \rangle = \langle \hat{c}_n^\dagger(t) \hat{c}_n(t) \rangle$  is the same whether the Hamiltonian in Eq. 4.25 refers to bosons or fermions, notwithstanding Pauli's exclusion principle holds for fermions whereas bosons allow for multiple occupation.

It is easy to show that the same holds for  $n$ -body observables of the form

$$\hat{O} = \sum_{nmijrs\dots} \alpha_{nm\dots} \hat{c}_n^\dagger \hat{c}_m \hat{c}_i^\dagger \hat{c}_j \hat{c}_s \dots + h.c. , \quad (4.59)$$

when the average is evaluated on an initial state of the form of Eq. 4.56 and the dynamics is ruled by a quadratic Hamiltonian such as in Eq. 4.25. A relevant example of a 2-body observable of the form of Eq. 4.59 independent from the statistics of the excitations is the density-density fluctuations  $\langle \hat{n}_i(t) \hat{n}_j(t) \rangle$ .

## 4.5.2 | Magnetisation transport

As it is well known, the Hamiltonian in Eq. 4.25 models also a 1D spin- $\frac{1}{2}$  chain with isotropic interactions on the XY plane, i.e.,

$$\hat{H} = \sum_i^N J_i (\hat{S}_i^x \hat{S}_{i+1}^x + \hat{S}_i^y \hat{S}_{i+1}^y) + h_i \hat{S}_i^z \quad (4.60)$$

when the standard Jordan-Wigner transformation is carried out [112]. Because of the Jordan-Wigner mapping, the (fermionic) Hamiltonian in Eq. 4.25 can model an XX spin- $\frac{1}{2}$  open chain, where the average total magnetisation (along the z-direction) of a set of spins residing on sites  $\{i\}$  is given by  $\langle \hat{S}^z \rangle = \sum_{\{i\}} \langle \hat{S}_i^z \rangle = \sum_{\{i\}} \frac{2\langle \hat{c}_i^\dagger \hat{c}_i \rangle - 1}{2}$ . As a consequence, the magnetisation of the receiver block evolves as

$$\langle \hat{S}_{\{r\}}^z(t) \rangle = \sum_{\{r\}} \langle \hat{c}_r^\dagger(t) \hat{c}_r(t) \rangle - \frac{n_r}{2} , \quad (4.61)$$

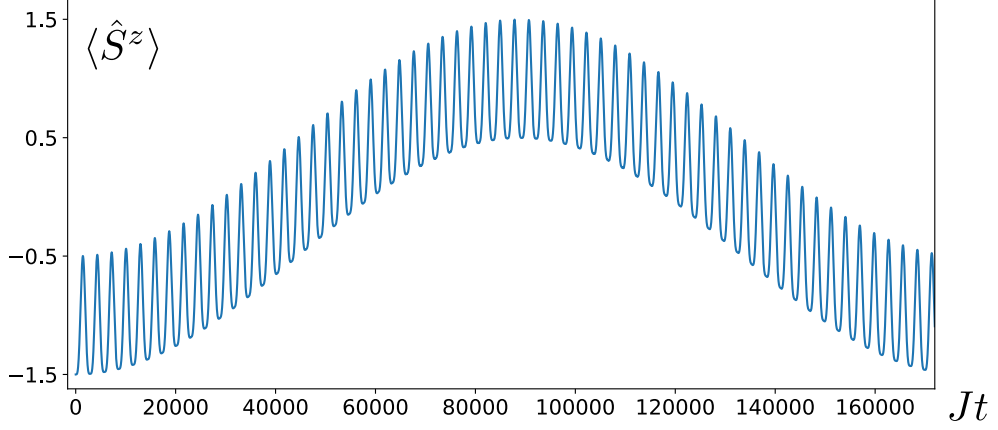


Figure 4.8: Average magnetisation of the receiver block, Eq. 4.62, for  $n_s = 3$  in a chain of  $N = 47$ . Notice that the occupation number entering Eq. 4.61 oscillates between two and three on a timescale much larger than the transition probability reported in Fig. 4.6

where the average is evaluated over the initial state having all the spins in the sender block flipped. In the Heisenberg picture and using Wick's theorem, it is possible to express the receiver's block magnetisation as a function of single-particle transition amplitudes  $f_i^j(t)$ :

$$\langle \hat{S}_{\{r\}}^z(t) \rangle = \sum_{i=\{s\}} \sum_{j=\{r\}} |f_i^j|^2 - \frac{n_r}{2} \equiv \|F_s^r(t)\|_F^2 - \frac{n_r}{2}, \quad (4.62)$$

where  $\|\bullet\|_F$  is the Frobenius matrix norm and  $F_s^r(t)$  is the submatrix defined in Eq. 4.31. The result for  $n_s = 3$  is shown in Fig. 4.8. Notice that, although the transition probability oscillates, for bosons, between 0 and 1 on a timescale of  $J$  in the the corresponding scenario in Fig. 4.6, the average number of bosons on the receiver block varies only between 2 and 3. Therefore, on a large time interval, with respect to  $J$ , around the transfer time  $\tau$  at least two excitations out of three are located on the receiver block irrespective of their bosonic or fermionic nature. Indeed, the dynamics of the occupation number  $\langle \hat{n}_i(t) \rangle$  of site  $i$  entering Eq. 4.61 is identical for bosons and fermions, as by the argument of Sec. 4.5.1. As an example, let us consider the case  $n_s = 2$ . Although the dynamics of the transition probability differs, as reported in Fig. 4.5, the subspace spanned by the two photons in the receiver block is composed by  $\{|11\rangle, \frac{1}{\sqrt{2}}(|02\rangle \pm |20\rangle)\}$ , which are all states having the same  $\langle \hat{n}_i(t) \rangle$ .

### 4.5.3 | Energy transport

The transfer of energy from one spatial location to another has always been a central topic in physics. Recently, a lot of attention has been devoted to the so-called quantum batteries, i.e., quantum devices able to store energy and release it upon demand at specific times [113–116]. Devising a protocol to extract the maximum amount of energy from a charged battery, establishing a bound on its amount, and stabilising the battery’s charge has been addressed in several works [117–121]. Another line of research is embodied by the investigation of the charging protocol of a quantum battery [122–124], and, apart from a few instances [125], mainly non-interacting systems embodying the quantum battery have been considered.

Our work can be immediately rephrased in terms of a charging protocol of a many-body quantum battery. Dubbing the sender block as charger, the receiver block as battery and the wire as a quantum cable connecting the charger to the battery, a natural set-up for charging a quantum battery is represented by Fig. 4.2.

Nevertheless, in order to reinterpret the excitations dynamics in Sec. 4.3 as a charging protocol, a few precautions are in place. As shown in Ref. [124], the charging protocol should involve a time-dependent Hamiltonian

$$\hat{H}(t) = \hat{H}_0 + \lambda(t)\hat{H}_1 \quad (4.63)$$

where  $\hat{H}_0 = \hat{H}_C + \hat{H}_w + \hat{H}_B$ , are the time-independent Hamiltonians of the charger, the wire, and the battery, respectively.  $\hat{H}_1$  is the Hamiltonian connecting the charger (battery) to the wire and  $\lambda(t)$  is the coupling constant responsible for switching on and off the interaction between the charger (battery) and the wire when the charging protocol starts and ends. Generally, it is assumed that  $\lambda(t)$  is given by a step-function having a value of 1 for  $t \in [0, \tau]$  and 0 otherwise. Because of that time dependence, energy may not be conserved and there could be some switching energy  $\delta E_{sw}$  injected or extracted from the system during the protocol. This can be evaluated [124] by

$$\delta E_{sw}(\tau) = \text{tr} [\hat{H}_1 (\rho(0) - \rho(\tau))] , \quad (4.64)$$

where  $\rho$  is the density matrix of the full system. By definition of the switching energy in Eq. 4.64, for  $[\hat{H}_0, \hat{H}_1] = 0$ , one has  $\delta E_{sw}(\tau) = 0$ . However, this is not the case for our model, since the commutator does not vanish. Nevertheless, evaluating Eq. 4.64, we obtain a zero switching energy due to the mirror-symmetry of our model. The two terms entering Eq. 4.64 are equivalent to

$$\text{tr} [\hat{H}_1 \rho(0)] = \langle \Psi(0) | \hat{c}_{n_C}^\dagger \hat{c}_{w_1} + \hat{c}_{n_w}^\dagger \hat{c}_{1_B} + h.c. | \Psi(0) \rangle , \quad (4.65a)$$

$$\text{tr} [\hat{H}_1 \rho(\tau)] = \langle \Psi(0) | \hat{c}_{n_C}^\dagger(\tau) \hat{c}_{w_1}(\tau) + \hat{c}_{n_w}^\dagger(\tau) \hat{c}_{1_B}(\tau) + h.c. | \Psi(0) \rangle , \quad (4.65b)$$

where the last equation is written in the Heisenberg representation. Eq. 4.65a is identically null because of the choice of the initial state of our system, whereas, expressing Eq. 4.65b in terms of single-particle transition amplitudes, results in

$$\text{tr} [\hat{H}_1 \rho(\tau)] = \sum_{n \in \{n_C\}} \left( (f_n^{n_C})^* f_n^{1_w} + (f_n^{n_w})^* f_n^{1_B} + c.c. \right), \quad (4.66)$$

with *c.c.* denoting complex conjugation. The above expression is identically null as each  $(f_n^i)^* f_n^{i+1}$  results to be purely imaginary according to the conditions outlined in Sec. 4.3.1 for mirror-symmetric matrices.

As a consequence, the figures of merit for the charging protocol of a quantum many-body system via a quantum wire, are those reported in Ref. [124]. The mean energy stored in the battery and the mean storing power are, respectively,

$$E_B(\tau) = \text{tr}[\mathcal{H}_B \rho_B(\tau)], \quad P_s(\tau) = \frac{E_B(\tau)}{\tau}. \quad (4.67)$$

Other useful quantities are the maximum energy stored and the maximum power,

$$\bar{E}_s(\tau) \equiv \max_{\tau} [E_s(\tau)] \equiv E(\bar{\tau}), \quad \bar{P}_s(\tau) \equiv \max_{\tau} [P_s(\tau)] \quad (4.68)$$

and their corresponding optimal charging times,

$$\bar{\tau} \equiv \min_{E(\bar{\tau})=\bar{E}_s(\tau)} [\tau], \quad \tilde{\tau} \equiv \min_{P(\tilde{\tau})=\bar{P}_s(\tau)} [\tau]. \quad (4.69)$$

Lastly, the charging power obtained at maximum energy is defined as,

$$\bar{P}_s(\tau) \equiv \frac{\bar{E}_s(\tau)}{\tau}, \quad (4.70)$$

which is generally different from the maximum power because the times at which maximum energy and maximum power are achieved,  $\bar{\tau}$  and  $\tilde{\tau}$  respectively, may not coincide. In this subsection we choose  $h > 1$ , so that the charger state with all spin aligned in the positive *z*-direction is the highest energy eigenstate of  $\hat{H}_B$ , with energy  $\frac{n_B h}{2}$ . Applying the same magnetic field  $h$  to the rest of the system, wire and battery, allows us to use the formalism of Sec. 4.3 to evaluate the above figures of merit, as a uniform magnetic field in Eq. 4.25 implies only an uniform shift by  $h$  of all single-particle eigenenergies, with the eigenvectors remaining unchanged. Such a uniform shift brings along only an irrelevant overall phase factor in the dynamics as it amounts to adding a constant to the Hamiltonian in Eq. 4.25.

Interestingly, only the one-body terms in  $\hat{H}_B$  contribute to the mean energy  $E_B(\tau)$  in Eq. 4.67. This can be immediately seen as, at time  $\tau$ , the density matrix of the battery  $\rho_B(\tau)$  represents the state with all the spins flipped as perturbative transfer has



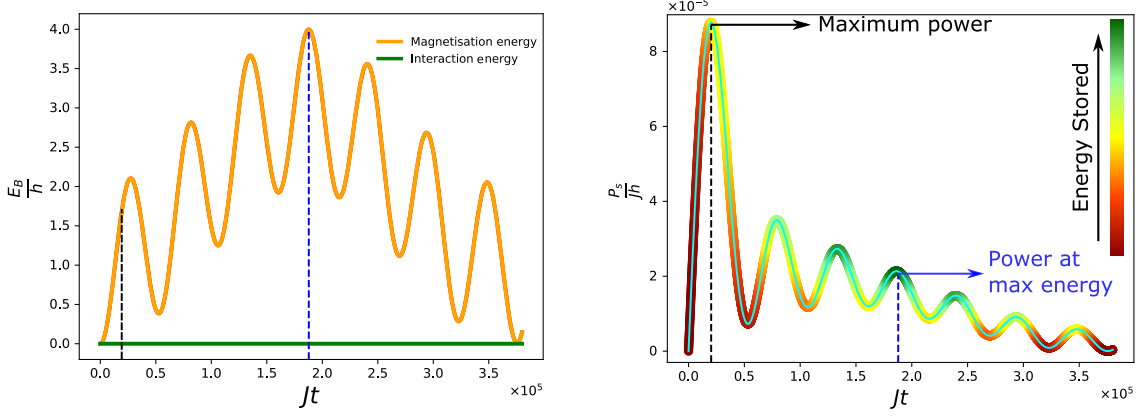


Figure 4.9: Energy and charging power for a battery made out of 4 qubits  $n_B = 4$ , left and right panel, respectively. The dotted line in the left panel corresponds to the transfer of the four excitations from the sender to the receiver. The orange line is the contribution of the one-body term in  $\hat{H}_B$ , whereas the green line that of the two-body term. In the right panel, the black dotted line is the time at which the maximum power is achieved, whereas the blue dotted line is the time at which the maximum energy is stored in the battery, Eq. (4.70). The corresponding energy stored in the battery is reported in the left figure by the same lines. The color of the curve  $P_s(\tau)$  indicates the amount of energy stored in the battery at that time. The length of the wire is 32, for a total length of the chain of 40.

occurred. In addition, it results also that the energy due to the inter-spin interaction term is vanishing at all times, as a result of the following equation

$$E_I \equiv \sum_{i \in \{n_B\}} \frac{1}{2} \langle \hat{c}_{i+1}^\dagger \hat{c}_i + h.c. \rangle = \sum_{\substack{i \in \{n_B\} \\ n \in \{n_C\}}} \left( (f_n^i)^* f_n^{i+1} + c.c. \right), \quad (4.71)$$

again because of the conditions on  $f_i^j(t)$  for mirror-symmetric matrices, as already derived for the switching energy  $\delta E_{sw}$ .

This allows us immediately to use our results to confirm that all the charger's energy is transferred to the battery and, remarkably, no energy is stored in two-body correlations at any time. This has several advantages: on the one hand, only single-qubit operations are necessary to extract the energy from the many-body battery and, on the other hand, the  $n_B$  spins embodying the battery can be split in independent, non-interacting partitions without any loss of the initially stored energy.

An instance of the charging process of a quantum many-body battery is shown in Fig. 4.9 for the case of  $n_s = 4$ . Notice that the power at maximum energy as by Eq. (4.70) is obtained at a considerably larger time than the maximum power, Eq. (4.68).

## 4.6 | Three qubit entanglement

Having derived in the previous section 4.3 the tools to obtain the receiver three qubit density matrix, in this section we will overview a few results about multipartite entanglement we will use to tackle the multipartite entanglement transfer problem.

Whereas two qubit entanglement criteria for an arbitrary density matrix have been derived [126] and entanglement monotones have a closed expression [127], for the entanglement shared among three qubits the scenario is much more complex, and, for arbitrary mixed states no closed expression of an entanglement measure is known.

One of the difficulties in characterizing the entanglement shared among three qubits is the existence of six different SLOCC (stochastic local operations and classical communication) classes for pure states: the *GHZ*- and *W*-class for genuinely entangled states, three classes are composed by a two-qubit Bell state and single qubit state embodying the bi-separable states with respect to each possible partition, and, finally, a product state of three qubits representing the fully separable state [128].

This classification has been extended to mixed states [129] giving rise to a hierarchy of entanglement where local POVMs can transform states only from a higher to a lower class, whereas each class is invariant under SLOCC, see Fig.4.6 for the schematic structure. However, while pure states that are biseparable with respect to each partition are also fully separable, the same does not hold for mixed states because of the existence of PPT entangled states.

For three qubits a pure state is called fully separable if it can be written in the form

$$|\Psi_{fs}\rangle = |\psi_1\rangle |\psi_2\rangle |\psi_3\rangle \quad (4.72)$$

and a mixed state belongs to the fully separable class  $S$  if it can be written as a convex combination of fully separable pure states

$$|\rho_{fs}\rangle = \sum_i p_i |\Psi_{fs}\rangle \langle \Psi_{fs}| . \quad (4.73)$$

A pure bi-separable state, belonging to the class  $B$ , is defined as being separable under one, or more, bi-partitions,  $\{1|23, 12|3, 13|2\}$ , as, e.g., in

$$|\Psi_{bs}\rangle = |\psi_{12}\rangle |\psi_3\rangle , \quad (4.74)$$

with qubits 1 and 2 possibly entangled. Consequently, a bi-separable mixed state reads

$$|\rho_{bs}\rangle = \sum_i p_i |\Psi_{bs}\rangle \langle \Psi_{bs}| . \quad (4.75)$$

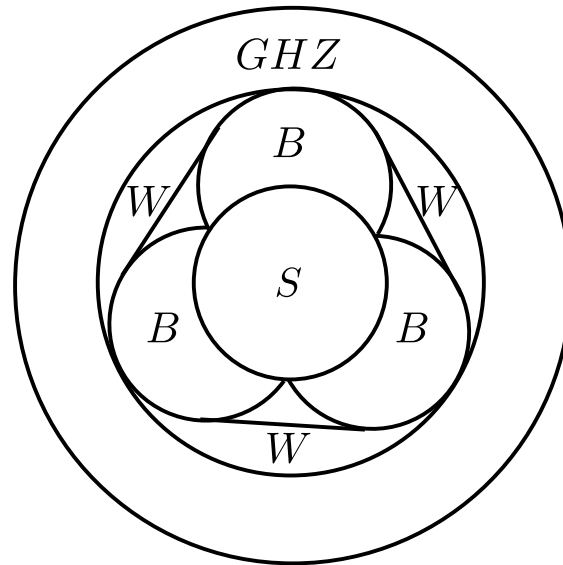


Figure 4.10: Schematic diagram of the classification of three qubit states:  $S$  fully separable,  $B$  bi-separable,  $W$  and  $GHZ$  non-separable.

If a mixed state can not be written as in Eqs. 4.73 or 4.75, it contains genuine multipartite entanglement, which can be of the  $W$  or of the  $GHZ$ -type. It holds that  $S \subset B \subset W \subset GHZ$  [129].

In order to determine to which SLOCC class a three qubit pure state belongs, one can rely on the three-tangle  $\tau$  [130] and the concurrence  $C$ . The  $GHZ$  class contains states with  $\tau > 0$ , whereas states in the  $W$  class have  $\tau = 0$  but finite  $C^{(12)}$ ,  $C^{(13)}$ , and  $C^{(23)}$ ; bi-separable states have only one of the above concurrences different from zero, and, finally, for fully separable states both  $\tau$  and all  $C^{(ij)}$  vanish. This classification extends to mixed states by considering the classes in its pure state decomposition and using the convex roof extension of a corresponding pure state entanglement measure: for  $GHZ$ -type entanglement  $\tau$  is finite, for  $W$ -type entanglement  $\tau = 0$  but the concurrence of genuine multipartite entanglement [131] is finite; whereas, for bi-separability, the square root of the global entanglement [132] is finite, and both the three-tangle and concurrence of genuine multipartite entanglement are zero. Finally, for states in the fully separable class, all entanglement measures vanish.

Generally, convex roof extensions of pure state entanglement measures are difficult to calculate as they involve an optimisation over an infinite number of convex decompositions into pure states of a mixed state. Although efficient numerical algorithms have been developed for several multipartite entanglement measures, see, e.g., Ref. [133], for full rank density matrices there is no efficient algorithm available to date.

An alternative to entanglement measures is given by entanglement witnesses (EW) [134]. An EW is an hermitian operator  $\mathcal{W}$  such that  $\text{Tr} [\mathcal{W}\rho] \geq 0$  on all states  $\rho$  not belonging to the entanglement class the EW aims at detecting. As such,  $\mathcal{W}$  is a witness in the sense it constitutes a sufficient, but not necessary criterion for detecting entanglement. For the GHZ-class several witnesses have been devised and their decomposition into local projective measurements have allowed to detect experimentally genuine multipartite entanglement [135].

In our analysis of the transfer of multipartite entanglement, we will use the entanglement witnesses of Ref. [129]

$$\mathcal{W} = \frac{1}{2}\mathbb{1} - |GHZ\rangle\langle GHZ|. \quad (4.76)$$

One has  $\text{Tr} [\mathcal{W}\rho] > 0$  on every biseparable state of Eq. 4.75, for  $-\frac{1}{4} < \text{Tr} [\mathcal{W}\rho] < 0$  the state  $\rho$  can belong either to the  $W$  or the  $GHZ$ -class, while only states belonging to the  $GHZ$  class have  $-\frac{1}{2} < \text{Tr} [\mathcal{W}\rho] < -\frac{1}{4}$ . For states belonging to the  $W \setminus B$  class, the following witness can be used  $\mathcal{W}_W = \frac{2}{3}\mathbb{1} - |W\rangle\langle W|$ .

In Ref. [136] a semidefinite programming (SDP) approach has been put forward in order to detect multipartite entanglement, although without distinguishing between the  $GHZ$ - and the  $W$ -type entanglement. Using convex optimisation technique, one is able to solve, for an arbitrary multipartite state  $\rho$ , the minimization problem

$$\min \text{Tr} [W\rho], \quad (4.77)$$

where  $W$  is a fully decomposable witness with respect to every bipartition of the multipartite system. Interestingly, (the negative of) Eq. 4.77 is also a multipartite entanglement monotone and can hence be used to quantify genuine multipartite entanglement [137].

Apart from entanglement witnesses, the quantification of entanglement in a three qubit mixed state via the tangle  $\tau$  is possible only in a few specific low-rank cases [138]. However, bipartite entanglement measures can be used on multipartite states by considering every possible partitions [139], and we will use in the following the tripartite negativity  $N_{ABC}$  proposed in Ref. [140]:

$$N^{(3)} = \sqrt[3]{N_{A|BC}N_{AB|C}N_{AC|B}} \quad (4.78)$$

where  $N_{X|YZ}$  is the negativity [141]

$$N_{X|YZ} = \frac{\sum_i |\lambda_i| - 1}{2}, \quad (4.79)$$

with  $\lambda$  being the eigenvalues of the partial transpose of  $\rho_{XYZ}$  with respect to the subsystem  $X$ . However, due to the Peres-Horodecki criterion [126, 142], for dimensions higher than  $2 \times 2$  and  $2 \times 3$ ,  $N_{X|YZ} > 0$  constitutes a sufficient, but not necessary condition for bipartite entanglement between the partitions  $X$  and  $YZ$ . Notice that  $N^{(3)}(\rho) > 0$  is a sufficient condition for distillability of a *GHZ* state from  $\rho$  [143].

Finally, let us also report for completeness, the concurrence between two qubits  $i$  and  $j$ ,  $C^{(ij)}$ , [127]. Because all the two-qubit density matrices  $\rho^{(ij)}$  are of *X*-type, with a single non-zero off-diagonal element, the concurrence reduces to [144]

$$C^{(ij)} = 2 \max \left[ 0, \left| \rho_{12}^{(ij)} \right| - \sqrt{\rho_{00}^{(ij)} \rho_{33}^{(ij)}} \right]. \quad (4.80)$$

### 4.6.1 | Entanglement transfer

Let us now finally illustrate the main results of this work: the transfer of multipartite entanglement via perturbative couplings between a sender and a receiver block connected by a quantum wire. As we are interested only in the receiver block, we renumber, for the sake of readability, the spins therein contained  $n = 1, 2, 3$ , starting from the edge. In Fig. 4.6.1 we report the results for two entanglement witnesses, respectively given by Eq. 4.76 and Eq. 4.77, the tripartite negativity  $N^{(3)}$ , Eq. 4.79, and the concurrence  $C^{(13)}$ , Eq. 4.80, between qubit 1 and 3 for a chain of length  $N = 19$  and  $J_0 = 0.01$  both on a time scale of  $T$  and  $\tilde{T}$ . Being the concurrence between neighboring qubits  $C^{(12)} = C^{(23)} = 0$ , and the witness  $\mathcal{W}_W$  detecting *W*-class states positive at all times when evaluated on the receiver density matrix,  $\text{Tr}[\mathcal{W}\rho_r] > 0$ , we argue that no *W*-entanglement is present at any time in the receiver spins.

Whereas the witness based on the fidelity with a *GHZ* state, Eq. 4.76, detects genuine multipartite entanglement at finite time-intervals, the witness in Eq. 4.77 detects genuine multipartite entanglement at any time but for discrete time points. The latter coincide with the times when the tripartite negativity  $N^{(3)}$  vanishes. There are regions where the witness  $-\frac{1}{4} < \text{Tr}[\mathcal{W}\rho] < 0$ , hence the tripartite entanglement could be either *GHZ* or *W*-type. However, the fact that  $C^{(12)} = C^{(23)} = 0$  is an indication that  $\rho$  belongs to the *GHZ*-class. The same holds for the regions where the multipartite entanglement monotone derived Eq. 4.77 gives a non-zero value.

We also observe that both  $N^{(3)}$  and  $-\text{Tr}[\mathcal{W}\rho]$  oscillate with period  $\tilde{T}$ , becoming vanishingly small when the concurrence between qubit 1 and 3 reaches its maximum value,

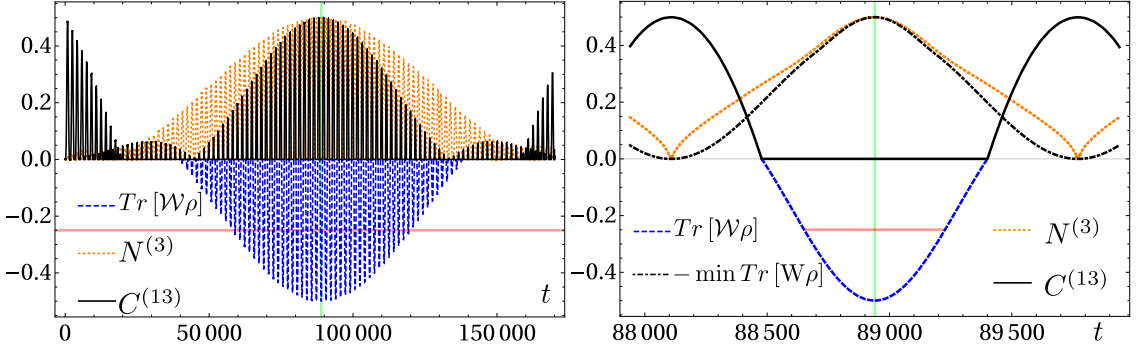


Figure 4.11: Witness  $\mathcal{W}$ , Eq 4.76, (blue dotted line) and  $W$ , Eq. 4.77, (black dotted line); tripartite negativity  $N^{(3)}$ , Eq. 4.78, (orange dotted line), and concurrence between qubit 1 and 3,  $C^{(13)}$ , Eq 4.80, (blue line) on a time scale of  $T = \frac{2\pi}{\omega_6}$  (upper panel) and a few  $\tilde{T} = \frac{2\pi}{\omega_5}$  (lower panel) around the maximum of the fidelity given by  $\tau = \frac{T}{2}$  (green vertical line). The horizontal red line is set at  $-\frac{1}{4}$  to detect *GHZ*-class entanglement via the witness  $\mathcal{W}$ . Notice that, around  $t = \tau$ ,  $C^{(13)}$  and  $N^{(3)}$  are oscillating in phase opposition.

$C^{(13)} = \frac{1}{2}$ . At these points  $t^*$  in time, the density matrix of the receiver block reads

$$\begin{aligned} \rho(t^*) &\simeq \frac{1}{2} |000\rangle\langle 000| + \frac{1}{2} \left( \frac{|110\rangle - |011\rangle}{\sqrt{2}} \right) \left( \frac{\langle 110| - \langle 011|}{\sqrt{2}} \right) \\ &= \frac{1}{2} |0_A 0_C\rangle\langle 0_A 0_C| \otimes |0_B\rangle\langle 0_B| \\ &+ \frac{1}{2} \left( \frac{|1_A 0_C\rangle - |0_A 1_C\rangle}{\sqrt{2}} \right) \left( \frac{\langle 1_A 0_C| - \langle 0_A 1_C|}{\sqrt{2}} \right) \otimes |1_B\rangle\langle 1_B|, \end{aligned} \quad (4.81)$$

which is a biseparable state under the partition  $AC|B$ . Therefore, we can conclude that these are the only (isolated) points in time where the state does not have any genuinely multipartite entanglement. Clearly, the reason for these oscillations is that one of the excitations is travelling with frequency  $\omega_5$  back and forth between the sender and the receiver block through the quantum wire exploiting the 1<sup>st</sup>-order triplet.

Analysing the short-time behaviour, we notice that qubits 1 and 3 get entangled with  $C^{(13)} = \frac{1}{2}$  already on a time-scale of  $\tilde{T}$ , whereas the tripartite negativity  $N^{(3)}$ , as well as the entanglement monotone  $-Tr[W\rho]$ , is very small, Fig. 4.6.1. The reason still being the presence of the 1<sup>st</sup>-order triplet, entering the transition amplitudes  $f_i^j$  with  $i = 1, 3$  and  $j = N-2, N$ . Whereas, in order to have finite genuinely tripartite entanglement one needs a finite probability to find three excitations on the receiver block, thus involving the two 2<sup>nd</sup>-order doublets, which is the only term entering the transition amplitude.

In Fig. 4.6.1 we test our protocol for increasing values of  $J_0$  and report a good transfer of genuine multipartite entanglement to the sender block in the weak-coupling regime,

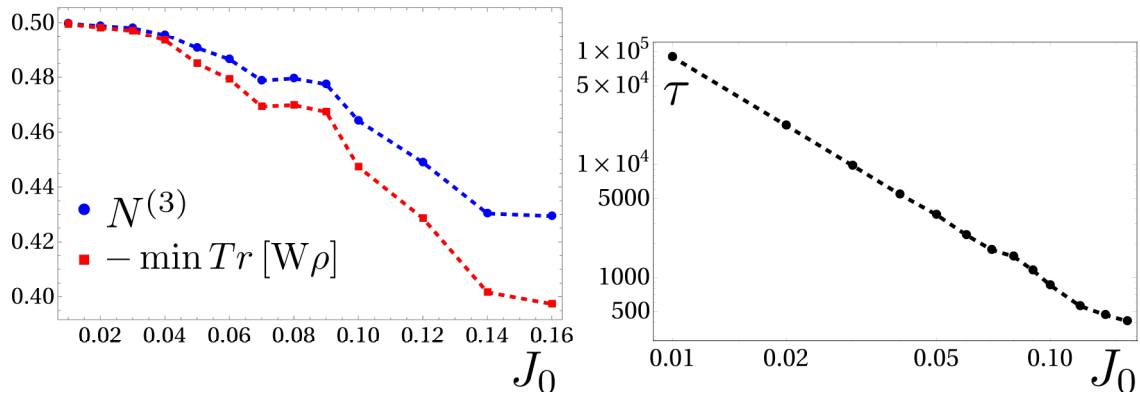


Figure 4.12: (left panel) Maximum tripartite negativity  $N^{(3)}$ , Eq. 4.78, blue dots, and witness  $W$ , Eq. 4.77, red square, as a function of the coupling  $J_0$  for a chain of length  $N = 23$ . (right panel) Time  $\tau$  at which the maximum are achieved vs  $J_0$  for the same parameters as in the left panel. Notice how the two entanglement monotones change outside the weak-coupling regime. Similarly, around the same values, the power law  $\tau \sim J_0^{-2}$ , obtained from 2<sup>nd</sup>-order perturbation theory in Ref. [4], starts to fail. Lines are for guiding the eyes.

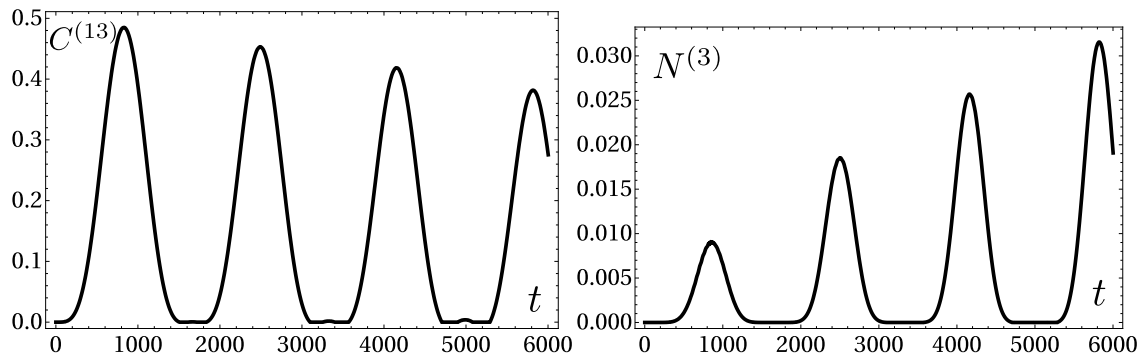


Figure 4.13: Short-time behaviour of the concurrence  $C^{(13)}$ , Eq 4.80, (left panel) and of the tripartite negativity  $N^{(3)}$ , Eq. 4.78 (right panel). Notice that, at variance with the time scale of  $T$ , on a times scale of the order of  $\tilde{T}$ , the two entanglement quantifiers are oscillating in phase.

say up to  $J_0 \simeq 0.1$ , after which a quick decay of the quality of the transfer is observed. Similarly, the transfer time  $\tau$  at which the maximum is obtained follows  $\tau \propto J_0^{-2}$  in the perturbative regime, before breaking down after  $J_0 \simeq 0.1$ .

Let us also add that  $C_{\#}^{(13)} = C^{(13)} = \frac{1}{2}$ , where  $C_{\#}^{(13)}$  is the concurrence of assistance [145],

evaluated by

$$C_{\#}^{(ij)} = \sum_{n=1}^4 \sqrt{\lambda_n}, \quad (4.82)$$

where  $\lambda_n$  are the eigenvalues of the matrix  $R = \rho(\hat{\sigma}^y \otimes \hat{\sigma}^y) \rho^* (\hat{\sigma}^y \otimes \hat{\sigma}^y)$ . This quantity is the maximum entanglement achievable between two qubits by means of LOCC operations on the complementary qubits, that is the sender and the wire qubits.

## 4.7 | Summary

In this chapter we have introduced quantum transport. We have seen the Green function formalism, which provides a useful tool for the calculation of the transported quantities along the physical medium. Here, we focused on the 1D-chain described by the tight-binding Hamiltonian (4.25). We showed in Sec. 4.3 that adjusting the hopping strength between the sites of the chain we can control the transfer of excitations between the two edges of the chain and regardless of the statistical nature of the particles, we were able to obtain high fidelity transfer. Furthermore we used the same model to transfer entanglement. Remarkably, one can use the perturbatively-perfect transfer to gain a little amount of entanglement between the sites of the receiver and make use of entanglement purification protocols for applications in quantum information technology.

Here, the 1D model was used for introducing the subject, and even though no optomechanics appears in this Chapter, we can use the same tools for analyzing the transfer of excitations in arrays of optomechanical cavities, as described for example in Chapter 2. However, we should notice that the system here presented shows Rabi-like oscillations for which the particles and the physical quantities of interest, keep on going back and forth on the chain. This behavior can be annoying, for example in a quantum battery, as it would require the user to switch off the connection exactly when the charging reaches the maximum. For this reason, a metamaterial with nonreciprocal behavior could be preferred for some applications and it could also prevent the back-propagation stemming from disorder in the system. In the next Chapter we will introduce topological insulators, metamaterials with the property of allowing nonreciprocal transport. We will introduce the mathematics that explains the physics and apply it on an array of optomechanical cavities.





# Topological insulators in Optomechanics

## 5.1 | Introduction

Topological insulators are one of the wonders of modern physics. They are materials where the topology of the Brillouin zone of the bulk Hamiltonian gives information on a finite size sample. Furthermore they are explained with a new kind of phase transition, called quantum phase transition, which are distinct from the ones described by the Landau theory. For instance, it does not depend on an order parameter, but it accounts for an abrupt change in the topological properties of the Hamiltonian. Moreover topological insulators find a very precious application for they allow back scattering immune propagation. Let's consider two materials with relative permittivity  $\varepsilon_1 > 0$  and  $\varepsilon_2 < 0$  respectively and a surface plan wave  $e^{\pm ikx}$  propagating on the interface between the two materials, with  $x$  being the direction parallel to the interface. The dispersion relation is [146]

$$k = \frac{\omega}{c} \sqrt{\frac{\varepsilon_1 \varepsilon_2}{\varepsilon_1 + \varepsilon_2}}, \quad (5.1)$$

where  $\omega$  is the wave frequency and the permittivity is a function of it,  $\varepsilon_{1,2} = \varepsilon_{1,2}(\omega)$ . If we consider, for instance, the Drude model [146], we have  $\varepsilon(\omega) = 1 - \omega_p^2/\omega^2$ , with  $\omega_p$  being the plasma frequency. The substitution of this relation in Eq. (5.1) leads to a reciprocal dispersion relation,  $\omega(k) = \omega(-k)$ . This means that for a given frequency we have both forward and backward propagating waves.

Whenever a wave propagating on the surface of this material encounters a discontinuity it undergoes through a partial reflection for the material allows the two directions of propagation.

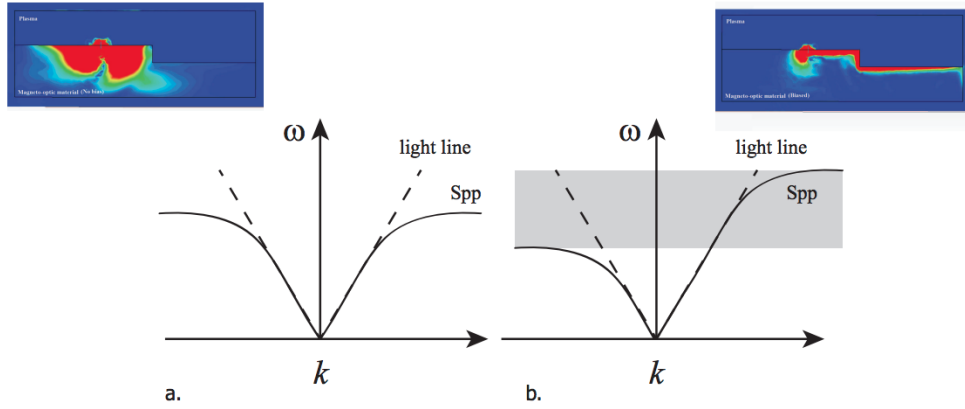


Figure 5.1: a. Dispersion of reciprocal SPP. Upper-left insert shows SPP power flow excited by a vertical dipole source near a step change in height at the interface between a reciprocal medium (below) and a different reciprocal medium (above), b. nonreciprocal SPP; shaded region depicts frequency range of uni-directional propagation. Upper-right insert is the same as upper-left insert, except that the lower medium is now non-reciprocal and we operate in the gap, ensuring one-way propagation, figure from [147].

However, if the material doesn't allow the counter-propagating wave for a certain frequency, the reflection will not occur. Upon the encountering of a discontinuity the wave will tour around it and continue its propagation without any losses. This condition comes from a non reciprocal dispersion relation and leads the wave propagation to be back-scattering immune. An example is shown in Fig. 5.1, where surface plasmon polaritons (SPP), a kind of electromagnetic wave circulating at the interface between two media [147], propagates in material with nonreciprocal dispersion relations.

One class of materials that allows this behavior is called topological insulator (TI). The TIs cannot be adiabatically transformed into a normal insulator, for this reason we say the two kinds are topologically distinct. In the next chapters we will give a formulation of the adiabatic theorem and a short introduction about topology and its role in solid state physics. In particular we will focus on 2D materials with broken time reversal symmetry, also called Chern insulators. Those are specific materials characterized by a topological invariant, the Chern number, related to the concepts of Berry phase and Berry curvature. After introducing these concepts we will apply them to a specific model in optomechanics, that is the focus of this thesis. But first we will do an historical journey of the physical phenomena that pushed into the discovery of those subject. In the next section we introduce the classical and quantum Hall effects.

## 5.2 | The classical Hall effect

The Hall effect played an important role in classical electromagnetism for the discovery the electrons are the carriers of the charge. If we take a conductor and move it perpendicularly to a magnetic field, the combination of the current and the Lorentz force induced by the magnetic field generates eventually, at equilibrium, an electric potential  $V_H$ , whose sign depends on the sign of the charge carriers. This effect is called classical Hall effect and  $V_H$  is called the Hall potential. Moreover the calculations allow us to get interesting insights about the conductivity and resistivity of the material in the two plane directions.

Let's take a particle of mass  $m$  and charge  $-e$  constrained to move on a plane  $(x, y)$  with velocity  $\vec{v} = (\dot{x}, \dot{y}, 0)$ . The particle is subject to a magnetic field  $\vec{B} = (0, 0, B)$  perpendicular to the plane in direction  $z$  as shown in the figure. The equation of motion is

$$m \frac{d\vec{v}}{dt} = -e\vec{v} \times B, \quad (5.2)$$

whose solution is

$$x(t) = x_c - r \sin(\omega_B t + \phi) \quad (5.3a)$$

$$y(t) = y_c + r \cos(\omega_B t + \phi). \quad (5.3b)$$

Hence, the particle is constrained to move in a circle of center  $(x_c, y_c)$ , radius  $r$  and phase  $\phi$  depending on the initial conditions. We also defined the cyclotron frequency  $\omega_B$ . We now consider a slightly more complicate model, the Drude model, where we add to the system and electric field  $\vec{E}$  and a linear friction term with coefficient  $\eta$ . The equation of motion becomes

$$m \frac{d\vec{v}}{dt} = -e\vec{E} - e\vec{v} \times \vec{B} - \eta\vec{v}. \quad (5.4)$$

At equilibrium, the l.h.s. of the equation of motion can be set to zero, and after defining the current density  $\vec{J} = -ne\vec{v}$ , with  $n$  being the charge carriers density, we get, in matrix notation,

$$\begin{pmatrix} 1 & m\omega_B/\eta \\ -m\omega_B/\eta & 1 \end{pmatrix} \vec{J} = \frac{e^2 n}{\eta} \vec{E}. \quad (5.5)$$

The relation above corresponds to the Ohm's law  $\vec{J} = \sigma \vec{E}$  of classical electromagnetism, with  $\sigma$  being the conductivity of the material. In this case  $\sigma$  represents a matrix with

different the diagonal and offdiagonal terms. This difference is the source of the Hall effect, since in a finite material  $V_H$  is given by the off diagonal terms.

## 5.3 | The Quantum Hall effect

In 1980 V. Klitzing [148] performed experiments on a 2-dimensional electron gas subject to a strong perpendicular magnetic field  $B$  and measured the electron hall conductance  $\sigma$ . With very surprise, for a large value of the magnetic field, the electron conductance doesn't change linearly with the magnetic field intensity, as expected for the classical Hall effect. For the observations of Klitzing, for which he was awarded the Nobel prize in 1985, the Hall conductance, after an initial linear behavior, reaches plateaus where it remains constant. After increasing the magnetic field it performs a jump into another plateau with higher value of  $\sigma_{xx}$  (see Fig. 5.2). The behavior of the conductivity in the other direction  $\sigma_{xy}$  is opposite, it is zero while it abruptly changes its value in correspondence of the jumps of  $\sigma_{xx}$ . Furthermore the hall conductivity is given by an integer times the ratio between two fundamental quantities: the electronic charge  $e$  and the Planck constant  $h$ ,

$$\sigma_{xx} = \nu \frac{e}{h}, \quad \text{with } \nu \in \mathbb{N}. \quad (5.6)$$

The center of the plateaus is given by the relation  $B = \frac{n_e}{\nu} \Phi_0$ , where  $n_e$  is the electron density and  $\Phi_0$  is the quantum flux. In fact it represents the flux of the magnetic field in the  $x - y$  plane. This relations is true only when  $\nu$  is an integer. This integer is the number of filled Landau levels, which we are going to discuss in the next section.

### 5.3.1 | The Landau problem

The Landau problem studies the dynamics of a charged particle constrained to move on the plane  $x - y$  subject to a magnetic field perpendicular to the plane  $\mathbf{B} = (0, 0, B)$ . The interaction between the particle and the magnetic field can be treated with the minimal coupling Hamiltonian

$$H = \frac{1}{2m} \left( \mathbf{p} - q\mathbf{A} \right)^2, \quad (5.7)$$

where  $m$  is the mass of the particle,  $q$  the charge and  $\mathbf{A}$  is the vector potential, such that  $\mathbf{B} = \nabla \times \mathbf{A}$ . We remember that  $\mathbf{A}$  is not univocally defined since it has gauge freedom. A

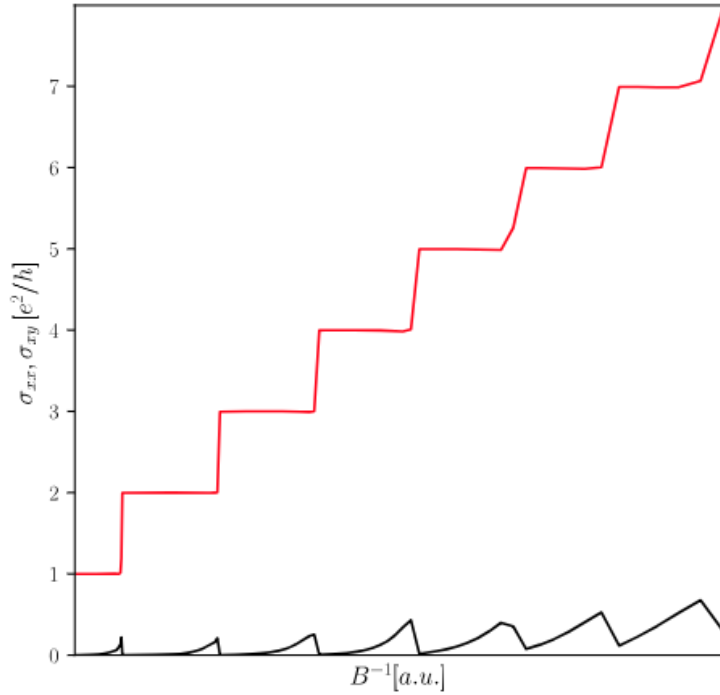


Figure 5.2: The Hall conductivities  $\sigma_{xx}, \sigma_{xy}$  in direction  $x$  and  $y$  respectively as a function of the inverse applied magnetic field  $B^{-1}$ . The conductivity  $\sigma_{xx}$  runs onto plateaus which have the integer values in unit of  $e^2/h$ . The conductivity  $\sigma_{xy}$  is null, but in correspondence of the jumps of  $\sigma_{xx}$ .

gauge transformation of  $\mathbf{A}$  leads the dynamics to be unchanged. We can indeed modify the vector potential  $\mathbf{A}$  with the transformation

$$\mathbf{A} \rightarrow \mathbf{A} + \nabla f, \quad (5.8)$$

where  $f$  is a scalar function of the coordinates. We take a suitable choice for  $\mathbf{A}$  to simplify the calculation. We consider the Landau gauge, s.t.

$$\mathbf{A} = \begin{pmatrix} 0 \\ Bx \\ 0 \end{pmatrix}, \quad (5.9)$$

for which the Hamiltonian becomes:

$$H = \frac{p_x^2}{2m} + \frac{1}{2m} (p_y - qBx)^2. \quad (5.10)$$

$p$  is the canonical momentum operator. We will see in this problem the difference between canonical and mechanical momentum. The canonical momentum is in quantum mechanics the generator of the translations and obeys the canonical commutation relations  $[x_i, p_j] = i\delta_{ij}\hbar$  with  $i, j$  labeling different directions. On the other hand, the mechanical momentum, here we call it  $\pi$ , comes from Newton's second law and it is defined by the relation  $\pi = m\dot{x}$ . We will use these two concepts in the resolution of the energy spectrum.

We first notice that the dynamics is gauge invariant. In this gauge the momentum in the  $y$  direction  $p_y$  commutes with the Hamiltonian, so we are able to find the eigenvalues of this operator and of the Hamiltonian simultaneously. We call  $\omega_B = \frac{qB}{m}$  the cyclotron frequency and we write Eq. (5.10) as:

$$H = \frac{p_x^2}{2m} + \frac{1}{2}m\omega_B^2 \left( x - \frac{p_y}{m\omega_B} \right)^2, \quad (5.11)$$

which we can recognize as the quantum harmonic oscillator shifted by a displacement  $\frac{p_y}{m\omega_B}$ . We define the magnetic length  $x_l = \sqrt{\frac{\hbar}{qB}}$ . It is the characteristic scale of quantum effects for a particle of charge  $q$  in a magnetic field  $B$ . With this definition the displacement assumes the value  $\frac{x_l^2 p_y}{\hbar}$ . Following the standard algebraic procedure we can find the spectrum of the harmonic oscillator. We define two new operators  $\pi_x = p_x$  and  $\pi_y = p_y - qBx$  which are also the mechanical momenta in the two directions since they satisfy the relation  $\pi = m\dot{x}$ . We can now define the raising and lowering ladder operators  $a, a^\dagger$  as

$$a = \frac{1}{\sqrt{2q\hbar B}}(\pi_x - i\pi_y), \quad a^\dagger = \frac{1}{\sqrt{2q\hbar B}}(\pi_x + i\pi_y), \quad (5.12)$$

that satisfy the canonical commutation relation  $[a, a^\dagger] = 1$ . The Hamiltonian becomes the standard one

$$H = \hbar\omega_B \left( a^\dagger a + \frac{1}{2} \right). \quad (5.13)$$

Even though the definition of the ladder operators is not quite canonical, as it involves the two directions of the mechanical momentum, the energy spectrum is the harmonic oscillator one, with

$$E_n = \hbar\omega_B \left( n + \frac{1}{2} \right), \quad n = 0, 1, \dots, \quad (5.14)$$

where  $n$  labels the Landau levels. If we take Eq. (5.10) we notice it has translational invariance in the  $y$  direction. For this reason we can find an ansatz of the form

$$\Psi_{p_y}(x, y) = e^{\frac{i}{\hbar}p_y y} \psi_{p_y}(x), \quad (5.15)$$

where we have a separable variable solution with a plane wave on the  $y$  direction that multiplies the function  $\psi_{p_y}(x)$ . The latter can be identified with the Hermite wavefunctions of the harmonic oscillator.

$$\psi_{p_y} = H_n \left( x + \frac{p_y}{\hbar} x_l^2 \right) \exp \left[ - \frac{(x - \frac{p_y}{\hbar} x_l^2)^2}{2x_l^2} \right], \quad (5.16)$$

where  $H_n$  is the properly normalized Hermite polynomial.

We see that the state  $\Psi_{p_y}(x, y)$  presents a large degeneracy given by the momentum  $p_y$ . In order to calculate the degeneracy we need to take a finite size sample with lengths  $L_x, L_y$  in the  $x$  and  $y$  directions respectively. Given the finite size of the sample the momentum  $p_y$  is quantized in units of  $2\pi\hbar/L_y$ . In the  $x$  direction the number of states is given by consideration of the wavefunction  $\psi_{p_y}(x)$ . We can indeed argue it is localized around the displacement  $x_l^2 p_y / \hbar$  with  $0 \leq x \leq L_x$ . If we define the area  $A = L_x L_y$  we get

$$N = \frac{L_y}{2\pi} \int_{-L_x/x_l^2}^0 dp_y = \frac{qBA}{2\pi\hbar} = \frac{AB}{\Phi_0} \quad (5.17)$$

states available, where  $\Phi_0$  is the quantum of flux defined in the previous section.

### 5.3.2 | The Symmetric Gauge

We want here to repeat the calculations under a different choice of gauge and see what changes and what remains invariant. We already know we expect the dynamics to be the same, but we also expect to have a different definition for the canonical momentum. We will show here that considering a different gauge can have more than a merely pedagogical purpose. We analyze the symmetric gauge, defined as

$$\mathbf{A} = \frac{1}{2} \begin{pmatrix} -By \\ Bx \\ 0 \end{pmatrix}. \quad (5.18)$$

With respect to the Landau gauge, the symmetric gauge loses the translational invariance in favor of rotational symmetry.

The mechanical momentum is, as before,  $\boldsymbol{\pi}^- = \mathbf{p} - q\mathbf{A}$ . We can define a new operator  $\boldsymbol{\pi}^+ = \mathbf{p} + q\mathbf{A}$  that differs from the mechanical momentum only for the plus sign. This operator is however very useful since for this particular gauge choice it commutes with both the mechanical momentum and the Hamiltonian (5.7).



We can define a new ladder operators  $b, b^\dagger$  defined in complete analogy with the operators  $a, a^\dagger$  in Eq. (5.12)

$$b = \frac{1}{\sqrt{2q\hbar B}}(\pi_x^\dagger - i\pi_y^\dagger), \quad b^\dagger = \frac{1}{\sqrt{2q\hbar B}}(\pi_x^\dagger + i\pi_y^\dagger). \quad (5.19)$$

Together with the operators  $a, a^\dagger$ , these new ladder operators can be used to build the whole Hilbert state. We can associate each state with the the two eigenvalues  $n, m$  of the siml-number operators  $a^\dagger a, b^\dagger b$ , such that

$$|n, m\rangle = \frac{a^{\dagger n} b^{\dagger m}}{\sqrt{n!m!}}|0, 0\rangle. \quad (5.20)$$

In this expression the energy depends on the eigenvalue  $n$ , as in Eq. (5.14), whereas  $m$  accounts for the degeneracy.

Now we have a phenomenological description of the integer quantum Hall effect. Up to this section we have been able to describe the quantized behavior of the conductivity of a  $2d$  material in the two directions, when this is subject to a perpendicular magnetic field. Furthermore we have been able to derive the quantized nature of the energetic levels and its quantum degeneracy. However we are still missing of an explanation for the connection among the two phenomena. In order to get this we need to recall the adiabatic theorem and the historical path that led to the discovery of topological insulators, which is the subject of this chapter.

## 5.4 | The adiabatic theorem

In this section we deal with the dynamics of a quantum state subject to a slowly varying Hamiltonian. This system has been treated since the dawn of quantum mechanics. The results are mainly based on the famous adiabatic theorem, originally addressed by Born and Fock in 1928 [149], which states that a physical system remains in its instantaneous eigenstate if a given perturbation is acting on it slowly enough and if there is a gap between the eigenvalue and the rest of the Hamiltonian's spectrum.

The original version of the theorem, then generalized by Kato in 1956, already involves many features of quantum mechanics. When we apply a time-independent Hamiltonian to a state  $|\Psi(t)\rangle$  we can obtain the time-independent Schrödinger equation

$$H|\Psi(t)\rangle = \sum_n c_n |n\rangle e^{-\frac{i}{\hbar}E_n t}, \quad (5.21)$$

where  $|n\rangle$  and  $E_n$  are respectively the eigenvectors and eigenvalues of the Hamiltonian  $H$ . The coefficients  $c_n$  are complex numbers with the normalization condition that

$\sum |c_n|^2 = 1$ . The time-independent Eq. (5.21) is a stationary equation. If the state is in the  $n$ -th state at  $t = 0$  it will remain in the same state, for any future time  $t$ , just picking up a phase  $-E_n t/\hbar$ , called dynamical phase. It is called dynamical phase because it depends on the temporal evolution of the system.

In the adiabatic theorem we consider instead a slow-varying time dependent Hamiltonian  $H(t)$  and the orthonormal set of instantaneous eigenstates  $\{|n(t)\rangle\}$ . Now the eigenvalue equation is time-dependent. For the  $n^{\text{th}}$  state it reads

$$H(t) |n(t)\rangle = E_n(t) |n(t)\rangle, \quad (5.22)$$

whose general solution can be expressed as

$$|\Psi(t)\rangle = \sum_n c_n(t) |n(t)\rangle e^{i\theta_n(t)}, \quad (5.23)$$

where the term  $\theta_n(t) = -\frac{1}{\hbar} \int_{t_0}^t E_n(t') dt'$  is the dynamical phase we already met in the time independent case. We can substitute this solution in the differential Schrödinger equation

$$i\hbar H |\Psi(t)\rangle = \frac{d}{dt} |\Psi(t)\rangle \quad (5.24)$$

and obtain a differential equation for the coefficients

$$\dot{c}_n = -c_n \langle n(t) | \frac{d}{dt} n(t) \rangle - \sum_{m \neq n} c_m \frac{\langle n | \frac{dH}{dt} | m \rangle}{E_m - E_n} e^{-i(\theta_n - \theta_m)}. \quad (5.25)$$

Now we consider the derivative of the Hamiltonian  $\frac{dH}{dt}$  to be extremely small so that we can neglect the last term in Eq. (5.25). This procedure is the adiabatic approximation. It is the important approximation we apply for deriving the adiabatic theorem. In this case we are able to solve the differential equation and obtain

$$c_n(t) = c_n(t_0) \exp \left( - \int_{t_0}^t \langle n(t') | \frac{d}{dt} n(t') \rangle dt' \right) = c_n(t_0) e^{i\gamma_n}. \quad (5.26)$$

The adiabatic theorem states that if the Hamiltonian is slowly varying the system will remain in its instantaneous eigenstate just picking up a phase  $\theta_n(t) + \gamma_n$ . The latter is called geometric phase and as opposed to the dynamical phase it does not depend on the temporal evolution itself, but rather on the geometric path traveled by the state. The geometric phase appears as a result of the adiabatic theorem and it is known since almost one century. However, in the early stage of quantum mechanics this phase had been totally ignored. The reason is that we can get rid of it by just applying a gauge transformation. We will see in the next section the importance of this extra phase.

## 5.5 | The geometric phase

The geometric phase  $\gamma_n$ , defined through Eq. (5.26), can be neglected just with a gauge transformation. We may define a new eigenvector

$$|\tilde{n}(t)\rangle = e^{i\gamma_n} |n(t)\rangle \quad (5.27)$$

for which the solution of the Schrödinger equation does not involve the geometric factor. It may seem there is no way we can, or should, take into account the geometric phase. However, there are some occasions when it is of major importance. For example, if we consider a cyclic evolution, the geometric phase  $\gamma_n$  depends on the geometry of the traveled path. In a cyclic path, the geometric phase is gauge invariant. We can show it considering a parameter dependent state  $|\Psi\rangle = |\Psi(\mathbf{R})\rangle$  and a parameter dependent Hamiltonian  $H = H(\mathbf{R}(t))$ , with  $\mathbf{R}$  being a vector taking values in the parameter space  $\mathcal{P}$ . Thus, we can think the temporal evolution as the curve

$$\mathcal{C} : t \rightarrow \mathbf{R}(t) \quad (5.28)$$

defined in the parameter space. The cyclicity of the Hamiltonian after a period  $T$  can be seen as a closed curve  $\mathcal{C}$ , such that  $\mathbf{R}(0) = \mathbf{R}(T)$ . If the period  $T$  is large enough we can apply the adiabatic approximation and obtain the solution (5.26).

For the sake of simplicity we consider the initial state Eq. (5.23) to be in one of the instantaneous eigenstates of the Hamiltonian,  $|n(\mathbf{R}(t))\rangle$ . Therefore, Eq. (5.23) becomes

$$|\Psi(T)\rangle = \exp\left(-\frac{i}{\hbar} \int_0^T dt E_n(\mathbf{R}(t))\right) \exp(i\gamma_n(T)) |n(\mathbf{R}(0))\rangle. \quad (5.29)$$

Two things are important in this equation. The first is that  $\gamma_n$  is not a function of the velocity  $\dot{\mathbf{R}}$ , but it rather depends on the endpoint  $T$  of the curve  $\mathcal{C}$ . This also marks the difference with the dynamical phase. The particular parametrization of the curve  $\mathcal{C}$  is no longer an important variable. The time  $T$  accounts only for the reaching of the final state in  $\mathbf{R}(T)$ . The second is that  $\gamma_n(T) \neq \gamma_n(0)$ . Thus, we can write

$$\frac{d}{dt} |n(\mathbf{R}(t))\rangle = \dot{\mathbf{R}} \cdot |\nabla_{\mathbf{R}} n(\mathbf{R})\rangle. \quad (5.30)$$

We then substitute Eq. (5.29) in the Schrödinger Equation (5.24). The geometric phase after a cycle  $\mathcal{C}$  takes the value:

$$\begin{aligned} \gamma_n(\mathcal{C}) &= i \oint_{\mathcal{C}} \langle n(\mathbf{R}) | \nabla_{\mathbf{R}} n(\mathbf{R}) \rangle \cdot d\mathbf{R} \\ &= -\text{Im} \oint_{\mathcal{C}} \langle n(\mathbf{R}) | \nabla_{\mathbf{R}} n(\mathbf{R}) \rangle \cdot d\mathbf{R}, \end{aligned} \quad (5.31)$$

where the last line comes from the normalization condition on  $|n(\mathbf{R})\rangle$ . In fact it is easy to see that  $\mathbf{A}_n = \langle n|\nabla_{\mathbf{R}}n\rangle$  is purely imaginary. We call  $\mathbf{A}_n$  the Berry connection of the  $n$ -th eigenstate. Moreover, if we constrain to a three dimensional parameter space  $\mathcal{P}$ , we see that we can exploit the Stokes theorem and write the integral in Eq. (5.31) as an integral over the surface  $\mathcal{F}$  enclosed by the curve  $\mathcal{C}$ :

$$\begin{aligned}\gamma_n(\mathcal{C}) &= \int_{\mathcal{F}} \nabla \times \mathbf{A}_n \cdot dS \\ &= \int_{\mathcal{F}} \mathbf{B}_n \cdot dS,\end{aligned}\tag{5.32}$$

and  $\mathbf{B}_n$  is called the Berry curvature of the  $n^{\text{th}}$  eigenstate. Note that the Berry curvature  $\mathbf{B}_n$  is gauge invariant. Each  $i^{\text{th}}$  component of the Berry connection can indeed be gauge transformed by a parameter dependent phase  $\alpha = \alpha(\mathbf{R})$  as

$$\tilde{A}_n^i = A_n^i - \partial_i \alpha.\tag{5.33}$$

For the curl of the gradient is identically zero we get the gauge invariance of  $\mathbf{B}_n$

$$\mathbf{B}_n = \nabla \times \mathbf{A}_n = \nabla \times \tilde{\mathbf{A}}_n\tag{5.34}$$

Eq. (5.32) also proves the gauge invariance of the geometric phase

In the following we derive a compact expression for  $\mathbf{B}_n$ . We exploit the identity

$$\begin{aligned}\nabla(H|n\rangle) &= (\nabla H)|n\rangle + H|\nabla n\rangle \\ &= E_n|\nabla n\rangle,\end{aligned}\tag{5.35}$$

and the definitions of  $\mathbf{A}_n, \mathbf{B}_n = \nabla \times \mathbf{A}_n$  to write:

$$\mathbf{B}_n = -\text{Im} \sum_{m \neq n} \frac{\langle n|\nabla H|m\rangle \times \langle m|\nabla H|n\rangle}{(E_n - E_m)^2}.\tag{5.36}$$

Equation (5.36) shows explicitly that  $\mathbf{B}_n$  is single valued and does not depend on the particular choice of phase for  $|n(\mathbf{R})\rangle$ , as opposed to  $\mathbf{A}_n$ . This ensures  $\gamma_n(\mathcal{C})$  to be single valued as well.

It is worth to notice also the surprising similarity between these quantities and the electromagnetic vector potential  $\vec{A}$  (that have gauge-dependent values) and the magnetic field  $\vec{B} = \nabla \times \vec{A}$  with gauge independent value. Actually we can say the vector potential is the Berry connection of electromagnetism. In the following section we will go deeper and give a relation between any gauge theory and the corresponding Berry connection. This will be done borrowing concepts from quantum field theory and differential geometry.

The gauge dependence of the vector potential has often given to the physicists the idea that only the fields are physical, whereas the potentials are just abstract mathematical concepts. The geometric phase, i.e. the integral of the gauge field along the curve, acquired by the system after a closed loop has instead an observable physical effect and it is the basis to understand the Aharonov-Bohm effect [150].

The notion of geometric phase had found many applications in physics both in classical and quantum mechanics, since the only requirements is the existence of an Hermitian Hamiltonian describing the dynamics. Also these concepts find applications in quantum mechanics for any statistics, with both bosonic and fermionic particles.

### 5.5.1 | A geometric approach to the Berry phase

In order to give a geometric description of the Berry phase we would need a bunch of concepts taken from differential geometry. Such concepts regard differentiable manifolds, one and two forms, and many other concepts related to tensor calculus. Even though the subject is very interesting and finds several application in physics, going through it would be beyond the purpose of this thesis and we refer to [151] for nice explanations. Here we just give a brief introduction and promptly go into the subject. Our framework is a differentiable manifold  $\mathcal{M}$ . This object can be described by a chart

$$\phi : \mathcal{U} \subset \mathcal{M} \rightarrow \mathcal{V} \subset \mathbb{R}^n, \quad (5.37)$$

which enables us to represent a subset  $\mathcal{U} \subseteq \mathcal{M}$  in an Euclidean space  $\mathcal{V} \subset \mathbb{R}^n$ . Hence, every point  $x$  of the manifold is actually represented by a set of coordinates given by the image of the chart  $\phi(x) \in \mathbb{R}^n$ . Thus, a point  $x \in \mathcal{M}$  can be written as

$$\phi(x) = (x_1, \dots, x_n). \quad (5.38)$$

On each point  $x$ , we can define the tangent space  $\mathcal{T}_x\mathcal{M}$ . We define a vector  $v \in \mathcal{T}_x\mathcal{M}$  as a functional that obeys the Leibniz rule. The differential geometry community is used to denote  $v = v^i e_i$  where the  $v^i$  are the coordinates of the vector and  $e_i$  are the basis vectors. The latter is often written  $\partial_i$  for we can prove the basis acts as a derivative. Here we make use of the Einstein notation where repeated indexes are summed together.

Furthermore we can define the dual space  $\mathcal{T}_x^*\mathcal{M}$  of the tangent space  $\mathcal{T}_x\mathcal{M}$ . An element  $w$  of the dual space can be written as  $w_i e^i$ , where  $w_i$  are the coordinates and  $e^i$  is the basis element. This is also denoted as  $dx^i$  and has a strong analogy with the differential used in the integral calculus. In fact an element of the dual space  $\mathcal{T}_x^*\mathcal{M}$  is called a differential form, or a 1-form.

The basis  $\{\partial_i\}$  and its dual  $\{dx^i\}$  satisfy the scalar product relation

$$\langle dx^i, \partial_j \rangle = \delta_j^i \text{ and } \langle w, v \rangle = w_i v^i. \quad (5.39)$$

An element of the form  $z = z_{ij} dx^i dx^j$  is called a 2-form. It consists in the tensor product of two 1-forms. We can define a  $p$ -form as

$$H = \frac{1}{p!} H_{i_1 \dots i_p} dx^{i_1} dx^{i_2} \dots dx^{i_p}. \quad (5.40)$$

The differentials are antisymmetric, i.e.  $dx^i dx^j = -dx^j dx^i$ . For analogy, let us notice that in integral calculus  $dx dy$  represents a patch of a surface. We can imagine that the order of  $dx^i$  and  $dx^j$  gives the direction of the little area.

Moreover, we define the differential operator  $d$  as the operator that takes a  $p$ -form and return a  $p + 1$ -form

$$dH = \frac{1}{p!} \partial_j H_{i_1 \dots i_p} dx^j dx^{i_1} dx^{i_2} \dots dx^{i_p}. \quad (5.41)$$

Thus, the 1-form  $w$  becomes

$$dw = \partial_i w_j dx^i dx^j = \frac{1}{2} (\partial_i w_j - \partial_j w_i) dx^i dx^j. \quad (5.42)$$

This notation has the advantage of being compact and reliable. On the other hand, quantum physicists are more familiar with the Dirac's notation where a vector  $v$  is expressed as a ket  $|v\rangle$  and the element of the dual space,  $w$ , is expressed as a bra  $\langle w|$ . The bracket product is how we write the scalar product (5.39). The Dirac notation can sometimes be very helpful for the calculations. In this thesis we will use the mathematics notation when we need to make some general argument and the quantum physics notation when we apply it to a physical system. However, the reader should now know they refer to the same concept.

In order to explain how the geometric phase arises in differential geometry we introduce the concept of parallel transport. We want to define a way to coherently transform a vector  $v_x \in \mathcal{T}_x \mathcal{M}$  to a vector  $v_{x'} \in \mathcal{T}_{x'} \mathcal{M}$ . Here, coherently means that the vector keeps the angles with the other vectors fixed. To give an example, if we have a vector  $u_x \perp v_x$ , i.e. the scalar product  $u_x \cdot v_x = 0$ , the new transported vectors  $u_{x'}$  should be perpendicular to  $v_{x'}$ . Therefore we want to have  $u_{x'} \cdot v_{x'} = 0$ . However,  $v_x$  and  $v_{x'}$  belong to different spaces. Hence, let us consider a curve  $\mathcal{C} : [0, 1] \rightarrow \mathbb{R}^n$  such that  $\mathcal{C}(0) = x$  and  $\mathcal{C}(1) = x'$ . In this way we have a mathematical object that connects the two points. In order to define the parallel transport we need to describe the derivative of

a vector along the direction of the curve. This is done through the covariant derivative  $\nabla$  which transforms the coordinates  $v^i$  of the vector  $v$  in the direction  $k$  of the curve as

$$\nabla_k v^i = \partial_k v^i + \Gamma_{kj}^i v^j. \quad (5.43)$$

The components of  $\Gamma$  are called the Christoffel symbols. When the map uses Cartesian coordinates, they vanish if the manifold is flat, thus the covariant derivative becomes the standard one. These symbols represents the right way to parallel transport a vector and relate two different vector spaces. Therefore they are sometimes referred as *connection*. It is not so surprising that the vector  $\mathbf{A}_n$  in Eq. (5.32) is called Berry connection. It represents how the instantaneous eigenstate  $|n(t)\rangle$  changes along the path.

Let us consider the simple example of a vector transported on a closed loop upon the  $S^2$  manifold, i.e. the 3D sphere. We define the sphere in  $\mathbb{R}^3$  with the spherical coordinates and we keep the radius fixed,  $r = 1$ . Hence, we define the smooth closed curve  $\mathcal{C} : [0, 1] \rightarrow S^2$  with  $\mathcal{C}(0) = \mathcal{C}(1)$ , that has with fixed polar angle  $\theta = \theta_0$  and free azimuthal angle  $\phi \in [0, 2\pi)$ ,

$$\mathcal{C} : t \rightarrow \begin{pmatrix} \sin \theta_0 \cos(2\pi t) \\ \sin \theta_0 \sin(2\pi t) \\ \cos(\theta_0) \end{pmatrix}, \quad (5.44)$$

so we are moving on the parallels of the sphere. The tangent vector is

$$u = \frac{1}{\sin \theta_0} (0, 1), \quad (5.45)$$

where  $\sin \theta_0$  is a normalization factor given by the natural metric on  $S^2$ . The parallel transport of a vector  $v = (v^\phi, v^\theta)$  is given by the solution of the equation

$$(u \cdot \nabla)v = 0, \quad (5.46)$$

that in this case, using the definition (5.45) and Eq. (5.43), corresponds to

$$0 = \partial_\phi v^j + v^k \Gamma_{k\phi}^j \quad (5.47a)$$

$$0 = \partial_\phi v^j + v^\theta \Gamma_{\theta\phi}^j + v^\phi \Gamma_{\phi\phi}^j, \quad (5.47b)$$

with  $j = \theta, \phi$ . We can perform all the calculations and find a surprise at the end. When we want to establish the angle between the vectors  $u$  and  $v$  we can calculate the inner product and yield

$$u \cdot v = v^\phi \sin \theta_0 \cos(\phi \cos \theta_0) - v^\theta \sin(\phi \cos \theta_0). \quad (5.48)$$

This equation shows that if we are not in the equator ( $\theta_0 = \pi/2$ ), then the vector  $v$  while travels around the path acquires a phase. Often this phase is not even a multiple of  $2\pi$ , and the transported vector gets a different direction. This extra phase is a geometric phase, because it does not depend on the velocity the vector has traveled, but only on the particular path followed as well as on the geometry of the manifold.

We now consider the quantum analogue of a vector transported on the sphere. The vector we transport here is the state  $|\psi\rangle$  of the system and we transport it along the curve  $\mathcal{C}$  with values in the parameter space. In order to represent the two-sphere  $S^2$  we consider the  $2 \times 2$  Hamiltonian defined by the vector of parameters  $\vec{x} = (x, y, z)$ :

$$H = \begin{pmatrix} z & x + iy \\ x - iy & -z \end{pmatrix}, \quad (5.49)$$

with the constrain that  $|\vec{x}| = 1$ . The two eigenstates  $|\pm_{\vec{x}}\rangle$  of the Hamiltonian also depend upon the parameters  $\vec{x}$ . We can start at  $t = 0$  from the system in the eigenstate  $|\psi(0)\rangle = |-\vec{x}\rangle$  and consider a time dependent Hamiltonian so that the system  $|\psi(t)\rangle$  performs a closed loop  $\mathcal{C}$  on this surface. We can use Eq. (5.36) to evaluate the Berry curvature  $\mathbf{B}_-$  and integrate it along the closed circle  $\mathcal{C}$  to infer the Berry phase. We get

$$\begin{aligned} \mathbf{B}_{\pm}(\vec{x}) &= -\text{Im} \left[ \frac{\langle \pm | \nabla_{\vec{x}} H | \mp \rangle \times \langle \mp | \nabla_{\vec{x}} H | \pm \rangle}{(E_+ - E_-)^2} \right] \\ &= -\text{Im} \left[ \frac{\langle \pm | \vec{\sigma} | \mp \rangle \times \langle \mp | \vec{\sigma} | \pm \rangle}{4} \right], \end{aligned} \quad (5.50)$$

where  $\vec{\sigma}$  is the standard vector of Pauli matrices and we substituted the eigenvalues  $E_{\pm} = \pm 1$  of  $H$ . Finally, the integration in Eq. (5.32) yields

$$\gamma_-(\mathcal{C}) = \frac{1}{2} \Omega_{\mathcal{C}}, \quad (5.51)$$

where  $\Omega_{\mathcal{C}}$  is the solid angle subtended by the curve  $\mathcal{C}$ . The new vector  $|\psi(t)\rangle$  has acquired a phase accordingly with the integral of the Berry curvature over the surface. On the other hand, if we started from the initial state  $|+\vec{x}\rangle$  the phase acquired by the state would be  $-\gamma(\mathcal{C})$ .

### 5.5.1.1 | The topological invariant

The geometrical concepts expressed above can be explained looking at the topology of the system. In order to fully express the mathematical idea we need an other few concepts from differential geometry. In general, the property that fully accounts for all the features of a differential form  $\omega$  is the possibility of integrate the form over a



geometric object  $\Gamma$  of the same dimension. Thus, a 1-form is integrable over a curve, a 2-form is integrable over a surface.

A differential form  $\omega$  is said to be closed if  $d\omega = 0$ . It is exact if it can be expressed as the differential of another form, i.e.  $\omega = dv$ , where the form  $v$  is called primitive of  $\omega$ . Thus, any exact form is also closed, since

$$ddv = 0. \quad (5.52)$$

One could argue that this is true also in the other way round, that is if we have a closed form, then this is also exact. It turns out that this depends on the topology of the space. If the manifold is a simply connected space, then this is true and any closed form is also exact. If the space is not simply connected than we can locally define a form  $v$  whose differential is  $\omega$ , but this property cannot be extended globally. The importance of this property shows up when we integrate the differential form  $\omega$ . For the Stokes theorem we have

$$\int_{\mathcal{M}} d\omega = \int_{\partial\mathcal{M}} \omega, \quad (5.53)$$

where  $\mathcal{M}$  is the manifold and  $\partial\mathcal{M}$  its border. This implies that if  $\omega$  is closed, than the integral is zero.

The connection between those concepts and the physics of topological insulators lies in the definition of the geometric phase  $\gamma$  as a surface integral of the Berry curvature. Equation (5.32) is in fact the Stokes theorem in 3 dimensions. The Berry curvature  $\mathbf{B}$  can be seen as the differential  $d\mathbf{A}$  of the Berry connection  $\mathbf{A}$ . If the space is not simply connected, one cannot find the global primitive of  $\mathbf{B}$  and the Berry phase results, in general, not equal to zero.

In order to provide a connection with quantum mechanics, we consider a particle moving on a non simply connected 2D system. Let's take the Hamiltonian (5.49). This is the same system as the previous one, but with length  $|\vec{x}|$  unfixed. Here the space of the parameters is a torus, defined in  $\mathbb{R}^3/0$ . The eigenvalues of this system are  $E_{\pm} = \pm|\vec{x}|$  and the eigenstates are not defined for  $\vec{x} = 0$ .

The Berry curvature gives

$$B^{\pm}(\vec{x}) = \pm \frac{\vec{x}}{2|\vec{x}|^3} \quad (5.54)$$

We now suppose to be in the momentum space and the strength  $\vec{x}$  of the coupling to be a function of the momenta, i.e.  $\vec{x} = \vec{x}(k_x, k_y)$ . The Brillouin zone (BZ) of the system

is a deformed torus. We define the Chern number  $Q$  as the flux of the Berry curvature through this torus:

$$Q = \frac{1}{2\pi} \int_{BZ} dx dy B(k_x, k_y). \quad (5.55)$$

A comparison with Eq. (5.51) shows that  $Q$  is an integer with modulus either 0 or 1 if the origin is outside or inside the torus. If the origin lies inside the torus  $Q$  can be either +1 or -1 depending on the orientation of the surface. It's worth to notice that Chern number is a topological invariant. It's value is ultimately given by the properties of the torus as a manifold. Moreover, any transformation that acts without changing the topology of the Brillouin zone is a adiabatic transformation a leaves the Chern number of the system invariant.

### 5.5.2 | Relation with the Abelian Gauge theory of Electromagnetism

The differential forms we encountered previously are very useful in electromagnetism and in quantum electrodynamics. They give an elegant description of the electromagnetic fields and of the vector and scalar potential. Indeed we know the magnetic field  $\mathbf{B}$  can be written as the curl of the vector potential  $\mathbf{A}$ , that is exactly Eq. (5.42) in 3 dimensions. In general we can describe all the classical electromagnetism with the use of a 4-dimensional tensor,  $F_{\mu\nu}$  defined as

$$F_{\mu\nu} = \begin{pmatrix} 0 & E_x/c & E_y/c & E_z/c \\ -E_x/c & 0 & -B_z & B_y \\ -E_y/c & B_z & 0 & -B_x \\ -E_z/c & -B_y & B_x & 0 \end{pmatrix}, \quad (5.56)$$

with  $c$  being the speed of light. The tensor above is a 2-form that can be obtained by applying the differential operator  $d$  on the 1-form  $\mathbf{A} = A_\mu dx^\mu$ , with  $\mathbf{A}$  being the 4-dimensional vector potential

$$\mathbf{A}_\mu = (\phi/c, A_x, A_y, A_z). \quad (5.57)$$

Thus, using Eq. (5.52), the homogeneous Maxwell equations can be written in the compact form  $dF = 0$ . The electromagnetic tensor is in fact a closed form, even though it is not globally exact. Therefore we can find the vector potential whose curl gives the magnetic field, but we can define it only locally. This as much to do with the gauge invariance of the theory. As we already highlighted in the previous sections the electro-

magnetic potential can be defined up to the gauge transformation

$$\mathbf{A} \rightarrow \mathbf{A} + \frac{1}{e} \nabla f, \quad (5.58)$$

with  $f$  being a scalar function of the coordinates and  $e$  the electronic charge. The electron field is transformed as  $\psi(x) \rightarrow e^{if(x)}$ . The gauge transformation shall leave the dynamics unchanged. Hence, we introduce the Lagrangian of quantum electrodynamics

$$\mathcal{L} = \bar{\psi}(i\gamma^\mu D_\mu - m)\psi - \frac{1}{4}F_{\mu\nu}F^{\mu\nu}, \quad (5.59)$$

which describes the dynamics of an electron interacting with the electromagnetic field. We will not enter in the details of quantum field theory, and we refer to Ref. [152] for the interested reader. For our purposes, we need just to know  $D_\mu$  is the covariant derivative. Given the transformation laws of  $\mathbf{A}$  and  $\psi$ , in order to keep the Lagrangian unchanged after a gauge transformation,  $D_\mu = \partial_\mu - ieA_\mu$ . Thus, it is straightforward to see in  $ie\mathbf{A}$  the connection of the space, as we did in Eq. (5.43).

The vector potential  $\mathbf{A}$  has a physical effect on the dynamics that was unknown in early quantum mechanics. However it enters in the minimal coupling Hamiltonian and we see it's responsible for the geometric phase (5.31). The experiment that showed it in 1959 is due to Aharanov and Bohm. Let's consider an infinite current carrying solenoid. We know the magnetic field of such a system is constrained to stay in the inside of the solenoid and no magnetic field is shown outside of it. Thus, we can define the vector potential  $\mathbf{A}$  in the region with zero magnetic field. Now let's take a traveling charged particle. The particle will take the phase  $\int_{\Gamma_1} \mathbf{A} \cdot dx$ , where  $\Gamma_1$  is the path along which the particle moves. However, if the particle travels through the path  $\Gamma_2$ , the phase acquired will be  $\int_{\Gamma_2} \mathbf{A} \cdot dx$ . The actual phase we will see is an interference pattern given by the all possible paths. The phase difference given by the paths  $\Gamma_1$  and  $\Gamma_2$  will be

$$\left( \int_{\Gamma_1} \mathbf{A} \cdot dx \right) - \left( \int_{\Gamma_2} \mathbf{A} \cdot dx \right) = \left( \int_{\Gamma_1 - \Gamma_2} \mathbf{A} \cdot dx \right), \quad (5.60)$$

which is ultimately the flux of the magnetic field  $\mathbf{B}$  on the surface with borders  $\Gamma_1 - \Gamma_2$ . Because of the particular choice of the system  $\mathbf{A}$  is defined in a non simply connected space, therefore it wasn't a exact form.

## 5.6 | 2D Chern insulators

A Chern insulator is a two-dimensional band insulator with non-vanishing Chern number. They are often associated with the quantum Hall effect. The relation lies in the fact

that Chern insulators are characterized by conductive edge states, which are not detected by the dispersion relation of the bulk Hamiltonian. However they emerge when we consider a finite size sample. Furthermore, as in the quantum Hall effect, the edge states are characterized by chirality.

Chern insulators made their appearance in the literature with a toy model introduced by Qi, Wu and Zhang (QWZ) [153]. In this model the bulk Hamiltonian in the momentum space  $H(k_x, k_y)$  is

$$H = \mathbf{d} \cdot \boldsymbol{\sigma}, \quad \mathbf{d} = \begin{pmatrix} \sin k_x \\ \sin k_y \\ u + \cos k_x + \cos k_y \end{pmatrix}. \quad (5.61)$$

We can see the similarity of the QWZ Hamiltonian with Eq. (5.49). As in the previous section, the components of  $\mathbf{d}$  are defined in  $\mathbb{R}^3/0$  and the parameters  $k_x, k_y$  describe the surface of a torus.

The spectrum of the  $2 \times 2$  Hamiltonian is composed by two bands with eigenvalues

$$E_{\pm}(k_x, k_y) = \pm |\mathbf{d}(k_x, k_y)| = \pm \sqrt{\sin^2 k_x + \sin^2 k_y + (u + \cos k_x + \cos k_y)^2} \quad (5.62)$$

For most of the values of  $u$  the spectrum shows a band gap and the Hamiltonian describes an insulator. The band gap is closed for those values of  $k$  s.t.  $\mathbf{d}(k) = 0$ . In the QWZ model, this condition is satisfied for  $u = -2, 0, 2$  at different points of the Brillouin zone depicted in Figure 5.3 and named in literature  $\Gamma = (0, 0)$ ,  $X = (0, \pm\pi)$  and  $M = (\pm\pi, \pm\pi)$ . Those points are also called Dirac points, since in the proximity of them the dispersion relations has a similar form as the Dirac equation of quantum field theory. We get this condition near the Fermi energy when the valence and conductive state touch and the band assumes the characteristic structure of two cones pointing towards. When we change the value of  $u$  the two vertices get near until the gap is closed and eventually the energy spectrum describes a conductor. In this case the Chern number is not defined. In order to show this behavior, we expand the Hamiltonian around the  $\Gamma$  point in the case  $u = -2$ . The Hamiltonian Eq. (5.61) becomes:

$$H(k_{0x} + q_x, k_{0y} + q_y) \sim q_x \sigma_x + q_y \sigma_y, \quad (5.63)$$

with eigenvalues  $E_{\pm}(q_x, q_y) = \pm q$ , and  $|q| = \sqrt{q_x^2 + q_y^2}$ . The linearity of the dispersion relation is typical of the Dirac mass-less equation. We can now analyze the nearly metallic case setting  $u \approx -2$  and look at the differences with the previous case. We expand the Hamiltonian and get

$$H(k_{0x} + q_x, k_{0y} + q_y) \sim (2 + u) \sigma_z + q_x \sigma_x + q_y \sigma_y. \quad (5.64)$$

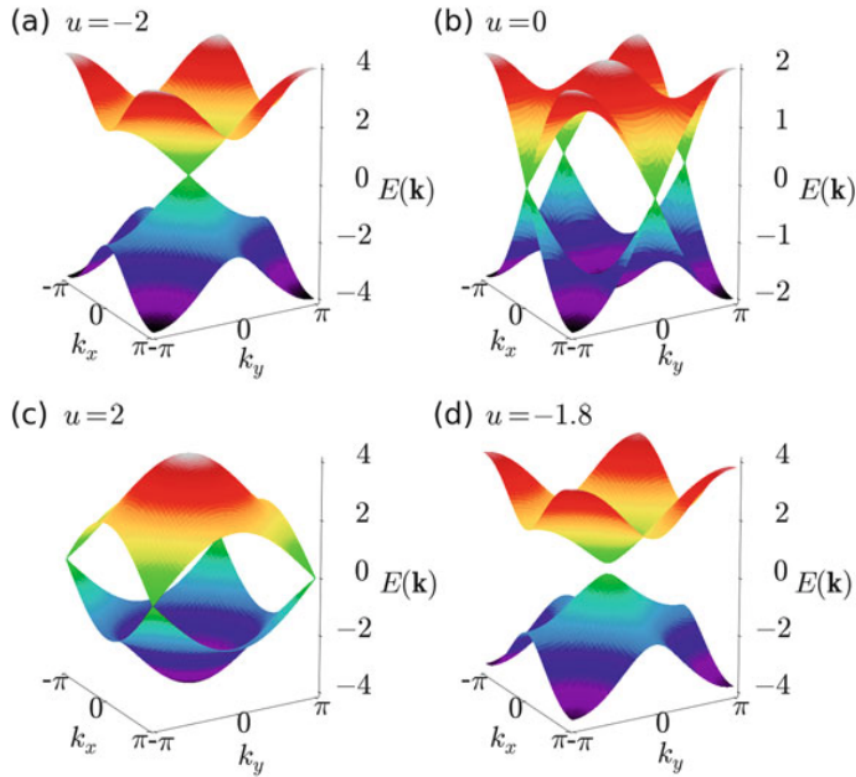


Figure 5.3: The bulk dispersion relation of the QWZ model, for various values of  $u$ , as indicated in the plots. In (a)–(c), the gapless cases are shown, where the bulk gap closes at so-called Dirac points. In (d), with a generic value  $u = -1.8$ , the system is insulating. Figure from [153]

The dispersion relations are  $E_{\pm} = \pm\sqrt{(2+u)^2 + q^2}$ . From the Hamiltonian in Eq. (5.64) we see that the term  $u \neq -2$  breaks the time reversal-symmetry that is a necessary, even though not sufficient, condition to have a Berry curvature different from zero. Here, it is crucial to relate the eigenvalues of the system with the topology of the Hamiltonian. When we vary the parameters  $k_x, k_y$  we create a surface in the space defined by the coordinates of  $\mathbf{d}$ . If this surface encloses the point  $\mathbf{0}$ , which is the point where the system is not defined, the flux of the Berry curvature will be in general, different from zero. A straight calculation of the Chern number  $Q$  leads to  $Q = 0$  if  $u < -2$  and  $Q = 1$  if  $u > -2$ . If we are able to control the value of  $u$  and change it from  $u < -2$  to  $u > -2$  we will pass through a topological phase transition, for when  $u = -2$  the surface defined by  $k_x, k_y$  intercepts the point  $\mathbf{d} = \mathbf{0}$ .

### 5.6.1 | The Harper-Hofstadter model

In this section we describe how Chern insulators arise in lattice models where the time-reversal symmetry is broken. In the QWZ model the crystal structure of the material was not important for obtaining the typical behavior of topological insulator. The same was for the quantum Hall effect, where the material was treated as a continuum. Usually the reason behind it is that the waist of the magnetic field used to break the time reversal symmetry of the system is much bigger than the lattice spacing. When this is not the case the lattice properties are essential.

A basic model for the description of a crystal is the tight binding model. In general tight-binding Hamiltonian can be written as the sum of hopping terms among lattice sites,

$$H_{\text{TB}} = \sum_{i,j} t_{ij} c_i^\dagger c_j. \quad (5.65)$$

Here  $c_i^\dagger$  and  $c_i$  are the creation and annihilation operators defined on the  $i^{\text{th}}$  site of the lattice. The matrix  $t$  with components  $t_{ij}$  contains both the on-site energy and the hopping constant between the sites.

In the Harper-Hofstadter (HH) model [154] we consider a charged particle hopping on a square lattice of lattice spacing one with periodic boundary conditions subject to an external magnetic field with fixed flux on the plaquette  $\phi$ . The Hofstadter Hamiltonian reads

$$H = -J \sum_{\langle i,j \rangle} \exp \left[ \int_{r_i}^{r_j} \mathbf{A} \cdot d\mathbf{l} \right] c_i^\dagger c_j + h.c., \quad (5.66)$$

where  $r_i$  is the coordinate of the  $i$ -th site,  $J$  is a real number and the sum is performed over the nearest neighbors of the square lattice.  $\mathbf{A}$  is the vector potential that generates a uniform magnetic field  $\mathbf{B}$  orthogonal to the lattice plane. The resulting flux of the magnetic field over a plaquette of the lattice is  $\phi = \frac{|\mathbf{B}|}{2\pi}$ . A suitable choice for the vector potential is the modified Landau gauge

$$\mathbf{A} = \begin{pmatrix} By \\ 0 \\ 0 \end{pmatrix}. \quad (5.67)$$

which leads the Hamiltonian in the position space to be

$$H = -J \sum_{x,y} \left( c_{x+1,y}^\dagger c_{x,y} e^{2\pi i \phi y} + c_{x,y+1}^\dagger c_{x,y} + h.c. \right), \quad (5.68)$$

Now we suppose the phase is a rational number  $\phi = p/q$ , with  $p, q \in \mathbb{N}$  coprime. With this condition we can see the system has translational invariance over the two directions of the plane. In particular, the phase acquired from the particle on the  $s$ -th line of the square lattice is the same acquired on the  $(s + yq)$ -th line, where  $s$  goes from 0 to  $q - 1$ . On the other hand, each column is invariant with respect to the next one.

In this way the system is composed by a unit cell with  $q$  sublattices. For simplicity we set the lattice spacing equal to 1. The wave function  $\Psi(s, \mu)$  is written in term of the unit cell  $\mu$  and of the sublattice  $s$ . For the Bloch theorem

$$\Psi(s, \mu + \hat{e}_x) = e^{ik_x} \Psi(s, \mu), \quad (5.69)$$

where  $\hat{e}_x$  is the unit vector on the  $x$ -axis and  $\mu + \hat{e}_x$  finds the next unit cell in the  $x$  direction. The periodicity on the  $y$ -axis is instead every  $q$  sites and it leads to

$$\Psi(s, \mu + \hat{e}_y) = e^{ik_y q} \Psi(s, \mu), \quad (5.70)$$

being  $\hat{e}_y$  the vector that accounts for translation on the  $y$ -axis of one unit cell.

Thanks to the Bloch theorem we can Fourier transform the Hamiltonian in Eq. (5.68) and write it in terms of the pseudomomenta  $(k_x, k_y)$  with values included in the set  $[-\pi, \pi] \times [-\frac{\pi}{q}, \frac{\pi}{q}]$ , which define the magnetic Brillouin zone (MBZ). To achieve this result we first transform the creation and annihilation operators as

$$c_{k_x, k_y, s} = \frac{1}{\sqrt{N}} \sum_{\mu} e^{-ik_x n_x} e^{-ik_y q n_y} c_{n_x, n_y, s}, \quad (5.71a)$$

$$c_{k_x, k_y, s}^{\dagger} = \frac{1}{\sqrt{N}} \sum_{\mu} e^{ik_x n_x} e^{ik_y q n_y} c_{n_x, n_y, s}^{\dagger}, \quad (5.71b)$$

where  $n_{x,(y)} = 1, 2, \dots, N_{x,(y)}$  and  $N_{x,(y)}$  is the number of sites in the  $x, (y)$  direction.  $N$  is the total number of unit cells,  $N = N_x N_y$ . It is worth to notice that the dependence on the site  $s$  remains. That is because the Bloch theorem on the  $y$  direction is applied on the unit cell composed on  $q$  elements and not on the single site. Finally the Hamiltonian reads

$$\begin{aligned} \frac{H}{J} &= \frac{1}{N} \sum_{n_x, n_y} \sum_{k_x, y, k'_x, y} (\exp[i(n_x + 1)k_x + in_y k_y q - i(n_x k'_x + n_y k'_y q + 2\pi s \phi)] c_{k_x, k_y, s}^{\dagger} c_{k_x, k_y, s} \\ &\quad + \exp[in_x k_x + i(n_y + 1)k_y q - in_x k'_x - in_y k'_y q] c_{k_x, k_y, s+1}^{\dagger} c_{k_x, k_y, s} + h.c.) \\ &= \sum_{\vec{k}} (e^{i(k_x + 2\pi s \phi)} a_{k_x, k_y, s}^{\dagger} c_{k_x, k_y, s} + e^{ik_y q} c_{k_x, k_y, s+1}^{\dagger} c_{k_x, k_y, s} + h.c.), \end{aligned} \quad (5.72)$$

that if expressed as a function of the momenta  $k_x, k_y$  becomes

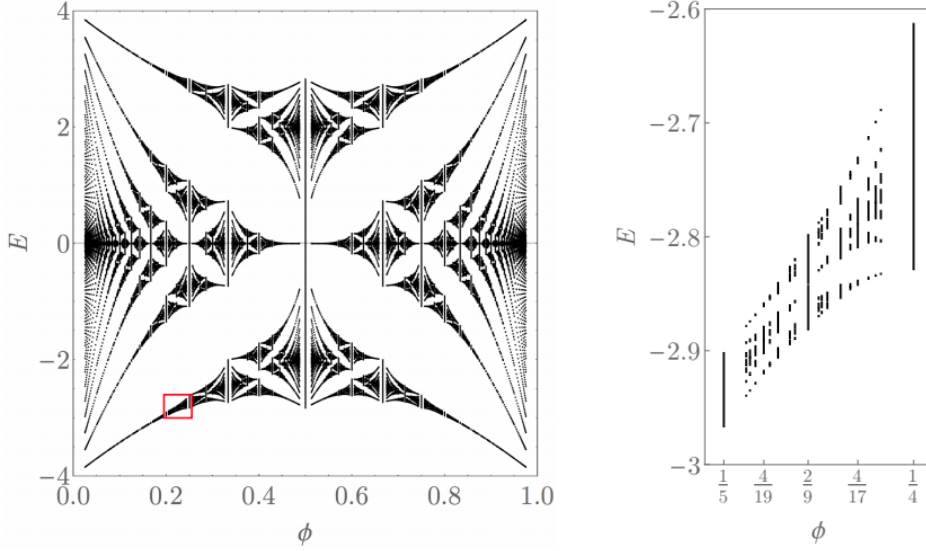


Figure 5.4: Hofstadter's Butterfly shows the fractal spectrum of the Hofstadter model (with energy  $E$ ) as a function of magnetic flux per plaquette,  $\phi$ . The entire pattern repeats for flux filling outside of the range 0 to 1. Landau level-like lines can be observed near to the points  $(0, 4)$  and  $(1/2, 2p2)$ , for example. On the right there is a zoom of the red block

$$\begin{aligned} \frac{H(k_x, k_y)}{J} &= e^{ik_y q} c_{k_x, k_y, s+1}^\dagger c_{k_x, k_y, s} + e^{-ik_y q} c_{k_x, k_y, s}^\dagger c_{k_x, k_y, s+1} \\ &\quad + 2 \cos(k_x + 2\pi\phi s) c_{k_x, k_y, s}^\dagger c_{k_x, k_y, s}. \end{aligned} \quad (5.73)$$

The eigenvalue equation  $H_s(k)\Psi_s(k) = E_s(k)\Psi_s(k)$ , where  $\Psi_s(k)$  is the eigenfunction in the momentum base, leads us to the Harper equation:

$$2 \cos(k_x + 2\pi\phi s)\Psi_s(k) + e^{ik_y q}\Psi_{s+1}(k) + e^{-ik_y q}\Psi_{s-1}(k) = \frac{E_s(k)}{J}\Psi_s(k). \quad (5.74)$$

From the Harper equation we can find the  $q$  eigenvalues that according to the value of  $\phi$  go to constitute the famous Hofstadter butterfly plotted in figure 5.4

### 5.6.2 | Application to optics

The quantum Hall effect and the Chern insulators were originally discovered in the context of charged particles such as electrons in a solid. The very notion of Chern insulator requires an external field able to break the time reversal symmetry and the magnetic field acts as requested on charged particles. Even the Berry connection and curvature



resemble mathematically the vector potential and the magnetic field. Nevertheless in the last decades many systems reproduced the role of a magnetic field on uncharged particles. In [155] the TRS is broken using the helical structure of nanotubes disposed on a hexagonal lattice. Other theoretical implementation consisted on harmonic modulation of a photonic crystal [156] or optomechanical induced non-reciprocity [157]. The effect of breaking the TRS can be given also by the use of a so-called synthetic magnetic field (SMF). In [158] the SMF is given modifying the length of the link resonator connecting two resonator disposed in a square lattice. Using a similar approach in the next section we will show evidences of a Chern insulator obtained in an optomechanical array.

## 5.7 | Nonreciprocal topological phononics in optomechanical arrays

This section is taken from our paper [6] and contains one of the main results obtained in these years of doctorate studies. In fact the topic of topological insulators has been only very recently applied in optomechanics [159][160]. In this work we successfully applied the physics described in the previous sections to obtain topological transport in optomechanical arrays. In this system, nearest neighbor coupling among the optomechanical resonator is only optical. In literature we can find works where the optical coupling among resonators can be manipulated to produce synthetic magnetic field[158]. Therefore, it's no surprise we obtained optical edge states, whose transport shows topological robustness against disorder. Nevertheless, the optomechanical coupling acting on each resonator, induces in the system mechanical edge states. Thus, we see phononic topological transport. We first introduce the model and then show the results.

### 5.7.1 | The model

Our basic building block will be an optomechanical microtoroid resonator [161]. These resonators are well-known to support simultaneous high-quality optical and mechanical modes together with an optomechanical interaction between the two. Our model consists of an array of such resonators, each of which is described by the Hamiltonian

$$\hat{H}_i = \omega_i \hat{a}_i^\dagger \hat{a}_i + \Omega_i \hat{b}_i^\dagger \hat{b}_i + g_i \hat{a}_i^\dagger \hat{a}_i (\hat{b}_i^\dagger + \hat{b}_i) + \mathcal{E}_i (\hat{a}_i e^{i\omega_L t} + \hat{a}_i^\dagger e^{-i\omega_L t}), \quad (5.75)$$

where  $\omega_i$  is the resonance frequency of the optical mode,  $\Omega_i$  that of the mechanical mode,  $\hat{a}_i$  and  $\hat{b}_i$  the annihilation operators corresponding to the two modes,  $g_i$  the op-

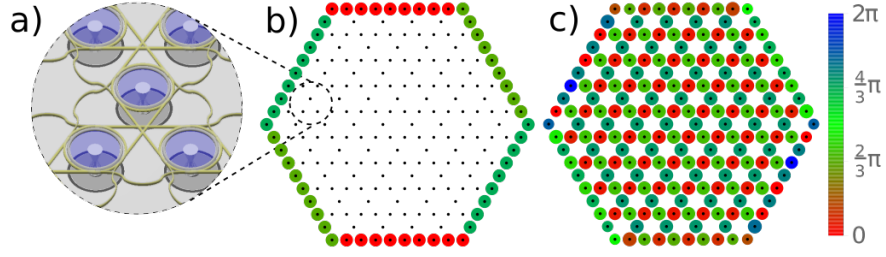


Figure 5.5: An optomechanical Kagome lattice. The unit cell of the lattice is composed of (a) two optomechanical resonators linked by an off-centre waveguide. This allows to (b) build a Kagome lattice of optomechanical resonators linked by non-intersecting waveguides. (c) We consider a finite hexagonal array of resonators driven optically at the edges. The driving fields have the same amplitude but different phases, as illustrated. This gives rise to (d) a stationary field where the optical fields in adjacent sublattices have a phase difference of  $2\pi/3$ .

omechanical coupling constant, and  $\mathcal{E}_i$  the strength of the optical driving field which is assumed to be monochromatic at a frequency  $\omega_L$ . Throughout this section we will be working in units such that  $\hbar = 1$  for convenience. The dynamics of resonator  $i$  also includes a dissipative component, which we model through the Liouvillian

$$\mathcal{L}_i[\bullet] = \frac{\kappa_i}{2}\mathcal{D}[\hat{a}_i, \bullet] + \frac{\gamma_i}{2}\mathcal{D}[\hat{b}_i, \bullet], \quad (5.76)$$

where  $\mathcal{D}[\hat{o}, \bullet] = \hat{o} \bullet \hat{o}^\dagger - \frac{1}{2}(\hat{o}^\dagger \hat{o} \bullet + \bullet \hat{o}^\dagger \hat{o})$ . Here,  $\kappa_i$  and  $\gamma_i$  are the dissipation rates of the optical and mechanical fields, and we have assumed a zero-temperature bath for both modes. The density matrix  $\rho_i$  for resonator  $i$  is thus governed by the master equation

$$\frac{d}{dt}\rho_i = -\iota[\hat{H}_i, \rho_i] + \mathcal{L}_i[\rho_i]. \quad (5.77)$$

A future direction of research will explore the effects of mechanical baths at non-zero temperatures. Let us remark, however, that with GHz-scale mechanical oscillation frequencies and present-day cryogenic techniques it is possible [81] to operate in a regime where the mechanical bath temperature is effectively zero.

Pairs of adjacent resonators are connected together by means of waveguides. Defining  $J_{ij}$  to be the complex coupling constant between resonators  $i$  and  $j$ , we thus have the Hamiltonian for the full system,

$$\hat{H} = \sum_i \hat{H}_i + \sum_{\langle i,j \rangle} (J_{ij} \hat{a}_i^\dagger \hat{a}_j + J_{ij}^* \hat{a}_i \hat{a}_j^\dagger), \quad (5.78)$$

where the second sum runs over all the pairs of resonators that are connected in this manner. We remark that the phase of  $J_{ij}$  originates from an asymmetric positioning

of the waveguide connecting pairs of resonators, as demonstrated in Ref. [158]. The dissipative part of the master equation is given by the Liouvillian  $\mathcal{L}[\bullet] = \sum_i \mathcal{L}_i[\bullet]$ . This model allows us to describe the system shown in Fig. 5.5(a)–(c).

The Hamiltonian Eq. (5.78) gives rise to non-linear equations of motion. To solve the equations governing the temporal evolution of the system we linearise the dynamics, as is commonly done in optomechanics [8]. Briefly, the fields are displaced by complex numbers  $\alpha_i$  and  $\beta_i$ , i.e.,  $\hat{a}_i \rightarrow \alpha_i + \hat{a}_i$  and  $\hat{b}_i \rightarrow \beta_i + \hat{b}_i$ , in the equations of motion; the right-hand side operators describe fluctuations about a classical state. In a frame rotating with a frequency  $\omega_L$  we find an approximate Hamiltonian governing the fluctuation operators

$$\hat{H}_i = -\Delta_i \hat{a}_i^\dagger \hat{a}_i + \Omega_i \hat{b}_i^\dagger \hat{b}_i + G_i (\hat{a}_i^\dagger + \hat{a}_i) (\hat{b}_i^\dagger + \hat{b}_i), \quad (5.79)$$

where we have defined  $G_i = \alpha_i g_i$  and the detuning  $\Delta_i = \omega_L - \omega_i$ . Exact numeric codes can be used to solve the classical equations for  $\alpha_i$  and  $\beta_i$ ; in our calculations we look for a self-consistent steady-state solution so that the linearised Hamiltonian, Eq. (5.79), is time-independent.

For ease of realisation, we specialise to the case where the driving field is applied only to the edges of the lattice, as shown in Fig. 5.5(c). The driving field is chosen to have the same magnitude all around the edge. Pairs of opposite edges are driven at the same phase, with a phase difference of  $2\pi/3$  between pairs of adjacent edges, increasing in the clockwise orientation. In the interior of the lattice, as shown in Fig. 5.5(c), this yields optical fields with magnitudes  $|\alpha_i|$  that depend only weakly on the site index  $i$  and whose phases are 0 on sublattice A,  $2\pi/3$  on sublattice B, and  $4\pi/3$  on sublattice C. As a figure of merit for the quality of our solution we define the *flatness*

$$F = \frac{\sum_i |\alpha_i|}{N \max_i \{|\alpha_i|\}}, \quad (5.80)$$

which ranges from  $1/N$  for a situation where only one node has  $\alpha_i \neq 0$ , to 1 when all the nodes have the same  $|\alpha_i|$ . In the work reported here we have  $F \geq 0.9$  for a lattice driven from its edges, representing a situation which is very close to ideal.

## 5.7.2 | Mechanical edge states

A convenient means to understand the nature of the topological states borne by the system is to move to reciprocal space. To do this we must cast the problem into a translationally invariant form. First, we assume that the parameters of the lattice nodes, i.e.,  $\Delta_i$ ,  $G_i$ , etc., are all identical and drop the index  $i$ ; second, we add periodic boundary conditions to the system. Equation (5.79), transformed in this manner, can then be written

as a function of the quasimomentum in the two directions,  $k_x$  and  $k_y$ . Before continuing let us remark that the Eq. (5.79) does not preserve the total number of excitations  $\sum_i(\hat{a}_i^\dagger \hat{a}_i + \hat{b}_i^\dagger \hat{b}_i)$ . We therefore need to apply the Bogoliubov–de Gennes (BdG) formalism, where we consider a particle–hole description of the system. Given the quadratic Hamiltonian, Eq. (5.79) with  $N$  sites, it is possible to use the bosonic Bogoliubov–de Gennes transformation to find the eigenvalues of the system. Let us call  $\vec{c}$  the vector of the operators  $\vec{c} = (\hat{a}_1, \hat{a}_2, \dots, \hat{a}_N, \hat{b}_1, \hat{b}_2, \dots, \hat{b}_N)$ . The Hamiltonian can subsequently be written

$$\hat{H} = \begin{pmatrix} \vec{c}^\dagger & \vec{c} \end{pmatrix} H_{\text{BdG}} \begin{pmatrix} \vec{c} \\ \vec{c}^\dagger \end{pmatrix}, \quad (5.81)$$

where  $H_{\text{BdG}}$  is a square matrix. In this picture, the temporal evolution of the operators can be written in the form

$$\frac{d}{dt} \begin{pmatrix} \vec{c} \\ \vec{c}^\dagger \end{pmatrix} = \sigma_z H_{\text{BdG}} \begin{pmatrix} \vec{c} \\ \vec{c}^\dagger \end{pmatrix}, \quad (5.82)$$

with  $\sigma_z$  being a diagonal  $4N \times 4N$  matrix with elements on the diagonal equal 1 for the first  $2N$  entries and  $-1$  for the last  $2N$ . The eigenvalues of the matrix  $\sigma_z H_{\text{BdG}}$  give the energies in the particle-hole description of the system [162]. As a consequence, for each eigenvalue  $E_{k_x, k_y}$  of the Hamiltonian we will find another eigenvalue with opposite sign,

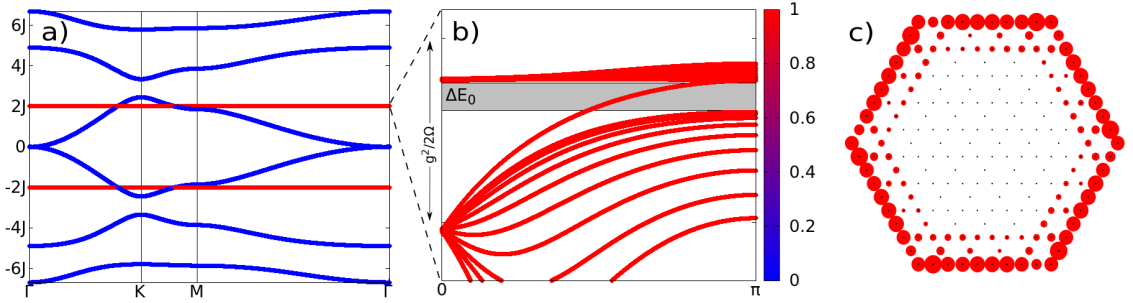


Figure 5.6: Band structure and edge state. (a) Bogoliubov–de Gennes particle–hole energies of the bulk Hamiltonian, Eq. (5.79), with quasi-momentum varying around the irreducible Brillouin zone of the Kagome lattice, passing through the symmetry points  $\Gamma$ ,  $K$ , and  $M$ . The colour indicates the nature of the corresponding state, ranging from fully optical (blue) to fully mechanical (red). (b) Dispersion relation of the infinite strip in the mechanical band. We find a state in the region where, in the periodic case, there was a band gap, labelled with  $\Delta E_0$ . The energy  $G^2/\Omega$  is indicated on the figure as a guide to the eye and to set the scale. (c) The state found in (b) that lies within the band-gap is mechanical in nature and confined to the edge of the finite array.

$-E_{k_x, k_y}$ . In Fig. 5.6(a) we show the dispersion relations in the BdG picture with quasimomenta lying on the path passing through the borders of the irreducible Brillouin zone of the Kagome lattice. Shown in the figure are the high symmetry points which form the corners of the first irreducible Brillouin zone  $\Gamma = (k_x = 0, k_y = 0)$ ,  $K = (2\pi/3, 2\pi/3)$ , and  $M = (\pi, 0)$ .

We set the mechanical frequency to coincide with an optical band. This choice leads to a repulsion between the optical and mechanical energy levels, creating a mechanical band whose size is of the order of  $g^2/\Omega$ . Inside this mechanical band, the optical features of the system induce a band gap. The emergence of edge states requires reducing the system to an infinite strip, i.e., where the periodic boundary conditions are applied in one direction only. As illustrated in Fig. 5.6(b), we subsequently find a mechanical edge state in the mechanical band gap. Restoring the finite size of our system fully, we find that the resulting mechanical edge state is as shown in Fig. 5.6(c). The fact that this edge state appears only when lift the boundary conditions is typical of Chern insulators. We remark that, despite the fact that this edge state is entirely mechanical in nature, it is induced in the mechanical oscillators indirectly through the optomechanical interaction and optical coupling between the nodes; there is no direct mechanical coupling between the nodes.

### 5.7.3 | Topologically protected transport

We now turn our attention to the transport properties of the system. To do this we calculate the correlation between a phonon injected into site  $j$  at time 0 transmitted to site  $i$  at time  $t$ . The Kubo Formula

$$G_{MM}(t, i, j) = \langle [\hat{b}_i(t), \hat{b}_j^\dagger(0)] \rangle \quad (5.83)$$

gives the intermediate quantity from which we derive the transmission probability

$$T_{MM}(t, i, j) = |G_{MM}(t, i, j)|^2. \quad (5.84)$$

We could analogously define the Kubo Formula and transmission probability for photons to be transmitted through the system ( $G_{OO}(t, i, j)$  and  $T_{OO}(t, i, j)$ ), for an injected photon to be detected as a phonon ( $G_{OM}(t, i, j)$  and  $T_{OM}(t, i, j)$ ), and for an injected phonon to be detected as a photon ( $G_{MO}(t, i, j)$  and  $T_{MO}(t, i, j)$ ).

The BdG description yields directly the matrices  $G(t)$  and, consequently,  $T(t)$ , which describe the correlations and transmission probabilities between all the creation and annihilation operators for all pairs of sites  $i$  and  $j$ ; i.e., the phonon–phonon elements of  $G(t)$  are  $G_{MM}(t, i, j)$ , etc., and similarly for  $T(t)$ . It is convenient for our purposes to

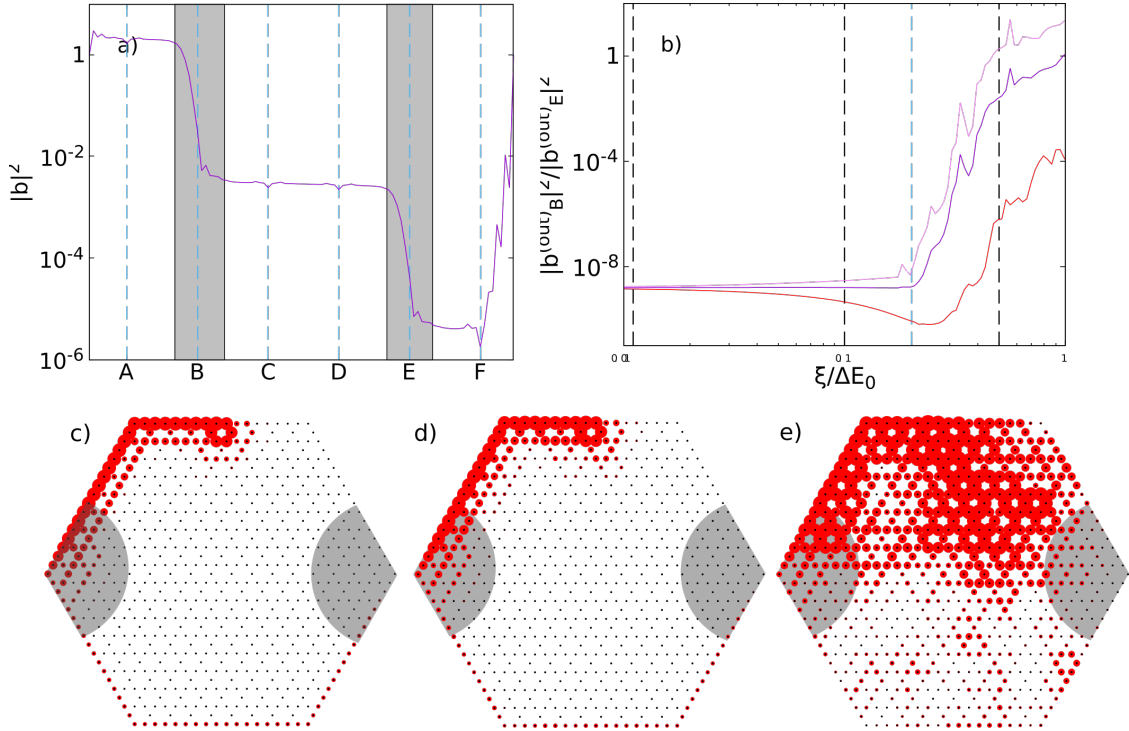


Figure 5.7: Topological transport. (a) Magnitude of the internal field on the borders of the lattice when phonons are injected from the site labelled O in (c). As a guide to the eye we label A, B, C, D, E and F the corners of the hexagon starting from the top-left one and proceeding in the counterclockwise direction. Note that the field diminishes greatly at the sinks, represented by the grey areas around points B and E. (b) Ratio between the mechanical output fields of the sinks at points B and E, as a function of increasing disorder. For values of the variance of the disorder until about  $0.2\Delta E_0$ , the edge state and transport are not affected greatly. Upon increasing the variance of disorder further we find a phase transition, with the ratio between the two output fields rapidly climbing to around 1, since for large disorder the band gap closes and there is no longer a preferred direction of transport. Each point in this plot is an average of 300 realisations, and the shaded region indicates the minimum and maximum values obtained. (c)–(e) Particular realisations of the internal field where the variance of the disorder equals 0,  $0.1\Delta E_0$ , and  $0.5\Delta E_0$ , respectively.

write  $G(t)$  in frequency space,  $G(\omega) = \int dt e^{i\omega t} G(t)$ . We use this formula to calculate the internal field of a perturbation propagating inside the array under different conditions. Our starting point, as mentioned earlier, is a lattice of identical sites. To this we add two extended mechanical sinks centred around corners B and E of the hexagon, as shown in Fig. 5.7(c)–(e). To avoid perturbing the edge state, these sinks were introduced through a smooth additional mechanical decay rate  $\gamma_{\text{ext},i}$ . The topological protection of the edge state means that if the function used were not smooth enough the edge state would simply avoid the source. In our case we use the Fermi function

$$\gamma_{\text{ext},i} = \frac{2\gamma_{\text{ext,max}}}{e^{d(i,j)/D} + 1}, \quad (5.85)$$

where  $i$  is the site in question,  $j$  is the site around which the sink is centred, i.e., the site at corner  $j = \text{B}$  or  $j = \text{E}$  in Fig. 5.7,  $d(i, j)$  quantifies the distance between the two sites, and  $D$  sets the size of the sink. The additional decay rate changes smoothly from  $\gamma_{\text{ext,max}}$  at the centre of the sink to zero when  $d(i, j) \gg D$ . In Fig. 5.7(a) and (c)–(e) we shade the two regions for which  $d(i, j) < D$  in grey.

In the following we shall be concerned only with transport of phonons through the system. We drive the mechanical system at position O with a frequency resonant with the edge state identified in Fig. 5.6. As illustrated clearly in Fig. 5.7(a) and (c), the mechanical excitation travels along the edge state in the counter-clockwise direction. The transmission amplitude decreases slightly along the way because of the intrinsic optical and mechanical losses of the structure. Eventually, the excitation enters the region of the sink centred around corner B, whereupon it suddenly decreases in amplitude. The absorption of the sink is not perfect, and some of the mechanical excitation reaches the second sink, centred around corner E. The rapid increase in Fig. 5.7(a) at corner F is due to the limited, but finite, propagation of the mechanical excitation in the “wrong,” clockwise, orientation.

In Fig. 5.7(a) the slope of the curve is not zero away from the sinks. As mentioned earlier this is due to the optical and mechanical losses inherent in the system, in conjunction with the finite velocity of the edge state. We verified this by comparing the observed slope  $\Gamma_{\text{obs}}$ , which is the same throughout the plot away from the shaded regions, to  $\Gamma_{\text{dir}}$ , derived directly from the band structure. To calculate  $\Gamma_{\text{dir}} = \Gamma/v$  we divided the decay rate  $\Gamma$  of the spectrum of the system, which is obtained from the full-width at half-maximum of the Lorentzian curve found at the frequency in question, by the velocity  $v$  of the edge state. This velocity is, in turn, calculated from the slope of the edge state at this frequency, and is derived from the dispersion relation shown in Fig. 5.6(b). We verified numerically that  $\Gamma_{\text{obs}}$  and  $\Gamma_{\text{dir}}$  are the same, to within numerical error, throughout this paper.

Having two sinks positioned symmetrically around the source allows us to demonstrate clearly the directional nature of edge-state transport and its robustness to disorder. One of the most technologically important features of edge states of a Chern insulator is that they minimise the effects of back-scattering. Whereas in ordinary conductors a wave that travels in one direction will be reflected off of a discontinuity, Chern insulators are immune to such scattering as long as it the discontinuity leaves unchanged the topology of the dispersion relation. To verify this statement and illustrate its implications in our system, we inserted mechanical disorder in the system. This is described by a modification of the Hamiltonian for each site,

$$\hat{H}_i \rightarrow \hat{H}_i + \delta\Omega_i \hat{b}_i^\dagger \hat{b}_i, \quad (5.86)$$

where  $\delta\Omega_i$  is a random variable drawn from a zero-mean Gaussian distribution with variance  $\sigma_\Omega$ . Our expectation is that the nature of the edge state and transport will remain relatively unaffected for small values of  $\sigma_\Omega$ , until the disorder is so large that the band gap closes.

To quantify the level of robustness against disorder we use the ratio between the absolute values of the output mechanical fields from the sinks centred at B and E. In turn, this is calculated using the input–output relation

$$\hat{b}_i^{(\text{out})} = \hat{b}_i^{(\text{in})} - \sqrt{\gamma_{\text{ext},i}} \hat{b}_i, \quad (5.87)$$

written for the mechanical fields, whereupon the relevant quantity is

$$T_{\text{B/E}} = \frac{|\hat{b}_{\text{B}}^{(\text{out})}|^2}{|\hat{b}_{\text{E}}^{(\text{out})}|^2}. \quad (5.88)$$

In Fig. 5.7(b) we illustrate this quantity as a function of increasing variance of the disorder. To ease interpretation we scale the disorder by the scale of the band gap,  $\Delta E_0$ . We can see that for  $\sigma_\Omega$  up to  $\sim 0.2\Delta E_0$  the disorder affects neither the direction of propagation of the edge state, as shown in Fig. 5.7(b), nor the nature of the edge state, as can be seen by comparing Fig. 5.7(d) to Fig. 5.7(c). At larger values of the disorder we encounter a phase transition where the slope of the curve in Fig. 5.7(b) suddenly changes. This indicates a breakdown of topologically-protected transport in the system, and coincides with the edge state losing its nature entirely, cf. Fig. 5.7(e).

## 5.8 | Summary

In this Chapter we introduced topological insulators and how they can be useful for cutting-edge technology. After a brief phenomenological introduction, we showed the



link between TIs with the quantum Hall effect and how it differs from the classical Hall effect. In particular we showed the discretization of the conductivity and how it can be related to the topology of the system. For example, in the Harper-Hofstadter model, from the Brillouin zone of the lattice system we can define a topological invariant, the Chern number, which ultimately accounts for the number of edge states through the bulk-edge correspondence.

Thus, we analyzed the quantum transport performed in a topological insulator made by an array of optomechanical cavities. Optical coupling between the toroids gives rise to an effective spin-orbit interaction for the photons in the array. Through the optomechanical interaction and a judicious choice of the optical driving field this gives rise to topologically protected mechanical edge states which are protected against fabrication and other disorder. This is a remarkable result, where the topological properties of the optical lattice have been inherited by the mechanical system through the optomechanical coupling. This opens the question whether it is possible for an open system to inherit the topological properties from the environment and although it has been partially investigated [163, 164] it misses a complete answer and it will be a future research line of the authors.

The mechanical edge state appeared in the energy gap between the optical and the mechanical bands. With perturbation theory we can estimate the band gap to be of the order of  $g^2$ . As  $g$  is usually very small, we expect to be difficult to exploit the exact frequency which allows topological transport. We need therefore to be very precise in the estimation of  $g$ , as this will lead to a precise estimation of the band gap. For this reason, we will talk in the next Chapter about estimation theory in quantum mechanics and apply the tools for the inference of the optomechanical coupling strength.

## Estimation theory and application in optomechanics

In the previous chapter we showed how to derive a phononic topological insulator by means of a displaced optical resonator in an optomechanical array. The topological transport properties we studied have a deep dependence upon the optomechanical coupling constant. Furthermore the system we presented is composed of several microresonators that can show defects in the coupling. To achieve the creation of topological-based technology one needs an extended knowledge of the Hamiltonian parameters. In this chapter we introduce the quantum estimation theory, a branch that teaches us how to obtain large information about the Hamiltonian parameters. In the framework of quantum estimation, we can see two main approaches, studied and applied intensively in the literature, the Bayesian approach and the Fisher approach. There is an important difference though, for they are based on very different assumptions. The Bayesian approach considers the parameter to be estimated as a random variable and relate to it a prior probability distribution. The goal of this first approach is to find the best estimation strategy among all the possible ones. Furthermore, it aims to optimize the strategy for all the possible values of the estimate. For this reason it is also called global estimation theory. On the other hand, the Fisher approach wants to investigate which one is the best measurement process for a specific value of the estimanda and therefore is called local estimation theory.

During the doctoral studies we applied the Bayesian theory to two system of interest, which led to two published papers [1][2]. The first regards the estimation of the coupling constant of a single optomechanical cavity. In our analysis we wanted to understand which measurement can give us the best estimation of the optomechanical coupling strength. The second system where we focused our attention is the Jaynes-Cumming

model for the matter-field interaction. Also in this second case we want to estimate the interaction strength. The reason why we focused on those two different systems had pedagogical purpose. We learned in our studies that, even though the two systems have a very different Hamiltonian and Hilbert spaces, they share something in common regarding the optimal strategy for the estimation of the coupling constant. We will see this in detail throughout this chapter. Finally we applied the Fisher approach for the estimation of the optomechanical coupling constant [3]. This analysis led us to discover the homodyne measurement is the optimal estimation strategy in terms of accuracy.

## 6.1 | Classical estimation theory

Estimation theory is a branch of statistical mathematics that aims to extract the maximum amount of information from a system. Thus, estimation theory investigates measurement processes and how they can be implemented to get the most out of it. It has clearly an important role in both classical and quantum physics, since measurements play an important role in the scientific approach to the understanding of Nature. Generally, we refer to classical estimation theory when it is applied to classical systems, and quantum estimation theory when quantum systems are involved. In this section we introduce classical estimation theory. Let's take a system  $S$  and suppose that it depends on  $M$  parameters  $\theta = (\theta_1, \dots, \theta_M)$ . Our goal is to infer the value of these parameters. Therefore, we perform  $n$  measurements on the system and we result with a set of data  $\mathbf{v} = (v_1, v_2, \dots, v_n)$ . In the real world, the system is always affected by some kind of noise. Even in the most perfect scenario, Nature guarantees a certain amount of noise given by the laws of quantum mechanics, as we have seen in chapter 3. For this reason, the data  $\mathbf{v}$  are random variables, which take their values with a conditional probability distribution  $p(\mathbf{v}|\theta)$  depending on the parameter values  $\theta_j$  with  $j = 1, \dots, M$ . Here, the investigation we are carrying out revolves around the resolution of this inverse statistical problem. We define  $M$  functions  $\hat{\theta}_j(\cdot)$  of the data and we call them estimators. In fact, they give an estimation of the parameters  $\theta_j$ . The result of the estimator  $\hat{\theta}_j = \hat{\theta}_j(\mathbf{v})$  is called estimate. In the further analysis we consider the estimation of a single parameter  $\theta$  and we therefore ignore the label  $j$ . However what we will say in this section can be extended easily to the case of multiple parameters.

One of the main issues of estimation theory is to define unequivocally what makes an estimator good, or even optimal. In fact, when we measure and apply an estimation strategy we may want to reduce the deviation of our outcomes, so that we result with high precision. Alternatively, we may want our estimate to be as close as possible to

the real value, resulting with a high accuracy. On second thought we may want to have a good enough combination of the two. For each choice there is a specific strategy that should be implemented. Estimation theory tries to solve this problem. In the literature we find two main methods which start from very different assumptions and lead to knowledge we cannot always relate together. They are the Bayes and the Fisher approaches.

### 6.1.1 | Bayesian approach

We can imagine the value of  $\theta$  is itself distributed with an a prior probability distribution  $z(\theta)$ . This can be given by first principles of the theory, or rather by past measurements. Hence, given the set of data  $\mathbf{v}$  we expect the probability of guessing the system has value  $\hat{\theta}$  in the infinitesimal range of parameters value  $d\hat{\theta}$

$$q(\hat{\theta}|\theta)d\hat{\theta} = \int d\mathbf{v}d\hat{\theta}\pi(\hat{\theta}|\mathbf{v})p(\mathbf{v}|\theta). \quad (6.1)$$

The probability distribution  $q$  is called posteriori distribution. When integrated over the volume  $d\hat{\theta}$  it gives the probability that the system has the specified value. It depends on the data set  $\mathbf{v}$  and, most important, on the functional  $\pi$  related to the measurement process, which is called strategy. Whether the estimate  $\hat{\theta}$  results from the data  $\mathbf{v}$  depends on the strategy  $\pi$ . For it gives a probability it is constrained to the conditions

$$0 \leq \pi(\hat{\theta}|\mathbf{v}) \leq 1, \quad \int_{\hat{\Omega}} \pi(\hat{\theta}|\mathbf{v}) = 1, \quad (6.2)$$

where  $\hat{\Omega}$  is the space of definition of the parameter  $\theta$ . Hence, the posteriori distribution gives us the new information we have extrapolated from the system after we have applied the measurement strategy  $\pi$ . Here the solution of the inverse problem is not a specific value for  $\theta$ , but rather it improves the quality of our information of it. The Bayesian approach attempts to improve the information we have on the parameters, addressing the analysis to a larger set of probability distributions, which can better describe the real distribution of  $\theta$ , and this is exactly the role of the posteriori distribution. We note an estimation always comes with a cost. In fact, we may associate the cost  $C(\hat{\theta}|\theta)$  to a wrong estimation. The Bayesian approach seeks to minimize the average of a cost function  $C(\hat{\theta}, \theta)$ , such that

$$\bar{C}[\pi] = \int \int d\theta d\hat{\theta} z(\theta) q(\hat{\theta}|\theta) C(\hat{\theta}, \theta) \quad (6.3)$$

$$= \int \int \int d\mathbf{v} d\theta d\hat{\theta} z(\theta) \pi(\hat{\theta}|\mathbf{v}) p(\mathbf{v}|\theta) C(\hat{\theta}, \theta). \quad (6.4)$$

Hence, the aim is to find the best strategy  $\pi(\hat{\theta}|\mathbf{v})$  that minimizes the average cost function  $\bar{C}[\pi]$ .

One common choice for the cost function  $C(\hat{\theta}|\theta)$  is the mean square error cost function:

$$C^{\text{MSE}}(\hat{\theta}|\theta) = (\hat{\theta} - \theta)^2. \quad (6.5)$$

so that the average cost function in Eq. (6.3) is the mean square error of the estimator  $\hat{\theta}$  averaged both on the data  $\mathbf{v}$  and the prior probability distribution  $z(\theta)$ .

### 6.1.2 | Classical Fisher information approach

In the Fisher approach, also known as frequentistic approach, the parameters  $\boldsymbol{\theta} = (\theta_1, \dots, \theta_M)$  are deterministic variables. It means we cannot associate any prior or posterior distribution function to any estimanda. We may have some uncertainty on it, but this is given by the little knowledge we have on the system. This uncertainty could in principle be overcome with an enough number of experiments and measurements. This is in line with the frequentistic definition of probability and it is the origin of the name.

The goal is to find the best estimators  $\hat{\theta}_i(\cdot)$  that minimizes the mean square error (MSE) deviation from the true value  $\theta_i$

$$\text{MSE}(\hat{\theta}_i) = \langle (\hat{\theta}_i(\mathbf{v}) - \theta_i)^2 \rangle = \int d^n \mathbf{v} p(\mathbf{v}|\boldsymbol{\theta}) (\hat{\theta}_i(\mathbf{v}) - \theta_i)^2. \quad (6.6)$$

The main result we are going to show in this section is obtained for unbiased estimators, where the mean value of the estimators  $\hat{\theta}_i$  coincides with the true value  $\theta_i$  for  $i = 1, \dots, M$

$$\langle \hat{\theta}_i \rangle = \int d^n \mathbf{v} p(\mathbf{v}|\boldsymbol{\theta}) \hat{\theta}_i(\mathbf{v}) = \theta_i. \quad (6.7)$$

We now derive the expression above for the  $k^{\text{th}}$  parameter, yielding

$$\frac{\partial \langle \hat{\theta}_i \rangle}{\partial \theta_j} = \int d^n \mathbf{v} \partial_{\theta_j} p(\mathbf{v}|\boldsymbol{\theta}) \hat{\theta}_i(\mathbf{v}) \quad (6.8)$$

$$= \delta_{ij}. \quad (6.9)$$

We then use the normalization of the probability  $\int d^n \mathbf{v} p(\mathbf{v}|\boldsymbol{\theta}) = 1$ , to express (6.8) as

$$\int d^n \mathbf{v} [\hat{\theta}_i(\mathbf{v} - \hat{i})] \partial_{\theta_j} p(\mathbf{v}|\boldsymbol{\theta}) = \delta_{ij}. \quad (6.10)$$

Let's now take the vectors  $\mathbf{y} = (y_1, \dots, y_M)$  and  $\mathbf{z} = (z_1, \dots, z_M)$ . We can use it to write

$$\int d^n \mathbf{v} \sum_i y_i [\hat{\theta}_i - \theta_i] \sum_j z_j \partial_{\theta_j} p(\mathbf{v}|\boldsymbol{\theta}) = \sum_i y_i z_i. \quad (6.11)$$

The expression above is nothing else than the expected value of the product  $\langle f(\mathbf{v})g(\mathbf{v})|\theta \rangle$  of the two functions

$$f(\mathbf{v}) = \sum_i y_i [\hat{\theta}_i - \theta_i] \quad (6.12)$$

$$g(\mathbf{v}) = \sum_i z_i \frac{\partial}{\partial \theta_i} \ln[p(\mathbf{v}|\theta)]. \quad (6.13)$$

Finally we can use Schwartz inequality to write

$$|\sum_i y_i z_i|^2 = \langle f(\mathbf{v})g(\mathbf{v})|\theta \rangle^2 \leq \langle f(\mathbf{v})^2|\theta \rangle \langle g(\mathbf{v})^2|\theta \rangle. \quad (6.14)$$

Therefore the substitution of the definitions for  $f$  and  $g$  leads to

$$\mathbf{y}^T \mathbf{z} \leq \left( \mathbf{y}^T \mathbf{B} \mathbf{y} \right) \left( \mathbf{z}^T \mathbf{A} \mathbf{z} \right), \quad (6.15)$$

where we have defined the matrices

$$A_{ij} = \left\langle \frac{\partial}{\partial \theta_i} \ln[p(\mathbf{v}|\theta)] \frac{\partial}{\partial \theta_j} \ln[p(\mathbf{v}|\theta)] \right\rangle \quad (6.16)$$

$$B_{ij} = \langle [\hat{\theta}_i - \theta_i][\hat{\theta}_j - \theta_j] \rangle. \quad (6.17)$$

Different inequalities are obtained for different substitutions of the vectors  $\mathbf{y}$  and  $\mathbf{z}$ . In particular, the choice  $\mathbf{z} = \mathbf{A}^{-1} \mathbf{y}$  leads to the Cramér-Rao bound

$$\text{MSE}(\hat{\theta}) \geq \frac{1}{NF[p(\theta)]}, \quad (6.18)$$

where  $N$  is the number of repeated experiments, and  $F$  is the Fisher information, which is defined as

$$F[p(\theta)] = \int dx \frac{1}{p(x|\theta)} \left[ \frac{\partial p(x|\theta)}{\partial \theta} \right]^2. \quad (6.19)$$

The Cramer-Rao theorem is the main result of this approach. It states that there exists a minimal value for the MSE caused by the parameter affection to the distribution of the data-set.

The Fisher information  $F$  is a function of the true value  $\theta$ . It gives the amount of information we can get from the data  $\mathbf{v}$  about the true value of the parameter. There are generally two approaches to the problem of finding the optimal estimator that saturates the Cramer-Rao bound. One is to find the optimal global estimator, that gives the best strategy for every value of  $\theta$ , whereas the second is the local approach where we find the best estimator in a neighborhood of a specific value  $\theta_0$ .

### 6.1.3 | Comparison between the approaches

The two approaches above are completely separated. The main difference is due to the nature of the parameter to estimate. The frequentistic approach requires a deterministic variable, whose value can be estimated with continuous repetitions of the experiment, whereas in the Bayesian approach we seek to estimate a random variable distributed with its own probability distribution, and repeated information leads to a better knowledge of the parameter distribution function. In this section we propose two examples that show how we should compare the two approaches.

The first problem we address, is a particular population size estimation. We suppose we have  $N$  balls in a lottery labeled from 1 to  $N$ , which is our unknown parameter. The procedure for the estimation is called sampling without replacement. For  $M$  times we remove a ball from the lottery and we read the number on it. The problem is also known as the german tank problem, and it has been used by the Allies to estimate the number of german tanks in World War II. The frequentist approach leads to a value of  $N$  given by the minimum-variance unbiased estimator [165]

$$\hat{N} = N_{\max}(1 + M^{-1}) - 1, \quad (6.20)$$

where  $N_{\max}$  is the maximum number extracted from the lottery. The variance of the estimator is

$$\text{MSE}[\hat{N}] = \frac{1}{M} \frac{(\hat{N} - M)(\hat{N} + 1)}{(M + 2)}. \quad (6.21)$$

The Bayesian approach leads to a very different estimation for  $N$ . The crucial part is the prior probability distribution of the estimanda, which could also be an improper uniform distribution,  $z(N) \propto 1$ , with  $N = N_{\max}, \dots, \infty$ . The result is obtained with the use of the Bayes formula

$$p(N|N_{\max}) = \frac{p(N_{\max}|N)p(N)}{p(N_{\max})} = \frac{p(N_{\max}|N)p(N)}{\sum_{N'=N_{\max}}^{\infty} p(N_{\max}|N')p(N')}. \quad (6.22)$$

The result for the improper prior uniform distribution is [166]

$$p(N|N_{\max}) = \frac{M-1}{N_{\max}} \binom{N_{\max}}{N} \binom{N}{M}^{-1}, \quad (6.23)$$

for  $N = N_{\max}, N_{\max} + 1, N_{\max} + 2, \dots$ , and 0 otherwise. The estimated  $N$  and variance are

$$\langle \hat{N} \rangle = \frac{M-1}{M-2}(N_{\max} - 1) \quad (6.24a)$$

$$\text{MSE}[\hat{N}|N_{\max}] = \frac{M-1}{(M-2)^2(M-3)}(N_{\max} - 1)(N_{\max} - M + 1), \quad (6.24b)$$

which are different from the ones calculated in the frequentist approach.

Let's now consider an example taken from physics, where eventually the Fisher and Bayes approach actually coincide in the limit of infinite measurements. We take a single photon and a beam splitter with transmission probability  $p$  and reflectivity  $q = 1 - p$ . After  $N$  photons are directed to the beam splitter  $n$  photons will eventually pass with probability

$$p_p^N(n) = \binom{N}{n} p^n (1-p)^{N-n}, \quad (6.25)$$

that is the binomial distribution. Following Eq. (6.19) we calculate  $F$  as:

$$F[p(p)] = \sum_{n=0}^N \frac{1}{p_p^N(n)} \binom{N}{n}^2 \left( n p^{n-1} (1-p)^{N-n} + p^n (1-p)^{N-n-1} \right)^2 = \frac{N}{p(1-p)} \quad (6.26)$$

Our aim is to find the estimator that saturates the CRB Eq. (6.18). We can easily check that the simple estimator  $\hat{p}_N(n) = n/N$  is the required one, in fact

$$\begin{aligned} \Delta^2 \hat{p}_N(n) &= \sum_{n=0}^N \binom{N}{n} p^n (1-p)^{N-n} \left( \frac{n}{N} - p \right)^2 \\ &= \frac{p(1-p)}{N}. \end{aligned} \quad (6.27)$$

We now analyze the same problem with the Bayesian approach. We express our ignorance stating that the a prior p.d.f. is  $z(p) = 1$ , that is the uniform distribution among all the possible values and corresponds to zero a prior knowledge. We calculate the MMSE estimator as:

$$\hat{p}_p^N(n) = \frac{n+1}{N+2}, \quad C[\hat{p}_N] = \frac{1}{6(N+2)}. \quad (6.28)$$

In the limit  $N \rightarrow \infty$  where the number of data is large the two methods are the same. This can be also checked calculating the variance of the estimator  $\hat{p}_N(n)$  found for the Fisher approach averaged on  $p$ , that leads to  $\Delta \hat{p}_N(n) = \frac{1}{6N}$ .

We can argue how an experimentalist should take the decision about which method he should apply. In fact he may consider the Bayesian approach and evaluate the prior



probability distribution applying the theory behind the system. Then, he should perform different experiments in order to reinforce this prior expectation. Once the experimentalist has a clear knowledge of the prior distribution, he could pass to the Fisher approach and consider the local estimation around the expected value. Therefore, even though the difference between the approaches is substantial, they can still be used by an experimentalist who wish to improve the measurement.

## 6.2 | Quantum estimation theory

In quantum mechanics the system is described by a density operator  $\rho(\lambda)$  which depends on a collection of parameters  $\lambda$ . Our purpose in this section is to introduce the basic concepts of quantum estimation theory adapting the results of section 6.5.1 to quantum mechanics. Quantum estimation theory attempts to find the best strategy for estimating one or more parameters of the density matrix [53]. We may want to estimate the value of a parameter  $\lambda$  which is in general not accessible by any direct measurement on the system. In quantum mechanics an observable is related to the existence of a Hermitian operator, and the set of eigenvalues and eigenstates of the system determine the actual value of the observable. However, if  $\lambda$  can not be represented with a Hermitian operator, there should be a way to access its value.  $\lambda$  can be a parameter of the Hamiltonian, a phase, or even a more complicate function of the state, such as the amount of entanglement or the entropy. This enters in a bigger framework of quantum state estimation that catches the main result we will show in this chapter. In this dissertation, we are going to focus on quantum parameter estimation.

In general a quantum measurement is a Positive Operator-Valued Measure (POVM)  $\Pi(\theta)$  with the property

$$0 \leq \Pi(\theta) \leq I, \quad (6.29)$$

where  $\Theta$  is the whole space where  $\lambda$  is defined and the subset  $\theta \subset \Theta$ . In fact, The POVM is related to the probability of having  $\lambda \in \theta$ . This requires the normalization condition  $\int_{\Theta} d\Pi(\lambda) = I$ , where  $d\Pi(\lambda)$  is an infinitesimal operator s.t.  $\Pi(\theta) = \int_{\theta} d\Pi(\lambda)$ . The POVM returns a probability when it is applied within the Bohr rule

$$p(x|\lambda) = \text{Tr}[\rho(\lambda)\Pi(x)], \quad (6.30)$$

where  $x$  is the outcome of the measurement. It is straightforward to show the normalization condition leads to  $\int_{\Theta} p(x|\lambda)d\lambda = 1$ .

### 6.2.1 | Quantum Bayesian strategy

In the Bayesian approach we still get the parameter  $\lambda$  to be a random variable. We can associate to it the prior probability  $z(\lambda)$  and consider everything as in the classical case. However the measurements now are described by POVM and need to change the definition of the posteriori probability distribution Eq. (6.1), that becomes

$$q(\hat{\lambda}|\lambda)d\hat{\lambda} = \text{Tr}[d\Pi(\hat{\lambda})\rho(\lambda)], \quad (6.31)$$

which is the infinitesimal form of the Bohr rule (6.30). The POV has the role of the strategy. The average cost function in Eq. (6.3) becomes

$$\bar{C}[\Pi] = \text{Tr}\left[\int d\lambda \int d\Pi(\hat{\lambda})z(\lambda)C(\hat{\lambda}, \lambda)\rho(\lambda)\right]. \quad (6.32)$$

Hence, the Bayesian approach in the quantum regime seeks to find the best POVM that minimizes the average cost function. We can find it solving

$$W(\hat{\lambda}) - L \geq 0, \quad (6.33a)$$

$$[W(\hat{\lambda}) - L]d\Pi(\hat{\lambda}) = 0, \quad (6.33b)$$

where  $W(\hat{\lambda})$  is the Hermitian risk operator

$$W(\hat{\lambda}) = \int_{\Theta} z(\lambda)C(\hat{\lambda}, \lambda)\rho(\lambda)d\lambda, \quad (6.34)$$

and  $L$  is the Hermitian Lagrange operator, defined as

$$L = \int_{\Theta} W(\hat{\lambda})d\Pi(\hat{\lambda}). \quad (6.35)$$

The minimization problem set above in the equations for the optimal strategy seek the POVM for which the risk  $W(\hat{\lambda})$  is at its minimum. Thus for the same POVM also the average cost reaches its minimum. The proof can be found in Ref. [53].

#### 6.2.1.1 | Quantum minimum mean-square error estimation

In order to solve the estimation problem we have to provide a cost function, a measure of the cost incurred upon making errors in the estimate of  $\lambda$ . Here, we wish to minimize the average squared cost of error, which is encoded in the cost function

$$C(\tilde{\lambda}, \lambda) = (\tilde{\lambda} - \lambda)^2, \quad (6.36)$$

where  $\tilde{\lambda}$  is the estimate of  $\lambda$ , and therefore a function of the measurement data.

Now, we are able to formulate the quantum estimation problem. We are looking for  $d\hat{\Gamma}(\tilde{\lambda})$ , which minimizes the average cost of this estimation strategy, see Eq. (6.32)

$$\bar{C} = \text{tr} \left\{ \int_{-\infty}^{\infty} \int_{-\infty}^{\infty} z(\lambda) C(\tilde{\lambda}, \lambda) \hat{\rho}(\lambda) d\hat{\Gamma}(\tilde{\lambda}) d\lambda \right\}, \quad (6.37)$$

under the constraints embodied in Eq. (6.29). This is a variational problem for the functional  $\bar{C}$ . To proceed, we consider each possible estimate  $\tilde{\lambda}$  to be an eigenvalue of the Hermitian operator

$$\hat{M} = \int_{-\infty}^{\infty} \tilde{\lambda} d\hat{\Gamma}(\tilde{\lambda}) = \int_{-\infty}^{\infty} \tilde{\lambda} |\tilde{\lambda}\rangle \langle \tilde{\lambda}| d\tilde{\lambda} \quad (6.38)$$

with eigenstates  $|\tilde{\lambda}\rangle$ . Thus, the average cost functional in Eq. (6.3), calculated using the cost function in Eq. (6.36), can be written as

$$\bar{C}[\hat{M}] = \text{tr} \left\{ \int_{-\infty}^{\infty} z(\lambda) (\hat{M} - \lambda \hat{I})^2 \hat{\rho}(\lambda) d\lambda \right\}. \quad (6.39)$$

For convenience, we now define the following operators ( $k = 0, 1, 2$ ):

$$\hat{\Gamma}_k = \int_{-\infty}^{\infty} \lambda^k z(\lambda) \hat{\rho}(\lambda) dg. \quad (6.40)$$

Now, let  $\epsilon$  be a real number and  $\hat{N}$  any Hermitian operator. Let  $\hat{M}_{\min}$  be the Hermitian operator which minimizes  $\bar{C}[\hat{M}]$ . Then, we have

$$\bar{C}[\hat{M}_{\min}] \leq \bar{C}[\hat{M}_{\min} + \epsilon \hat{N}], \quad (6.41)$$

because the sum of Hermitian operators is itself a Hermitian operator. Evaluating the right-hand side of the inequality and using the operators defined in Eq. (6.40), we obtain

$$\begin{aligned} \bar{C}[\hat{M}_{\min} + \epsilon \hat{N}] &= \bar{C}[\hat{M}_{\min}] + \epsilon \text{tr} \{ \hat{N} (\hat{\Gamma}_0 \hat{M}_{\min} + \hat{M}_{\min} \hat{\Gamma}_0 - 2\hat{\Gamma}_1) \} \\ &\quad + \epsilon^2 \text{tr} \{ \hat{\Gamma}_0 \hat{N}^2 \}. \end{aligned} \quad (6.42)$$

By differentiating this relation with respect to  $\epsilon$  and equating the result to zero, one is able to show that the unique Hermitian operator  $\hat{M}_{\min}$  minimizing  $\bar{C}$  must satisfy [42]

$$\hat{\Gamma}_0 \hat{M}_{\min} + \hat{M}_{\min} \hat{\Gamma}_0 = 2\hat{\Gamma}_1. \quad (6.43)$$

The average minimum cost of error for this measurement is

$$\begin{aligned} \bar{C}_{\min} &= \text{tr} \{ \hat{\Gamma}_0 \hat{M}_{\min}^2 - 2\hat{\Gamma}_1 \hat{M}_{\min} + \hat{\Gamma}_2 \} \\ &= \text{tr} \{ \hat{\Gamma}_2 - \hat{M}_{\min} \hat{\Gamma}_0 \hat{M}_{\min} \}, \end{aligned} \quad (6.44)$$

where we have used the relation in Eq. (6.43) to simplify the result. In order to determine  $\hat{M}_{\min}$  we thus have to solve the operator equation Eq. (6.43). It has been shown in Ref. [42] that the unique solution of this equation can be written as

$$\hat{M}_{\min} = 2 \int_0^{\infty} \exp(-\hat{\Gamma}_0 x) \hat{\Gamma}_1 \exp(-\hat{\Gamma}_0 x) dx. \quad (6.45)$$

A comment about this solution is in order. The operator that we have found does not necessarily represent the best estimator of  $\lambda$ , but rather the measurement operator which protects best against information loss, no matter what the true value of  $\lambda$  is. Further discussion about this subtlety and its relation to biased estimators can be found in the illuminating monograph by Jaynes [167].

### 6.2.1.2 | Quantum maximum likelihood estimation

The maximum likelihood estimator (MLE) considers minimization of the cost function

$$C(\tilde{\lambda}, \lambda) = -\delta(\tilde{\lambda} - \lambda), \quad (6.46)$$

averaged over all the possible outcomes  $\tilde{\lambda}$  of the estimanda  $\lambda \in \Omega$ . In the case of  $\Omega$  being a discrete set, the analogue of Eq. (6.46) would be  $C(\tilde{\lambda}, \lambda) = -1$  if  $\tilde{\lambda} = \lambda$  and 0 otherwise. In the continuous this cost function assumes the form above. Hence, the average cost function in Eq. (6.37) becomes

$$\bar{C}[\Pi] = \text{Tr} \left[ \int d\Pi(\lambda) z(\lambda) \rho(\lambda) \right] \quad (6.47)$$

and we are looking for the infinitesimal operators  $d\Pi(\lambda)$  which maximize  $\bar{C}$ . In order to solve this maximization problem we need some assumptions. First of all, we write the density operator  $\rho(\lambda)$  in some basis, yielding

$$\rho(\lambda) = \sum_{n,m} \rho_{n,m}(\lambda) |n\rangle \langle m|, \quad \text{with } \sum_n \rho_{nn}(\lambda) = 1 \quad \forall \lambda, \quad (6.48)$$

and the functions  $\rho_{nm}(\lambda)$  are known. Then, we assume the infinitesimal operators  $d\Pi(\lambda)$  can be written in the same basis as

$$d\Pi(\lambda) = \sum_{nm} \pi_{nm}(\lambda) d\lambda, \quad \text{with } \pi_{nm} = \pi_{mn}^*, \quad \forall n, m. \quad (6.49)$$

The latter condition ensures the self-adjointness of the infinitesimal generator. We remember that when integrated over the set  $\Omega$  the POVM gives back the identity operator and this is reflected into the conditions

$$\int_{\Omega} d\lambda \pi_{nm} = 1 \quad (6.50a)$$

$$\int_{\Omega} d\lambda \pi_{nm} = 0, \quad \text{for } n \neq m. \quad (6.50b)$$

Therefore, the average cost function can be written as sum of products of functions as

$$\bar{C}[\Pi] = \sum_{n=m} \left[ \int d(\lambda) z(\lambda) \sum_{n'} \pi_{nn'} \rho_{n'm}(\lambda) \right]. \quad (6.51)$$

In order to find the expression for the functions  $\pi_{nm}(\lambda)$  we can therefore try to maximize the average cost maximizing all the singular contributions from  $z(\lambda) \sum_{n'} \pi_{nn'} \rho_{n'm}$ . We first make the transformation

$$\langle \sqrt{z(\lambda)} \rho_{nm}(\lambda) \rightarrow \rho_{nm}(\lambda), \quad \langle \sqrt{z(\lambda)} \pi_{nm}(\lambda) \rightarrow \pi_{nm}(\lambda), \quad (6.52)$$

so that we absorbed the term  $z(\lambda)$  into the other functions. Hence, we consider a Hilbert space  $\mathcal{H}$  of definitions of the functions  $\pi_{nm}(\lambda)$  and  $\rho_{nm}(\lambda)$  for all the possible values of  $n, m$ , and we expand  $\rho_{nm}(\lambda)$  in one orthogonal basis  $\{\psi_n(\lambda)\}$  provided by the Hilbert space as

$$\rho_{nm}(\lambda) = \sum_k p_k^{nm} \psi_k(\lambda), \quad (6.53)$$

where the coefficient  $p_k^{nm}$  can be obtained from the inner product  $\langle \rho_{nm}, \psi_k \rangle$ . Finally the solutions for  $\pi_{nm}(\lambda)$  are the ones that are as parallel as possible to  $\rho_{nm}(\lambda)$  and satisfy the conditions (6.50). The calculation of the expansion can be extremely cumbersome but there are cases when it leads to a result. We will show in section 6.5.2 an example.

## 6.2.2 | Quantum Fisher information approach

As in classical estimation theory, the Fisher approach focuses around the Cramer-Rao theorem. In quantum mechanics we can obtain a lower bound for the MSE as in Eq. (6.18). However, the procedure has some difficulties, which arise from the derivative of the density operator  $\rho(\lambda)$  with respect to the parameter  $\lambda$ , as we did in the proof of the

classical Cramér-Rao bound. The density operator may not commute for different parameter values,  $\rho(\lambda), \rho(\lambda')$ , therefore we can have troubles in defining the derivative operator.

However here we consider the symmetric logarithmic derivative operator  $L_\lambda$ , such that

$$L[\rho(\lambda)]\rho(\lambda) + \rho(\lambda)L[\rho(\lambda)] = 2\partial_\lambda\rho(\lambda). \quad (6.54)$$

Therefore we have, for the derivative appearing in Eq. (6.8)

$$\partial_\lambda p(x|\lambda) = \text{Tr}[\partial_\lambda\rho(\lambda)\Pi(x)] \quad (6.55a)$$

$$= \text{Re}\{\text{Tr}[\rho(\lambda)\Pi(x)L_\lambda]\}. \quad (6.55b)$$

The Fisher information  $F$  assumes the form

$$F[p(\lambda)] = \int dx \frac{\text{Re}\{\text{Tr}[\rho(\lambda)\Pi(x)L_\lambda]\}^2}{\text{Tr}[\rho(\lambda)\Pi(x)]}. \quad (6.56)$$

In order to find the best achievable value of the Fisher information we should optimize among all the possible POVM  $\{\Pi(x)\}$ .

$$\begin{aligned} F(p(\lambda)) &\leq \int dx \left| \frac{\text{Tr}[\rho(\lambda)\Pi(x)L_\lambda]}{\sqrt{\text{Tr}[\rho(\lambda)\Pi(x)]}} \right|^2 \\ &= \int dx \left| \text{Tr} \left[ \frac{\sqrt{\rho(\lambda)}\sqrt{\Pi(x)}}{\sqrt{\text{Tr}[\rho(\lambda)\Pi(x)]}} \sqrt{\Pi(x)}L_\lambda\sqrt{\rho(\lambda)} \right] \right|^2 \\ &\leq \int dx \text{Tr}[\Pi(x)L_\lambda\rho(\lambda)L_\lambda] \\ &= \text{Tr}[L_\lambda\rho(\lambda)L_\lambda] = \text{Tr}[\rho(\lambda)L_\lambda^2]. \end{aligned} \quad (6.57)$$

We define the last line of the inequality above the quantum Fisher information (QFI)

$$H(\lambda) = \text{Tr}[\rho(\lambda)L_\lambda^2], \quad (6.58)$$

which depends on the state and on the parameter to be estimated. Thus, we can write the quantum Cramér-Rao bound as

$$\text{Var}(\lambda) \geq \frac{1}{NH[\rho(\lambda)]}, \quad (6.59)$$

where  $N$  is the number of repeated measurements. It's important to note that the QFI does not depend on the particular measure we choose, but only on the dependence of

the state upon the parameter  $\lambda$ . Classical Fisher information is always below the QFI. Hence the QFI approach aims to find the estimator whose Fisher information saturates the Quantum Cramér Rao-bound, so that the measurement is optimal and the variance is lowered to its minimum. This operation can be done globally but is more often performed locally, looking for the small perturbation around a supposed true value  $\lambda$ .

### 6.2.3 | Comparison between Quantum Fisher and Bayes approaches.

The equation (6.59) gives us the maximum information we could ever extract from the system  $\rho(\lambda)$  and the minimum variance we could obtain in the estimation of the parameter  $\lambda$ . We stress again the fact that this equation doesn't depend on the particular choice of the estimator. Moreover, the Fisher approach tells us that the best estimator is the one whose classical Fisher information equals the QFI.

In the Bayesian approach we seek to find the estimator that minimizes a certain cost. But even if what we want to minimize is the variance, we still start from completely separated argument that make very difficult the comparison between the two approaches. In the Bayesian approach the variance is minimized averaging above all the possible true values for  $\lambda$ .

Let's suppose we calculated the QFI for the system  $\rho(\lambda)$  and contemporary we have provided one of the possible solutions to the minimization problems in Eqs. (6.33a) and (6.33b). If the cost function is the mean square error expressed in Eq. (6.5) we can use the Personick solution [42]. We call  $\hat{M}$  the MMSE operator for the parameter  $\lambda$  we want to estimate. Here  $\hat{M}$  is a real hermitian operator  $\hat{M} = \sum_{i,j} m_{i,j} |i\rangle\langle j|$  and  $\{|i\rangle\}$  is a basis of the density operator  $\rho_\lambda$ . After the experiment and the measurement we are able to find the posterior probability distribution given by:

$$p(i|\lambda) = \langle i|\rho_\lambda|i\rangle. \quad (6.60)$$

We can now calculate the classical Fisher information for the just obtained posterior probability  $p(i|\lambda)$  and we call it  $F_0$  and compare it with the QFI for  $\rho(\lambda)$ . Those values are unlikely to be the same, but the procedure doesn't stop here. We now recalculate a new MMSE operator  $\hat{M}_1$  with a new prior probability function  $p(i|\lambda)$  and calculate a new classical Fisher information  $F_1$ . The latter is going to be closer to the QFI  $h_\lambda$  than  $F_0$  and if we repeat this procedure enough times, we will get always closer to the QFI, reaching it in the limit of  $N \rightarrow \infty$  experiments. This property is called asymptotic efficiency.

## 6.3 | Bayesian estimation of the optomechanical coupling strength

This section contains our contributions to the Bayesian approach of quantum estimation theory applied to a simple optomechanical system composed by a cavity and a mechanical oscillator coupled together. The dynamics of the system follows the full non-linear optomechanical Hamiltonian ( $\hbar = 1$ )

$$\hat{H}(g) = \omega_c \hat{a}^\dagger \hat{a} + \omega_m \hat{b}^\dagger \hat{b} + g \hat{a}^\dagger \hat{a} (\hat{b}^\dagger + \hat{b}), \quad (6.61)$$

where we have stressed the dependence upon the coupling constant  $g$ . Our goal is to find the minimum mean square error measurement  $\hat{M}_{\min}$  for the estimation of the parameter  $g$ . However, we need to stress the fact that any feasible experiment will perform measurements on the optical field and not on the whole system. Therefore we will be interested in the in the field density operator obtained tracing out the mechanical system. In Chapter 2 we have given the field density operator  $\rho_F$  in the form

$$\hat{\rho}_F = \text{tr}_{\text{mech}} \{ |\Psi(t)\rangle \langle \Psi(t)| \} = \sum_{n,m=0}^{\infty} A_{n,m} |n\rangle_c \langle m| \quad (6.62)$$

with

$$A_{n,m} = a_n a_m^* e^{-g^2 f_{n,m}^{(2)}(t) + g f_{n,m}^{(1)}(t) - f_{n,m}^{(0)}(t)}, \quad (6.63)$$

where the explicit forms of  $f_{n,m}^{(2)}$ ,  $f_{n,m}^{(1)}$  and  $f_{n,m}^{(0)}$  depend on the initial state  $|\text{psi}\rangle_m$  of the mechanical oscillator. We assumed the initial optical density operator to be  $\sum_n a_n a_m^* |n\rangle \langle m|$ . We start from Eq. (6.45), which express  $\hat{M}_{\min}$  as a function of the operators  $\hat{\Gamma}_k$ , with  $k = 0, 1, 2$  defined in Eq. (6.40). The average minimum cost is given by Eq. (6.44). We can evaluate all the  $\hat{\Gamma}_k$  by using the form of  $\hat{\rho}_F(g)$  in Eq. (2.30), thus obtaining ( $k = 0, 1, 2$ )

$$\hat{\Gamma}_k = \sum_{n,m=0}^{\infty} a_n a_m^* A_{n,m}^{(k)} \exp(-\gamma_{n,m}) |n\rangle_c \langle m|, \quad (6.64)$$

with

$$A_{n,m}^{(0)} = \frac{1}{\sigma^j}, \quad (6.65a)$$

$$A_{n,m}^{(1)} = \frac{g_0 + f_{n,m}^{(1)}(t)\sigma^2}{\sigma^3}, \text{ and} \quad (6.65b)$$

$$A_{n,m}^{(2)} = \frac{\left(g_0 + f_{n,m}^{(1)}(t)\sigma^2\right)^2 + \sigma^2\sigma'^2}{\sigma^5}, \quad (6.65c)$$



where we have also introduced

$$\gamma_{n,m} = \{2g_0^2 f_{n,m}^{(2)}(t) - 2g_0 f_{n,m}^{(1)}(t) + 2f_{n,m}^{(0)}(t)\sigma'^2 - [f_{n,m}^{(1)}(t)]^2\sigma^2\} / (2\sigma'^2), \quad (6.66a)$$

$$\sigma'^2 = 2f_{n,m}^{(2)}(t)\sigma^2 + 1. \quad (6.66b)$$

The simplest non-trivial case results when  $a_n = 0$  for  $n > 1$  in Eq. (2.23). In order to maximize the absolute values of the off-diagonal elements of the density matrix we choose  $a_0 = a_1 = 1/\sqrt{2}$ . This specific choice is due to the fact that the unknown parameter  $g$  is only present in the off-diagonal elements, as can be seen from Eqs. (2.32). Here, the estimate  $\tilde{g}$  is simply one of the two eigenvalues of  $\hat{M}_{\min}$ , which turn up as a result of applying the two projective measurements defined by their accompanied eigenvectors. Furthermore, we need to define the a priori probability density function  $z(g)$  of the estimanda  $g$ . We choose  $g$  to be normal distributed around  $g_0$  with variance  $\sigma$ , i.e.

$$z(g) = \frac{1}{\sqrt{2\pi\sigma^2}} e^{-\frac{(g-g_0)^2}{2\sigma^2}}. \quad (6.67)$$

We set

$$g_0 = \frac{\omega_c}{L} \sqrt{\langle \hat{x}^2 \rangle_0} = \frac{\omega_c}{L} \sqrt{\frac{\hbar}{2m\omega_m}}, \text{ and} \quad (6.68a)$$

$$\sigma^2 = \left(\frac{\omega_c}{L}\right)^2 \sqrt{\langle \hat{x}^4 \rangle_0 - \langle \hat{x}^2 \rangle_0^2} = \left(\frac{\omega_c}{L}\right)^2 \frac{\hbar}{\sqrt{2}m\omega_m}, \quad (6.68b)$$

where  $L$  is the length of the cavity,  $m$  is the mass of the mechanical oscillator, and  $\langle \hat{A} \rangle_0$  is the expectation value of operator  $\hat{A}$ , acting only on the Hilbert space of the mechanical oscillator, in the ground state [8, 9]. For the sake of simplicity we perform our calculations in the rotating frame of the single-mode field, i.e.,  $\hat{\rho}_F \rightarrow \hat{U}\hat{\rho}_F\hat{U}^\dagger$  with  $\hat{U} = \exp\{-i\omega_c t \hat{a}^\dagger \hat{a}\}$ .

### 6.3.0.1 | Coherent state

We determine  $\hat{M}_{\min}$  from the  $\hat{\Gamma}_k$  in Eq. (6.64) by using Eq. (6.45). One can obtain analytical results taking the explicit forms of the functions  $f^{(i)}$  for the coherent state (see Eqs. (2.32)), (with  $i = 0, 1, 2$ ) and substituting them in Eq. (6.64); however, due to their complex structure we omit their explicit presentation here. Instead, we focus on numerical solutions. First, we investigate the average minimum cost of error  $\bar{C}_{\min}$ ; Fig. 6.1 shows  $\bar{C}_{\min}$  as a function of time, which decreases until it reaches its minimum and then returns asymptotically to its initial value, which is equal to  $\sigma^2$ . At  $t = 0$ , where no interaction occurred, the eigenvalues of  $\hat{M}_{\min}$  are  $g_0$  and zero. The probability of measuring the eigenvalue zero is zero and therefore the estimate is  $g_0$ . It is immediate from the

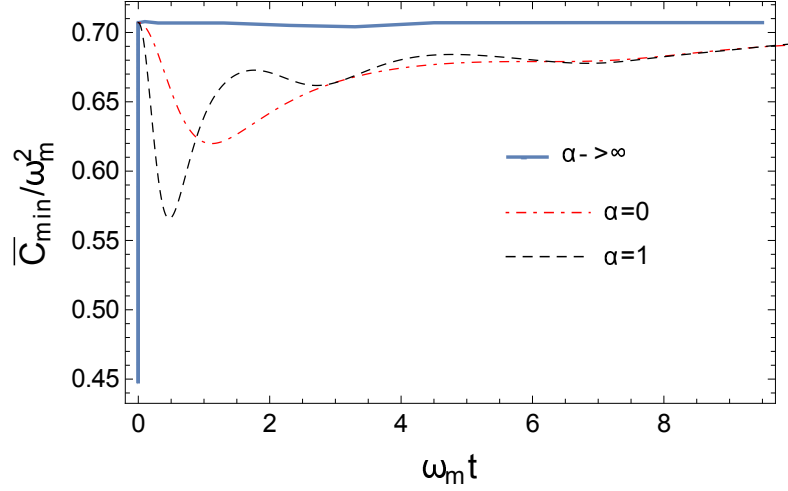


Figure 6.1: The average minimum cost of error  $\bar{C}_{\min}/\omega_m^2$ , as a function of  $\omega_m t$ . We consider the amplitude  $\alpha$  of the initial coherent state of the mechanical oscillator to be real; see Eqs. (2.32). We set  $g_0/\omega_m = 1$  and  $\sigma/\omega_m = 2^{-1/4}$ . All curves are characterized by one global minimum which decreases with increasing  $\alpha$ .

form of the prior probability distribution  $z(g)$  in Eq. (6.67) that the average minimum cost of error is  $\sigma^2$ , or simply the variance of  $z(g)$ , at  $t = 0$ .

In the opposite limit,  $t \rightarrow \infty$ , the average minimum cost of error  $\bar{C}_{\min}$  is also  $\sigma^2$ ; however, the estimates or the eigenvalues of  $\hat{M}_{\min}$  are  $g_0$ , as can be seen in Fig. 6.2. This means that for long interaction times the inference of the parameter  $g$  from the measurement data only yields the mean  $g_0$  of the probability distribution  $z(g)$ . Since the average minimum cost of error attains its maximum at both  $t = 0$  and  $t \rightarrow \infty$ , we are going to neglect these situations and focus on intermediate times, when  $\bar{C}_{\min}$  decreases. The fact that average minimum cost of error reaches a minimum at a finite time implies the existence of a particular duration for the interaction that yields the greatest amount of information on  $g$ . For each set of parameters, we can determine the time  $t^*$  as the time when  $\bar{C}_{\min}$  reaches its minimum value. We can work backwards to obtain the specific  $\hat{M}_{\min}^* = \hat{M}_{\min}(t = t^*)$  to be measured, which is the measurement that best protects against information loss.

The value of  $\alpha$ , the amplitude of the initial mechanical oscillator coherent state, has a strong influence on the value of  $t^*$ . We show in Fig. 6.1 that the limit  $\alpha \rightarrow \infty$ , with  $\alpha \in \mathbb{R}$ , results in  $t^* = 0$  and the lowest observed value for  $\bar{C}_{\min} \approx 0.636\sigma^2$ . However, the eigenvalues of  $\hat{M}_{\min}^*$  are still zero and  $g_0$  at  $t = 0$ , from which it follows that highly excited initial states of the mechanical oscillator result in an estimation scenario where

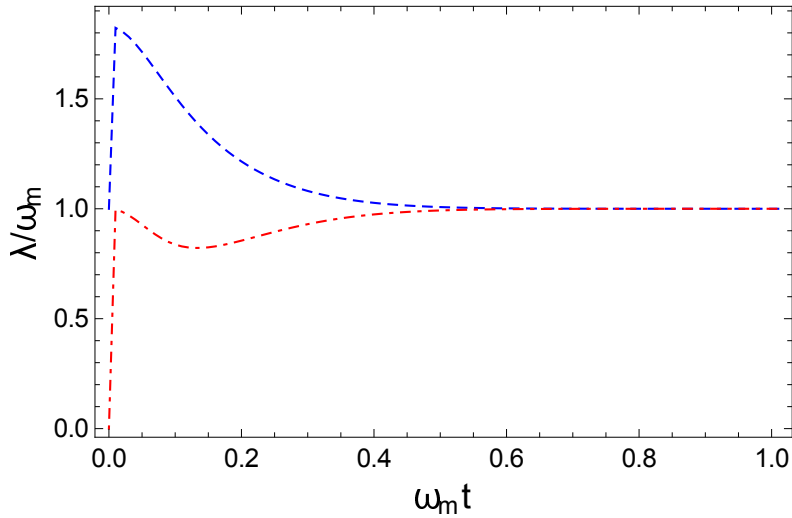


Figure 6.2: The two eigenvalues of the operator  $\hat{M}_{\min}$  to be measured, shown as a function of  $\omega_m t$ . We set  $g_0/\omega_m = 1$ ,  $\sigma/\omega_m = 2^{-1/4}$ , and  $\alpha = 0$ . The initial value of the two eigenvalues are  $g_0$  and zero. There is a jump in these values when  $\omega_m t$  becomes larger than zero, i.e., when the interaction is turned on. For large interaction times, the eigenvalues tend to the same value  $g_0$ .

measuring  $M_{\min}^*$  merely reinforces prior knowledge and yields only the mean  $g_0$  of the prior probability distribution  $z(g)$ . In the next step, we investigate the position of the minimum for  $\alpha \in \mathbb{C}$ , to deduce its dependence on the phase of  $\alpha$ . Fig. 6.3 shows a shift of  $t^*$  towards higher values and an increase of the minimum value of  $\bar{C}_{\min}$  as the imaginary part of  $\alpha$  gets larger. We see that the case with very large  $|\alpha|$  may lead to inconclusive measurement scenarios because  $\bar{C}_{\min}$  is only significantly smaller than its maximum for a short time period. This observation is of significance in the discussion of initial thermal states, since it implies that higher initial temperatures will degrade the quality of the estimation procedure.

Let us turn our attention to  $\hat{M}_{\min}^*$ , which has already been defined as the optimal measurement, made at the time  $t^*$  that minimizes the average minimum cost of error. Every outcome of the measurement of  $\hat{M}_{\min}^*$  is an estimate of  $g$ . The most important quantity for a possible experimental implementation is the average estimate at  $t = t^*$

$$h(g) = \text{tr}\{\hat{M}_{\min}^* \hat{\rho}_F(g)\}. \quad (6.69)$$

Thus, measurement data determine the value of  $h(g)$ . From this, one may deduce the value of  $g$ . In Fig. 6.4, we show the curves of  $h(g)$  for different values of the real parameter  $\alpha$ .  $t^*$  is independently calculated for each specific initial state. When  $\alpha = 0$ , the

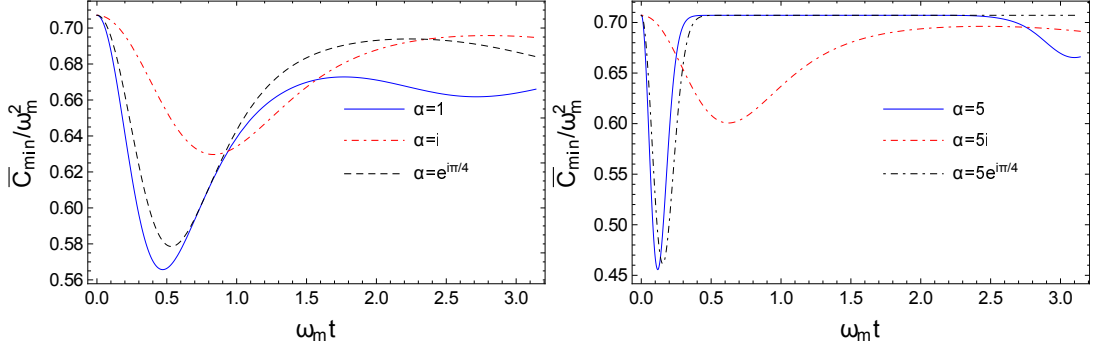


Figure 6.3: The average minimum cost of error  $\bar{C}_{\min}/\omega_m^2$  as a function of  $\omega_m t$ . We set  $g_0/\omega_m = 1$  and  $\sigma/\omega_m = 2^{-1/4}$ . The imaginary part of  $\alpha$  shifts the value of the minimum to the right. Minima occurring at longer times are also less pronounced. Top:  $|\alpha| = 1$ . Bottom:  $|\alpha| = 5$ .

average estimator is an even function of  $g$ . This is a direct consequence of our particular choice of the cost function (6.36), which is also an even function.

Before turning our attention to initial thermal states, let us conclude this section by summarizing the measurement procedure. Given a specific initial state, the system is allowed to evolve for a time  $t^*$ . At this point in time, one would conduct a measurement of  $\hat{M}_{\min}^*$ . This process is repeated, obtaining an average measurement,  $h(g)$ . Using calculations of the kind shown in Fig. 6.4 allows one to work backward and obtain  $g$ .

### 6.3.0.2 | Thermal state

Similar to the case for an initial coherent state for the mechanical oscillator, an initial thermal state exhibits an average minimum cost of error  $\bar{C}_{\min}$  that is equal to  $\sigma^2$  for  $t = 0$  and  $t \rightarrow \infty$ . In these limits, the eigenvalues of  $\hat{M}_{\min}$  have the same values as for the coherent state, so our earlier observations hold for the present case as well. In Fig. 6.5, we show the time dependence of  $\bar{C}_{\min}$  and the average estimator  $h(g)$  for different average phonon numbers  $n_{\text{th}}$  obtained from the density matrix (2.30) with the help of the expressions in Eq. (2.45). One can observe that an increase in the value of  $n_{\text{th}}$  increases  $\bar{C}_{\min}$  for most times, while it does not induce any significant change in the average estimator  $h(g)$ . Furthermore, the oscillations seen in Fig. 6.1 for longer interaction times are damped by the increase of  $n_{\text{th}}$ . Thus, in the context of this optimal estimation scenario the lower the temperature  $T$  of the mechanical oscillator, the less sensitive is the average minimum cost of error. This provides additional impetus to one of the central pillars of optomechanical experiments, which is to cool down the mechanical oscillator

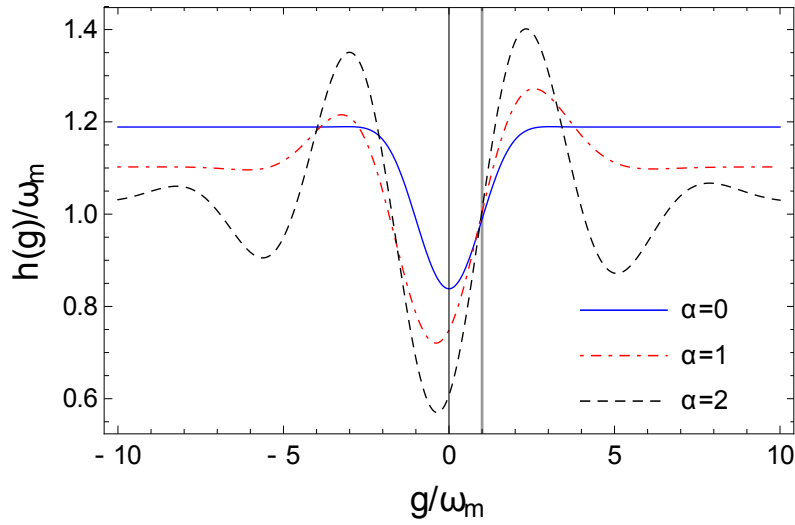


Figure 6.4: The average estimator  $h(g)/\omega_m$  as a function of  $g/\omega_m$ . We consider the amplitude  $\alpha$  of the initial coherent state of the mechanical oscillator to be real. We set  $g_0/\omega_m = 1$  and  $\sigma/\omega_m = 2^{-1/4}$ . The time is such that the average minimum cost of error  $\bar{C}_{\min}$  attains its minimum. The mean value  $g_0$  of the prior probability distribution function  $z(g)$  is depicted by a vertical line.

to temperatures as low as possible [8].

### 6.3.0.3 | Squeezed state

We make use of Eqs. (2.55) to construct the density matrix in Eq. (2.31). The properties of  $\bar{C}_{\min}$  and  $\hat{M}_{\min}$  for  $t = 0$  and  $t \rightarrow \infty$  are essentially the same as in the two cases discussed above. Let us recall that, in our discussion above, we showed that for an initial coherent state  $|\alpha\rangle$  of the mechanical oscillator large  $|\alpha|^2$  reduces the average minimum cost of error  $\bar{C}_{\min}$ , but at the expense of pushing the minimum towards very short interaction times, which leads to inconclusive measurement scenarios. In our discussion above we also identified a preferable scenario where  $|\alpha|^2$  is large but with approximately equal real and imaginary parts. In the case of initial squeezed states, Fig. 6.6 shows an interesting effect, namely the squeezing parameter  $\zeta$  may also reduce the average minimum cost of error. The average estimator  $h(g)$  is again an even function, this time because we have chosen two squeezed states without displacement. The cost of error  $\bar{C}_{\min}$  attains a minimum when the squeezing angle lies between the position and momentum quadratures of the oscillator. This can be understood as an effective continuous sampling of the noise ellipse during the evolution of the system for the first fraction of a mechanical

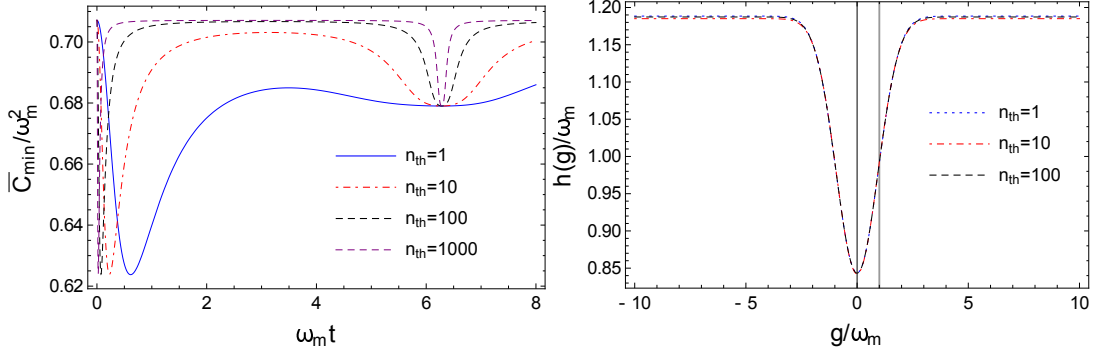


Figure 6.5: Left: The average minimum cost of error  $\bar{C}_{\min}/\omega_m^2$  as a function of  $\omega_m t$ . We set  $g_0/\omega_m = 1$  and  $\sigma/\omega_m = 2^{-1/4}$ . The oscillations at  $\omega_m t \approx 2\pi$  are damped by the increase of the average phonon number  $n_{\text{th}}$ . Right: The average estimator  $h(g)/\omega_m$  as a function of  $g/\omega_m$ . The time is such that the average minimum cost of error  $\bar{C}_{\min}$  attains its minimum. The mean value  $g_0$  of the prior probability distribution function  $z(g)$  is depicted by a vertical line.

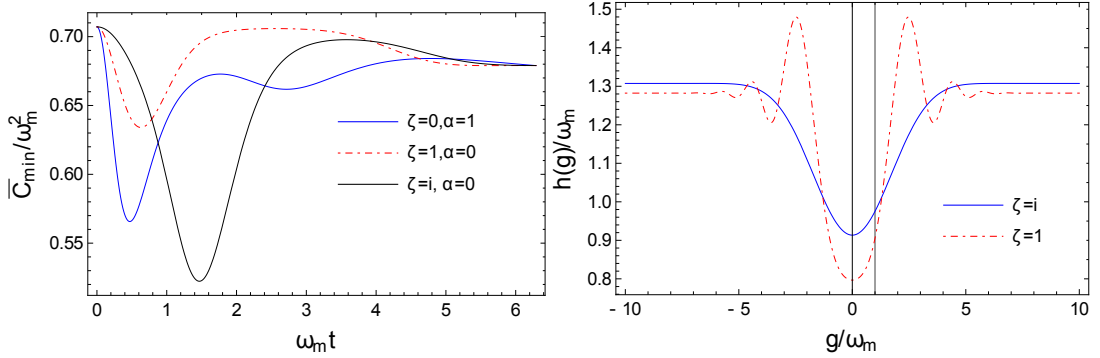


Figure 6.6: Left: The average minimum cost of error  $\bar{C}_{\min}/\omega_m^2$  as a function of  $\omega_m t$ . We set  $g_0/\omega_m = 1$  and  $\sigma/\omega_m = 2^{-1/4}$ . The case without squeezing, i.e.  $\zeta = 0$ , has identical behavior to that in Fig. 6.1. Right The average estimator  $h(g)/\omega_m$  as a function of  $g/\omega_m$  for  $\alpha = 0$ . The time is such that the average minimum cost of error  $\bar{C}_{\min}$  attains its minimum. The mean value  $g_0$  of the prior probability distribution function  $z(g)$  is depicted by a vertical line.

time-period. Squeezing along either position or momentum quadrature will result in a greater uncertainty, whereas squeezing at an angle half-way between these two quadratures allows the measurement to take place with the least possible uncertainty.

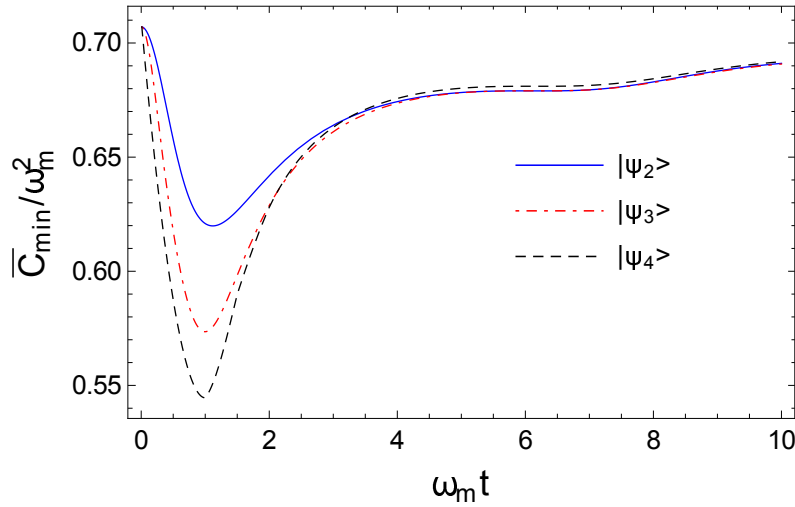


Figure 6.7: The average minimum cost of error  $\bar{C}_{\min}/\omega_m^2$  as a function of  $\omega_m t$  for different initial states of the optical field. We set  $g_0/\omega_m = 1$ ,  $\sigma/\omega_m = 2^{-1/4}$ , and the mechanical oscillator initially in the ground state.  $|\psi_N\rangle_c$ , defined in Eq. (6.70), is the initial optical state.

#### 6.3.0.4 | Different initial photonic states

So far we have discussed in detail the estimation problem of the optomechanical coupling  $g$  for the simplest initial state of the single-mode field. In this section, we consider the situation where the optical field may have more than one photon, and where the mechanical oscillator is initially in the ground state. Since  $\hat{\rho}_F(g)$  depends on  $g$  only in its off-diagonal elements, we therefore set the amplitude of all participating photon number states to be equal. This ensures the maximum allowed absolute value for the off-diagonal elements in the density matrix. Due to the added complexity of dealing with Eq. (6.45) we restrict our comparison to the following family of initial states of the optical field, indexed by the parameter  $N = 2, 3, 4$ :

$$|\psi_N\rangle_c = \sum_{n=0}^{N-1} a_n |n\rangle_c = \frac{1}{\sqrt{N}} \sum_{n=0}^{N-1} |n\rangle_c. \quad (6.70)$$

Our earlier investigations consider exclusively the case  $N = 2$ .

Fig. 6.7 shows that the average minimum cost of error is reduced as the number of the photons in the initial state increases. This can be understood by examining carefully the Hamiltonian in Eq. (6.61), which reveals that the interaction between the single mode field and the mechanical oscillator gets stronger with increased number of participating photons. Thus, we have a better chance to estimate the optomechanical coupling  $g$ . The

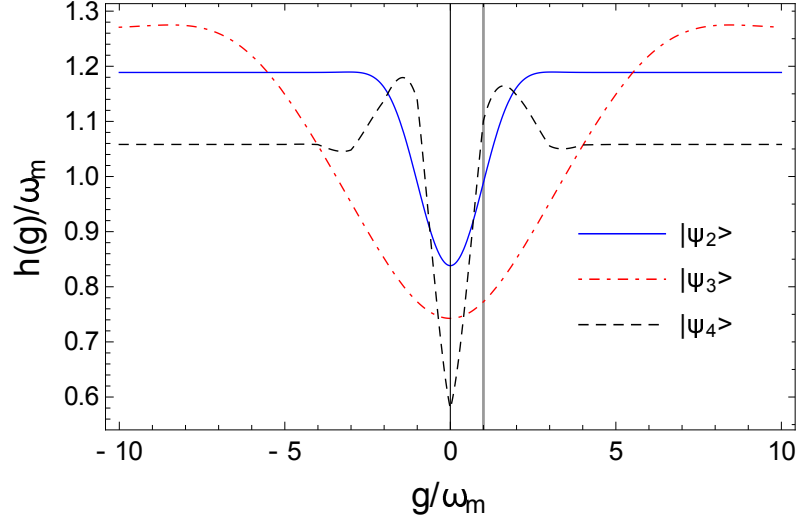


Figure 6.8: The average estimator  $h(g)/\omega_m$  as a function of  $g/\omega_m$ . We set  $g_0/\omega_m = 1$ ,  $\sigma/\omega_m = 2^{-1/4}$ , and the mechanical oscillator initially in the ground state. The time is such that the average minimum cost of error  $\bar{C}_{\min}$  attains its minimum. The mean value  $g_0$  of the prior probability distribution function  $z(g)$  is depicted by a vertical line.

time  $t^*$  when  $\bar{C}_{\min}$  attains its minimum does not change markedly with  $N$ . We have also calculated the average estimator  $h(g)$  for  $t^*$ ; Fig. 6.8 shows the three curves obtained. Since the mechanical oscillator is initially in the ground state in every case, all curves are even.

## 6.4 | Quantum Cramér–Rao-type inequality

In the preceding sections we discussed the properties of the optimum Hermitian operator  $\hat{M}_{\min}$  which minimizes the average cost in Eq. (6.3), and the eigenvalues of which are the estimates of the unknown optomechanical coupling strength  $g$ . An important task is to find out the accuracy with which  $g$  can be estimated. We would like to employ here the quantum Cramér–Rao inequality, which is widely used in the case of unbiased estimators [168, 169]. In the present case, however, we have a biased estimator

$$\text{tr}\{\hat{\rho}_F(g)(\hat{M}_{\min} - g\hat{I})\} = f(g), \quad (6.71)$$

where  $f(g)$  is the bias of the estimation and is not necessarily equal to zero. To properly account for this situation, we have to review the derivation of the Cramér–Rao inequality.



Let us first, however, deal with an extra issue regarding the derivative of the density matrix  $\hat{\rho}_F(g)$  with respect to the parameter  $g$ . For concreteness, let us recall the density matrix  $\hat{\rho}_F(g)$  from Eq. (2.30), together with Eqs. (2.32), and observe that

$$\hat{\rho}_F(g) = \sum_{n,m=0}^{\infty} a_n a_m^* e^{-a_1(n-m)^2 + a_2(n^2 - m^2) - a_3(n-m)} |n\rangle \langle m|, \quad (6.72)$$

where

$$a_1 = \frac{g^2}{\omega_m^2} [1 - \cos(\omega_m t)], \quad (6.73)$$

$$a_2 = i \frac{g^2}{\omega_m^2} [\omega_m t - \sin(\omega_m t)], \text{ and} \quad (6.74)$$

$$a_3 = i\omega_c t - \frac{g}{\omega_m} [\alpha^* (1 - e^{i\omega_m t}) - \alpha (1 - e^{-i\omega_m t})]. \quad (6.75)$$

Therefore,

$$\frac{\partial \hat{\rho}_F(g)}{\partial g} = -\frac{\partial a_1}{\partial g} [\hat{a}^\dagger \hat{a}, [\hat{a}^\dagger \hat{a}, \hat{\rho}_F(g)]] + \frac{\partial a_2}{\partial g} [(\hat{a}^\dagger \hat{a})^2, \hat{\rho}_F(g)] - \frac{\partial a_3}{\partial g} [\hat{a}^\dagger \hat{a}, \hat{\rho}_F(g)] = \mathcal{L}[\hat{\rho}_F(g)], \quad (6.76)$$

which demonstrates that  $\mathcal{L}[\hat{\rho}_F(g)]$  does not have the form of either a right logarithmic or a symmetrized logarithmic derivative of the density matrix  $\hat{\rho}_F(g)$  by default. Therefore, we need the spectral decomposition of  $\hat{\rho}_F(g)$  to construct at least the symmetrized logarithmic derivative operator, which is very challenging due to the fact that we have to deal with states defined on an infinite dimensional Hilbert space. Although this problem can be easily circumvented in numerical simulations, here we are motivated to derive an analytically expressible lower bound. This situation will result in a departure from the standard analysis [169]. In the standard proof, a Cauchy–Schwarz–Bunyakovsky inequality is employed, which suggests that in our new situation we would have to introduce the operator  $\hat{\rho}_F^{-1/2}(g)$ . This operator does not exist when the spectrum of  $\hat{\rho}_F(g)$  contains zero (e.g., a pure state). We avoid this situation by following a different path.

In order to derive a lower bound for the mean-squared error,

$$\text{MSE}(\hat{M}_{\min}) = \text{tr} \left\{ \hat{\rho}_F(g) (\hat{M}_{\min} - g\hat{I})^2 \right\}, \quad (6.77)$$

we define

$$x_1(g) = \text{tr} \left\{ \hat{\rho}_F^2(g) \hat{M}_{\min} \right\}, \quad (6.78)$$

and then we differentiate both sides with respect to the parameter  $g$ ,

$$\text{tr} \left\{ \left( \frac{\partial \hat{\rho}_F(g)}{\partial g} \hat{\rho}_F(g) + \hat{\rho}_F(g) \frac{\partial \hat{\rho}_F(g)}{\partial g} \right) \hat{M}_{\min} \right\} = x_1'(g). \quad (6.79)$$

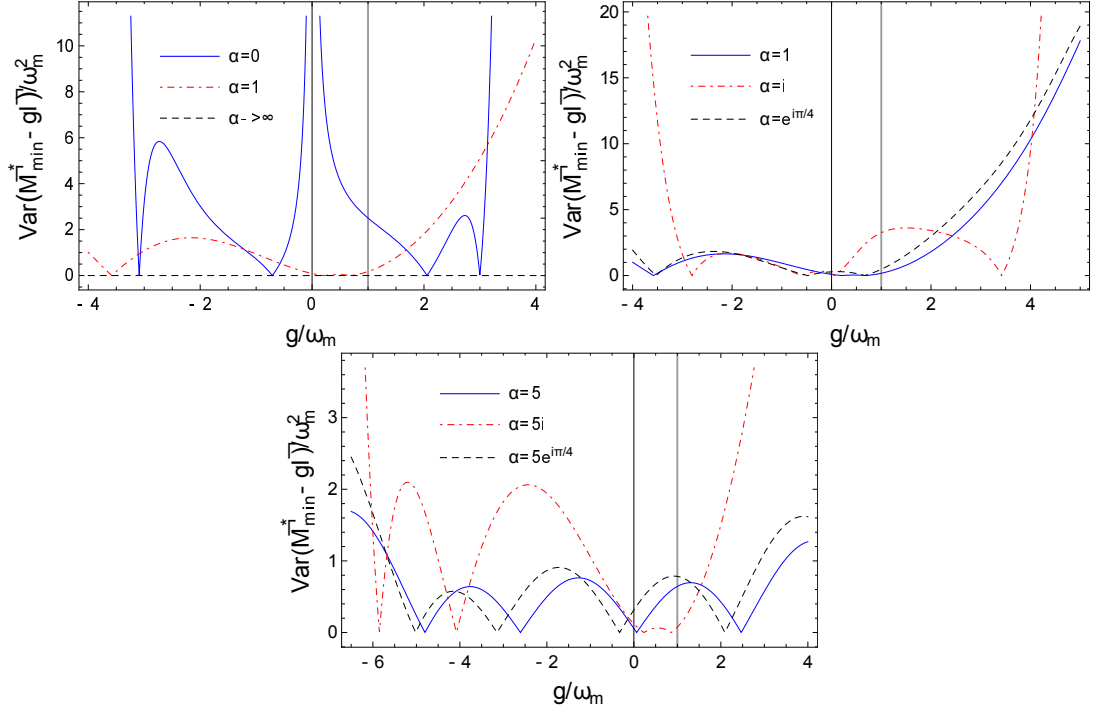


Figure 6.9: The lower bound of the mean-squared error as a function of  $g/\omega_m$ . We set  $g_0/\omega_m = 1$  and  $\sigma/\omega_m = 2^{-1/4}$ . The time is such that the average minimum cost of error  $\bar{C}_{\min}$  attains its minimum. Compare the top figure with Fig. 6.1, and the bottom two with Fig. 6.3. See also Fig. 6.4 for the corresponding average estimator.

We also define  $x_2(g) = \text{tr}\{\hat{\rho}_F^2(g)\}$ , and find

$$\text{tr}\left\{\left(\frac{\partial\hat{\rho}_F(g)}{\partial g}\hat{\rho}_F(g) + \hat{\rho}_F(g)\frac{\partial\hat{\rho}_F(g)}{\partial g}\right)g\hat{I}\right\} = gx_2'(g). \quad (6.80)$$

Subtracting Eq. (6.80) from Eq. (6.79), we obtain

$$\begin{aligned} \text{tr}\left\{\left(\frac{\partial\hat{\rho}_F(g)}{\partial g}\hat{\rho}_F(g) + \hat{\rho}_F(g)\frac{\partial\hat{\rho}_F(g)}{\partial g}\right)(\hat{M}_{\min} - g\hat{I})\right\} &= x_1'(g) - gx_2'(g) \\ &= x(g), \end{aligned} \quad (6.81)$$

where the last equality defines the function  $x(g)$ . We make use of Eq. (6.76) and write Eq. (6.81) as

$$\text{tr}\{(\mathcal{L}[\hat{\rho}_F]\hat{\rho}_F + \hat{\rho}_F\mathcal{L}[\hat{\rho}_F])(\hat{M}_{\min} - g\hat{I})\} = x(g), \quad (6.82)$$

where for the sake of notational simplicity we have omitted the argument  $g$  of  $\hat{\rho}_F(g)$ .

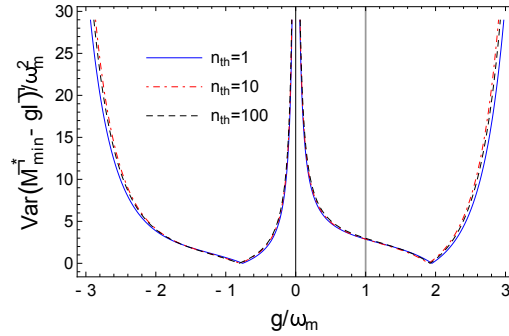


Figure 6.10: The lower bound of the mean-squared error as a function of  $g/\omega_m$ . The curves were evaluated using the method and the parameters of Fig. 6.5.

Before continuing, we discuss an issue connected with the boundedness of  $\hat{\rho}_F$ . The Banach space of the Hilbert–Schmidt operators is defined as

$$\mathcal{B}_2(\mathcal{H}) := \left\{ \hat{X} \in \mathcal{B}(\mathcal{H}) : \text{tr}\{\hat{X}^\dagger \hat{X}\} < \infty \right\}, \quad (6.83)$$

where  $\mathcal{B}(\mathcal{H})$  is Banach space of all bounded operators defined on the Hilbert space  $\mathcal{H}$ . The space  $\mathcal{B}_2(\mathcal{H})$  with the inner product

$$\langle A, B \rangle = \text{tr}\{A^\dagger B\}, \quad (6.84)$$

where  $A, B \in \mathcal{B}_2(\mathcal{H})$ , is a Hilbert space [170]. The Cauchy–Schwartz–Bunyakovsky inequality reads

$$|\text{tr}\{A^\dagger B\}| \leq \sqrt{\text{tr}\{A^\dagger A\} \text{tr}\{B^\dagger B\}}. \quad (6.85)$$

In our case the Hilbert space is the symmetric Fock space, i.e.,  $\mathcal{H} = \Gamma_s(\mathbb{C})$ , and  $\mathcal{L}$  contains powers of  $\hat{a}^\dagger \hat{a}$ , which is an unbounded operator. This clearly shows that our proof is limited to density matrices which fulfill the conditions  $\hat{\rho}_F^{1/2} (\hat{a}^\dagger \hat{a})^2 \hat{\rho}_F, \hat{\rho}_F^{1/2} \hat{a}^\dagger \hat{a} \hat{\rho}_F \hat{a}^\dagger \hat{a} \in \mathcal{B}_2(\Gamma_s(\mathbb{C}))$ . These conditions, together with the cyclic property of the trace, imply that  $\hat{\rho}_F^{1/2} \mathcal{L}(\hat{\rho}_F)$  is a Hilbert–Schmidt operator. Similarly, the condition  $\hat{\rho}_F^{1/2} \hat{M}_{\min} \in \mathcal{B}_2(\Gamma_s(\mathbb{C}))$  may restrict further the set of the density matrices. In other words, there are restrictions on the choice of the  $a_n$  in the initial state Eq. (2.23). In the case of finite dimensional examples, i.e, if there exists an  $N > 0$  such that  $a_n = 0$  for  $n \geq N$ , these complications do not arise, because all matrices are Hilbert–Schmidt operators. This is the typical case encountered in numerical simulations.

Now, provided that  $\hat{\rho}_F^{1/2} \mathcal{L}[\hat{\rho}_F]$  and  $\hat{\rho}_F^{1/2} \hat{M}_{\min}$  are Hilbert–Schmidt operators, Eq. (6.82) implies

$$|x(g)| = \left| \text{tr}\left\{ \mathcal{L}(\hat{\rho}_F) \hat{\rho}_F^{1/2} \hat{\rho}_F^{1/2} (\hat{M}_{\min} - g\hat{I}) \right\} + \text{tr}\left\{ \hat{\rho}_F^{1/2} \mathcal{L}(\hat{\rho}_F) (\hat{M}_{\min} - g\hat{I}) \hat{\rho}_F^{1/2} \right\} \right|. \quad (6.86)$$

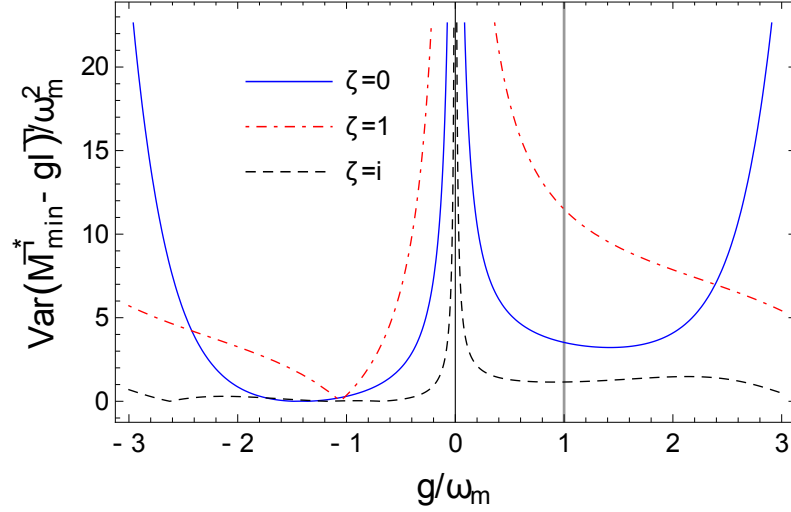


Figure 6.11: The lower bound of the mean-squared error as a function of  $g/\omega_m$ . The curves were evaluated using the method and the parameters of Fig. 6.6.

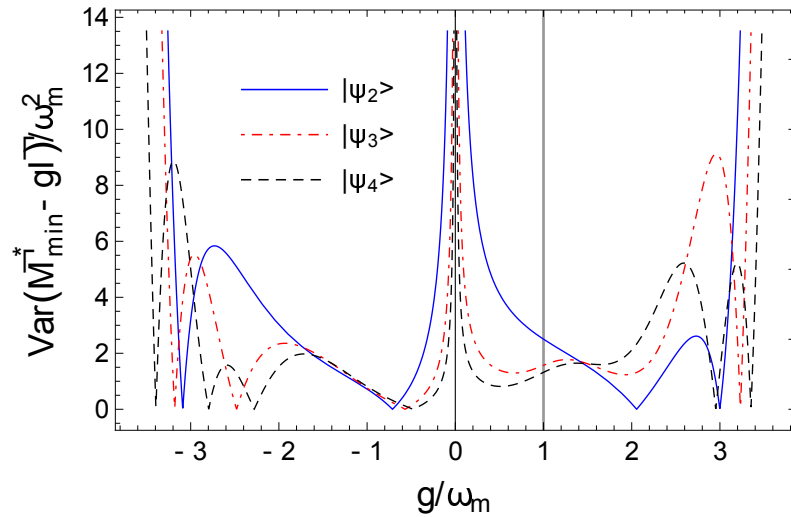


Figure 6.12: The lower bound of the mean-squared error as a function of  $g/\omega_m$ . The curves were evaluated using the method and the parameters of Fig. 6.8.

Applying first the subadditivity of the absolute value and then the Cauchy–Schwarz–Bunyakovsky inequality (6.85) twice, we find

$$|x(g)| \leq 2 \operatorname{tr} \left\{ \hat{\rho}_F (\mathcal{L}[\hat{\rho}_F])^2 \right\} \operatorname{Var}(\hat{M}_{\min} - g\hat{I}), \quad (6.87)$$

where we have used the fact that  $(\mathcal{L}[\hat{\rho}_F])^\dagger = \mathcal{L}[\hat{\rho}_F]$ , as can be deduced from Eq. (6.76). Finally, we obtain a lower bound for the mean-squared error

$$\operatorname{MSE}(\hat{M}_{\min}) \geq \frac{|x(g)|}{2 \operatorname{tr} \left\{ \hat{\rho}_F (\mathcal{L}[\hat{\rho}_F])^2 \right\}}. \quad (6.88)$$

The quantity on the right of this inequality is very similar to the standard quantum Cramér–Rao bound. In this expression, the function of  $x(g)$  in the numerator represents the fact that the estimator is biased, and includes information about the purity of the density matrix  $\hat{\rho}_F(g)$ . The denominator has a similar but slightly more complicated structure than the quantum Fisher information [171], due to our approach to finding the derivative of  $\hat{\rho}_F(g)$  with respect to the optomechanical coupling  $g$ .

We shall now apply the technique we just described to study the same cases as we did above, allowing us to study how the the mean-squared error behaves in each case.

#### 6.4.0.1 | Coherent state

We investigate numerically the lower bound of the mean-squared error. We consider  $g_0$  and  $\sigma$  to be the same as in Eqs. (6.68). In Fig. 6.9, we recall the results of Figs. 6.1 and 6.3, and show the behavior of the lower bound of the mean-squared error as a function of  $g/\omega_m$ . The most interesting feature occurs when  $|\alpha|$  grows, where the lower bound is the smallest. This may seem to suggest that measurement strategies perform better under these conditions. However, this in apparent contrast with our findings in Sec. 2.2.1. What we can deduce is that measurements made with large  $|\alpha|$  may simply return  $g_0$ , i.e., our prior expectation, for the value of the coupling strength. In such circumstances, we gain no information about the system; these scenarios are therefore to be avoided.

#### 6.4.0.2 | Thermal state

Let us consider again the parameters of Fig. 6.5, where we have seen that the average estimator is insensitive to the change of the average phonon number  $n_{\text{th}}$ , i.e., the change in the temperature of the mechanical oscillator. Here, we observe the same effect for the lower bound of the mean-squared error, (see Fig. 6.10). These findings indicate that

the accuracy of the measurements cannot be improved or worsened with the change of the  $n_{\text{th}}$ . However, we have demonstrated an increase in the average minimum cost of error as  $n_{\text{th}}$  is increasing. Therefore, in accordance with intuition, high temperatures once again lead to inconclusive estimation results.

#### 6.4.0.3 | Squeezed state

As we have seen in Fig. 6.6 for the average minimum cost of error, squeezing is beneficial in the sense of reducing the mean-squared error. In Fig. 6.11 we see the lower bound of the mean-squared error may also be reduced by squeezing, in a manner that depends highly on the squeezing angle as well as the magnitude of the squeezing. This is, once again, in accordance with our earlier arguments and with intuition.

#### 6.4.0.4 | Different initial photon states

Finally, we compare the lower bound of the mean-squared error for the three different initial single-mode field states given in Eq. (6.70), with the mechanical oscillator again assumed to be in its ground state. The time  $t^*$ , when the average minimum cost of error  $\bar{C}_{\text{min}}$  attains its minimum is taken to be the same as in Fig. 6.8. The lower bound of the mean-squared error, as shown in Fig. 6.12, generally decreases with the photon number states in the initial state. This is in agreement with our findings in Fig. 6.7, namely that the average minimum cost of error is reduced by the increase of the photon number states. This also suggests that the initial preparation of the optical field is crucial to the outcome of the estimation procedure, with an equally weighted superposition of many photon number states being preferable. For ranges of values of  $g$ , however, either this improvement with increasing  $N$  is not seen, or in some cases, the situation worsens as  $N$  increases.

We conclude from this qualitative assessment that preparation of initial states of both the optical field and mechanical oscillator is crucial to obtaining more precise measurement outcomes, and consequently better estimations of the optomechanical coupling strength.

## 6.5 | Optimal estimation of matter–field coupling strength in the dipole approximation

This section is taken from our paper [2]. Here we continue our investigations of the Bayesian-inference approach with a focus on one-parameter estimation scenarios in or-

der to gain a better insight into the properties of the estimators [1]. We shall consider the problem of estimating the dipole coupling of matter–field interactions [172]. Due to the widespread applications of these interactions in, e.g., quantum communication [74], a precise determination of the dipole coupling has increasing technological, as well as fundamental, relevance. While quantum electrodynamics gives a straightforward recipe for calculating this matter–field coupling [77], experimental limitations on precision inherently introduce probabilistic variations in this parameter. Therefore, the only way to gain some knowledge is to perform measurements on the physical system and obtain data, from which the value of the dipole coupling can be inferred. A possible way of doing this optimally is the application of the Bayesian-inference approach. In addition to the determination of the minimum mean–square error estimator for a Gaussian p.d.f. [1], we now consider also a uniform prior p.d.f., and perform our calculations using both the minimum mean–square error and the maximum likelihood estimators. The method presented in the previous section and elaborated upon here should be distinguished from the quantum Fisher information approach [173], which has also been successfully applied to systems with matter–field interactions [174, 175].

In our model, two-level systems (TLSs) transit through a cavity supporting a single-mode of the radiation field and are then measured. We trace out the single-mode radiation field and concentrate on the resulting density matrix, subject to the quantum estimation procedure. Spontaneous decay of the TLS is also taken into account. In the case of the minimum mean–square error estimator we invoke the method applied in our previous work [1], demonstrating that the resulting optimal detection strategy can be related to implementable measurement setups in experimentally relevant situations. The problem of determining the maximum likelihood estimator is centered around the resolution of identity and integration with respect to an operator valued measure, see Dobrakov’s integral in Ref. [176]. Due to our motivations being rooted in physics we choose to avoid generalized theories of the Lebesgue integral [177], instead making a simple ansatz for the POVM with the help of square-integrable functions. This construction allows us to determine the maximum likelihood estimators for both the uniform and Gaussian prior p.d.f. We will present numerical calculations of the average cost functions, the average estimates and lower bounds of the mean–squared error of the obtained biased estimators.

This section is organized as follows. In Sec. 6.5.1 we discuss the model and determine the state of the TLS following its interaction with the single-mode radiation field. Spontaneous decay of the TLS is also considered. In Sec. 6.6.1 we recapitulate some basic facts about quantum estimation theory and introduce the formalism used throughout the whole manuscript. We then address the problem of determining the minimum mean–

square error estimator in Sec. 6.6.2. In Sec. 6.5.2 maximum likelihood estimators are discussed. Finally, we discuss our work and draw our conclusions in Sec. 6.5.3.

### 6.5.1 | The Jaynes-Cumming model

In this section we discuss a cavity QED model consisting a two-level system (TLS) interacting with a single-mode electromagnetic cavity. The TLS, generally implemented as a flying atom, is injected into the cavity and emerges from the cavity and is detected after interacting with the electromagnetic field. The setup, illustrated in Fig. 6.13, is one of the best suited for our estimation procedure, because it is under exquisite experimental control [172, 178], and because it allows repeated measurements to be made using several TLS interacting sequentially with the field. In fact, this is a very important point in estimation scenarios because the use of  $N$  independent and identical systems reduces the lower bound of the estimation accuracy by a factor of  $N^{-1}$  [53]. Therefore, it is assumed that before each TLS enters the cavity, the single-mode field is always reset to the same initial state. The state of each TLS entering the cavity is also assumed to be the same. In practice, the controlled motion of an atom into and out of the cavity may be realized using an optical conveyor belt, i.e., a moving dipole trap, into which atoms are loaded from a magneto–optical trap. In our discussion, we present the solution to this elementary model and determine the state of the atom by tracing out the state of the electromagnetic field. The optimal estimator for the matter–field coupling will be subsequently determined for each presented estimation scenario.

Let us consider a TLS with ground state  $|g\rangle$  and excited state  $|e\rangle$ . Cavity leakage and spontaneous decay of the TLS are present; nonetheless, it is assumed that the coupling strength of the matter–field interaction is much larger than the damping rate of the two decoherence sources. Therefore, the joint TLS–field state during the matter–field interaction time can effectively be described by a purely unitary evolution. In the dipole and rotating–wave approximations, the Hamiltonian in the time-independent interaction picture reads [179, 180] ( $\hbar = 1$ ):

$$\hat{H} = \frac{\Delta}{2} \hat{\sigma}_z + g(\hat{a} \hat{\sigma}_+ + \hat{a}^\dagger \hat{\sigma}_-), \quad (6.89)$$

where  $\hat{\sigma}_z = |e\rangle \langle e| - |g\rangle \langle g|$ , and  $\hat{\sigma}_+ = |e\rangle \langle g|$  is the raising and  $\hat{\sigma}_- = |g\rangle \langle e|$  the lowering operator.  $\hat{a}$  and  $\hat{a}^\dagger$  are the annihilation and creation operators of the field mode.  $\Delta = \omega_{e \leftrightarrow g} - \omega_c$  is the detuning between the cavity field mode resonance frequency  $\omega_c$  and the TLS transition frequency  $\omega_{e \leftrightarrow g}$ . Finally,  $g$  is the dipole coupling strength, which involves the normalized mode function of the single-mode radiation field and the transition dipole moment between  $|g\rangle$  and  $|e\rangle$ .



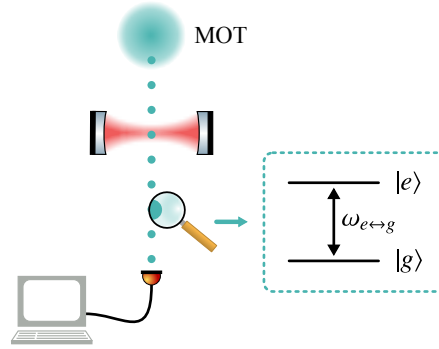


Figure 6.13: Schematic representation of a quantum estimation scenario based on cavity QED. The atoms (grey dots) implementing the two-level systems are captured from a background gas by a magneto–optical trap and loaded into an optical conveyor belt. The atoms move with the help of the conveyor belt into and out of the cavity and towards a detector. The transition frequency of the atom is  $\omega_{e\leftrightarrow g}$ . Further details about the scheme are in the text.

We suppose that at  $t = 0$  there are no correlations between the field and the TLS. Furthermore, we set the TLS to be initially in the excited state. Thus, our general initial quantum state reads

$$|\psi(t=0)\rangle = |e\rangle \otimes \sum_{n=0}^{\infty} a_n |n\rangle, \quad (6.90)$$

where  $|n\rangle$  ( $n \in \mathbb{N}_0$ ) are the normalized photon number states and  $\sum_{n=0}^{\infty} |a_n|^2 = 1$ . The time evolution is governed by the Schrödinger equation acting on the initial state (6.90) yields

$$|\psi(t)\rangle = \sum_{n=1}^{\infty} c_{e,n-1}(t) |e, n-1\rangle + c_{g,n}(t) |g, n\rangle, \quad (6.91)$$

where [77]

$$\begin{aligned} c_{e,n-1}(t) &= e^{-i\frac{\Delta t}{2}} \left[ \cos(\lambda_n t) + i \frac{\Delta}{2\lambda_n} \sin(\lambda_n t) \right] a_{n-1}, \\ c_{g,n}(t) &= -ie^{i\frac{\Delta t}{2}} \frac{g\sqrt{n}}{\lambda_n} \sin(\lambda_n t) a_{n-1}, \end{aligned}$$

and where  $\lambda_n = \sqrt{\Delta^2/4 + g^2 n}$  is the effective Rabi frequency. The state of the TLS upon emerging from the cavity is obtained by tracing out the state of the field,

$$\begin{aligned} \hat{\rho}(g, t) &= \text{Tr}_F\{|\psi(t)\rangle \langle \psi(t)|\} \\ &= \begin{bmatrix} a_{ee}(t) & a_{eg}(t) \\ a_{eg}^*(t) & 1 - a_{ee}(t) \end{bmatrix}, \end{aligned} \quad (6.92)$$

where

$$a_{ee}(t) = \sum_{n=1}^{\infty} |a_{n-1}|^2 \left[ \cos^2(\lambda_n t) + \frac{\Delta^2}{4\lambda_n^2} \sin^2(\lambda_n t) \right], \quad (6.93)$$

$$\begin{aligned} a_{eg}(t) &= \sum_{n=1}^{\infty} a_n a_{n-1}^* \left[ \cos(\lambda_{n+1} t) + i \frac{\Delta}{2\lambda_{n+1}} \sin(\lambda_{n+1} t) \right] \\ &\quad \times \frac{ig\sqrt{n}}{\lambda_n} \sin(\lambda_n t) e^{-i\Delta t}. \end{aligned} \quad (6.94)$$

In the next stage of the experiment, the TLS flies from the cavity to the detector. During this time spontaneous emission may occur. We include this effect in our calculations by using a simple Markovian description

$$\frac{d\hat{\rho}}{dt} = \frac{\gamma}{2} (2\hat{\sigma}_- \hat{\rho} \hat{\sigma}_+ - \hat{\sigma}_+ \hat{\sigma}_- \hat{\rho} - \hat{\rho} \hat{\sigma}_+ \hat{\sigma}_-), \quad (6.95)$$

where  $\gamma$  is the spontaneous emission rate of the TLS. Equation (6.95) is written in the frame rotating at the resonance frequency of the TLS. Two characteristic times enter our discussion:  $\tau_c$ , the duration of the matter–field interaction in the cavity, and  $\tau_f$ , the flying time from the cavity to the detector. The solution in Eq. (6.92) at  $t = \tau_c$  can be considered as the initial condition for Eq. (6.95). Thus, the state of the TLS reaching the detector is

$$\hat{\rho}(g) = \begin{bmatrix} a_{ee}(g, \tau_c) e^{-\gamma\tau_f} & a_{eg}(g, \tau_c) e^{-\gamma\tau_f/2} \\ a_{eg}^*(g, \tau_c) e^{-\gamma\tau_f/2} & 1 - a_{ee}(g, \tau_c) e^{-\gamma\tau_f} \end{bmatrix}. \quad (6.96)$$

Equation (6.96) yields a complete description of our setup and it applies to all the possible initial conditions of the field. A major theme of our subsequent discussion will be the analysis of Eq. (6.96) in the context of quantum estimation theory, where we shall seek optimal estimators for the coupling strength  $g$ .

The Bayesian formulation of the estimation problem seeks for the best estimator which minimizes the average cost of its application. In order to solve this estimation problem we have to provide an a priori p.d.f.  $z(g)$  of  $g$  to be estimated and a cost function  $C(\tilde{g}, g)$ , which assesses the cost of error in the estimate. Now, combining the Bayesian estimation procedure with the strategy represented by the POVM and including the integral representation, we obtain for the average cost, Eq. (6.3),

$$\bar{C} = \text{Tr} \left\{ \int_{\Theta} dg \int_{\Theta} d\hat{\Pi}(\tilde{g}) z(g) C(\tilde{g}, g) \hat{\rho}(g) \right\}. \quad (6.97)$$

We are looking for the  $d\hat{\Pi}(\tilde{g})$  which minimizes  $\bar{C}$ . Our problem has thus been rephrased as a variational problem formulated on the space of all POVMs. In order to solve this

problem one ought to first define  $C(\tilde{g}, g)$ . In this section we will employ the frequently used quadratic cost function

$$C(\tilde{g}, g) = (\tilde{g} - g)^2, \quad (6.98)$$

which leads to the minimum mean–square error (MMSE) estimator, and the delta-valued cost function

$$C(\tilde{g}, g) = -\delta(\tilde{g} - g), \quad (6.99)$$

which leads to the maximum likelihood (ML) estimator [53].

In the following sections we will investigate both the MMSE and the ML estimation scenarios for different prior probabilistic density functions. In order to gain insight into the structure of  $\hat{M}_{\min}$  for this particular system, let us concentrate on resonant interactions  $\Delta = \omega_{e \leftrightarrow g} - \omega_c = 0$ . We also consider the initial state of the single-mode field in Eq. (6.90) to be the ground state,  $a_0 = 1$ . In this case Eq. (6.96) reads

$$\hat{\rho}(g) = \begin{bmatrix} \cos^2(g\tau_c)e^{-\gamma\tau_f} & 0 \\ 0 & 1 - \cos^2(g\tau_c)e^{-\gamma\tau_f} \end{bmatrix}. \quad (6.100)$$

We assume that the random variable  $g$  to be estimated is characterized by its mean value  $g_0$  and variance  $\sigma^2$ , as we did in Sec. 6.3. In order to connect these parameters to experimental setups, we start with the position-dependent dipole coupling of the matter–field interaction [77],

$$g(\vec{r}_q) = -\sqrt{\frac{\hbar\omega_c}{2\epsilon_0}} \langle g | \hat{d} | e \rangle \cdot \vec{u}(\vec{r}_q) / \hbar,$$

where  $\hat{d}$  is the dipole operator,  $\epsilon_0$  the permittivity of vacuum, and  $\vec{r}_q$  the position vector. The normalized mode function of the single-mode radiation field,  $\vec{u}(\vec{r})$ , is a solution to the Helmholtz equation and fulfills the Coulomb gauge and the cavity boundary conditions. However, every passing TLS also experiences changes in the dipole coupling due to the waist of the field mode. Experimental studies usually integrate the collected data over the flying time through the cavity and thus obtain an average coupling strength  $g_0$ ; cf., for example, Ref. [181]. This method results also in a variance  $\sigma^2$  of the measured coupling strength. In the following, we are going to discuss two prior p.d.f. whose mean values and variances coincide with the values defined here.

### 6.5.1.1 | Gaussian probability density function

In this subsection we consider  $\Theta = \mathbb{R}$  and the prior p.d.f.

$$z(g) = \frac{1}{\sqrt{2\pi\sigma^2}} e^{-\frac{(g-g_0)^2}{2\sigma^2}}, \quad g \in \Theta. \quad (6.101)$$

As  $z(g)$  and the density matrix in Eq. (6.100) are given, the operators defined in Eq. (6.40) can be evaluated explicitly, yielding

$$\begin{aligned}\hat{\Gamma}_0 &= \begin{bmatrix} ae^{-\gamma\tau_f} & 0 \\ 0 & 1 - ae^{-\gamma\tau_f} \end{bmatrix}, \\ a &= \frac{1 + e^{-2\sigma^2\tau_c^2} \cos(2g_0\tau_c)}{2}, \\ \hat{\Gamma}_1 &= \begin{bmatrix} be^{-\gamma\tau_f} & 0 \\ 0 & g_0 - be^{-\gamma\tau_f} \end{bmatrix}, \\ b &= \frac{g_0 + e^{-2\sigma^2\tau_c^2} [g_0 \cos(2g_0\tau_c) - 2\sigma^2\tau_c \sin(2g_0\tau_c)]}{2}, \\ \hat{\Gamma}_2 &= \begin{bmatrix} ce^{-\gamma\tau_f} & 0 \\ 0 & g_0^2 + \sigma^2 - ce^{-\gamma\tau_f} \end{bmatrix},\end{aligned}$$

and

$$c = \frac{(g_0^2 + \sigma^2) [1 + e^{-2\sigma^2\tau_c^2} \cos(2g_0\tau_c)]}{2} - 2g_0\sigma^2\tau_c e^{-2\sigma^2\tau_c^2} \sin(2g_0\tau_c) - 2\sigma^4\tau_c^2 e^{-2\sigma^2\tau_c^2} \cos(2g_0\tau_c).$$

Now, Eq. (6.45) can be directly calculated and the MMSE estimator reads

$$\hat{M}_{\min} = \begin{bmatrix} \frac{b}{a} & 0 \\ 0 & \frac{g_0 - be^{-\gamma\tau_f}}{1 - ae^{-\gamma\tau_f}} \end{bmatrix}. \quad (6.102)$$

The average minimum cost of error is

$$\begin{aligned}\bar{C}_{\min} &= g_0^2 + \sigma^2 - \left( \frac{g_0 - be^{-\gamma\tau_f}}{1 - ae^{-\gamma\tau_f}} \right)^2 \\ &\quad - ae^{-\gamma\tau_f} \left[ \frac{b^2}{a^2} - \left( \frac{g_0 - be^{-\gamma\tau_f}}{1 - ae^{-\gamma\tau_f}} \right)^2 \right].\end{aligned}$$

To illustrate the meaning of the MMSE estimator  $\hat{M}_{\min}$  and the average minimum cost of error  $\bar{C}_{\min}$  we consider a situation where the experimentalist, based on their prior expectations of the coupling strength  $g$ , sets the duration of the matter–field interaction  $\tau_c = \pi/(2g_0)$ . This reflects the fact that the experimentalist expects the TLS to emit a photon into the field mode and fly towards the detectors in its ground state. This setup yields

$$\hat{M}_{\min} = \begin{bmatrix} g_0 & 0 \\ 0 & g_0 \end{bmatrix}, \quad \bar{C}_{\min} = \sigma^2,$$

which means that the estimates  $\tilde{g}$  are always,  $g_0$  no regardless of the result of the measurement. Furthermore, the average minimum cost of error is  $\sigma^2$ . Thus, this scenario simply reinforces prior expectations on the true value of  $g$ . Another inconclusive setup would be when  $\tau_c = \pi/g_0$ , i.e., the experimentalist expects that the TLS will not emit a photon into the field mode.

A much more interesting scenario is when  $\tau_c = \pi/(4g_0)$  or in other words the experimentalist expects the TLS to emit a photon with 50% probability. Now, we have

$$\hat{M}_{\min} = \begin{bmatrix} g_0 - \frac{\sigma^2 \pi}{2g_0} e^{-\frac{\pi^2}{8} \frac{\sigma^2}{g_0^2}} & 0 \\ 0 & g_0 + \frac{\sigma^2 \pi}{2g_0} \frac{1}{2e^{\gamma\tau_f} - 1} e^{-\frac{\pi^2}{8} \frac{\sigma^2}{g_0^2}} \end{bmatrix},$$

and

$$\bar{C}_{\min} = \sigma^2 - \frac{\sigma^4 \pi^2}{4g_0^2} \frac{1}{2e^{\gamma\tau_f} - 1} e^{-\frac{\pi^2}{4} \frac{\sigma^2}{g_0^2}}.$$

Measuring the TLS in the excited state results the estimate

$$\tilde{g} = g_0 - \frac{\sigma^2 \pi}{2g_0} e^{-\frac{\pi^2}{8} \frac{\sigma^2}{g_0^2}},$$

with probability

$$p = \cos^2 \left( \frac{\pi}{4} \frac{g}{g_0} \right) e^{-\gamma\tau_f}.$$

The destructive effects of the spontaneous decay are revealed here, because when  $\gamma\tau_f \gg 1$  this probability reduces to zero and therefore the measurement cannot obtain the estimate belonging to the excited state of the TLS. When the measurement yields the other outcome, the state is projected onto the ground state of the TLS, and the resulting estimate is

$$\tilde{g} = g_0 + \frac{\sigma^2 \pi}{2g_0} \frac{1}{2e^{\gamma\tau_f} - 1} e^{-\frac{\pi^2}{8} \frac{\sigma^2}{g_0^2}}$$

with probability

$$p = 1 - \cos^2 \left( \frac{\pi}{4} \frac{g}{g_0} \right) e^{-\gamma\tau_f}. \quad (6.103)$$

When  $\gamma\tau_f \gg 1$ , this result is obtained with certainty, and the resulting estimate is simply  $g_0$  and  $\bar{C}_{\min} = \sigma^2$ . Again our prior expectations of the true value of  $g$  are reinforced. In general, the average estimate is

$$\begin{aligned} E[\tilde{g} | g] &= \text{Tr}\{\hat{M}_{\min} \hat{\rho}(g)\} \\ &= g_0 - \cos \left( \frac{\pi}{2} \frac{g}{g_0} \right) \frac{\sigma^2 \pi}{2g_0} \frac{1}{2e^{\gamma\tau_f} - 1} e^{-\frac{\pi^2}{8} \frac{\sigma^2}{g_0^2}}, \end{aligned} \quad (6.104)$$

which is conditioned on the true value of  $g$ . Performing several measurements with identical TLSs yields an average estimate from which one may deduce the value of  $g$ . When the standard deviation  $\sigma$  of the prior p.d.f. is set very large compared to the prior mean  $g_0 \ll \sigma$ , we allow the true value of  $g$  to be far from the prior mean. In this context the estimates turn out to be again  $g_0$  and accordingly the average minimum cost of error is  $\sigma^2$ . In the case when the true value of  $g$  is  $g_0$ , we find  $E[\tilde{g} | g_0] = g_0$ .

In the next step, the accuracy with which  $g$  can be estimated is characterized by the mean–squared error  $E[(\tilde{g} - g)^2 | g]$ . The lower bound of the mean–squared error is given by a quantum Cramér–Rao-type inequality [53]

$$E[(\tilde{g} - g)^2 | g] = \text{Tr}\{(\hat{M}_{\min} - g\hat{I})^2 \hat{\rho}(g)\} \geq \frac{|x'(g)|}{\text{Tr}\{\hat{\rho}(g)\hat{L}^2\}}, \quad (6.105)$$

where

$$x'(g) = \text{Tr}\{\hat{M}_{\min} \frac{\partial}{\partial g} \hat{\rho}(g)\},$$

and the symmetrized logarithmic derivative  $\hat{L}$  of the density matrix  $\hat{\rho}(g)$  is defined as

$$\frac{\partial \hat{\rho}(g)}{\partial g} = \frac{1}{2} [\hat{L}\hat{\rho}(g) + \hat{\rho}(g)\hat{L}].$$

If we consider the spectral decomposition

$$\hat{\rho}(g) = \cos^2(g\tau_c) e^{-\gamma\tau_f} |e\rangle \langle e| + (1 - \cos^2(g\tau_c) e^{-\gamma\tau_f}) |g\rangle \langle g|,$$

then

$$\hat{L} = -2\tau_c \tan(g\tau_c) |e\rangle \langle e| + \tau_c \frac{\sin(2g\tau_c) e^{-\gamma\tau_f}}{1 - \cos^2(g\tau_c) e^{-\gamma\tau_f}} |g\rangle \langle g|.$$

Hence, we have

$$E[(\tilde{g} - g)^2 | g] \geq \frac{1 - \cos^2(g\tau_c) e^{-\gamma\tau_f}}{4\tau_c \sin^2(g\tau_c)} \left| \sin(2g\tau_c) \right| \frac{|g_0 - b/a|}{1 - ae^{-\gamma\tau_f}}. \quad (6.106)$$

In the inconclusive cases when the experimentalist sets the interaction times either to  $\pi/(2g_0)$  or  $\pi/g_0$  the inequality in Eq. (6.106) yields

$$E[(\tilde{g} - g)^2 | g] \geq 0,$$

which also means that when we bolster our prior knowledge then the lower bound of the accuracy is the smallest. Now, for the interesting case of  $\tau_c = \pi/(4g_0)$ , we find

$$E[(\tilde{g} - g)^2 | g] \geq \frac{1 - \cos^2\left(\frac{\pi}{4} \frac{g}{g_0}\right) e^{-\gamma\tau_f}}{\sin^2\left(\frac{\pi}{4} \frac{g}{g_0}\right)} \left| \sin\left(\frac{\pi}{2} \frac{g}{g_0}\right) \right| \frac{\sigma^2 e^{-\frac{\pi^2}{8} \frac{\sigma^2}{g_0^2}}}{2 - e^{-\gamma\tau_f}}.$$

It is worth noting that in inconclusive situation  $\gamma\tau_f \gg 1$ , when the estimate of the coupling strength is  $g_0$ , the lower bound of the mean–squared error increases. This fact is in contrast with the inconclusive scenarios where  $\tau_c = \pi/(2g_0)$  and  $\tau_c = \pi/g_0$ , where the left-hand side of the quantum Cramér–Rao inequality is zero, the minimum allowed value. It seems in the context of our system that the extremal behaviors of lower bounds on the accuracy are related only to inconclusive estimation scenarios.

### 6.5.1.2 | Uniform probability density function

In this subsection we consider a uniform prior p.d.f. As the only prior knowledge about the coupling  $g$  is its mean value  $g_0$  and variance  $\sigma^2$ , we set the parameter space  $\Theta = [g_0 - \sqrt{3}\sigma, g_0 + \sqrt{3}\sigma]$  and p.d.f.

$$z(g) = \frac{1}{2\sqrt{3}\sigma}, \quad g \in \Theta. \quad (6.107)$$

Similarly to the previous subsection we determine the operators defined in Eq. (6.40)

$$\hat{\Gamma}_0 = \begin{bmatrix} a'e^{-\gamma\tau_f} & 0 \\ 0 & 1 - a'e^{-\gamma\tau_f} \end{bmatrix},$$

$$a' = \frac{1}{2} + \frac{\sin(2\sqrt{3}\sigma\tau_c) \cos(2g_0\tau_c)}{4\sqrt{3}\sigma\tau_c},$$

$$\hat{\Gamma}_1 = \begin{bmatrix} b'e^{-\gamma\tau_f} & 0 \\ 0 & g_0 - b'e^{-\gamma\tau_f} \end{bmatrix}, \quad (6.108)$$

$$b' = \frac{g_0}{2} - \frac{\sin(2g_0\tau_c) \sin(2\sqrt{3}\sigma\tau_c)}{8\sqrt{3}\sigma\tau_c^2}$$

$$+ \frac{\sqrt{3}\sigma \sin(2g_0\tau_c) \cos(2\sqrt{3}\sigma\tau_c) + g_0 \cos(2g_0\tau_c) \sin(2\sqrt{3}\sigma\tau_c)}{4\sqrt{3}\sigma\tau_c}, \quad (6.109)$$

and

$$\hat{\Gamma}_2 = \begin{bmatrix} c'e^{-\gamma\tau_f} & 0 \\ 0 & g_0^2 + \sigma^2 - c'e^{-\gamma\tau_f} \end{bmatrix},$$

$$c' = \frac{g_0^2 + \sigma^2}{2} + \frac{(g_0^2 + 3\sigma^2) \sin(2\sqrt{3}\sigma\tau_c) \cos(2g_0\tau_c)}{4\sqrt{3}\sigma\tau_c}$$

$$+ \frac{\sqrt{3}\sigma \cos(2\sqrt{3}\sigma\tau_c) \cos(2g_0\tau_c) - g_0 \sin(2\sqrt{3}\sigma\tau_c) \sin(2g_0\tau_c)}{4\sqrt{3}\sigma\tau_c^2}$$

$$- \frac{\sin(2\sqrt{3}\sigma\tau_c) \cos(2g_0\tau_c)}{8\sqrt{3}\sigma\tau_c^3} + \frac{g_0 \sin(2g_0\tau_c) \cos(2\sqrt{3}\sigma\tau_c)}{2\tau_c}. \quad (6.110)$$

As the structure of the operators  $\hat{\Gamma}_k$  ( $k = 0, 1, 2$ ) is the same as in the previous subsection, where we have considered the Gaussian p.d.f., we obtain for the MMSE estimator

$$\hat{M}_{\min} = \begin{bmatrix} \frac{b'}{a'} & 0 \\ 0 & \frac{g_0 - b'e^{-\gamma\tau_f}}{1 - a'e^{-\gamma\tau_f}} \end{bmatrix}.$$

The average minimum cost of error is

$$\begin{aligned} \bar{C}_{\min} &= g_0^2 + \sigma^2 - \left( \frac{g_0 - b'e^{-\gamma\tau_f}}{1 - a'e^{-\gamma\tau_f}} \right)^2 \\ &- a'e^{-\gamma\tau_f} \left[ \frac{b'^2}{a'^2} - \left( \frac{g_0 - b'e^{-\gamma\tau_f}}{1 - a'e^{-\gamma\tau_f}} \right)^2 \right]. \end{aligned}$$

The two cases discussed  $\tau_c = \pi/(2g_0)$  and  $\tau_c = \pi/g_0$  were found to be inconclusive in the previous subsection. It is immediate to see from the structure of  $\hat{\Gamma}_k$  that for a uniform prior p.d.f. these cases are not indecisive any more. Thus, supposing that nothing is known in advance about the true value of  $g$  in the interval  $[g_0 - \sqrt{3}\sigma, g_0 + \sqrt{3}\sigma]$  actually reduces the number of inconclusive scenarios. Let us also reconsider  $\tau_c = \pi/(4g_0)$ , i.e., the experimentalist expects the TLS to emit a photon with 50% probability, which was seen to be an interesting case of the previous subsection. The MMSE estimator is, in this case,

$$\hat{M}_{\min} = \begin{bmatrix} g_0(1+x) & 0 \\ 0 & g_0 \left( 1 - \frac{x}{2e^{\gamma\tau_f} - 1} \right) \end{bmatrix},$$

with

$$x = \frac{2}{\pi} \cos \left( \frac{\sqrt{3}\pi \sigma}{2 g_0} \right) - \frac{4}{\sqrt{3}\pi^2} \frac{g_0}{\sigma} \sin \left( \frac{\sqrt{3}\pi \sigma}{2 g_0} \right).$$

The average minimum cost of error is

$$\bar{C}_{\min} = \sigma^2 - g_0^2 \frac{x^2}{2e^{\gamma\tau_f} - 1}.$$

Measuring the TLS in the excited state results in the estimate

$$\tilde{g} = g_0(1+x),$$

with probability

$$p = \cos^2 \left( \frac{\pi g}{4 g_0} \right) e^{-\gamma\tau_f}.$$



Once again we find that when  $\gamma\tau_f \gg 1$  this probability reduces to zero and therefore a measurement cannot yield this estimate. Finding the TLS in the ground state results in the estimate

$$\tilde{g} = g_0 \left( 1 - \frac{x}{2e^{\gamma\tau_f} - 1} \right),$$

with probability

$$p = 1 - \cos^2 \left( \frac{\pi}{4} \frac{g}{g_0} \right) e^{-\gamma\tau_f}.$$

The situation is the same as that for the Gaussian prior p.d.f., i.e., when  $\gamma\tau_f \gg 1$  one measures the TLS to be in the ground state with certainty, the estimate is simply  $g_0$ , and  $\bar{C}_{\min} = \sigma^2$ . In any case, the average estimator is

$$E[\tilde{g} | g] = g_0 + g_0 x \frac{2 \cos^2 \left( \frac{\pi}{4} \frac{g}{g_0} \right) - 1}{2e^{\gamma\tau_f} - 1}.$$

We note again the case when the true value of  $g$  is  $g_0$ , then  $E[\tilde{g} | g_0] = g_0$ . If  $\gamma\tau_f \gg 1$  then the average estimator is also  $g_0$  no matter what the true value of  $g$  is; this is again an inconclusive scenario.

With the uniform prior p.d.f., the quantum Cramér–Rao inequality is

$$E [(\tilde{g} - g)^2 | g] \geq \frac{1 - \cos^2(g\tau_c) e^{-\gamma\tau_f}}{4\tau_c \sin^2(g\tau_c)} \left| \sin(2g\tau_c) \right| \frac{|g_0 - b'/a'|}{1 - a'e^{-\gamma\tau_f}}, \quad (6.111)$$

which yields, when  $\tau_c = \pi/(4g_0)$ ,

$$E [(\tilde{g} - g)^2 | g] \geq \frac{1 - \cos^2 \left( \frac{\pi}{4} \frac{g}{g_0} \right) e^{-\gamma\tau_f}}{\pi \sin^2 \left( \frac{\pi}{4} \frac{g}{g_0} \right)} \left| \sin \left( \frac{\pi}{2} \frac{g}{g_0} \right) \right| \frac{2g_0^2 |x|}{2 - e^{-\gamma\tau_f}}.$$

The next subsection focuses on numerical simulations in order to understand the role of the detuning  $\Delta$  and an initial field state with mean photon number larger than zero. We will investigate the deviations from the analytical results of this section and understand the changes inflicted on the estimates, the minimum average cost of error, and the left-hand side of the quantum Cramér–Rao inequality.

### 6.5.1.3 | Numerical results

In the previous subsections we have calculated analytically the MMSE estimators for both the Gaussian (6.101) and the uniform (6.107) p.d.f. We have presented the simplest scenario, where the cavity field mode is initially in the ground state,  $a_0 = 1$ , which led to a diagonal form of the density matrix (6.100). Furthermore, we have considered the single-mode field to be in resonance with the TLS transition,  $\Delta = \omega_{e \leftrightarrow g} - \omega_c = 0$ , which

has allowed us to perform the integrations in Eq. (6.40). Here, we show the numerical results obtained in more general cases, where the initial state of the field mode is a more general coherent state  $|\alpha\rangle$ , and where we may have non-zero detuning  $\Delta \neq 0$ . The coherent state is defined through the parameter  $\alpha$  [73],

$$|\alpha\rangle = \sum_{n=0}^{\infty} e^{-\frac{|\alpha|^2}{2}} \frac{\alpha^n}{\sqrt{n!}} |n\rangle, \quad \alpha = |\alpha|e^{i\phi}, \quad (6.112)$$

where  $|n\rangle$  ( $n \in \mathbb{N}_0$ ) are the photon number states and  $\phi$  is the complex phase of  $\alpha$ ; the mean photon number of this coherent state is  $|\alpha|^2$ . Here, we set  $\phi = 0$ .

**Gaussian p.d.f. and resonant interaction  $\Delta = 0$ .**—The two parameters of the Gaussian p.d.f. are its mean  $g_0$  and variance  $\sigma^2$ . To simplify the analysis we set  $\gamma\tau_f = 0$ , so that no spontaneous emission may occur. First of all we present the eigenvalues, i.e, the estimates, of the operator  $\hat{M}_{\min}$  for different values of  $\alpha$ . In the case  $\alpha = 0$ , already treated in the previous subsection, one of the eigenvalues of  $\hat{M}_{\min}$  has a discontinuity at  $g_0\tau_c = 0$ . This can be shown by explicitly taking the limit

$$\lim_{\tau_c \rightarrow 0^+} \frac{g_0 - b}{1 - a} = \frac{g_0(3\sigma^2 + g_0^2)}{\sigma^2 + g_0^2}, \quad (6.113)$$

with  $a$  and  $b$  defined in Eq. (6.102). For  $g_0\tau_c = 0$  the function  $\frac{g_0 - b}{1 - a}$  is not defined and the eigenvalue can be obtained only by starting again the whole calculation from Eq. (6.100). The other eigenvalue is continuous and its value tends to  $g_0$ . At  $g_0\tau_c = 0$  the eigenvalues of  $\hat{M}_{\min}$  are  $g_0$  and 0. This simply due to the fact that no interaction occurred. Thus, estimates give either the prior expected coupling value or no coupling at all. When  $|\alpha|$  increases, i.e., the initial average photon number becomes larger, an analytical calculation is not possible. The numerical results in Fig. 6.14 show the eigenvalues of  $\hat{M}_{\min}$ . When  $g_0\tau_c$  tends to infinity all curves approach the prior expected value  $g_0$ , and the measurement is again inconclusive.

In Fig. 6.15 the average minimum cost of error,  $\bar{C}_{\min}$ , is plotted for different values of  $|\alpha|$ . At  $g_0\tau_c = 0$  we find  $\bar{C}_{\min} = \sigma^2$ , equal to the prior variance. The plots show that there are global minima of  $\bar{C}_{\min}$ , which define the recommended values of  $g_0\tau_c$  for the experimental detection. For a fixed value of  $g_0$ , we denote the recommended interaction time as  $\tau_c^*$ . This value depends on  $|\alpha|$  and decreases with increasing  $|\alpha|$ . As more photons are involved in the interaction, i.e., the TLS and the field mode undergo many exchanges of photons, more information gets lost in the different photon number states  $|n\rangle$ . Therefore, the lowest average minimum cost of error is obtained when the field is in the vacuum state,  $|\alpha\rangle = |0\rangle$ . However, more photons in the interaction result in the appearance of higher Rabi frequencies  $g\sqrt{n}$ , which in turn means that the minimum value

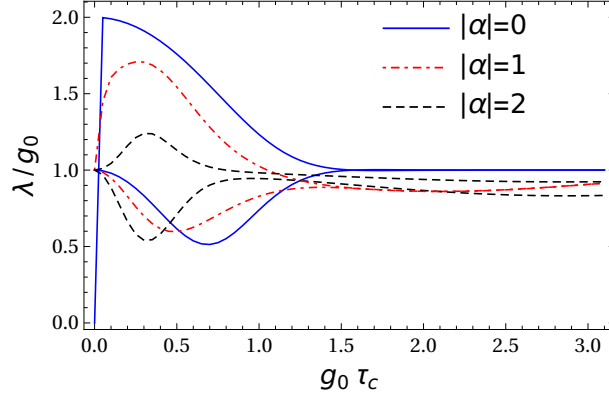


Figure 6.14: The eigenvalues of  $\hat{M}_{\min}/g_0$  as a function of  $g_0\tau_c$  in the case of the Gaussian prior p.d.f., with mean  $g_0$  and variance  $\sigma^2/g_0^2 = 1$ . In the case  $\alpha = 0$  the two initial eigenvalues are 0 and  $g_0$ . When  $|\alpha| > 0$ , the initial eigenvalues start from  $g_0$ . For large values of  $g_0\tau_c$ , the eigenvalues tend to the same value  $g_0$ . We set  $\gamma\tau_f = 0$ , such that no spontaneous decay occurs.

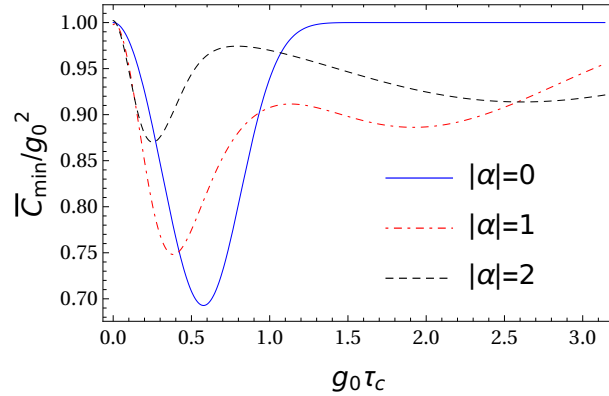


Figure 6.15: The average minimum cost of error  $\bar{C}_{\min}/g_0^2$  as a function of  $g_0\tau_c$  in the case of the Gaussian prior p.d.f., with mean  $g_0$  and variance  $\sigma^2/g_0^2 = 1$ . We set  $\gamma\tau_f = 0$ , such that no spontaneous decay occurs. Each curve has a global minimum that decreases and shifts to larger values of  $g_0\tau_c$  with increasing  $|\alpha|$ .

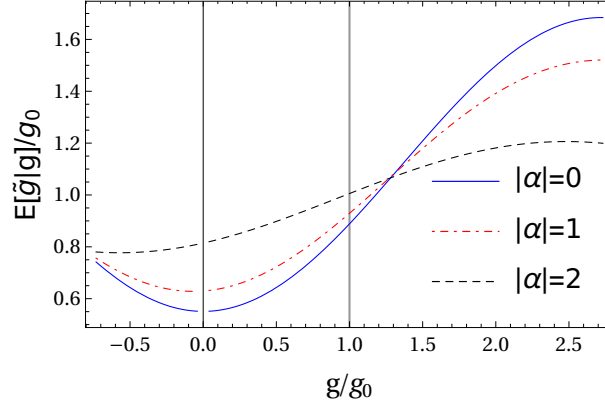


Figure 6.16: The average estimator  $E[\tilde{g}|g]/g_0$  as a function of  $g/g_0$  for the Gaussian prior p.d.f. We set  $\sigma^2/g_0^2 = 1$  and  $\gamma\tau_f = 0$ . The time is such that the average minimum cost of error  $\bar{C}_{\min}$  attains its minimum. The mean value  $g_0$  of the prior p.d.f. is depicted by a vertical line.

is reached quicker. We note that different  $\alpha$  with the same absolute value show the same behavior both for the eigenvalues of  $\hat{M}_{\min}$  and  $\bar{C}_{\min}$ , thus the mean photon number is the only significant variable for the estimation of the dipole coupling strength.

Next, we calculate the average estimator  $E[\tilde{g}|g]$ , which is determined from the measurement data and from which the value of  $g$  can be deduced. Repeated measurements of  $\hat{M}_{\min}$  at  $\tau_c = \tau_c^*$  give different outcomes whose average is related with the true value  $g$ . Fig. 6.16 shows some curves for different values of  $\alpha$  which clearly demonstrate that the obtained MMSE estimator is biased. Furthermore, using Eq. (6.105) we plot in Fig. 6.17 the lower bounds of the mean–squared error for different values of  $|\alpha|$ . In the case  $g = g_0$ , the lower bound of the mean–squared error decreases whenever  $|\alpha| \neq 0$ . By taking into account the behavior of the average estimate  $E[\tilde{g}|g]$ , which at  $g = g_0$  approaches the value of  $g_0$  with increasing  $|\alpha|$  (see Fig. 6.16), we can conclude that increasing values of  $|\alpha|$  lead to measurement strategies which reinforce our prior expectations.

**Uniform prior p.d.f. and resonant interaction  $\Delta = 0$ .**—The two parameters of the uniform p.d.f. are again the mean  $g_0$  and the variance  $\sigma^2$ . We assume again that no spontaneous emission occurs, i.e.,  $\gamma\tau_f = 0$ . In Fig. 6.18 the measurement estimates, or the eigenvalues of the MMSE operator  $\hat{M}_{\min}$ , are shown. If  $\alpha = 0$ , these eigenvalues show a discontinuity around at  $g_0\tau_c = 0$ , as in the case of Gaussian p.d.f., which can be seen from the analytical calculation of  $\hat{M}_{\min}$ . The corresponding limit reads

$$\lim_{\tau_c \rightarrow 0^+} \frac{g_0 - b'}{1 - a'} = \frac{g_0(3\sigma^2 + g_0^2)}{\sigma^2 + g_0^2}, \quad (6.114)$$

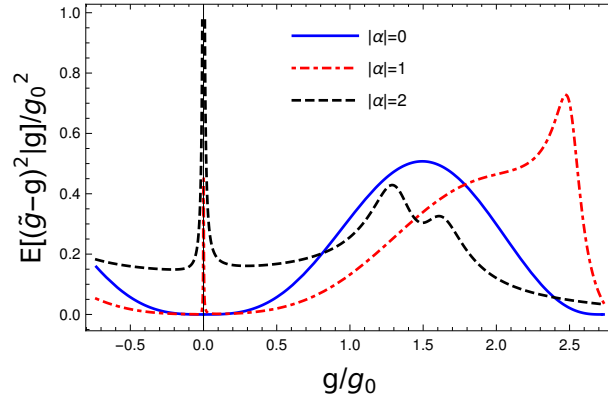


Figure 6.17: The lower bound of the mean–squared error as a function of  $g/g_0$  for the Gaussian prior p.d.f. Here,  $\sigma^2/g_0^2 = 1$ ,  $\gamma\tau_f = 0$  and the interaction time is such that the average minimum cost of error  $\bar{C}_{\min}$  attains its minimum.

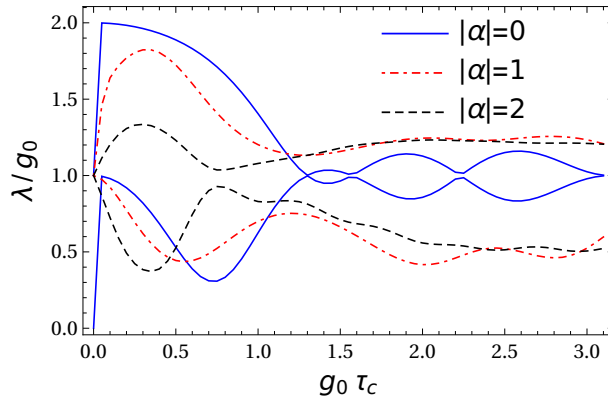


Figure 6.18: The eigenvalues of  $\hat{M}_{\min}/g_0$  as a function of  $g_0\tau_c$  in the case of the uniform prior p.d.f. with mean  $g_0$  and variance  $\sigma^2/g_0^2 = 1$ . In the case  $\alpha = 0$  the two initial eigenvalues are 0 and  $g_0$ . When  $|\alpha| > 0$ , the initial eigenvalues start from  $g_0$ . For large values of  $g_0\tau_c$ , the eigenvalues tend to the same value  $g_0$ , but slower than in Fig. 6.14. We set  $\gamma\tau_f = 0$ .

with  $a'$  and  $b'$  defined as in Eq. (6.108). If  $|\alpha| > 0$  the eigenvalues are continuous. They both start from the prior mean value  $g_0$  and show large oscillations in time. In Fig. 6.19 the average minimum cost of error  $\bar{C}_{\min}$  is plotted for different values of  $|\alpha|$ . It is seen that  $\bar{C}_{\min}$  always starts from the prior variance  $\sigma^2$  and reaches a minimum that depends on  $|\alpha|$ . As in the Gaussian prior p.d.f. case, the absolute value of  $\alpha$  is sufficient to characterize completely these minima.

In Fig. 6.20, the average estimator  $E[\tilde{g}|g]$  for different values of  $|\alpha|$  is given. This is

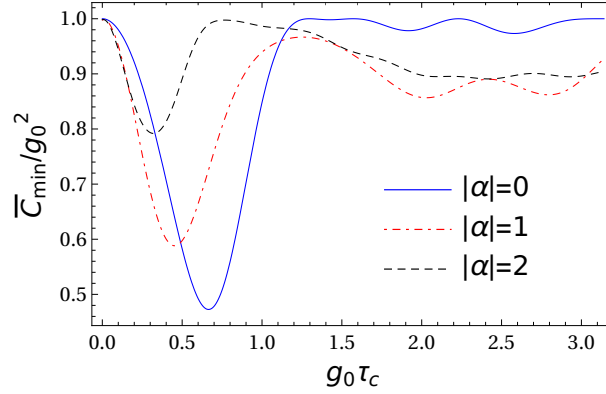


Figure 6.19: The average minimum cost of error  $\bar{C}_{\min}/g_0^2$  as a function of  $g_0\tau_c$  in the case of the uniform prior p.d.f. with mean  $g_0$  and variance  $\sigma^2/g_0^2 = 1$ . We set  $\gamma\tau_f = 0$ . Each curve has a global minimum that decreases and appears for larger values of  $g_0\tau_c$  with increasing  $|\alpha|$ . Compare with Fig. 6.15.

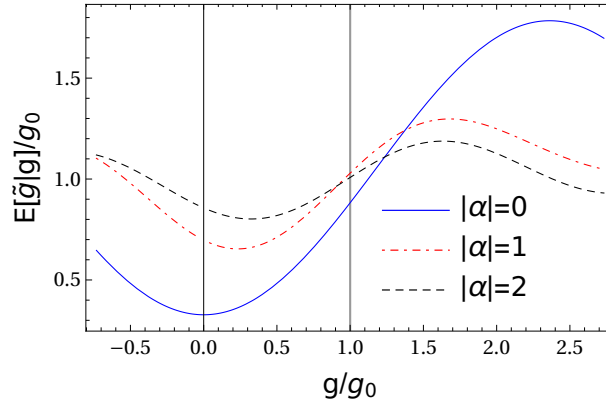


Figure 6.20: The average estimator  $E[\tilde{g}|g]/g_0$  as a function of  $g/g_0$  for the uniform prior p.d.f. We set  $\sigma^2/g_0^2 = 1$  and  $\gamma\tau_f = 0$ . The time is such that the average minimum cost of error  $\bar{C}_{\min}$  attains its minimum. The mean value  $g_0$  of the prior p.d.f. is depicted by a vertical line.

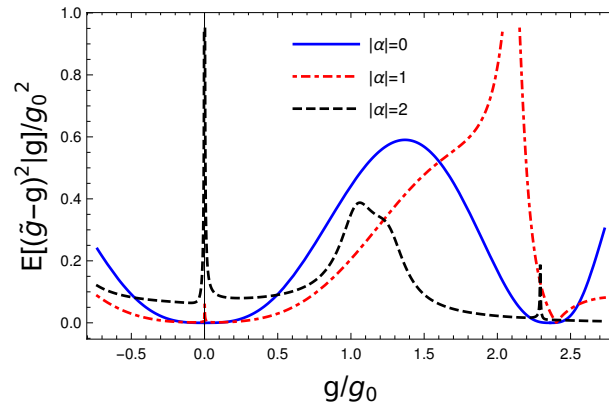


Figure 6.21: The lower bound of the mean–squared error as a function of  $g/g_0$  for the uniform prior p.d.f. We set  $\sigma^2/g_0^2 = 1$ ,  $\gamma\tau_f = 0$ , and the interaction time is such that the average minimum cost of error  $\bar{C}_{\min}$  attains its minimum.

calculated for the time  $\tau_c = \tau_c^*$  when  $\bar{C}_{\min}$  attains its minimum. The lower bound of the mean–squared error is shown in Fig. 6.21. The behavior of all these curves resembles the the Gaussian p.d.f. case, which has already been discussed.

**Role of the detuning  $\Delta$  and the flight time  $\tau_f$ .**—In order to demonstrate the properties of non-zero detuning in a simple way we have considered set  $\alpha = 0$ ,  $\gamma\tau_f = 0$ , and  $\tau_c = \tau_c^*$ , where the average minimum cost of error reaches its minimum. Figure 6.22 shows that the minimum of the average minimum cost of error occurs at  $\Delta = 0$ , for both the Gaussian and the uniform prior p.d.f. Non-zero detuning decreases the probability of the transition occurring in the TLS and, increasing the the average cost of error. Another interesting feature of the off-resonant case is that for  $g_0\tau_c \rightarrow \infty$ ,  $\bar{C}_{\min}$  does not approach  $\sigma^2$  as in Figs. 6.15 and 6.19, but a value depending on both  $\Delta$  and the prior variance  $\sigma^2$ . The influence of the flight time  $\tau_f$  on the estimation scenario is clearly destructive, as we have shown in the previous subsections. Therefore, it is interesting to compare these deleterious effects on the two different prior p.d.f. considered in this work. Due to our previous findings we have set  $\Delta = 0$ , initial single-mode field in the ground state, i.e.,  $\alpha = 0$ , and  $\tau_c = \tau_c^*$ . Fig. 6.23 shows that the average minimum cost of error at  $\tau_c^*$  reaches its minimum for  $\gamma\tau_f = 0$ , and approaches its maximum  $\sigma^2$  when  $\gamma\tau_f \rightarrow \infty$ .

In summary, we have been able to identify the most ideal scenario for the implementation of a MMSE estimator. Non-zero detuning, the occurrence of the spontaneous emission and initial states of the field with non-zero mean photon number should be avoided. If this situation is approximately achievable in some experimental setup than the interaction time  $\tau_c$  has to be fixed to values between  $0.6/g_0$  and  $0.7/g_0$ , which is

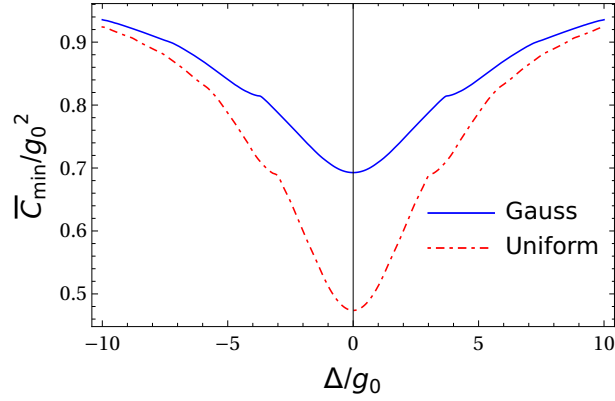


Figure 6.22: The average minimum cost of error  $\bar{C}_{\min}/g_0^2$  reached at  $\tau_c = \tau_c^*$  as a function of the detuning  $\Delta$ . The lowest average minimum cost of error is at resonance  $\Delta = 0$ . We set  $\gamma\tau_f = 0$ ,  $\alpha = 0$  and  $\sigma^2/g_0^2 = 1$ .

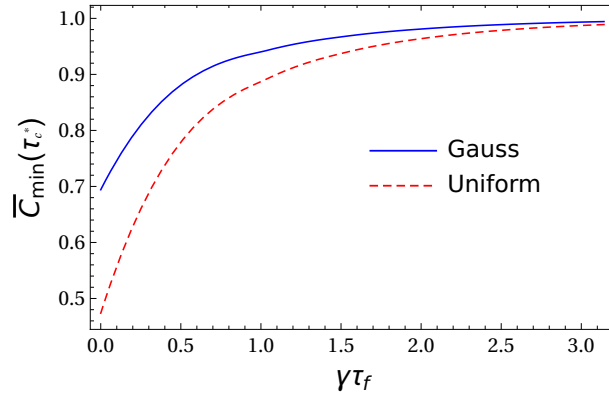


Figure 6.23: The average minimum cost of error  $\bar{C}_{\min}(\tau_c^*)/g_0^2$  reached at  $\tau_c = \tau_c^*$  as a function of  $\gamma\tau_f$ . The minimum is reached when  $\gamma\tau_f = 0$  and approaches its limit value  $\sigma^2/g_0^2 = 1$  with increasing  $\gamma\tau_f$ . We set  $\Delta = 0$  and  $\alpha = 0$ .



before the appearance of the so-called collapse phenomena in the population inversion of the TLS [77].

## 6.5.2 | Maximum-likelihood estimator

In this section we are going to determine the ML estimator. The variational problem for the average cost in Eq. (6.3) reads

$$\bar{C}[\hat{\Pi}] = \text{Tr} \left\{ \int_{\Theta} d\hat{\Pi}(\tilde{g}) z(\tilde{g}) \hat{\rho}(\tilde{g}) \right\}, \quad (6.115)$$

where we are looking for those infinitesimal operators  $d\hat{\Pi}(\tilde{g})$  for which  $\bar{C}$  is maximum (due to the negative sign involved in the cost function Eq. (6.46)). In order to gain insight, we employ the density matrix in Eq. (6.100)

$$\hat{\rho}(g) = \begin{bmatrix} \cos^2(g\tau_c) e^{-\gamma\tau_f} & 0 \\ 0 & 1 - \cos^2(g\tau_c) e^{-\gamma\tau_f} \end{bmatrix},$$

where the detuning  $\Delta = 0$  and the initial state of the field is in the ground state. Integrals of  $d\hat{\Pi}(\tilde{g})$  on compact intervals result in elements of the POVM, thus the following construction

$$d\hat{\Pi}(\tilde{g}) = \begin{bmatrix} f_I(\tilde{g}) + f_z(\tilde{g}) & f_x(\tilde{g}) - if_y(\tilde{g}) \\ f_x(\tilde{g}) + if_y(\tilde{g}) & f_I\tilde{g} - f_z(\tilde{g}) \end{bmatrix} d\tilde{g}, \quad (6.116)$$

with  $f_I, f_z, f_y$ , and  $f_x$  being real functions, ensures the self-adjointness of the infinitesimal generator. We are going to employ this ansatz and solve the variational problem in Eq. (6.115). Only after this step we are going to impose the constraints of the POVM in Eq. (6.123). In the following we reconsider the two cases of the p.d.f.  $z(g)$  used in Sec. 6.6.2.

### 6.5.2.1 | Gaussian probability density function

We assume again that  $g$  is characterized by its mean value  $g_0$  and variance  $\sigma^2$ . The prior p.d.f. is set to be Eq. (6.101) with  $\Theta = \mathbb{R}$ . Then the average cost function reads

$$\bar{C} = \frac{1}{\sqrt{2\pi\sigma^2}} \int_{\mathbb{R}} e^{-\frac{(\tilde{g}-g_0)^2}{2\sigma^2}} [f_I(\tilde{g}) - f_z(\tilde{g}) (1 - e^{-\gamma\tau_f}) + f_z(\tilde{g}) \cos(2\tilde{g}\tau_c) e^{-\gamma\tau_f}] d\tilde{g}. \quad (6.117)$$

We have recast the variational problem to an equivalent one where we search for the real functions  $f_I$  and  $f_z$  such that  $\bar{C}$  in Eq. (6.117) is maximum. As  $\bar{C}$  does not depend on  $f_x$  and  $f_y$  we set them to zero. Upon applying the transformation  $\tilde{g} \rightarrow \sigma x + g_0$ , Eq. (6.117)

becomes

$$\begin{aligned} \bar{C} = & \frac{1}{\sqrt{2\pi}} \int_{\mathbb{R}} dx e^{-x^2/2} [f_z(\sigma x + g_0) (e^{-\gamma\tau_f} - 1) \\ & + f_z(\sigma x + g_0) \cos(2\sigma x\tau_c + 2g_0b\tau_c)e^{-\gamma\tau_f} + f_I(\sigma x + g_0)]. \end{aligned} \quad (6.118)$$

The above variational problem can be solved if we focus on square integrable functions which form the Hilbert space  $\mathbb{L}^2(\mathbb{R})$  (see Ref. [182]). We consider now the following functions:

$$\Psi_n(x) = e^{-x^2/2} \frac{H_n(x)}{\sqrt{\sqrt{\pi}2^n n!}}, \quad n = 0, 1, 2, \dots \quad (6.119)$$

where  $H_n(x)$  is the  $n^{\text{th}}$ -order Hermite polynomial with the property

$$\int_{\mathbb{R}} H_n(x)H_m(x)e^{-x^2} dx = \sqrt{\pi}2^n n! \delta_{nm}.$$

Thus, the functions in Eq. (6.119) form an orthonormal basis in  $\mathbb{L}^2(\mathbb{R})$ , in which the inner product is given by the integral

$$\langle f, g \rangle = \int_{\mathbb{R}} \overline{f(x)}g(x)dx.$$

In the next step we make use of the fact that every function in the Hilbert space can be expanded in the orthonormal basis. Hence,

$$f_I(\sigma x + g_0) = \sum_{n=0}^{\infty} \gamma_n^I \Psi_n(x), \quad f_z(\sigma x + g_0) = \sum_{n=0}^{\infty} \gamma_n^z \Psi_n(x), \quad (6.120)$$

$$\cos(2\sigma x\tau_c + 2g_0\tau_c)e^{-x^2/2} = \sum_{n=0}^{\infty} \gamma_n^c \Psi_n(x),$$

and, with the help of an integral formula involving Hermite polynomials [183, 184], we have

$$\gamma_n^c = \langle \cos(2\sigma x\tau_c + 2g_0\tau_c)e^{-x^2/2}, \Psi_n(x) \rangle = \frac{\pi^{1/4}}{\sqrt{2^n n!}} \times \begin{cases} (-1)^{n/2} (2\sigma\tau_c)^n e^{-\sigma^2\tau_c^2} \cos(2g_0\tau_c) & n \text{ is even,} \\ (-1)^{(n+1)/2} (2\sigma\tau_c)^n e^{-\sigma^2\tau_c^2} \sin(2g_0\tau_c) & n \text{ is odd.} \end{cases}$$

Now, upon substituting these expansions into Eq. (6.118) and taking into account the properties of the orthonormal basis, we obtain

$$\bar{C} = \frac{1}{\sqrt{2}\sqrt{\pi}} \left[ \gamma_0^I - \gamma_0^z (1 - e^{-\gamma\tau_f}) + \frac{e^{-\gamma\tau_f}}{\pi^{1/4}} \sum_{n=0}^{\infty} \gamma_n^z \gamma_n^c \right], \quad (6.121)$$

where we have used the relation  $e^{-x^2/2}/\pi^{1/4} = \Psi_0(x)$ . We observe that  $\bar{C}$  depends only on  $\gamma_0^I$ , the first coefficient in the expansion of  $f_I(ax + b)$ , and therefore we set  $\gamma_n^I = 0$  for  $n \neq 0$ . Thus,

$$f_I(\sigma x + g_0) = \frac{\gamma_0^I}{\pi^{1/4}} e^{-x^2/2},$$

and replacing  $\sigma x + g_0$  with  $x$  we have

$$f_I(x) = \frac{\gamma_0^I}{\pi^{1/4}} e^{-\frac{(x-g_0)^2}{2\sigma^2}}.$$

Furthermore,  $\bar{C}$  is maximum with respect to  $\{\gamma_n^z\}_{n=0}^\infty$  whenever  $\gamma_n^z = \text{constant} \times \gamma_n^c$  or in other words the functions  $\cos(2\sigma x \tau_c + 2g_0 \tau_c) e^{-x^2/2}$  and  $f_z(\sigma x + g_0)$  are parallel with respect to the inner product  $\langle \cdot, \cdot \rangle$ . In fact, this means that

$$f_z(x) = c \times \cos(2\tau_c x) e^{-\frac{(x-g_0)^2}{2\sigma^2}}, \quad c > 0.$$

We recall the following condition on the POVM

$$\int_{\mathbb{R}} d\hat{\Pi}(x) = \hat{I},$$

which, due to Eq. (6.116), is equivalent to

$$\begin{aligned} \int_{\mathbb{R}} f_I(x) dx &= 1, \text{ and} \\ \int_{\mathbb{R}} f_z(x) dx &= \sigma \int_{\mathbb{R}} f_z(\sigma x + g_0) dx = 0. \end{aligned}$$

Then  $\gamma_0^I = 1/\sqrt{2\sqrt{\pi}\sigma^2}$  and  $\gamma_n^z = 0$  for even  $n$ , the latter being due to the fact that integration of a symmetric function about the origin over the whole real line is zero and every odd term of the orthonormal basis is such a function. We hence have

$$\int_{\mathbb{R}} \Psi_n(x) = 0, \quad n \text{ is odd.}$$

Thus,

$$\begin{aligned} f_I(x) &= \frac{1}{\sqrt{2\pi}\sigma^2} e^{-\frac{(x-g_0)^2}{2\sigma^2}}, \text{ and} \\ f_z(\sigma x + g_0) &= c \times \sum_{n \text{ odd}} \gamma_n^c \Psi_n(x). \end{aligned} \tag{6.122}$$

There is one more requirement, namely that

$$\int_{\Delta} d\hat{\Pi}(x) = \hat{\Pi}(\Delta)$$

is a positive semidefinite operator with a spectrum confined to the interval  $[0, 1]$  for every compact interval  $\Delta$  in  $\mathbb{R}$ . This equivalent to

$$0 \leq \int_{\Delta} [f_I(x) \pm f_z(x)] dx \leq 1, \quad \forall \Delta \in \mathbb{R}. \quad (6.123)$$

We consider the compact interval  $\Delta = [a, b]$  with arbitrary  $a, b \in \mathbb{R}$  and  $b > a$ . Using the results of Eq. (6.121), we have

$$\sum_{n \text{ odd}}^{\infty} \gamma_n^c \Psi_n(x) = -\sin(2g_0\tau_c) \sin(2\sigma x\tau_c) e^{-x^2/2}.$$

In view of the above relation,

$$0 \leq \int_a^b e^{-x^2/2} \left[ \frac{1}{\sqrt{2\pi}} \pm c \times \sigma \sin(2g_0\tau_c) \sin(2\sigma x\tau_c) \right] dx \leq 1,$$

where we have again employed the variable transformation  $x \rightarrow \sigma x + g_0$  in Eq. (6.123). In order to analyze right-hand side inequality we first make some observations. The area under the function  $e^{-x^2/2}/\sqrt{2\pi}$  around the origin contributes the most due to the properties of the error function  $\text{erf}(x)$  [100] and  $\sin(2\sigma x\tau_c)e^{-x^2/2}$  is an odd function. Therefore, if the following inequalities

$$\begin{aligned} 0 &\leq \int_0^{\frac{\pi}{2\sigma\tau_c}} e^{-x^2/2} \left[ \frac{1}{\sqrt{2\pi}} - c \times y \sin(2\sigma x\tau_c) \right] dx, \\ \int_0^{\frac{\pi}{2\sigma\tau_c}} e^{-x^2/2} \left[ \frac{1}{\sqrt{2\pi}} + c \times y \sin(2\sigma x\tau_c) \right] dx &\leq 1, \\ y &= \sigma |\sin(2g_0\tau_c)|, \end{aligned}$$

with  $\sigma, \tau_c > 0$  and  $2g_0\tau_c \neq \pi + k\pi$  ( $k \in \mathbb{Z}$ ) hold, then no matter how we choose our intervals the condition (6.123) is fulfilled. In the case when  $2g_0\tau_c = \pi + k\pi$  ( $k \in \mathbb{Z}$ ), condition (6.123) is automatically satisfied. Making use of the error function, we obtain

$$\begin{aligned} c &\leq \frac{2}{\sqrt{2\pi\sigma^2} |\sin(2g_0\tau_c)| e^{-2\sigma^2\tau_c^2}} \\ &\quad \times \frac{\text{erf}\left(\frac{\pi}{2\sqrt{2\sigma}\tau_c}\right)}{\text{erf}\left(\frac{\pi+4i\sigma^2\tau_c^2}{2\sqrt{2\sigma}\tau_c}\right) + \text{erf}\left(\frac{\pi-4i\sigma^2\tau_c^2}{2\sqrt{2\sigma}\tau_c}\right)} = c_1, \text{ and} \\ c &\leq \frac{2}{\sqrt{2\pi\sigma^2} |\sin(2g_0\tau_c)| e^{-2\sigma^2\tau_c^2}} \\ &\quad \times \frac{2 - \text{erf}\left(\frac{\pi}{2\sqrt{2\sigma}\tau_c}\right)}{\text{erf}\left(\frac{\pi+4i\sigma^2\tau_c^2}{2\sqrt{2\sigma}\tau_c}\right) + \text{erf}\left(\frac{\pi-4i\sigma^2\tau_c^2}{2\sqrt{2\sigma}\tau_c}\right)} = c_2. \end{aligned} \quad (6.124)$$

As our original task was to maximize the average cost function  $\bar{C}$ , therefore, the relevant functions read

$$f_1(x) = \frac{1}{\sqrt{2\pi\sigma^2}} e^{-\frac{(x-g_0)^2}{2\sigma^2}}, \text{ and}$$

$$f_z(x) = -c_{\max} \sin(2g_0\tau_c) \sin(2\tau_c(x-g_0)) e^{-\frac{(x-g_0)^2}{2\sigma^2}},$$

with  $c_{\max} = \min\{c_1, c_2\}$ . Together with the ansatz (6.116) we have determined the ML estimators. Finally, the maximum of the average cost function reads

$$\begin{aligned} \bar{C}_{\max} &= \frac{1}{\sqrt{4\pi\sigma^2}} + c_{\max} \frac{e^{-\gamma\tau_f}}{\sqrt{2}} e^{-2\sigma^2\tau_c^2} \sin^2(2g_0\tau_c) \underbrace{\sum_{n \text{ odd}} \frac{(2\sigma^2\tau_c^2)^n}{n!}}_{\sinh(2\sigma^2\tau_c^2)} \\ &= \frac{1}{\sqrt{4\pi\sigma^2}} + c_{\max} e^{-\gamma\tau_f} \frac{1 - e^{-4\sigma^2\tau_c^2}}{2\sqrt{2}} \sin^2(2g_0\tau_c). \end{aligned} \quad (6.125)$$

The three inconclusive cases identified for the MMSE estimator, i.e.,  $\gamma\tau_f \gg 1$ ,  $\tau_c = \pi/g_0$ , and  $\tau_c = \pi/(2g_0)$ , reduce the value of  $\bar{C}_{\max}$ . It becomes clear that, whichever strategy is adopted, these cases should be avoided. The conditional p.d.f.  $p(\tilde{g}|g)$ , is not an even function of the variable  $g - \tilde{g}$ , and therefore the ML estimate will be biased.

Here, the quantum Cramér–Rao inequality has the same form as in Eq. (6.88), i.e.,

$$\mathbb{E}[(\tilde{g} - g)^2|g] \geq \frac{|x'(g)|}{\text{Tr}\{\hat{\rho}(g)\hat{L}^2\}} \quad (6.126)$$

but

$$x'(g) = \int_{-\infty}^{\infty} \tilde{g} \text{Tr}\left\{\frac{\partial}{\partial g} \hat{\rho}(g) d\hat{\Pi}(\tilde{g})\right\},$$

and, similarly to Sec. 6.6.2,

$$\hat{L} = -2\tau_c \tan(g\tau_c) |e\rangle \langle e| + \tau_c \frac{\sin(2g\tau_c) e^{-\gamma\tau_f}}{1 - \cos^2(g\tau_c) e^{-\gamma\tau_f}} |g\rangle \langle g|.$$

Inserting Eq. (6.116) and Eq. (6.125) into Eq. (6.126), we obtain

$$\mathbb{E}[(\tilde{g} - g)^2|g] \geq \frac{1 - \cos^2(g\tau_c) e^{-\gamma\tau_f}}{2\tau_c \sin^2(g\tau_c)} |\sin(2g\tau_c)| \times \left| \int_{-\infty}^{\infty} x f_z(x) dx \right|. \quad (6.127)$$

### 6.5.2.2 | Uniform probability density function

As in the previous subsection we assume that the coupling strength  $g$  has mean value  $g_0$  and variance  $\sigma^2$ . The prior p.d.f. is set to be Eq. (6.107) with  $\Theta = [g_0 - \sqrt{3}\sigma, g_0 + \sqrt{3}\sigma]$ . Now, the average cost function reads

$$\bar{C} = \frac{1}{2\sqrt{3}\sigma} \int_{g_0 - \sqrt{3}\sigma}^{g_0 + \sqrt{3}\sigma} [f_1(\tilde{g}) - f_z(\tilde{g}) (1 - e^{-\gamma\tau_f}) + f_z(\tilde{g}) \cos(2\tilde{g}\tau_c) e^{-\gamma\tau_f}] d\tilde{g}. \quad (6.128)$$

We employ the transformation  $\tilde{g} \rightarrow \sqrt{3}\sigma x + g_0$  and obtain

$$\begin{aligned} \bar{C} = & \frac{1}{2} \int_{-1}^1 \left[ f_I(\sqrt{3}\sigma x + g_0) - f_z(\sqrt{3}\sigma x + g_0) (1 - e^{-\gamma\tau_f}) \right. \\ & \left. + f_z(\sqrt{3}\sigma x + g_0) \cos(2\sqrt{3}\sigma x\tau_c + 2g_0\tau_c) e^{-\gamma\tau_f} \right] dx. \end{aligned}$$

This time the Hilbert space is  $\mathbb{L}^2([-1, 1])$  and we choose the following orthonormal basis [182]:

$$\begin{aligned} \Psi_{n,e}(x) &= \frac{1}{\sqrt{2}} \cos(n\pi x), \\ \Psi_{n,o}(x) &= \frac{1}{\sqrt{2}} \sin(n\pi x), \quad n \in \mathbb{Z}. \end{aligned} \tag{6.129}$$

where  $\Psi_{0,e}(x) = 1/\sqrt{2}$  and  $\Psi_{0,o}(x) = 0$ . Every function can be expanded in this orthonormal basis. Thus,

$$\begin{aligned} f_I(\sqrt{3}\sigma x + g_0) &= \sum_{i=e,0} \sum_{n=0}^{\infty} \gamma_{n,i}^I \Psi_{n,i}(x), \\ f_z(\sqrt{3}\sigma x + g_0) &= \sum_{i=e,0} \sum_{n=0}^{\infty} \gamma_{n,i}^z \Psi_{n,i}(x), \\ \cos(2\sqrt{3}\sigma x\tau_c + 2g_0\tau_c) &= \sum_{i=e,0} \sum_{n=0}^{\infty} \gamma_{n,i}^c \Psi_{n,i}(x), \end{aligned}$$

and

$$\begin{aligned} \gamma_{n,e}^c &= \langle \cos(2\sqrt{3}\sigma x\tau_c + 2g_0\tau_c), \Psi_{n,e}(x) \rangle \\ &= \frac{4\sqrt{3}\sigma\tau_c \sin(2\sqrt{3}\sigma\tau_c) \cos(2g_0\tau_c)}{\sqrt{2}(12\sigma^2\tau_c^2 - n^2\pi^2)} \cos(n\pi), \text{ and} \\ \gamma_{n,o}^c &= \langle \cos(2\sqrt{3}\sigma x\tau_c + 2g_0\tau_c), \Psi_{n,o}(x) \rangle \\ &= -\frac{n\pi \sin(2\sqrt{3}\sigma\tau_c) \sin(2g_0\tau_c)}{\sqrt{2}(12\sigma^2\tau_c^2 - n^2\pi^2)} \cos(n\pi). \end{aligned} \tag{6.130}$$

Now, taking into account the properties of this orthonormal basis, we obtain

$$\bar{C} = \frac{1}{2} \left[ \gamma_0^I - \gamma_0^z (1 - e^{-\gamma\tau_f}) + e^{-\gamma\tau_f} \sum_{i=e,o} \sum_{n=0}^{\infty} \gamma_{n,i}^z \gamma_{n,i}^c \right],$$

a very similar expression to Eq. (6.121). We observe again that  $\bar{C}$  depends only on  $\gamma_0^I$  and therefore we set  $\gamma_n^I = 0$  for  $n \neq 0$ . The condition on the POVM

$$\int_{g_0 - \sqrt{3}\sigma}^{g_0 + \sqrt{3}\sigma} d\hat{\Pi}(x) = \hat{I},$$

results in

$$\int_{g_0-\sqrt{3}\sigma}^{g_0+\sqrt{3}\sigma} f_I(x) dx = \int_{g_0-\sqrt{3}\sigma}^{g_0+\sqrt{3}\sigma} \frac{\gamma_0^I}{\sqrt{2}} dx = 1$$

and thus  $\gamma_0^I = 1/(\sqrt{6}\sigma)$ . Similarly to the previous subsection, we have

$$\int_{g_0-\sqrt{3}\sigma}^{g_0+\sqrt{3}\sigma} f_z(x) dx = \sqrt{3}\sigma \int_{-1}^1 f_z(\sqrt{3}\sigma x + g_0) dx = 0,$$

which yields  $\gamma_{0,e}^z = 0$ . As we would like to maximize  $\bar{C}$ , therefore, we set  $\gamma_{n,i}^z = \text{constant} \times \gamma_{n,i}^c$  for  $n \neq 0$  ( $i \in \{e, o\}$ ), a similar geometrical strategy to the one employed in the previous subsection. Thus,

$$\begin{aligned} f_I(x) &= \frac{1}{2\sqrt{3}\sigma}, \text{ and} \\ f_z(x) &= c \times \left[ \cos(2x\tau_c) - \frac{\sin(2\sqrt{3}\sigma\tau_c) \cos(2g_0\tau_c)}{2\sqrt{3}\sigma\tau_c} \right], \end{aligned} \quad (6.131)$$

with  $c > 0$ . Imposing the constraint that

$$\int_{\Delta} d\hat{\Gamma}(x) = \hat{\Gamma}(\Delta)$$

is a positive semidefinite operator with a spectrum confined to the interval  $[0, 1]$  for every compact interval  $\Delta$  in  $[g_0 - \sqrt{3}\sigma, g_0 + \sqrt{3}\sigma]$ , we find

$$0 \leq \int_a^b [f_I(x) \pm f_z(x)] dx \leq 1, \quad (6.132)$$

where  $b \leq g_0 + \sqrt{3}\sigma$  and  $a \geq g_0 - \sqrt{3}\sigma$ . After performing the definite integral, we get

$$\begin{aligned} 0 \leq x \pm \frac{c}{\tau_c} \left[ \sin(x2\sqrt{3}\sigma\tau_c) \cos(y2g_0\tau_c) \right. \\ \left. - x \sin(2\sqrt{3}\sigma\tau_c) \cos(2g_0\tau_c) \right] \leq 1, \quad x = \frac{b-a}{2\sqrt{3}\sigma} \in [0, 1], \\ y = \frac{b+a}{2g_0} \in \left[ 1 - \sqrt{3}\sigma(1-x)/g_0, 1 + \sqrt{3}\sigma(1-x)/g_0 \right], \end{aligned} \quad (6.133)$$

with  $g_0 \neq 0$ . It is interesting to note the extreme cases  $x = 0$  and  $x = 1$ , when the term

$$f_{\pm}(x, y, c) = x \pm \frac{c}{\tau_c} \left[ \sin(x2\sqrt{3}\sigma\tau_c) \cos(y2g_0\tau_c) - x \sin(2\sqrt{3}\sigma\tau_c) \cos(2g_0\tau_c) \right] \quad (6.134)$$

is equal to 0 and 1, respectively. The functions  $f_+(x, y, c)$  and  $f_-(x, y, c)$  are continuous in  $x$  and have extrema, where they can violate the conditions of being smaller than 1 and greater than 0. The strategy is to find these points  $x_{\text{ext}} = x_{\text{ext}}(c)$ . Upon replacing these

back to into Eq. (6.133) one is able to find  $c_{\max}$ . In order to demonstrate the procedure, let us consider  $2\sqrt{3}\sigma\tau_c = 2g_0\tau_c = \pi/2$ . Then, Eq. (6.134) reads

$$f_{\pm}(x, y, c) = x \pm \frac{c}{\tau_c} \sin\left(x\frac{\pi}{2}\right) \cos\left(y\frac{\pi}{2}\right),$$

$$x \in [0, 1], \quad y \in [x, 2-x].$$

The two extrema of  $f_{-}(x, y, c)$  are found at  $y = x$  (minimum) and  $y = 2 - x$  (maximum), yielding

$$1 - \frac{c\pi}{2\tau_c} \cos(x_{\min}^{-}\pi) = 0,$$

$$1 + \frac{c\pi}{2\tau_c} \cos(x_{\max}^{-}\pi) = 0.$$

These equations, together with Eq. (6.133), result in

$$c \leq \frac{2\tau_c}{\pi} = c_1.$$

$f_{+}(x, y, c)$  has two extrema at  $y = x$  (maximum) and  $y = 2 - x$  (minimum), and therefore we have

$$c \leq \frac{2\tau_c}{\pi} = c_2 = c_1.$$

Finally, the task to maximize  $\bar{C}$  yields

$$c_{\max} = \min\{c_1, c_2\} = c_1. \quad (6.135)$$

The functions defining the ML estimator through the ansatz (6.116) finally read

$$f_I(x) = \frac{1}{2\sqrt{3}\sigma}, \text{ and}$$

$$f_z(x) = c_{\max} \times \left[ \cos(2x\tau_c) - \frac{\sin(2\sqrt{3}\sigma\tau_c) \cos(2g_0\tau_c)}{2\sqrt{3}\sigma\tau_c} \right].$$

The maximum of the average cost function is

$$\bar{C}_{\max} = \frac{1}{2\sqrt{3}\sigma} + c_{\max} \left[ \frac{1}{2} - \frac{\sin^2(2\sqrt{3}\sigma\tau_c) \cos^2(2g_0\tau_c)}{12\sigma^2\tau_c^2} + \frac{\sin(4\sqrt{3}\sigma\tau_c) \cos(4g_0\tau_c)}{8\sqrt{3}\sigma\tau_c} \right] e^{-\gamma\tau_f}. \quad (6.136)$$

The conditional p.d.f.  $p(\tilde{g}|g)$  is again not an even function of the variable  $g - \tilde{g}$ . Therefore the ML estimate, as in the case of the prior Gaussian p.d.f., will be biased.



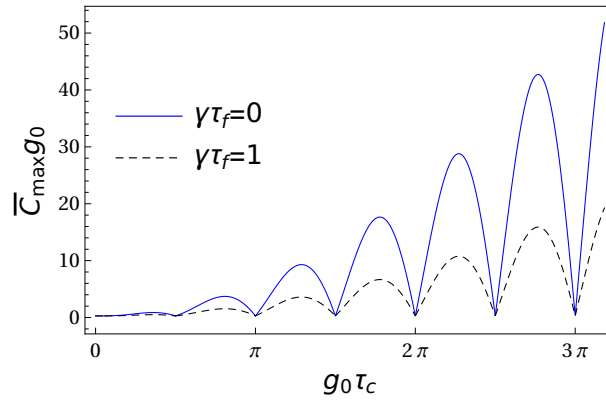


Figure 6.24: The average maximum cost function  $\bar{C}_{\max} g_0$  as a function of  $g_0 \tau_c$  in the case of the Gaussian prior p.d.f. We set  $\sigma^2/g_0^2 = 1$ . We see that spontaneous decay reduces the average cost function.

In the special case  $2\sqrt{3}\sigma\tau_c = 2g_0\tau_c = \pi/2$  discussed earlier,

$$\bar{C}_{\max} = \frac{1}{4g_0} (2 + e^{-\gamma\tau_f}),$$

and the average estimator reads

$$\begin{aligned} E[\tilde{g}|g] &= \int_0^{\frac{\pi}{2\tau_c}} \tilde{g} p(\tilde{g}|g) d\tilde{g} \\ &= g_0 + \frac{4g_0}{\pi^2} \left[ 1 - 2e^{-\gamma\tau_f} \cos^2\left(\frac{g}{g_0} \frac{\pi}{4}\right) \right]. \end{aligned}$$

Furthermore the inequality for the mean–squared error in Eq. (6.127) yields

$$E[(\tilde{g} - g)^2|g] \geq \frac{8g_0^2}{\pi^2} \frac{1 - \cos^2\left(\frac{\pi}{4} \frac{g}{g_0}\right) e^{-\gamma\tau_f}}{\pi \sin^2\left(\frac{\pi}{4} \frac{g}{g_0}\right)} \left| \sin\left(\frac{\pi}{2} \frac{g}{g_0}\right) \right|.$$

### 6.5.2.3 | Numerical results

In the previous subsections we have calculated analytically the ML estimators for both the Gaussian (6.101) and the uniform (6.107) prior p.d.f. Due to the analytically involved solutions we have used the density matrix in Eq. (6.100), where  $\Delta = 0$  and the field mode is initially in the vacuum state. Therefore, the only parameters left for the numerical investigations are the spontaneous decay rate  $\gamma\tau_f$  and the interaction time  $\tau_c$ . We have shown in the case of the uniform prior p.d.f. that in Eq. (6.136) the calculation of  $c_{\max}$  is very intricate and very much depends on the relation between the variance  $\sigma^2$  and the

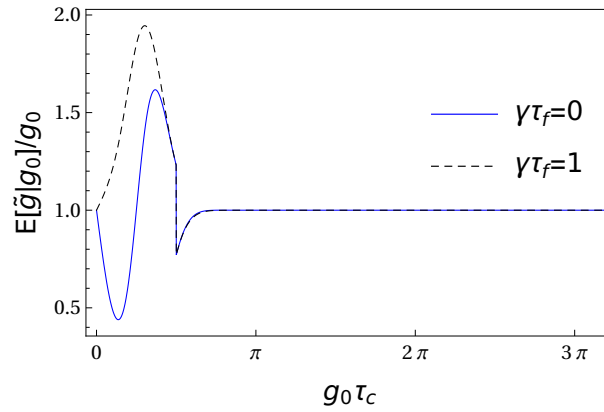


Figure 6.25: The average estimator  $E[\tilde{g}|g_0]/g_0$  as a function of  $g_0\tau_c$  in the case of the Gaussian prior p.d.f. We set  $\sigma^2/g_0^2 = 1$ . There is a jump at  $g_0\tau_c = \pi/2$  due to the properties of  $c_{\max}$  defined in Eqs. (6.124) and (6.125).

mean  $g_0$ . Therefore, we consider here only the ML estimator obtained for the Gaussian prior p.d.f.

Figure 6.24 shows the numerical evaluation of the average maximum cost function  $\bar{C}_{\max}$ . It shows that the best time to perform the measurements is approximately  $g_0\tau_c = \frac{\pi}{4} + k\pi$ , cf. Eq. (6.125), with  $k \in \mathbb{N}_0$  and with better results as  $k$  increases. This means that longer is the interaction between the field and the TLS, the bigger the average cost becomes. The spontaneous decay rate  $\gamma\tau_f$  affects the quality of the estimation by reducing  $\bar{C}_{\max}$ . However, on the other hand Fig. 6.25 shows that the average estimate conditioned on the mean  $g_0$ , a possible true value of  $g$ , for long interaction times is simply equal to our prior expectation. This type of dichotomy has been found by us [1], where a more optimal average cost function merely leads to the reinforcement of our prior knowledge. Finally, the lower bound of the mean–squared error in Fig. 6.26 demonstrates the decrease of the accuracy of the estimation caused by the increase of  $\gamma\tau_f$ .

### 6.5.3 | Remarks

We have discussed Bayesian-inference approaches with a special focus on the dipole coupling of matter–field interactions. Our scheme is based on two-level systems (TLSs) which transit through a cavity and interact with a single-mode radiation field. The state of the TLS is subsequently measured. Spontaneous emission of the excited state of the TLS is taken into account. Our protocol assumes that all the TLS are prepared initially in the excited states, and that the cavity field is reset before the transit of each TLS. We

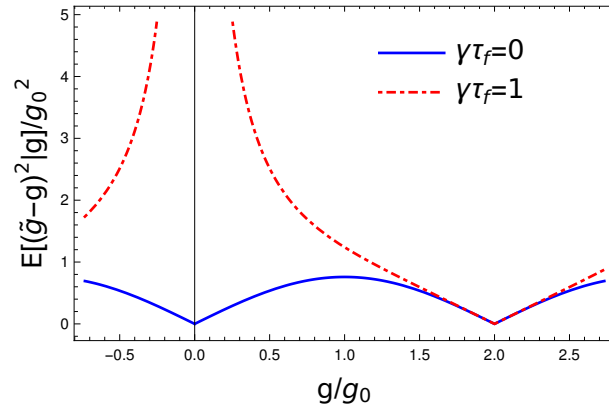


Figure 6.26: The lower bound of the mean–squared error as a function of  $g/g_0$  for the Gaussian prior p.d.f. We set  $\sigma^2/g_0^2 = 1$  and the interaction time  $\tau_c = \pi/(4g_0)$ .

have derived the minimum mean–square error (MMSE) estimator for both the Gaussian and the uniform probability density functions (p.d.f.) with given mean and variance. It has been demonstrated that the detuning between the TLS transition frequency and the cavity resonance frequency has a destructive effect on parameter estimation. Furthermore, spontaneous emission, as well as too long or too short interaction times, all result in the reinforcement of our prior expectations. In the case of resonant interactions with initial ground state of the field mode we have explicitly shown that the MMSE estimator  $\hat{M}_{\min}$  is diagonal in the basis of the qubit. Dividing  $\hat{M}_{\min}$  in Eq. (6.102) by the prior mean  $g_0$  results in a positive-operator valued measurement (POVM) element associated with an inefficient measurement scenario:

$$\hat{\Pi} = \eta_1 |e\rangle \langle e| + \eta_2 |g\rangle \langle g|, \quad 0 \leq \eta_1, \eta_2 \leq 1,$$

where the detection efficiencies are characterized by  $\eta_1$  and  $\eta_2$ . These efficiencies are known functions of the priorly expected parameter values according to Eq. (6.102). For example, in the experiment described in Ref. [185], the final state of the TLS leaving the cavity is detected with the help of a push-out laser. This method has the potential to perform the above described inefficient measurement scenario. Furthermore, we have computed the average estimator and showed the biased nature of the obtained MMSE estimators. We have determined the lower bound of the mean–squared error with the help of a quantum Cramér–Rao type inequality by constructing the symmetrized logarithmic derivative of the density matrix subject to estimation. These calculations have been performed for initial coherent field states. The increase of the initial mean photon number decreases the effectivity of the estimation scenario due to the fact that a lot of

information is deposited in the photon number states, which in turn are traced out to obtain the state of the TLS subject to the measurements. We have also found that the mean–square error estimation scenario is optimal, and our prior expectations are not reinforced, when the TLS emits a photon into the single-mode field with 50% probability. This is in contrast with many experimental situations, where every parameter is tuned such that every TLS emits a photon in the cavity thus realizing the so-called one-atom maser [179].

In the case of the maximum-likelihood (ML) approach the method used for the determination of the MMSE estimator cannot be applied. The observation strategy formulated with the help of the infinitesimal operators has led us to a pure mathematical problem. We have constructed these infinitesimal operators with the help of square integrable functions, which form a Hilbert space with the respective inner product. In the case of the Gaussian prior p.d.f. the Hilbert space is  $\mathbb{L}^2(\mathbb{R})$  with the orthonormal basis formed by Hermite polynomials. The Hilbert space for the uniform prior p.d.f. case is  $\mathbb{L}^2([-1, 1])$  with an orthonormal basis formed by sine and cosine functions. We have used the geometrical properties of these Hilbert spaces in order to optimize the average cost function. In order to be able to solve this problem we have considered the detuning to be zero and the initial state of the field to be the vacuum state. Aside from the main result of determining the ML estimator and the optimized average cost function, we have shown that effects of spontaneous emission are again destructive, and that long interaction times lead to inconclusive estimation scenarios. For both the Gaussian and the uniform a priori p.d.f., the POVM elements are diagonal in the basis of the qubit and as we have discussed in the case of the MMSE estimator one may implement such quantum measurements in experiment.

A few generic comments on all of the strategies presented throughout the manuscript are in order. The measurement data with the implemented POVM determines the average estimate or the a posteriori p.d.f. from which one may infer the value of the matter–field coupling constant. The lower bound of the mean–squared error characterizes the accuracy, but we have found that better accuracy, defined in this way, is usually associated with inconclusive scenarios. Therefore, if we would like to compare the different methods then it has to be done through the average cost function. In this context, we can conclude that the choice of the uniform prior p.d.f. is more suited for the model presented here, as shown in, e.g., Fig. 6.22.

In view of recent developments in quantum information protocols based on matter–field interactions, our work can be seen as the step before the real-world application of such protocols, establishing the tools for the optimal estimation of the dipole coupling strength. While we have not been able to solve completely all the problems related to the

Bayesian approach in the context of matter–field interactions, our results already allow us to make several important observations, which are crucial prior to the experimental implementation of any quantum information protocol.

In closing, we note that whereas our discussion has been framed exclusively in the language of cavity QED and the interaction between TLSs and electromagnetic cavity modes, our framework may be applicable more broadly. For example, in hybrid optomechanical systems where a bosonic mode (corresponding to the mechanical motion of a high-quality mechanical oscillator) is coupled to a TLS, the dynamics is governed by a Hamiltonian similar in structure to Eq. (6.89). The application of our techniques to this and similar scenarios is deferred to future work.

## 6.6 | Application of Fisher information approach to optomechanics

In the previous sections we applied the Bayesian inference for the estimation of the optomechanical coupling strength and for the estimation of the matter field coupling. Here, we conclude the chapter with our contribution taken from the published paper [3], where we applied the Fisher approach for the estimation of the linear optomechanical coupling strength  $g$ . Our starting point is a single cavity described by the linear optomechanical quantum Langevin equation (3.50)

$$\dot{u}(t) = Au(t) + \eta(t), \quad (6.137)$$

where we have defined the vector of operators  $u(t) = (\delta\hat{q}(t), \delta\hat{p}(t), \delta\hat{X}(t), \delta\hat{Y}(t))^T$  and

$$\eta(t) = \begin{pmatrix} 0, \hat{\xi}(t), \sqrt{\kappa_{\text{in}}}\hat{X}_{\text{in}}(t) + \sqrt{\kappa_{\text{loss}}}\hat{X}_{\text{loss}}(t), \\ \sqrt{\kappa_{\text{in}}}\hat{Y}_{\text{in}}(t) + \sqrt{\kappa_{\text{loss}}}\hat{Y}_{\text{loss}}(t) \end{pmatrix}^T.$$

One should note that the steady-state amplitude depends on the value of  $g$ , making  $\alpha$  a function of  $g$ , i.e.  $\alpha = \alpha(g)$ . The same is valid for the detuning  $\Delta = \Delta(g)$ . Therefore for a fixed value of  $P$ , the bistability depends explicitly also on  $g$ , which is yet unknown. A good strategy here is to define an interval, depending on our prior knowledge, for the possible values of  $g$  and adjust the power of laser  $P$  such that the bistability is completely avoided. Hence, we should be sure that our dynamics is stable applying the Routh-

Hurwitz criterion on the dynamical matrix, see Eq. (3.51),

$$A = \begin{pmatrix} 0 & \frac{1}{m} & 0 & 0 \\ -m\omega_m^2 & -\gamma & \sqrt{2}\hbar g\alpha(g) & 0 \\ 0 & 0 & -\frac{\kappa}{2} & \Delta(g) \\ \sqrt{2}g\alpha(g) & 0 & -\Delta(g) & -\frac{\kappa}{2} \end{pmatrix}, \quad (6.138)$$

where we have made explicit the dependence of  $\alpha$  and  $\Delta$  on  $g$ . Finally, the aim is to find the autocorrelation matrix  $\sigma$  which describes the steady Gaussian state, solving the Lyapunov equation (3.56)

$$A\sigma + \sigma A^T = -D, \quad (6.139)$$

where the matrix  $D$  depends on the noise correlations, and has been given in Chapter 3. However, we need to keep in mind that any experimental apparatus does not have direct access to the cavity field, but only to the output field, which escapes the cavity. We can calculate the fluctuations of this field around its stationary state with the use of the input–output relations

$$\hat{a}_{\text{out}} = \sqrt{\kappa_{\text{in}}}\delta\hat{a} - \hat{a}_{\text{in}}. \quad (6.140)$$

In practice, one selects different modes by opening a filter in a certain interval of time or in different frequency intervals. Hence we can define  $N$  independent output modes following the approach of Ref. [102]:

$$\hat{a}_{k,\text{out}}(t) = \int_{-\infty}^t ds g_k(t-s)\hat{a}_{\text{out}}(s), \quad k = 1, \dots, N, \quad (6.141)$$

where  $g_k(s)$  is the filter function defining the  $k^{\text{th}}$  mode. Here we will make use of the filter function

$$g_k(t) = \frac{\theta(t) - \theta(t - \tau)}{\sqrt{\tau}} e^{-i\Omega_k t}, \quad (6.142)$$

with  $\Omega_j - \Omega_l = \frac{2\pi}{\tau}n$ ,  $n \in \mathbb{N}$ . The  $k^{\text{th}}$  mode is centered at the frequency  $\Omega_k$  and has a bandwidth  $1/\tau$ . Making use of the input–output relations (6.140) we obtain the correlation matrix  $\sigma_{k,\text{out}}$  of the output field quadratures  $\hat{X}_{k,\text{out}}$  and  $\hat{Y}_{k,\text{out}}$  related to a filter

centered at frequency  $\Omega_k$  as

$$\langle \hat{X}_{k,\text{out}} \hat{X}_{k,\text{out}} \rangle(\tau) = \frac{1}{2} \kappa \tau \text{sinc}^2 \left( \frac{\Omega_k \tau}{2} \right) [(\sigma_{xx} - \sigma_{yy}) \cos(\Omega_k \tau) + \sigma_{xx} + 2\sigma_{xy} \sin(\Omega_k \tau) + \sigma_{yy}] + \text{sinc}(2\Omega_k \tau) \quad (6.143a)$$

$$\langle \hat{X}_{k,\text{out}} \hat{Y}_{k,\text{out}} \rangle(\tau) = \frac{1}{2} \kappa \tau \text{sinc} \left( \frac{\Omega_k \tau}{2} \right)^2 [(\sigma_{yy} - \sigma_{xx}) \sin(\Omega_k \tau) + 2\sigma_{xy} \cos(\Omega_k \tau)] \quad (6.143b)$$

$$\langle \hat{Y}_{k,\text{out}} \hat{Y}_{k,\text{out}} \rangle(\tau) = \frac{1}{2} \kappa \tau \text{sinc}^2 \left( \frac{\Omega_k \tau}{2} \right) [(\sigma_{yy} - \sigma_{xx}) \cos(\Omega_k \tau) + \sigma_{xx} - 2\sigma_{xy} \sin(\Omega_k \tau) + \sigma_{yy}] + \text{sinc}(2\Omega_k \tau) \quad (6.143c)$$

where  $\sigma_{AB} = \langle \delta \hat{A} \delta \hat{B} \rangle$  ( $A, B \in \{X, Y\}$ ) are the entries of matrix  $\sigma$ , which are obtained in Eq. (3.56), and  $\text{sinc}(x)$  is the unnormalized sinc function  $\text{sinc}(x) = \sin(x)/x$ . The shifted operators are fully characterized in the stationary state by the correlation matrix, since all noises involved obey this property and the equations of motion are linear. One can thus deduce that their properties can also be described by a zero-mean Gaussian state. Similarly, the output field fluctuations are given by the Gaussian Wigner function

$$W(\xi) = \frac{1}{\sqrt{2\pi \det(\sigma_{k,\text{out}})}} e^{-\frac{1}{2} \xi^T \sigma_{k,\text{out}}^{-1} \xi}, \quad (6.144)$$

where  $\xi = (X_{k,\text{out}}, Y_{k,\text{out}})^T$  and  $\sigma_{k,\text{out}}$  is the correlation matrix. The above Wigner function depends on the optomechanical coupling strength  $g$  through  $\sigma_{k,\text{out}}$ , and is a function of the correlation matrix of the cavity optomechanical system. In our subsequent discussion we analyze Eq. (6.144) in the context of a quantum estimation strategy based on the quantum Fisher information. Our task will be to seek optimal balanced homodyne photodetection measurement strategies.

## 6.6.1 | Phase space quantum and classical Fisher Information

In this section we derive the quantum Fisher information (QFI)  $H_g$  of the optomechanical coupling strength for a general Gaussian state, employing the phase-space description provided by the Wigner quasi-probability distribution 6.144. The QFI defines a lower bound for the mean squared error (MSE) of an estimation setup, which is ensured by the quantum Cramér–Rao theorem [53]

$$\text{MSE}(g) \geq \frac{|x'(g)|}{H_g}, \quad (6.145)$$

where  $|x'(g)|$  is the derivative of the average estimator. When the estimator is unbiased, then  $|x'(g)| = 1$ . The QFI is given as

$$H_g = \text{Tr}[\hat{\rho} \hat{L}_g^2], \quad (6.146)$$

where  $\hat{L}_g$  is the symmetric logarithmic derivative (SLD) defined by the equation

$$\partial_g \hat{\rho} = \frac{1}{2} \{ \hat{\rho}, \hat{L}_g \}. \quad (6.147)$$

We are going to use this general formalism to the Gaussian state obtained in Eq. (6.144). A Gaussian state is completely determined by its first and second moments; however, here we have that the first moment is zero following the argument in Sec. 6.5.1. Since the density operator  $\hat{\rho}$  of a Gaussian state can be expressed in an exponential form [89] we can write the operator  $\hat{L}_g$  as a function of the covariance matrix  $\sigma_{k,\text{out}}$ . We neglect all subscripts in the subsequent discussion, because from now on we focus on one mode of the electromagnetic field that is detected.

In order to find SLD we use the Weyl transform on the operator, obtaining

$$L(x, p) = \xi^T \Phi \xi - \nu, \quad (6.148)$$

where the explicit forms of  $\Phi$  and  $\nu$  are

$$\Phi = -\frac{1}{2} \partial_g (\sigma^{-1}) \quad (6.149)$$

$$\nu = -\frac{1}{2} \partial_g \ln(\det \sigma) = \text{Tr}[\Phi \sigma]. \quad (6.150)$$

It is worth noticing that the quadratic nature of  $L(x, p)$  is ensured by the Gaussian form of  $W(x, p)$ .

We use the SLD to calculate the QFI  $H_g$  related to the parameter  $g$  following Eq. (6.146). However the calculation of the Weyl transform of  $\hat{L}_g^2$  is not straightforward. In order to calculate it we need first to Weyl transform the function  $L(x, p)$  back to the operator  $\hat{L}_g$  yielding

$$\hat{L} = \Phi_{11} \hat{x}^2 + \Phi_{12} (\hat{x} \hat{p} + \hat{p} \hat{x}) + \Phi_{22} \hat{p}^2 - \nu \hat{I}. \quad (6.151)$$

Now, one is able to calculate  $\hat{L}_g^2$  and after performing the symmetric ordering and the Weyl transform on it we find  $L^{(2)}(x, p)$  as

$$\begin{aligned} L^2(x, p) &= \Phi_{11}^2 x^4 + 4\Phi_{11}\Phi_{12} p x^3 + 4\Phi_{12}^2 p^2 x^2 \\ &\quad + 2\Phi_{11}\Phi_{22} p^2 x^2 + 4\Phi_{12}\Phi_{22} p^3 x + \Phi_{22}^2 p^4 \\ &\quad - 2\nu L(x, p) - \nu^2 - \frac{1}{2} \det(\Phi). \end{aligned} \quad (6.152)$$



The QFI obtained as the mean value of  $\hat{L}^2$  on the state  $\hat{\rho}$  can be calculated by the phase-space formalism

$$\begin{aligned} H(g) &= \int dx dp L^{(2)}(x, p) W(x, p) \\ &= 3\text{Tr}[(\Phi\sigma)^2] - 2\nu\text{Tr}[\Phi\sigma] + 2\det(\sigma)\det(\Phi) \\ &\quad - \frac{1}{2}\det(\Phi) + \nu^2. \end{aligned} \quad (6.153)$$

We will make use of Eq. (6.153) to determine the QFI of the output field. Combining together (6.153) and (6.149) we obtain the QFI for a two dimensional Gaussian state with zero mean

$$H(g) = \frac{1}{2}\text{Tr}[(\partial_g(\sigma^{-1})\sigma)^2] - \frac{1}{8}\det[\partial_g(\sigma^{-1})]. \quad (6.154)$$

The quantum Cramér–Rao bound (6.145) for an unbiased estimator is saturated only if we implement the best strategy (POVM) that minimizes the MSE of the parameter estimation. This strategy is usually very difficult to find and may be impossible to implement [1]. However, we can find for each practical measurement strategy the maximum amount of Fisher information it can provide. Measurements on quantum systems provide a probability density function which depends on the parameter to be estimated. The amount of information on the unknown parameter carried by this probability density function can be measured by the so-called classical Fisher information (CFI)

$$F_g = \int dx P(x|g) \left( \partial_g \log P(x|g) \right)^2, \quad (6.155)$$

where  $P(x|g)$  is the conditional probability of obtaining the output of the measure  $x$  when the true value of the parameter is  $g$ . In quantum mechanics the conditional probability is given by the relation  $P(x|g) = \text{Tr}[\hat{\rho}_g \Pi_x]$ . Here, we consider that the measurements are performed by balanced homodyne photodetection (BHD) [55]. This makes use of two photodetectors, each with quantum efficiency  $\eta$ . In BHD the data recorded is proportional to the difference of the measured photon numbers  $n_{1,2}$  of the two photodetectors, yielding

$$P_\theta(n|g) = \sum_{m=0}^{\infty} \langle : e^{-\eta(\hat{n}_1 + \hat{n}_2)} \frac{(\eta\hat{n}_1)^{n+m}}{(n+m)!} \frac{(\eta\hat{n}_2)^m}{m!} : \rangle_{\hat{\rho}_g \otimes \hat{\rho}_{LO}}$$

where  $\hat{\rho}_{LO}$  is the state of the local oscillator, considered to be a coherent state  $\hat{\rho}_{LO} = |\alpha_{LO}\rangle\langle\alpha_{LO}|$ . The symmetric order denoted by  $::$  helps us to find the Weyl transform of the element  $\Pi_k^\eta(x, p)$  of the BHD POVM,

$$\Pi_k^\eta(x, p) = \exp \left[ - \frac{2\eta \left( k - \frac{x \cos \theta + p \sin \theta}{\sqrt{2}} \right)^2}{1 - \eta} \right] \quad (6.156)$$

obtained in the limit of  $|\alpha_{\text{LO}}| \gg 1$ . The parameter  $\theta$  is the angle of the coherent state  $|\alpha_{\text{LO}}\rangle$ , i.e.,  $\theta = \arg(\alpha_{\text{LO}})$  and defines the quadrature that is measured. The conditional probability is

$$P_{\theta}^{\eta}(k) = \sqrt{\frac{2\eta}{\pi(1-\eta)}} \int dx dp W(x, p) \Pi_k^{\eta}(x, p). \quad (6.157)$$

Using the condition (6.144) for the Wigner function leads to

$$P_{\theta}^{\eta}(k) = \frac{1}{\pi} \sqrt{\frac{2\eta}{1-\eta+2\eta R_{\theta}^T \sigma R_{\theta}}} e^{-\frac{2\eta k^2}{1-\eta+2\eta R_{\theta}^T \sigma R_{\theta}}},$$

where we have defined  $R_{\theta} = (\cos \theta, \sin \theta)^T$ . Now, we can calculate the CFI with the help of Eq. (6.155), yielding

$$F_g^{\eta} = 2 \left( \frac{\eta R_{\theta}^T \partial_g \sigma R_{\theta}}{1-\eta+2\eta R_{\theta}^T \sigma R_{\theta}} \right)^2. \quad (6.158)$$

Eq. (6.158) is a novel and compact form for the classical Fisher information of the BHD. Notice that in the case of perfect detectors ( $\eta \rightarrow 1$ ) Eq. (6.156) reduces to a Dirac delta  $\Pi_k^1(x, p) \rightarrow \delta(k - R^T \zeta)$ . In this case the CFI assumes the form

$$F_g^1 = \left( \frac{R_{\theta}^T \partial_g \sigma R_{\theta}}{R_{\theta}^T \sigma R_{\theta}} \right)^2. \quad (6.159)$$

## 6.6.2 | Results

In section 6.5.1 we have calculated the covariance matrix (6.143a) of the output field escaping the cavity and characterized by the filter function (6.142). In section 6.6.1 we have calculated the general form of the quantum Fisher information (QFI) of Gaussian states with zero mean, like the output field, and the classical Fisher information (CFI) of balanced homodyne photodetection (BHD) measurements. In this section we numerically investigate and compare QFI and CFI for an experimentally feasible situation. We consider the cavity to possess equal internal and external decay rates  $\kappa_{\text{in}} = \kappa_{\text{loss}} = \kappa$  and our detector to stay on for a temporal window of length  $\tau = 1/\kappa$ . For our numerical analysis we take the experimental values from [186], which are  $\kappa/2\pi = 18.5$  MHz,  $\gamma/2\pi = 130$  Hz,  $\omega_m/2\pi = 1.14$  MHz,  $T = 11$  K,  $m = 16$  ng, and the power of the laser  $P = 1 \mu\text{W}$ . Although the subject is to estimate the optomechanical coupling strength, we still need to set a central value around which we conduct our investigations. The coupling  $g$  appears in the interaction Hamiltonian with the dimensionality of  $[\text{Hz} \cdot \text{m}^{-1}]$ , whereas in the optomechanics community is common to refer to the coupling strength  $g$  in Hertz [8]. We solve this issue with a transformation of the coupling

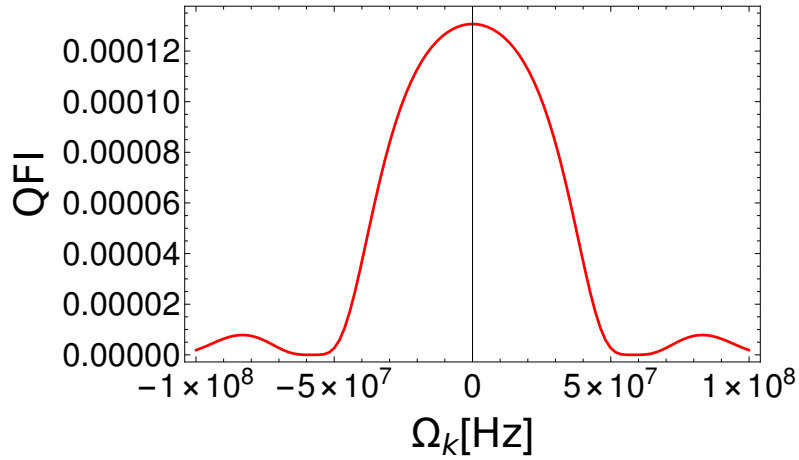


Figure 6.27: Quantum Fisher information (QFI) as a function of the filter function's center frequency  $\Omega_k$ . In the rotating frame the peak of QFI is at  $\Omega_k = 0$ , which corresponds to maximum accuracy reached in the estimation scenario. This also means that in the laboratory frame measurements should be performed around the frequency of the driving laser  $\omega_L$ . The parameters are  $\kappa/2\pi = 18.5$  MHz,  $\gamma/2\pi = 130$  Hz,  $g/2\pi = 129$  Hz,  $\omega_m/2\pi = 1.14$  MHz,  $m = 16$  ng,  $T = 11$  K,  $\Delta_0 = -2\kappa$  and the cutoff frequency  $\Omega = 5\omega_m$ .

strength  $g \rightarrow g\sqrt{\frac{2m\omega_m}{\hbar}}$ . This value according to Ref. [186] is chosen to be  $g/2\pi = 129$  Hz. In order to work in the high-temperature limit  $k_B T \gg \hbar\Omega \gg \hbar\omega_m$ , we set the cutoff frequency  $\Omega$  in Eq. (3.48) to  $5\omega_m$ . In our subsequent numerical investigations the detuning  $\Delta_0$  is always chosen in such way that bistability of the mechanical oscillator is avoided [187]. As a next step we need to understand which central frequency of the filter function  $\Omega_k$  gives us the best accuracy on the estimation of the coupling strength  $g$ . Therefore, we have calculated QFI as a function of  $\Omega_k$ , which has a peak at  $\Omega_k = 0$ , as shown in Fig. 6.27. Since we are in the rotating frame, this means that our detector filter function peaks at the laser frequency  $\omega_L$ .

Our goal is to find conditions for which the BHD results the best achievable estimation strategy. This would correspond to the saturation of the quantum Cramér–Rao bound. The outcome of the BHD depends on the quantum efficiency of the detectors  $\eta$  and on the quadrature phase  $\theta$  we choose to measure. Figs. 6.28 show the CFI as a function of these parameters. We notice that in the case of ideal detectors, i.e.,  $\eta = 1$ , the optimal choice for the phase  $\theta = \theta_{\max}$  leads the CFI to saturate the upper limit given by the QFI. This is a remarkable result that allows us to consider BHD as the optimal measurement that gives us the best estimate of  $g$ . In fact Fig. 6.28 b) shows that the detector's efficiency

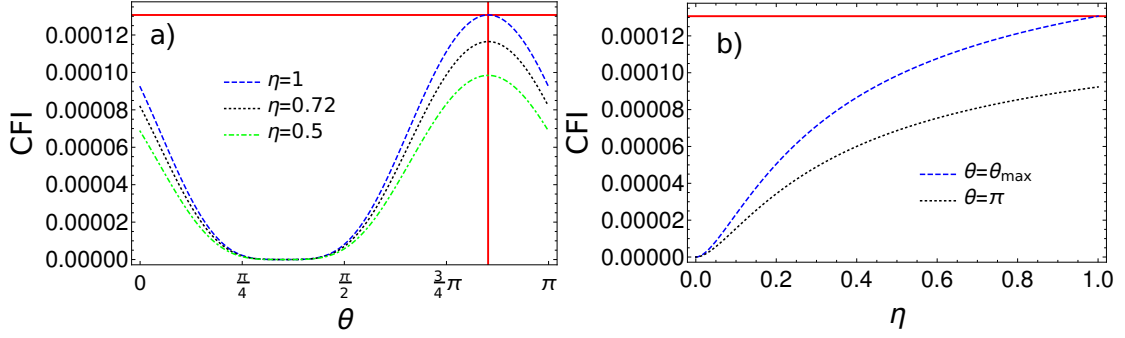


Figure 6.28: a) Classical Fisher information (CFI) as a function of the quadrature phase  $\theta$  for different values of  $\eta$ . b) CFI as a function of  $\eta$  for two different choices of  $\theta$ .  $\Omega_k = 0$  and the rest of the parameters are the same of Fig. 6.27.

$\eta$  is a very important parameter that affects the quality of the measurement, although it is no surprise that ideal photodetection results an optimal measurement scenario.

In general, an analytical solution for  $\theta_{\max}$  is very cumbersome, because the global maximum of either Eq. (6.158) or Eq. (6.159) depends on the entries of  $\sigma$  in Eq.(6.144), which are very complicated functions of the parameters of the system. However, the angle  $\theta_{\max}$  can be understood in the following way. Let us consider (6.159), which is the square of a generalized Rayleigh quotient for the self-adjoint matrix pairs  $(\partial_g \sigma, \sigma)$  (see for example Ref. [188]). Assuming that  $\sigma$  is positive definite, i.e, does not describe a pure state, we would like to maximize

$$f(\theta) = \frac{R_\theta^T \partial_g \sigma R_\theta}{R_\theta^T \sigma R_\theta}. \quad (6.160)$$

The maximum value that  $f(\theta)$  can reach is the maximum eigenvalue  $\lambda_{\max}$  of  $\sigma^{-1/2} \cdot \partial_g \sigma \cdot \sigma^{-1/2}$  when  $R_\theta$  is equal to the corresponding eigenvector  $v_{\max}$ , which automatically defines  $\theta_{\max}$ . In the case of (6.158) we have a squared sum of generalized Rayleigh quotients [189] and now  $\theta_{\max}$  can mostly be found by computational efforts.

Our numerical investigations show that the value of  $\theta_{\max}$  is most sensitive to changes in the value of detuning  $\Delta_0$  as well of the central frequency of the filter function  $\Omega_k$ . In order to gain some insight, we show in Fig. 6.29 a) the dependence of  $\theta_{\max}$  with respect to  $\Omega_k$ . We can see  $\theta_{\max}$  as a function of  $\Omega_k$  follows an inverted ramp function. The ramp starts at  $\kappa^2/\Delta_0$  and has a period of  $3\kappa$ . In the limit  $\Delta_0 \rightarrow -\infty$ ,  $\theta_{\max}$  tends to  $\pi$ . This is demonstrated in Fig.6.29 b), which shows the value of  $\theta_{\max}$  as a function of the ratio  $-\Delta_0/\kappa$ .

In the case of ideal detectors, i.e.  $\eta = 1$ , and choosing  $\theta = \theta_{\max}$  the curve of CFI as a function of  $\Omega_k$  perfectly overlaps with the curve of QFI on Fig. 6.27. Thus, we can definitely set  $\Omega_k = 0$  for the rest of our numerical analysis, because this choice guarantees

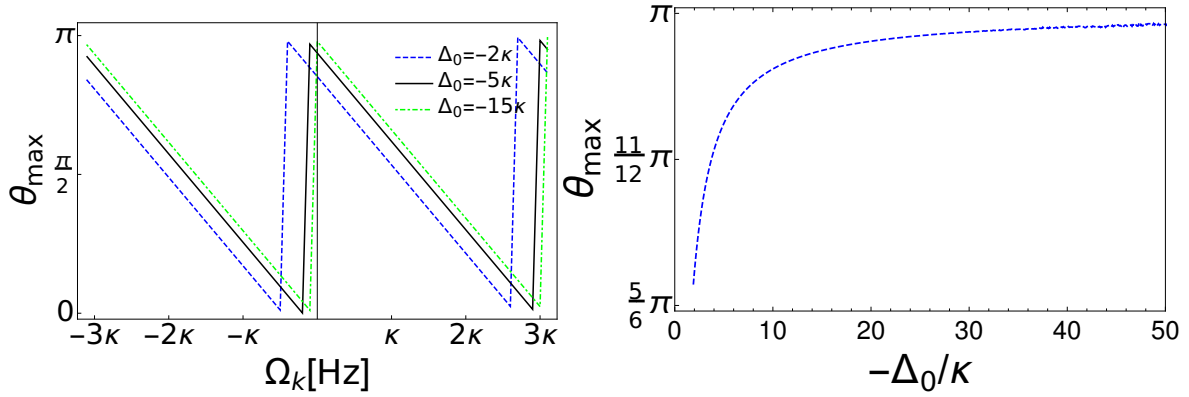


Figure 6.29: a) The quadrature phase  $\theta_{\max}$  as a function of the filter function's center frequency  $\Omega_k$  and for different values of the detuning  $\Delta_0$ . b)  $\theta_{\max}$  as a function of the detuning  $\Delta_0$  for  $\Omega_k = 0$ . All other parameters are the same of Fig. 6.27.

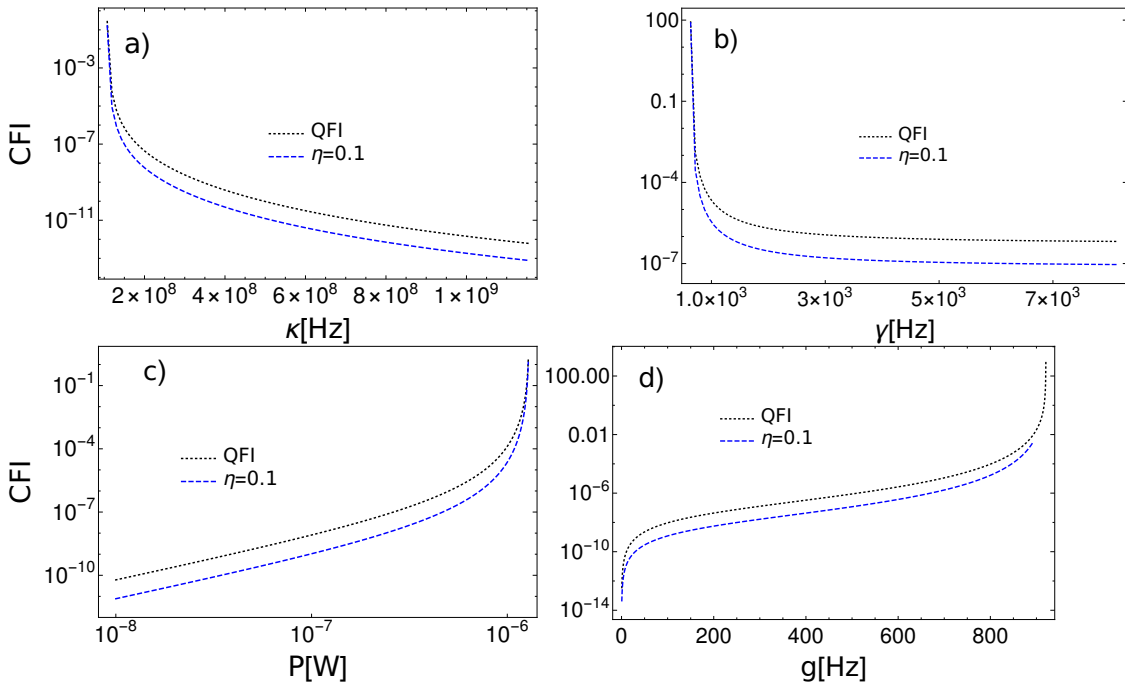


Figure 6.30: Classical Fisher information (CFI) as the function of the parameters  $\kappa$ ,  $\gamma$ ,  $P$  and  $g$ . We set  $\Delta_0 = -2\kappa$  and  $\Omega_k = 0$ . In the different figures we keep constant the parameter values of Fig. 6.27 and vary: a) the optical decay rate  $\kappa$ ; b) the mechanical decay rate  $\gamma$ ; c) the power of the driving laser  $P$ ; and in d) the value of the coupling constant  $g$ .

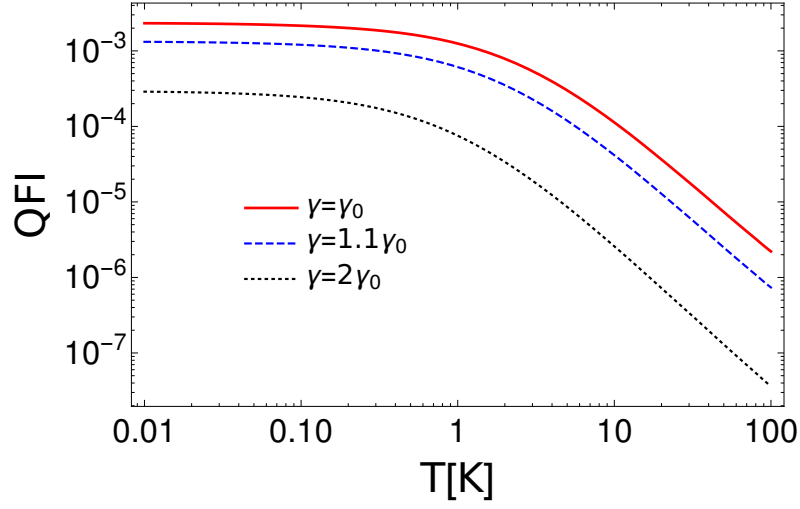


Figure 6.31: Semilogarithmic plot of the quantum Fisher Information (QFI) as a function of the mechanical bath temperature  $T$  for different values of the mechanical decay rate  $\gamma$ . Increasing  $\gamma$  leads to lower values of QFI.  $\gamma_0/2\pi = 130$  Hz and the rest of the parameters are the same of Fig. 6.27.

the maximum accuracy in the estimation scenario. Now, we show the CFI, calculated numerically as we vary selected parameters that appear in the dynamical matrix  $A$  of Eq. (3.51). The ranges of the plots are given by the stability conditions imposed on the system. Figs. 6.30 a) and 6.30 b) show the CFI as a function of the optical and mechanical decay rate respectively. These curves illustrate that increasing the decay rates lowers the accuracy of the estimation of the optomechanical coupling strength  $g$ . The opposite behavior is obtained increasing the power of the driving laser  $P$ , see Fig. 6.30 c). In this case a higher  $P$  leads to a higher value for the stationary field amplitude  $|\alpha|$ , which leads to more significant contribution to the dynamics from the optomechanical interaction as it appears in the interaction Hamiltonian  $g\alpha(a^\dagger + a)(b^\dagger + b)$ . Fig. 6.30 d) shows the CFI for different values of the optomechanical coupling strength. We remind the reader that the true value of  $g$  is yet unknown. The CFI has its minimum for  $g = 0$ , meaning that the accuracy is lower when the system experiences weaker optomechanical interactions. Conversely, the CFI increases monotonically with the value of  $g$  and it reaches its maximum when the system is on the threshold of the instability.

Fig. 6.31 shows the QFI as a function of the temperature of the mechanical bath. For high temperature the state tends to the maximally mixed state, regardless the value of  $g$ , and the QFI decreases. For this reason making measurements at low temperatures increases the estimation accuracy. QFI shows a sudden drop for a temperature around

1 K. This value depends on the particular choice of the spectral density (3.48) of the Brownian noise and on the other parameters of the system. As expected, increasing the value of  $\gamma$  leads to lower values of QFI, the accuracy of the estimation becomes worse.

## 6.7 | Summary

In this Chapter we have introduced estimation theory focusing in the quantum version of the theory. Two prominent approaches have been considered, the Bayesian and the frequentistic approach. The Bayesian approach starts from a prior probability distribution for the true value of the parameter to be estimated. Indeed, the prior probability can be given by previous measurements, or by the physics of the system. After measurements, the probability distribution is updated with the outcomes giving a posteriori distribution and a new estimation for the true value. This exploits the Bayes rule for conditional probabilities. On the other hand, the frequentistic approach blames the uncertainty in our knowledge to a little number of measurements. For this reason the frequentistic philosophy believes the uncertainty of the estimate could be reduced to its minimum, if an infinite number of data is provided. This approach aims to find this minimum and gives its value for a given measurement apparatus, and this is the meaning we should give to the Fisher information and its quantum counterpart.

Here, we applied this analysis for the inference of the optomechanical coupling strength, finding very different results, which accounts for the different nature of the two approaches. In the Bayes approach, the POVM which minimizes the mean-squared error of the estimate does not correspond to any implementable measurement, at least with current technology. On the other hand, following the Fisher approach, our analysis suggests that balanced homodyne photodetection plays a fundamentally important role in the estimation of the optomechanical coupling strength. However, it must be mentioned that our work is valid only for unbiased estimators. In both cases, finding the smallest lower bound for the mean-squared error might reinforce our prior expectation of the value of the optomechanical coupling strength. It is also important to mention that the use of  $N$  independent and identical repetitions of the measurement scenario reduces the lower bound of the mean-squared error by a factor of  $N^{-1}$  [190].

Finally, our work bridges cavity optomechanics and inference techniques with the help of experimentally plausible models and parameter values and could serve as a guide for the optimal experimental characterization of optomechanical systems, which plays important roles in the application of these models for quantum transport and optomechanically-based information devices.

## Conclusion and outlooks

This thesis has covered a broad spectrum and different branches of condensed matter and theoretical physics. The main focus has been presented in Chapter 2, optomechanics, which will have a prominent role in future quantum technologies. Here, we introduced the subject and derived the Hamiltonian which better describes the dynamics in Sec. 2.2, starting from classical arguments and then applying the canonical quantization. The quadratic nature of the Hamiltonian makes very difficult to solve the Schrödinger equation, but in special cases which are shown in Sec. 2.2.1. Usually, in a feasible experimental scenario, a strong laser drives the system to a Gaussian steady state and the dynamics is described by means of the fluctuation operators around their mean value. Thus, the dynamics of the system gets to be linear in the fluctuation operators and we can easily find a solution of the equations of motion. This procedure and the mathematics behind it is described in Secs. 2.3, 2.4 and 2.5.

In Chapter 3 we went into the details of the equations of motions, applying the formalism of open quantum system. In particular we focused on the classical Langevin equation in Sec. 3.2 and its quantum counterpart in Sec. 3.3, in order to find the input-output relation in 3.3.2 and the equation of motions for the optomechanical cavity in Sec. 3.4. The open quantum system description is necessary as the optomechanical cavity is driven by a laser and subject to external noise. The laser provides Markovian noise to the electromagnetic field inside the cavity and the mechanical motion experiences quantum Brownian noise coming from the environment. Brownian noise is intrinsically non-Markovian and this results into more cumbersome equations. Nevertheless, in Sec. 3.4 we found a description of the Gaussian steady state in terms of the covariance matrix of the optomechanical operators.

Chapter 4 gets into the heart of the thesis and of the doctoral work. Here we introduced quantum transport and showed the relevant Green-Kubo formalism in Sec. 4.2, which



allowed us to relate the Green's function with the transport properties of the system. In Sec. 4.3 we analyzed a one dimensional chain described by tight-binding Hamiltonian and composed by three blocks, the sender, the wire and the receiver. The three block are coupled together with a weak coupling and we set our initial state to be localized in the sender. The energy spectrum provided by the weak coupling leads the dynamics to follow a Rabi-like cycle that transfers the state from the sender to the receiver. Here we analyzed the transfer probability and the dynamics for excitations of fermionic and bosonic nature finding the similarities and differences between them. In general we found that the fermionic dynamics gives the envelop curve of the bosonic dynamics, with the result that the transfer is performed in similar time for the two species. In Sec. 4.6 we analyzed the transfer of entanglement in the same system. Different measures of entanglement for a tripartite system had been analyzed in order to give a strong statement about the performance of the transfer. This system has little to do with optomechanics, however, it allowed us to introduce quantum transport and to see a system where you can have high fidelity transfer. We leave for future works the analysis of the performance of the transport under external noise. Furthermore we can associate to each site two different coupled modes resembling an optomechanical cavity and check the different behaviors obtained. As a final remark on this work, we need to acknowledge the periodic nature of the transfer. Even though this system has been proposed for charging quantum batteries and can indeed have many applications on this field, the reader should notice it does not allow the receiver to be connected to the system for an indefinitely amount of time. This issue can be solved disconnecting the battery after half period of the Rabi cycle, however this solution may not be satisfactory to most. For this reason, in Chapter 5 we showed particular materials which allow only one direction of propagation and they are called topological insulators. We introduced in Sec. 5.2 and 5.3 the classical and quantum Hall effect respectively as they provide a basis for understanding the topic. They also represent the first example where topological insulators arise in physical systems. We then put a focus on the mathematics of topological insulators in Sec. 5.5. They are called topological because their properties strictly depend on the topology of the parameter space where they are defined. Once this relation had been made clear, topology has been used to describe very different physical phenomena, from the Aharonov-Bohm effect in classical electromagnetism to gauge theories in quantum mechanics. The link is in the appearance of a geometric phase which directly comes from the topology of the space where the quantum states are defined. Moreover, given a symmetry of the system and a gauge theory we can relate it to a geometric phase and consequently to a geometric invariant. In condensed matter physics Chern insulators are topological insulators defined on a 2d lattice. The

parameter space we consider is the Brillouin zone. Breaking the time-reversal symmetry of the system leads to a system with back-scattering immune conductive states, called edge states. In Sec. 5.7 we applied the theory on an array composed by optomechanical microresonators. In order to break the time-reversal symmetry we built the lattice connecting the microresonators through a non symmetric optical wave-guide. Analyzing the spectrum of the system we discovered the presence of mechanical edge modes able to topologically transport phonons through the array. We tested the transport inserting mechanical disorder in the system, confirming the robustness of the transport. For a high level of disorder the topology of the system is changed and the system experiences a topological phase transition, losing the edge modes. The mechanical edge modes in our system are to be found in a band gap that is created by the avoided crossing between the optical and mechanical band. As a note, the spacing is given by the optomechanical coupling, therefore we need a good knowledge of the coupling strength in order to locate the edge states.

What underlies our ability of controlling and using these systems for cutting-edge technological applications is, ultimately, the knowledge we have of the system's parameters. In Chapter 6 we introduced parameter estimation theory. This tool teaches us how we can extrapolate the maximum information from a system in order to infer the parameters value. Two main approaches are used, the Bayesian and the frequentistic, or Fisher, approach. Both are described respectively in the classical theory in Secs. 6.1.1 and 6.1.2, and in the quantum theory in Secs. 6.2.1 and 6.2.2. Bayes approach considers the parameter distributed as a random variable with its own probability distribution function. At the same time the estimation of the parameter is naturally subject to a possibility of a mistake and some errors can be bigger than others. Therefore Bayes approach considers a cost function in order to quantify the amount of error and it seeks to find an estimation strategy which minimizes the average cost function. Fisher approach, on the other hand considers the parameter having a fixed value and our uncertainty on it is given by the low number of data on the system we have. As in the frequentistic approach to probability any uncertainty on the parameter value could be in theory solved for a number of data that goes to infinity. The goal of this approach is to find the best strategy which minimizes the mean-squared error associated with the measurement. In Sec. 6.3 we applied quantum Bayesian estimation to the inference of the optomechanical coupling strength and in Sec. 6.5 we applied it to the estimation of the dipole-matter interaction coupling strength. For both the systems we found the optimal strategy is not implementable directly in a laboratory, if not for some particular cases. However, Bayesian strategy offers a crucial starting point for the estimation of a parameters, since what it does is to update the probability distribution function of the random param-

eter with the new information acquired from the data. It is at this point the cunning experimentalist passes into the Fisher approach and tries to maximize the precision of the measurement around the most probable value. Indeed, in Sec 6.6 we analyzed the estimation of the optomechanical coupling following the Fisher approach. We calculated the quantum and classical Fisher information, which are related to the variance of the estimate thanks to the Cramér–Rao theorem. The quantum Fisher information is a property of the quantum state and it gives the minimum amount of variance one could ever get from a single measurement. The classical Fisher information is a property of the state as well as of the measurement we perform. The purpose of this analysis is to find a measurement for which the classical Fisher information is as large as the quantum Fisher information. We accomplished this task finding the ideal balanced homodyne detection has equal classical and quantum Fisher information.

Future works will aim to apply multiparameter investigation on optomechanical system. As mentioned above, a laser with a frequency centered in correspondence of an optical mode of the cavity and with bandwidth narrower than the spacing between the optical modes is able to populate only that particular mode and the description we found in Sec. 2.2 can be quite accurate. However nothing prevents us to consider several mechanical modes each of them coupled with the electromagnetic field with its own coupling. We look further into applying estimation theory to this problem which can give us more insight about the physics of optomechanics. Furthermore, the transport properties of the materials (either topological or not), can be obtained with the Green–Kubo formula. This results in a straightforward relation between the transport coefficients and the correlations among the operators. An analysis of the optimal measurements is in order, to maximize the amount of information we may obtain for the inference of the transport parameters.

---

## References

- [1] József Zsolt Bernád, Claudio Sanavio, and André Xuereb. Optimal estimation of the optomechanical coupling strength. *Phys. Rev. A*, 97:063821, Jun 2018. doi: 10.1103/PhysRevA.97.063821. URL <https://link.aps.org/doi/10.1103/PhysRevA.97.063821>.
- [2] József Zsolt Bernád, Claudio Sanavio, and André Xuereb. Optimal estimation of matter-field coupling strength in the dipole approximation. *Phys. Rev. A*, 99:062106, Jun 2019. doi: 10.1103/PhysRevA.99.062106. URL <https://link.aps.org/doi/10.1103/PhysRevA.99.062106>.
- [3] Claudio Sanavio, József Zsolt Bernád, , and André Xuereb. Fisher information based estimation of optomechanical coupling strengths. *arXiv e-prints*, art. arXiv:2002.03249, February 2020.
- [4] Wayne Jordan Chetcuti, Claudio Sanavio, Salvatore Lorenzo, and Tony J G Apollaro. Perturbative many-body transfer. *New Journal of Physics*, 22(3):033030, mar 2020. doi: 10.1088/1367-2630/ab7a33. URL <https://doi.org/10.1088/1367-2630/ab7a33>.
- [5] Tony J.G. Apollaro, Claudio Sanavio, Wayne Jordan Chetcuti, and Salvatore Lorenzo. Multipartite entanglement transfer in spin chains. *Physics Letters A*, page 126306, 2020. ISSN 0375-9601. doi: <https://doi.org/10.1016/j.physleta.2020.126306>. URL <http://www.sciencedirect.com/science/article/pii/S0375960120301055>.
- [6] Claudio Sanavio, Vittorio Peano, and André Xuereb. Nonreciprocal topological phononics in optomechanical arrays. *Phys. Rev. B*, 101:085108, Feb 2020. doi: 10.1103/PhysRevB.101.085108. URL <https://link.aps.org/doi/10.1103/PhysRevB.101.085108>.
- [7] C. E. Guillaume. The nobel prize in physics 1920. URL <https://www.nobelprize.org/prizes/physics/1920/guillaume/lecture/>.
- [8] Markus Aspelmeyer, Tobias J. Kippenberg, and Florian Marquardt. Cavity optomechanics. *Rev. Mod. Phys.*, 86:1391–1452, 12 2014. doi: 10.1103/RevModPhys.86.1391. URL <https://link.aps.org/doi/10.1103/RevModPhys.86.1391>.
- [9] C. K. Law. Interaction between a moving mirror and radiation pressure: A hamiltonian formulation. *Phys. Rev. A*, 51:2537–2541, 3 1995. doi: 10.1103/PhysRevA.51.2537. URL <https://link.aps.org/doi/10.1103/PhysRevA.51.2537>.

- [10] R. W. Andrews, R. W. Peterson, T. P. Purdy, K. Cicak, R. W. Simmonds, C. A. Regal, and K. W. Lehnert. Bidirectional and efficient conversion between microwave and optical light. *Nature Physics*, 10:321, March 2014. URL <https://doi.org/10.1038/nphys2911>.
- [11] Mian Zhang, Shreyas Shah, Jaime Cardenas, and Michal Lipson. Synchronization and Phase Noise Reduction in Micromechanical Oscillator Arrays Coupled through Light. *Physical Review Letters*, 115(16):163902, October 2015. doi: 10.1103/PhysRevLett.115.163902. URL <https://link.aps.org/doi/10.1103/PhysRevLett.115.163902>.
- [12] Chandrasekhar Ramanathan, Paola Cappellaro, Lorenza Viola, and David G Cory. Experimental characterization of coherent magnetization transport in a one-dimensional spin system. *New Journal of Physics*, 13(10):103015, oct 2011. doi: 10.1088/1367-2630/13/10/103015. URL <https://doi.org/10.1088/1367-2630/13/10/103015>.
- [13] Daichi Hirobe, Masahiro Sato, Takayuki Kawamata, Yuki Shiomi, Ken-ichi Uchida, Ryo Iguchi, Yoji Koike, Sadamichi Maekawa, and Eiji Saitoh. One-dimensional spinon spin currents. *Nature Physics*, 13:30 EP –, Sep 2016. URL <https://doi.org/10.1038/nphys3895>.
- [14] Takeshi Fukuhara, Adrian Kantian, Manuel Endres, Marc Cheneau, Peter Schauß, Sebastian Hild, David Bellem, Ulrich Schollwöck, Thierry Giamarchi, Christian Gross, Immanuel Bloch, and Stefan Kuhr. Quantum dynamics of a mobile spin impurity. *Nature Physics*, 9:235 EP –, Feb 2013. URL <https://doi.org/10.1038/nphys2561>. Article.
- [15] Johannes Zeiher, Jae-yoon Choi, Antonio Rubio-Abadal, Thomas Pohl, Rick van Bijnen, Immanuel Bloch, and Christian Gross. Coherent many-body spin dynamics in a long-range interacting ising chain. *Phys. Rev. X*, 7:041063, Dec 2017. doi: 10.1103/PhysRevX.7.041063. URL <https://link.aps.org/doi/10.1103/PhysRevX.7.041063>.
- [16] Matthias Christandl, Nilanjana Datta, Artur Ekert, and Andrew J. Landahl. Perfect state transfer in quantum spin networks. *Phys. Rev. Lett.*, 92:187902, May 2004. doi: 10.1103/PhysRevLett.92.187902. URL <https://link.aps.org/doi/10.1103/PhysRevLett.92.187902>.
- [17] Gurmeet Kaur and Paola Cappellaro. Initialization and readout of spin chains for quantum information transport. *New Journal of Physics*, 14(8):083005, aug 2012. doi: 10.1088/1367-2630/14/8/083005. URL <https://doi.org/10.1088/1367-2630/14/8/083005>.
- [18] C. Di Franco, M. Paternostro, and M. S. Kim. Perfect state transfer on a spin chain without state initialization. *Phys. Rev. Lett.*, 101:230502, Dec 2008. doi: 10.1103/PhysRevLett.101.230502. URL <https://link.aps.org/doi/10.1103/PhysRevLett.101.230502>.
- [19] Robert J. Chapman, Matteo Santandrea, Zixin Huang, Giacomo Corrielli, Andrea Crespi, Man-Hong Yung, Roberto Osellame, and Alberto Peruzzo. Experimental perfect state transfer of an entangled photonic qubit. *Nature Communications*, 7:11339 EP –, Apr 2016. URL <https://doi.org/10.1038/ncomms11339>. Article.
- [20] S. Lorenzo, T. J. G. Apollaro, A. Sindona, and F Plastina. Quantum-state transfer via resonant tunnelling through local-field-induced barriers. *Phys. Rev. A*, 87:042313, 2013.

- [21] Guilherme M. A. Almeida, Francesco Ciccarello, Tony J. G. Apollaro, and Andre M. C. Souza. Quantum-state transfer in staggered coupled-cavity arrays. *Phys. Rev. A*, 93:032310, Mar 2016. doi: 10.1103/PhysRevA.93.032310. URL <https://link.aps.org/doi/10.1103/PhysRevA.93.032310>.
- [22] L Banchi, T J G Apollaro, A Cuccoli, R Vaia, and P Verrucchi. Long quantum channels for high-quality entanglement transfer. *New Journal of Physics*, 13(12):123006, dec 2011. doi: 10.1088/1367-2630/13/12/123006. URL <https://doi.org/10.1088/1367-2630/13/12/123006>.
- [23] T. J. G. Apollaro, L. Banchi, A. Cuccoli, R. Vaia, and P. Verrucchi. 99%-fidelity ballistic quantum-state transfer through long uniform channels. *Phys. Rev. A*, 85:052319, May 2012. doi: 10.1103/PhysRevA.85.052319. URL <https://link.aps.org/doi/10.1103/PhysRevA.85.052319>.
- [24] Guilherme M. A. Almeida. Interplay between speed and fidelity in off-resonant quantum-state-transfer protocols. *Phys. Rev. A*, 98:012334, Jul 2018. doi: 10.1103/PhysRevA.98.012334. URL <https://link.aps.org/doi/10.1103/PhysRevA.98.012334>.
- [25] Rafael Vieira and Gustavo Rigolin. Almost perfect transport of an entangled two-qubit state through a spin chain. *Physics Letters A*, 382(36):2586 – 2594, 2018. ISSN 0375-9601. doi: <https://doi.org/10.1016/j.physleta.2018.07.027>. URL <http://www.sciencedirect.com/science/article/pii/S0375960118307710>.
- [26] Rúben Sousa and Yasser Omar. Pretty good state transfer of entangled states through quantum spin chains. *New Journal of Physics*, 16(12):123003, 2014. URL <http://stacks.iop.org/1367-2630/16/i=12/a=123003>.
- [27] Salvatore Lorenzo, Tony J. G. Apollaro, Andrea Trombettoni, and Simone Paganelli. 2-qubit quantum state transfer in spin chains and cold atoms with weak links. *International Journal of Quantum Information*, 15(05):1750037, 2017. doi: 10.1142/S021974991750037X. URL <https://doi.org/10.1142/S021974991750037X>.
- [28] T J G Apollaro, S Lorenzo, A Sindona, S Paganelli, G L Giorgi, and F Plastina. Many-qubit quantum state transfer via spin chains. *Physica Scripta*, 2015(T165):014036, 2015. URL <http://stacks.iop.org/1402-4896/2015/i=T165/a=014036>.
- [29] Michael A. Nielsen and Isaac L. Chuang. *Quantum Computation and Quantum Information: 10th Anniversary Edition*. Cambridge University Press, New York, NY, USA, 10th edition, 2011. ISBN 1107002176, 9781107002173.
- [30] Sebastian Deffner and Steve Campbell. *Quantum Thermodynamics*. 2053-2571. Morgan and Claypool Publishers, 2019. ISBN 978-1-64327-658-8. doi: 10.1088/2053-2571/ab21c6. URL <http://dx.doi.org/10.1088/2053-2571/ab21c6>.
- [31] Mohammad Hafezi and Peter Rabl. Optomechanically induced non-reciprocity in microring resonators. *Opt. Express*, 20(7):7672–7684, Mar 2012. doi: 10.1364/OE.20.007672. URL <http://www.opticsexpress.org/abstract.cfm?URI=oe-20-7-7672>.
- [32] Mohammad Hafezi, Eugene A. Demler, Mikhail D. Lukin, and Jacob M. Taylor. Robust optical delay lines with topological protection. *Nature Physics*, 7:907 EP –, Aug 2011. URL <https://doi.org/10.1038/nphys2063>.

- [33] M. Hafezi, S. Mittal, J. Fan, A. Migdall, and J. M. Taylor. Imaging topological edge states in silicon photonics. *Nature Photonics*, 7(12):1001–1005, 2013. doi: 10.1038/nphoton.2013.274.
- [34] S. Hossein Mousavi, Alexander B. Khanikaev, and Zheng Wang. Topologically protected elastic waves in phononic metamaterials. *Nature Communications*, 6:8682, November 2015. ISSN 2041-1723. doi: 10.1038/ncomms9682. URL <http://www.nature.com/ncomms/2015/151104/ncomms9682/full/ncomms9682.html>.
- [35] Christian Brendel, Vittorio Peano, Oskar J. Painter, and Florian Marquardt. Pseudomagnetic fields for sound at the nanoscale. *Proc. Nat. Acad. Sci. U.S.A.*, 114(17), 2017. ISSN 0027-8424. URL <https://www.pnas.org/content/114/17/E3390>.
- [36] Christian Brendel, Vittorio Peano, Oskar Painter, and Florian Marquardt. Snowflake phononic topological insulator at the nanoscale. *Physical Review B*, 97(2):020102, January 2018. doi: 10.1103/PhysRevB.97.020102. URL <https://link.aps.org/doi/10.1103/PhysRevB.97.020102>.
- [37] Si-Yuan Yu, Cheng He, Zhen Wang, Fu-Kang Liu, Xiao-Chen Sun, Zheng Li, Hai-Zhou Lu, Ming-Hui Lu, Xiao-Ping Liu, and Yan-Feng Chen. Elastic pseudospin transport for integratable topological phononic circuits. *Nature Communications*, 9(1):3072, August 2018. ISSN 2041-1723. doi: 10.1038/s41467-018-05461-5. URL <https://doi.org/10.1038/s41467-018-05461-5>.
- [38] Jinwoong Cha, Kun Woo Kim, and Chiara Daraio. Experimental realization of on-chip topological nanoelectromechanical metamaterials. *Nature (London)*, 564(7735):229–233, 2018. ISSN 1476-4687. doi: 10.1038/s41586-018-0764-0. URL <https://doi.org/10.1038/s41586-018-0764-0>.
- [39] V. Peano, C. Brendel, M. Schmidt, and F. Marquardt. Topological phases of sound and light. *Phys. Rev. X*, 5:031011, Jul 2015. doi: 10.1103/PhysRevX.5.031011. URL <https://link.aps.org/doi/10.1103/PhysRevX.5.031011>.
- [40] John P. Mathew, Javier del Pino, and Ewold Verhagen. Synthetic gauge fields for phonon transport in a nano-optomechanical system.
- [41] Jari Kaipio and Erkki Somersalo. Statistical inverse problems. *J. Comput. Appl. Math.*, 198(2):493–504, 01 2007. ISSN 0377-0427. doi: 10.1016/j.cam.2005.09.027. URL <http://dx.doi.org/10.1016/j.cam.2005.09.027>.
- [42] S. Personick. Application of quantum estimation theory to analog communication over quantum channels. *IEEE Transactions on Information Theory*, 17(3):240–246, 05 1971. ISSN 0018-9448. doi: 10.1109/TIT.1971.1054643.
- [43] A.S Holevo. Statistical decision theory for quantum systems. *Journal of Multivariate Analysis*, 3(4): 337 – 394, 1973. ISSN 0047-259X. doi: [https://doi.org/10.1016/0047-259X\(73\)90028-6](https://doi.org/10.1016/0047-259X(73)90028-6). URL <http://www.sciencedirect.com/science/article/pii/0047259X73900286>.
- [44] Carl W. Helstrom. Quantum detection and estimation theory. *Journal of Statistical Physics*, 1(2): 231–252, 06 1969. ISSN 1572-9613. doi: 10.1007/BF01007479. URL <https://doi.org/10.1007/BF01007479>.

- [45] K. Macieszczak, M. Fraas, and R. Demkowicz-Dobrzański. Bayesian quantum frequency estimation in presence of collective dephasing. *New J. Phys.*, 16:113002, 2014. doi: 10.1088/1367-2630/16/11/113002.
- [46] W. Rzadkowski and R. Demkowicz-Dobrzański. Discrete-to-continuous transition in quantum phase estimation. *Phys. Rev. A*, 96:032319, 2017. doi: 10.1103/PhysRevA.96.032319.
- [47] J. Rubio and J. Dunningham. Quantum metrology in the presence of limited data. *New J. Phys.*, 21:043037, 2019. doi: 10.1088/1367-2630/ab098b.
- [48] G. A. Brawley, M. R. Vanner, P. E. Larsen, S. Schmid, A. Boisen, and W. P. Bowen. Nonlinear optomechanical measurement of mechanical motion. *Nat. Commun.*, 7:10988, 2016. doi: 10.1038/ncomms10988.
- [49] Sankhā A. Bhattacharyya. *Indian J. Stat.*, 8:201, 1946.
- [50] E. W. Barankin. Locally best unbiased estimates. *Ann. Math. Statist.*, 20:477, 1949. URL <http://www.jstor.org/stable/2236306>.
- [51] C. R. Rao. Information and accuracy attainable in the estimation of statistical parameters. *Bull. Calcutta Math. Soc.*, 37:81, 1945.
- [52] H. Cramér. Princeton University Press, 1946.
- [53] Carl W. Helstrom. *Quantum detection and estimation theory / Carl W. Helstrom*. Academic Press New York, 1976. ISBN 0123400503.
- [54] M. G. A. Paris. Quantum estimation for quantum technology. *Int. J. Quantum Inf.*, 7:125, 2009.
- [55] A. I. Lvovsky and M. G. Raymer. Continuous-variable optical quantum-state tomography. *Rev. Mod. Phys.*, 81:299, 2009. doi: 10.1103/RevModPhys.81.299.
- [56] J. Kepler. *De cometis libelli tres*. Kepler, J., 1619.
- [57] E. F. Nichols and G. F. Hull. A preliminary communication on the pressure of heat and light radiation. *Phys. Rev. (Series I)*, 13:307–320, 11 1901. doi: 10.1103/PhysRevSeriesI.13.307. URL <https://link.aps.org/doi/10.1103/PhysRevSeriesI.13.307>.
- [58] W. Crookes. On attraction and repulsion resulting from radiation. *Phil. Trans. R. Soc.*, 164, 1874. URL <http://doi.org/10.1098/rstl.1874.0015>.
- [59] P. Lebedev. The experimental study of the pressure of the light. *Annalen der Physik*, 433, 6 1901.
- [60] R. Frisch. Experimenteller nachweis des einsteinschen strahlungsrückstoßes. *Zeitschrift für Physik*, 86:42–48, 1 1933. doi: 10.1007/BF01340182.
- [61] Richard A. Beth. Mechanical detection and measurement of the angular momentum of light. *Phys. Rev.*, 50:115–125, 7 1936. doi: 10.1103/PhysRev.50.115. URL <https://link.aps.org/doi/10.1103/PhysRev.50.115>.



- [62] A. Ashkin. Trapping of atoms by resonance radiation pressure. *Phys. Rev. Lett.*, 40:729–732, 3 1978. doi: 10.1103/PhysRevLett.40.729. URL <https://link.aps.org/doi/10.1103/PhysRevLett.40.729>.
- [63] William D. Phillips. Nobel lecture: Laser cooling and trapping of neutral atoms. *Rev. Mod. Phys.*, 70: 721–741, Jul 1998. doi: 10.1103/RevModPhys.70.721. URL <https://link.aps.org/doi/10.1103/RevModPhys.70.721>.
- [64] Immanuel Bloch, Jean Dalibard, and Wilhelm Zwerger. Many-body physics with ultracold gases. *Rev. Mod. Phys.*, 80:885–964, 7 2008. doi: 10.1103/RevModPhys.80.885. URL <https://link.aps.org/doi/10.1103/RevModPhys.80.885>.
- [65] Paolo Polimeno, Alessandro Magazzù, Maria Antonia Iatì, Francesco Patti, Rosalba Saija, Cristian Degli Esposti Boschi, Maria Grazia Donato, Pietro G. Gucciardi, Philip H. Jones, Giovanni Volpe, and Onofrio M. Maragò. Optical tweezers and their applications. *Journal of Quantitative Spectroscopy and Radiative Transfer*, 218:131 – 150, 2018. ISSN 0022-4073. doi: <https://doi.org/10.1016/j.jqsrt.2018.07.013>. URL <http://www.sciencedirect.com/science/article/pii/S002240731830445X>.
- [66] S. Mancini and P. Tombesi. Quantum noise reduction by radiation pressure. *Phys. Rev. A*, 49: 4055–4065, 5 1994. doi: 10.1103/PhysRevA.49.4055. URL <https://link.aps.org/doi/10.1103/PhysRevA.49.4055>.
- [67] K. Jacobs, P. Tombesi, M. J. Collett, and D. F. Walls. Quantum-nondemolition measurement of photon number using radiation pressure. *Phys. Rev. A*, 49:1961–1966, 3 1994. doi: 10.1103/PhysRevA.49.1961. URL <https://link.aps.org/doi/10.1103/PhysRevA.49.1961>.
- [68] Stefan L. Danilishin and Farid Ya. Khalili. Quantum measurement theory in gravitational-wave detectors. *Living Reviews in Relativity*, 15(1):5, 4 2012. ISSN 1433-8351. doi: 10.12942/lrr-2012-5. URL <https://doi.org/10.12942/lrr-2012-5>.
- [69] C. K. Law. Effective hamiltonian for the radiation in a cavity with a moving mirror and a time-varying dielectric medium. *Phys. Rev. A*, 49:433–437, 01 1994. doi: 10.1103/PhysRevA.49.433. URL <https://link.aps.org/doi/10.1103/PhysRevA.49.433>.
- [70] R. Loudon. Radiation pressure and momentum in dielectrics. *Fortschritte der Physik*, 52(11-12):1134–1140, 2004. doi: 10.1002/prop.200410183. URL <https://onlinelibrary.wiley.com/doi/abs/10.1002/prop.200410183>.
- [71] Günter Plunien, Berndt Müller, and Walter Greiner. The casimir effect. *Physics Reports*, 134(2):87 – 193, 1986. ISSN 0370-1573. doi: [https://doi.org/10.1016/0370-1573\(86\)90020-7](https://doi.org/10.1016/0370-1573(86)90020-7). URL <http://www.sciencedirect.com/science/article/pii/0370157386900207>.
- [72] A. Xuereb and M. Paternostro. Selectable linear or quadratic coupling in an optomechanical system. *Physical Review A*, 87:023830, 2013.
- [73] Perelomov A. *Generalized Coherent States and Their Applications*. Springer-Verlag Berlin Heidelberg, 1986. doi: 10.1007/2F978-3-642-61629-7.

- [74] J Z Bernád, H Frydrych, and G Alber. Centre-of-mass motion-induced decoherence and entanglement generation in a hybrid quantum repeater. *Journal of Physics B: Atomic, Molecular and Optical Physics*, 46(23):235501, 2013. URL <http://stacks.iop.org/0953-4075/46/i=23/a=235501>.
- [75] Roy J. Glauber. Photon correlations. *Phys. Rev. Lett.*, 10:84–86, 02 1963. doi: 10.1103/PhysRevLett.10.84. URL <https://link.aps.org/doi/10.1103/PhysRevLett.10.84>.
- [76] E. C. G. Sudarshan. Equivalence of semiclassical and quantum mechanical descriptions of statistical light beams. *Phys. Rev. Lett.*, 10:277–279, 04 1963. doi: 10.1103/PhysRevLett.10.277. URL <https://link.aps.org/doi/10.1103/PhysRevLett.10.277>.
- [77] Wolfgang P. Schleich. *Quantum Optics in Phase Space*. John Wiley and Sons, Ltd, 2005. ISBN 9783527602971. doi: 10.1002/3527602976. URL <https://onlinelibrary.wiley.com/doi/abs/10.1002/3527602976>.
- [78] C. W. Gardiner and M. J. Collett. Input and output in damped quantum systems: Quantum stochastic differential equations and the master equation. *Phys. Rev. A*, 31:3761–3774, Jun 1985. doi: 10.1103/PhysRevA.31.3761. URL <https://link.aps.org/doi/10.1103/PhysRevA.31.3761>.
- [79] T. J. Kippenberg and K. J. Vahala. Cavity optomechanics: Back-action at the mesoscale. *Science*, 321(5893):1172–1176, 2008. ISSN 0036-8075. doi: 10.1126/science.1156032. URL <http://science.sciencemag.org/content/321/5893/1172>.
- [80] Cheng Yang, Lin Zhang, and Weiping Zhang. Squeezed cooling of mechanical motion beyond the resolved-sideband limit. *EPL (Europhysics Letters)*, 122(1):14001, 2018. URL <http://stacks.iop.org/0295-5075/122/i=1/a=14001>.
- [81] Jasper Chan, T. P. Mayer Alegre, Amir H. Safavi-Naeini, Jeff T. Hill, Alex Krause, Simon Gröblacher, Markus Aspelmeyer, and Oskar Painter. Laser cooling of a nanomechanical oscillator into its quantum ground state. *Nature*, 478:89 EP –, 10 2011. URL <https://doi.org/10.1038/nature10461>.
- [82] H.-P. Breuer and F. Petruccione. *The theory of open quantum systems*. Oxford University Press, Oxford, 2002. doi: 10.1093/9780199213900.
- [83] D. Manzano. A short introduction to the lindblad master equation. *AIP Advances*, 10(2):025106, 2020. doi: 10.1063/1.5115323. URL <https://doi.org/10.1063/1.5115323>.
- [84] Vittorio Giovannetti and David Vitali. Phase-noise measurement in a cavity with a movable mirror undergoing quantum brownian motion. *Phys. Rev. A*, 63:023812, Jan 2001. doi: 10.1103/PhysRevA.63.023812. URL <https://link.aps.org/doi/10.1103/PhysRevA.63.023812>.
- [85] C.W. Gardiner. *Quantum noise*. Springer series in synergetics. Springer-Verlag, 1991. ISBN 9783540536086. URL <https://books.google.com/books?id=nMfvAAAAAAAJ>.
- [86] P D Drummond and D F Walls. Quantum theory of optical bistability. i. nonlinear polarisability model. *Journal of Physics A: Mathematical and General*, 13(2):725–741, feb 1980. doi: 10.1088/0305-4470/13/2/034. URL <https://doi.org/10.1088/0305-4470/13/2/034>.

- [87] A. Dorsel, J. D. McCullen, P. Meystre, E. Vignes, and H. Walther. Optical bistability and mirror confinement induced by radiation pressure. *Phys. Rev. Lett.*, 51:1550–1553, Oct 1983. doi: 10.1103/PhysRevLett.51.1550. URL <https://link.aps.org/doi/10.1103/PhysRevLett.51.1550>.
- [88] Bonny L. Schumaker. Quantum mechanical pure states with gaussian wave functions. *Physics Reports*, 135(6):317 – 408, 1986. ISSN 0370-1573. doi: [https://doi.org/10.1016/0370-1573\(86\)90179-1](https://doi.org/10.1016/0370-1573(86)90179-1). URL <http://www.sciencedirect.com/science/article/pii/0370157386901791>.
- [89] G. Adam. Density matrix elements and moments for generalized gaussian state fields. *Journal of Modern Optics*, 42(6):1311–1328, 1995. doi: 10.1080/09500349514551141. URL <https://doi.org/10.1080/09500349514551141>.
- [90] R. Zwanzig and Inc Books24x7. *Nonequilibrium Statistical Mechanics*. OUP USA, 2001. ISBN 9780195140187. URL <https://books.google.com/books?id=oKpMwAAQBAJ>.
- [91] Umberto Marini Bettolo Marconi, Andrea Puglisi, Lamberto Rondoni, and Angelo Vulpiani. Fluctuation–dissipation: Response theory in statistical physics. *Physics Reports*, 461(4):111 – 195, 2008. ISSN 0370-1573. doi: <https://doi.org/10.1016/j.physrep.2008.02.002>. URL <http://www.sciencedirect.com/science/article/pii/S0370157308000768>.
- [92] R Kubo. The fluctuation-dissipation theorem. *Reports on Progress in Physics*, 29(1):255–284, jan 1966. doi: 10.1088/0034-4885/29/1/306. URL <https://doi.org/10.1088/0034-4885/29/1/306>.
- [93] Florian Marquardt, Joe P. Chen, A. A. Clerk, and S. M. Girvin. Quantum theory of cavity-assisted sideband cooling of mechanical motion. *Phys. Rev. Lett.*, 99:093902, Aug 2007. doi: 10.1103/PhysRevLett.99.093902. URL <https://link.aps.org/doi/10.1103/PhysRevLett.99.093902>.
- [94] G. W. Ford, J. T. Lewis, and R. F. O’Connell. Quantum langevin equation. *Phys. Rev. A*, 37:4419–4428, Jun 1988. doi: 10.1103/PhysRevA.37.4419. URL <https://link.aps.org/doi/10.1103/PhysRevA.37.4419>.
- [95] A. O. Caldeira and A. J. Leggett. Path integral approach to quantum brownian motion. *Physica*, 121A:587, 1983. doi: 10.1016/0378-4371(83)90013-4.
- [96] A. K. Tagantsev and S. A. Fedorov. Quantum-limited measurements using an optical cavity with modulated intrinsic loss. *Phys. Rev. Lett.*, 123:043602, 2019. doi: 10.1103/PhysRevLett.123.043602.
- [97] B. Kappler H.-P. Breuer and F. Petruccione. The time-convolutionless projection operator technique in the quantum theory of dissipation and decoherence. *Ann. Phys.*, 291:36, 2001. doi: 10.1006/aphy.2001.6152.
- [98] V. Giovannetti and D. Vitali. Phase-noise measurement in a cavity with a movable mirror undergoing quantum brownian motion. *Phys. Rev. A*, 63:023812, 2001. doi: 10.1103/PhysRevA.63.023812.
- [99] A. Garg, J. N. Onuchic, and V. Ambegaokar. Effect of friction on electron transfer in biomolecules. *J. Chem. Phys.*, 83:4491, 1985. doi: 10.1063/1.449017.
- [100] Milton Abramowitz and Irene A. Stegun. *Handbook of Mathematical Functions with Formulas, Graphs, and Mathematical Tables*. Dover, New York, ninth dover printing, tenth gpo printing edition, 1964.

- [101] F. R. Gantmacher. *Applications of the Theory of Matrices*. Wiley, New York, 1959. doi: 10.1126/science.131.3398.405-a.
- [102] C. Genes, A. Mari, P. Tombesi, and D. Vitali. Robust entanglement of a micromechanical resonator with output optical fields. *Phys. Rev. A*, 78:032316, 2008. doi: 10.1103/PhysRevA.78.032316.
- [103] R Zwanzig. Time-correlation functions and transport coefficients in statistical mechanics. *Annual Review of Physical Chemistry*, 16(1):67–102, 1965. doi: 10.1146/annurev.pc.16.100165.000435. URL <https://doi.org/10.1146/annurev.pc.16.100165.000435>.
- [104] Claudio Albanese, Matthias Christandl, Nilanjana Datta, and Artur Ekert. Mirror inversion of quantum states in linear registers. *Phys. Rev. Lett.*, 93:230502, Nov 2004. doi: 10.1103/PhysRevLett.93.230502. URL <https://link.aps.org/doi/10.1103/PhysRevLett.93.230502>.
- [105] Leonardo Banchi and Ruggero Vaia. Spectral problem for quasi-uniform nearest-neighbor chains. *Journal of Mathematical Physics*, 54(4):043501, 2013. doi: 10.1063/1.4797477. URL <https://doi.org/10.1063/1.4797477>.
- [106] H. Bruus, K. Flensberg, and Oxford University Press. *Many-Body Quantum Theory in Condensed Matter Physics: An Introduction*. Oxford Graduate Texts. OUP Oxford, 2004. ISBN 9780198566335. URL <https://books.google.com/books?id=v5vhg1tYLC8C>.
- [107] Antoni Wójcik, Tomasz Łuczak, Paweł Kurzyński, Andrzej Grudka, Tomasz Gdala, and Małgorzata Bednarska. Unmodulated spin chains as universal quantum wires. *Phys. Rev. A*, 72:034303, Sep 2005. doi: 10.1103/PhysRevA.72.034303. URL <https://link.aps.org/doi/10.1103/PhysRevA.72.034303>.
- [108] Giulia Gualdi, Vojtech Kostak, Irene Marzoli, and Paolo Tombesi. Perfect state transfer in long-range interacting spin chains. *Phys. Rev. A*, 78:022325, Aug 2008. doi: 10.1103/PhysRevA.78.022325. URL <https://link.aps.org/doi/10.1103/PhysRevA.78.022325>.
- [109] Analia Zwick, Gonzalo A Álvarez, Guy Bensky, and Gershon Kurizki. Optimized dynamical control of state transfer through noisy spin chains. *New Journal of Physics*, 16(6):065021, jun 2014. doi: 10.1088/1367-2630/16/6/065021. URL <https://doi.org/10.1088/1367-2630/16/6/065021>.
- [110] Tony J. G. Apollaro, Guilherme M. A. Almeida, Salvatore Lorenzo, Alessandro Ferraro, and Simone Paganelli. Spin chains for two-qubit teleportation. *Phys. Rev. A*, 100:052308, Nov 2019. doi: 10.1103/PhysRevA.100.052308. URL <https://link.aps.org/doi/10.1103/PhysRevA.100.052308>.
- [111] W. Son, L. Amico, F. Plastina, and V. Vedral. Quantum instability and edge entanglement in the quasi-long-range order. *Phys. Rev. A*, 79:022302, Feb 2009. doi: 10.1103/PhysRevA.79.022302. URL <https://link.aps.org/doi/10.1103/PhysRevA.79.022302>.
- [112] Elliott Lieb, Theodore Schultz, and Daniel Mattis. Two soluble models of an antiferromagnetic chain. *Annals of Physics*, 16(3):407–466, 1961. doi: [http://dx.doi.org/10.1016/0003-4916\(61\)90115-4](http://dx.doi.org/10.1016/0003-4916(61)90115-4).
- [113] Robert Alicki and Mark Fannes. Entanglement boost for extractable work from ensembles of quantum batteries. *Physical Review E*, 87(4):042123, apr 2013. ISSN 1539-3755. doi: 10.1103/PhysRevE.87.042123. URL <https://link.aps.org/doi/10.1103/PhysRevE.87.042123>.

- [114] Felix C Binder, Sai Vinjanampathy, Kavan Modi, and John Goold. Quantacell: powerful charging of quantum batteries. *New Journal of Physics*, 17(7):075015, jul 2015. doi: 10.1088/1367-2630/17/7/075015. URL <https://doi.org/10.1088/1367-2630/17/7/075015>.
- [115] Francesco Campaioli, Felix A. Pollock, and Sai Vinjanampathy. Quantum Batteries - Review Chapter. *arXiv e-prints*, art. arXiv:1805.05507, May 2018.
- [116] Stefano Gherardini, Francesco Campaioli, Filippo Caruso, and Felix C. Binder. Stabilizing Open Quantum Batteries by Sequential Measurements. *arXiv e-prints*, art. arXiv:1910.02458, Oct 2019.
- [117] A. E. Allahverdyan, R. Balian, and Th. M. Nieuwenhuizen. Maximal work extraction from finite quantum systems. *EPL (Europhysics Letters)*, 67(4):565, 2004. URL <http://stacks.iop.org/0295-5075/67/i=4/a=565>.
- [118] Karen V. Hovhannisyanyan, Martí Perarnau-Llobet, Marcus Huber, and Antonio Acín. Entanglement generation is not necessary for optimal work extraction. *Phys. Rev. Lett.*, 111:240401, Dec 2013. doi: 10.1103/PhysRevLett.111.240401. URL <https://link.aps.org/doi/10.1103/PhysRevLett.111.240401>.
- [119] Sergi Julia-Farre, Tymoteusz Salamon, Arnau Riera, Manabendra N. Bera, and Maciej Lewenstein. Bounds on Capacity and Power of Quantum Batteries. *arXiv e-prints*, art. arXiv:1811.04005, Nov 2018.
- [120] Davide Rossini, Gian Marcello Andolina, and Marco Polini. Many-body localized quantum batteries. *Phys. Rev. B*, 100:115142, Sep 2019. doi: 10.1103/PhysRevB.100.115142. URL <https://link.aps.org/doi/10.1103/PhysRevB.100.115142>.
- [121] Alan C. Santos, Barış Çakmak, Steve Campbell, and Nikolaj T. Zinner. Stable adiabatic quantum batteries. *Phys. Rev. E*, 100:032107, Sep 2019. doi: 10.1103/PhysRevE.100.032107. URL <https://link.aps.org/doi/10.1103/PhysRevE.100.032107>.
- [122] Francesco Campaioli, Felix A. Pollock, Felix C. Binder, Lucas Céleri, John Goold, Sai Vinjanampathy, and Kavan Modi. Enhancing the charging power of quantum batteries. *Phys. Rev. Lett.*, 118:150601, Apr 2017. doi: 10.1103/PhysRevLett.118.150601. URL <https://link.aps.org/doi/10.1103/PhysRevLett.118.150601>.
- [123] Gian Marcello Andolina, Maximilian Keck, Andrea Mari, Michele Campisi, Vittorio Giovannetti, and Marco Polini. Extractable work, the role of correlations, and asymptotic freedom in quantum batteries. *Phys. Rev. Lett.*, 122:047702, Feb 2019. doi: 10.1103/PhysRevLett.122.047702. URL <https://link.aps.org/doi/10.1103/PhysRevLett.122.047702>.
- [124] Gian Marcello Andolina, Donato Farina, Andrea Mari, Vittorio Pellegrini, Vittorio Giovannetti, and Marco Polini. Charger-mediated energy transfer in exactly solvable models for quantum batteries. *Phys. Rev. B*, 98:205423, Nov 2018. doi: 10.1103/PhysRevB.98.205423. URL <https://link.aps.org/doi/10.1103/PhysRevB.98.205423>.
- [125] Thao P. Le, Jesper Levinsen, Kavan Modi, Meera M. Parish, and Felix A. Pollock. Spin-chain model of a many-body quantum battery. *Phys. Rev. A*, 97:022106, Feb 2018. doi: 10.1103/PhysRevA.97.022106. URL <https://link.aps.org/doi/10.1103/PhysRevA.97.022106>.

- [126] Asher Peres. Separability criterion for density matrices. *Phys. Rev. Lett.*, 77:1413–1415, Aug 1996. doi: 10.1103/PhysRevLett.77.1413. URL <https://link.aps.org/doi/10.1103/PhysRevLett.77.1413>.
- [127] William K. Wootters. Entanglement of formation of an arbitrary state of two qubits. *Phys. Rev. Lett.*, 80:2245–2248, Mar 1998. doi: 10.1103/PhysRevLett.80.2245. URL <https://link.aps.org/doi/10.1103/PhysRevLett.80.2245>.
- [128] W. Dür, G. Vidal, and J. I. Cirac. Three qubits can be entangled in two inequivalent ways. *Phys. Rev. A*, 62:062314, Nov 2000. doi: 10.1103/PhysRevA.62.062314. URL <https://link.aps.org/doi/10.1103/PhysRevA.62.062314>.
- [129] A. Acín, D. Bruß, M. Lewenstein, and A. Sanpera. Classification of Mixed Three-Qubit States. *Physical Review Letters*, 87(4):040401, jul 2001. ISSN 0031-9007. doi: 10.1103/PhysRevLett.87.040401. URL <https://link.aps.org/doi/10.1103/PhysRevLett.87.040401>.
- [130] Valerie Coffman, Joydip Kundu, and William K. Wootters. Distributed entanglement. *Phys. Rev. A*, 61:052306, Apr 2000. doi: 10.1103/PhysRevA.61.052306. URL <https://link.aps.org/doi/10.1103/PhysRevA.61.052306>.
- [131] Zhi-Hao Ma, Zhi-Hua Chen, Jing-Ling Chen, Christoph Spengler, Andreas Gabriel, and Marcus Huber. Measure of genuine multipartite entanglement with computable lower bounds. *Phys. Rev. A*, 83:062325, Jun 2011. doi: 10.1103/PhysRevA.83.062325. URL <https://link.aps.org/doi/10.1103/PhysRevA.83.062325>.
- [132] David A. Meyer and Nolan R. Wallach. Global entanglement in multiparticle systems. *Journal of Mathematical Physics*, 43(9):4273–4278, 2002. doi: 10.1063/1.1497700. URL <https://doi.org/10.1063/1.1497700>.
- [133] Géza Tóth, Tobias Moroder, and Otfried Gühne. Evaluating convex roof entanglement measures. *Phys. Rev. Lett.*, 114:160501, Apr 2015. doi: 10.1103/PhysRevLett.114.160501. URL <https://link.aps.org/doi/10.1103/PhysRevLett.114.160501>.
- [134] Barbara M. Terhal. Bell inequalities and the separability criterion. *Physics Letters A*, 271(5):319 – 326, 2000. ISSN 0375-9601. doi: [https://doi.org/10.1016/S0375-9601\(00\)00401-1](https://doi.org/10.1016/S0375-9601(00)00401-1). URL <http://www.sciencedirect.com/science/article/pii/S0375960100004011>.
- [135] Mohamed Bourennane, Manfred Eibl, Christian Kurtsiefer, Sascha Gaertner, Harald Weinfurter, Otfried Gühne, Philipp Hyllus, Dagmar Bruß, Maciej Lewenstein, and Anna Sanpera. Experimental detection of multipartite entanglement using witness operators. *Phys. Rev. Lett.*, 92:087902, Feb 2004. doi: 10.1103/PhysRevLett.92.087902. URL <https://link.aps.org/doi/10.1103/PhysRevLett.92.087902>.
- [136] Bastian Jungnitsch, Tobias Moroder, and Otfried Gühne. Taming Multiparticle Entanglement. *Physical Review Letters*, 106(19):1–4, may 2011. ISSN 0031-9007. doi: 10.1103/PhysRevLett.106.190502. URL <http://link.aps.org/doi/10.1103/PhysRevLett.106.190502>.
- [137] Barış Çakmak, Steve Campbell, Bassano Vacchini, Özgür E. Müstecaplıoğlu, and Mauro Paternostro. Robust multipartite entanglement generation via a collision model. *Phys. Rev. A*, 99:012319, Jan 2019. doi: 10.1103/PhysRevA.99.012319. URL <https://link.aps.org/doi/10.1103/PhysRevA.99.012319>.

- [138] Christopher Eltschka and Jens Siewert. Quantifying entanglement resources. *Journal of Physics A: Mathematical and Theoretical*, 47(42):424005, oct 2014. doi: 10.1088/1751-8113/47/42/424005. URL <https://doi.org/10.1088/1751-8113/47/42/424005>.
- [139] Chang shui Yu and He shan Song. Free entanglement measure of multiparticle quantum states. *Physics Letters A*, 330(5):377 – 383, 2004. ISSN 0375-9601. doi: <https://doi.org/10.1016/j.physleta.2004.07.054>. URL <http://www.sciencedirect.com/science/article/pii/S0375960104010722>.
- [140] C. Sabín and G. García-Alcaine. A classification of entanglement in three-qubit systems. *The European Physical Journal D*, 48(3):435–442, jun 2008. ISSN 1434-6060. doi: 10.1140/epjd/e2008-00112-5. URL <http://www.springerlink.com/index/10.1140/epjd/e2008-00112-5>.
- [141] G. Vidal and R. F. Werner. Computable measure of entanglement. *Physical Review A - Atomic, Molecular, and Optical Physics*, 65(3):1–11, 2002. ISSN 10502947. doi: 10.1103/PhysRevA.65.032314.
- [142] Michał Horodecki, Paweł Horodecki, and Ryszard Horodecki. Separability of mixed states: necessary and sufficient conditions. *Physics Letters A*, 223(1):1 – 8, 1996. ISSN 0375-9601. doi: [https://doi.org/10.1016/S0375-9601\(96\)00706-2](https://doi.org/10.1016/S0375-9601(96)00706-2). URL <http://www.sciencedirect.com/science/article/pii/S0375960196007062>.
- [143] W. Dür, J. I. Cirac, and R. Tarrach. Separability and distillability of multiparticle quantum systems. *Physical Review Letters*, 83(17):3562–3565, 1999. ISSN 10797114. doi: 10.1103/PhysRevLett.83.3562.
- [144] Luigi Amico, Andreas Osterloh, Francesco Plastina, Rosario Fazio, and G. Massimo Palma. Dynamics of entanglement in one-dimensional spin systems. *Physical Review A*, 69(2):022304, feb 2004. ISSN 1050-2947. doi: 10.1103/PhysRevA.69.022304. URL <http://link.aps.org/doi/10.1103/PhysRevA.69.022304>.
- [145] T. Laustsen, Frank Verstraete, and Steven J. van Enk. Local vs. joint measurements for the entanglement of assistance. *Quantum Information & Computation*, 3(1):64–83, 2003. URL <http://portal.acm.org/citation.cfm?id=2011514>.
- [146] H R. Raether. *Surface Plasmons on Smooth and Rough Surface and Gratings*. Springer Tracts in Modern Physics, 1988.
- [147] George Hanson, Ali Hassani Gangaraj, and Andrei Nemilentsau. Notes on photonic topological insulators and scattering-protected edge states - a brief introduction. *arXiv:1602.02425v2*, 05 2016.
- [148] Klaus von Klitzing. The quantized hall effect. *Rev. Mod. Phys.*, 58:519–531, 07 1986. doi: 10.1103/RevModPhys.58.519. URL <https://link.aps.org/doi/10.1103/RevModPhys.58.519>.
- [149] M. Born and V. Fock. Beweis des adiabatsatzes. *Zeitschrift für Physik*, 51(3):165–180, 3 1928. ISSN 0044-3328. doi: 10.1007/BF01343193. URL <https://doi.org/10.1007/BF01343193>.
- [150] MV Berry. Quantum phase corrections from adiabatic iteration. *Proceedings of the royal society of London, series A: mathematical and physical sciences*, 414(1846):31–46, 1987.
- [151] Sean M. Carroll. *Spacetime and Geometry: An Introduction to General Relativity*. Cambridge University Press, 2019. doi: 10.1017/9781108770385.

- [152] A. Zee. *Quantum Field Theory in a Nutshell: Second Edition*. In a Nutshell. Princeton University Press, 2010. ISBN 9781400835324. URL <https://books.google.com/books?id=n8Mmbjtco78C>.
- [153] J.K. Asbóth, L. Oroszlány, and A.P. Pályi. *A Short Course on Topological Insulators: Band Structure and Edge States in One and Two Dimensions*. Lecture Notes in Physics. Springer International Publishing, 2016. ISBN 9783319256078. URL <https://books.google.com/books?id=RWKhCwAAQBAJ>.
- [154] Douglas R. Hofstadter. Energy levels and wave functions of bloch electrons in rational and irrational magnetic fields. *Phys. Rev. B*, 14:2239–2249, Sep 1976. doi: 10.1103/PhysRevB.14.2239. URL <https://link.aps.org/doi/10.1103/PhysRevB.14.2239>.
- [155] Mikael C. Rechtsman, Julia M. Zeuner, Yonatan Plotnik, Yaakov Lumer, Daniel Podolsky, Felix Dreisow, Stefan Nolte, Mordechai Segev, and Alexander Szameit. Photonic floquet topological insulators. *Nature*, 496:196 EP –, 4 2013. URL <https://doi.org/10.1038/nature12066>.
- [156] Kejie Fang, Zongfu Yu, and Shanhui Fan. Realizing effective magnetic field for photons by controlling the phase of dynamic modulation. *Nature Photonics*, 6:782 EP –, 10 2012. URL <https://doi.org/10.1038/nphoton.2012.236>. Article.
- [157] Mohammad Hafezi and Peter Rabl. Optomechanically induced non-reciprocity in microring resonators. *Opt. Express*, 20(7):7672–7684, 03 2012. doi: 10.1364/OE.20.007672. URL <http://www.opticsexpress.org/abstract.cfm?URI=oe-20-7-7672>.
- [158] M. Hafezi, S. Mittal, J. Fan, A. Migdall, and J. M. Taylor. Imaging topological edge states in silicon photonics. *Nature Photonics*, 7:1001 EP –, 10 2013. URL <https://doi.org/10.1038/nphoton.2013.274>. Article.
- [159] V. Peano, C. Brendel, M. Schmidt, and F. Marquardt. Topological phases of sound and light. *Phys. Rev. X*, 5:031011, Jul 2015. doi: 10.1103/PhysRevX.5.031011. URL <https://link.aps.org/doi/10.1103/PhysRevX.5.031011>.
- [160] H. Xu, Luyao Jiang, A. A. Clerk, and J. G. E. Harris. Nonreciprocal control and cooling of phonon modes in an optomechanical system. *Nature*, 568(7750):65–69, Apr 2019. ISSN 1476-4687. doi: 10.1038/s41586-019-1061-2. URL <https://doi.org/10.1038/s41586-019-1061-2>.
- [161] T. J. Kippenberg, H. Rokhsari, T. Carmon, A. Scherer, and K. J. Vahala. Analysis of radiation-pressure induced mechanical oscillation of an optical microcavity. *Phys. Rev. Lett.*, 95:033901, 07 2005. doi: 10.1103/PhysRevLett.95.033901. URL <https://link.aps.org/doi/10.1103/PhysRevLett.95.033901>.
- [162] Stephen Powell, Ryan Barnett, Rajdeep Sensarma, and Sankar Das Sarma. Bogoliubov theory of interacting bosons on a lattice in a synthetic magnetic field. *Phys. Rev. A*, 83:013612, 01 2011. doi: 10.1103/PhysRevA.83.013612. URL <https://link.aps.org/doi/10.1103/PhysRevA.83.013612>.
- [163] A. Metelmann and A. A. Clerk. Nonreciprocal photon transmission and amplification via reservoir engineering. *Phys. Rev. X*, 5:021025, Jun 2015. doi: 10.1103/PhysRevX.5.021025. URL <https://link.aps.org/doi/10.1103/PhysRevX.5.021025>.



- [164] Sebastian Diehl, Enrique Rico, Mikhail A. Baranov, and Peter Zoller. Topology by dissipation in atomic quantum wires. *Nature Physics*, 7(12):971–977, Dec 2011. ISSN 1745-2481. doi: 10.1038/nphys2106. URL <https://doi.org/10.1038/nphys2106>.
- [165] Leo A. Goodman. Some practical techniques in serial number analysis. *Journal of the American Statistical Association*, 49(265):97–112, 1954. doi: 10.1080/01621459.1954.10501218.
- [166] Michael Höhle and Leonhard Held. Bayesian estimation of the size of a population, 2006. URL <http://hdl.handle.net/10419/30999>. urn:nbn:de:bvb:19-epub-2094-7.
- [167] E. T. Jaynes. *Probability Theory: The Logic of Science*. Cambridge University Press, 2003. doi: 10.1017/CBO9780511790423.
- [168] C. Helstrom. The minimum variance of estimates in quantum signal detection. *IEEE Transactions on Information Theory*, 14(2):234–242, 03 1968. ISSN 0018-9448. doi: 10.1109/TIT.1968.1054108.
- [169] Carl W. Helstrom. Estimation of a displacement parameter of a quantum system. *International Journal of Theoretical Physics*, 11(6):357–378, 12 1974. ISSN 1572-9575. doi: 10.1007/BF01809715. URL <https://doi.org/10.1007/BF01809715>.
- [170] M. Reed and B. Simon. Ii - hilbert spaces. In MICHAEL REED and BARRY SIMON, editors, *Methods of Modern Mathematical Physics*, pages 36 – 66. Academic Press, 1972. ISBN 978-0-12-585001-8. doi: <https://doi.org/10.1016/B978-0-12-585001-8.50008-8>. URL <http://www.sciencedirect.com/science/article/pii/B9780125850018500088>.
- [171] Samuel L. Braunstein and Carlton M. Caves. Statistical distance and the geometry of quantum states. *Phys. Rev. Lett.*, 72:3439–3443, 05 1994. doi: 10.1103/PhysRevLett.72.3439. URL <https://link.aps.org/doi/10.1103/PhysRevLett.72.3439>.
- [172] J. M. Raimond, M. Brune, and S. Haroche. Manipulating quantum entanglement with atoms and photons in a cavity. *Rev. Mod. Phys.*, 73:565–582, Aug 2001. doi: 10.1103/RevModPhys.73.565. URL <https://link.aps.org/doi/10.1103/RevModPhys.73.565>.
- [173] Rafal Demkowicz-Dobrzański, Marcin Jarzyna, and Jan Kołodyński. Chapter four. In E. Wolf, editor, *Quantum Limits in Optical Interferometry*, volume 60 of *Progress in Optics*, pages 345 – 435. Elsevier, 2015. doi: <https://doi.org/10.1016/bs.po.2015.02.003>. URL <http://www.sciencedirect.com/science/article/pii/S0079663815000049>.
- [174] Matteo Brunelli, Stefano Olivares, and Matteo G. A. Paris. Qubit thermometry for micromechanical resonators. *Phys. Rev. A*, 84:032105, 09 2011. doi: 10.1103/PhysRevA.84.032105. URL <https://link.aps.org/doi/10.1103/PhysRevA.84.032105>.
- [175] Matteo Brunelli, Stefano Olivares, Mauro Paternostro, and Matteo G. A. Paris. Qubit-assisted thermometry of a quantum harmonic oscillator. *Phys. Rev. A*, 86:012125, 07 2012. doi: 10.1103/PhysRevA.86.012125. URL <https://link.aps.org/doi/10.1103/PhysRevA.86.012125>.
- [176] Ivan Dobrakov. On integration in banach spaces, ii. *Czechoslovak Mathematical Journal*, 20(4):680–695, 1970. URL <http://eudml.org/doc/12558>.

- [177] K. Yosida. *Functional Analysis*. Springer-Verlag Berlin Heidelberg, 2004. doi: 10.1007/978-3-642-61859-8.
- [178] L Förster, W Alt, I Dotsenko, M Khudaverdyan, D Meschede, Y Miroshnychenko, S Reick, and A Rauschenbeutel. Number-triggered loading and collisional redistribution of neutral atoms in a standing wave dipole trap. *New Journal of Physics*, 8(10):259–259, oct 2006. doi: 10.1088/1367-2630/8/10/259. URL <https://doi.org/10.1088/1367-2630/8/10/259>.
- [179] E. T. Jaynes and F. W. Cummings. “comparison of quantum and semiclassical radiation theory with application to the beam maser,“. *Proc. IEEE*, 51:89, 1963. doi: doi:10.1109/PROC.1963.1664.
- [180] H. Paul. Induzierte emission bei starker einstrahlung. *Annalen der Physik*, 466(7-8):411–412, 1963. doi: 10.1002/andp.19634660710. URL <https://onlinelibrary.wiley.com/doi/abs/10.1002/andp.19634660710>.
- [181] Sébastien Gleyzes, Stefan Kuhr, Christine Guerlin, Julien Bernu, Samuel Deléglise, Ulrich Busk Hoff, Michel Brune, Jean-Michel Raimond, and Serge Haroche. Quantum jumps of light recording the birth and death of a photon in a cavity. *Nature*, 446:297 EP –, Mar 2007. URL <https://doi.org/10.1038/nature05589>.
- [182] M. Reed and B. Simon. I - functional analysis. In MICHAEL REED and BARRY SIMON, editors, *Methods of Modern Mathematical Physics*. Academic Press, 1980. doi: <https://doi.org/10.1016/B978-0-12-585001-8.50008-8>. URL <http://www.sciencedirect.com/science/article/pii/B9780125850018500088>.
- [183] G. Dattoli, A. Renieri, and A. Torre. Generalized polynomials and derivation of integrals involving products of hermite polynomials. *Rad. Phys. Chem*, 53:391–395, 1998.
- [184] L. Galué. Evaluation of some integrals involving hermite polynomials. *Math. Balkanica*, 13:377, 1999.
- [185] S. Kuhr, W. Alt, D. Schrader, I. Dotsenko, Y. Miroshnychenko, W. Rosenfeld, M. Khudaverdyan, V. Gomer, A. Rauschenbeutel, and D. Meschede. Coherence properties and quantum state transportation in an optical conveyor belt. *Phys. Rev. Lett.*, 91:213002, Nov 2003. doi: 10.1103/PhysRevLett.91.213002. URL <https://link.aps.org/doi/10.1103/PhysRevLett.91.213002>.
- [186] M. Rossi, D. Mason, J. Chen, and A. Schliesser. Observing and verifying the quantum trajectory of a mechanical resonator. *Phys. Rev. Lett.*, 123:163601, 2019. doi: 10.1103/PhysRevLett.123.163601.
- [187] M. Karuza, C. Biancofiore, M. Galassi, R. Natali, G. Di Giuseppe, P. Tombesi, and D. Vitali. Quantum dynamics of a vibrational mode of a membrane within an optical cavity. *AIP Conference Proceedings*, 361:1363, 2011. doi: 10.1063/1.3630212.
- [188] R. A Horn and C. R. Johnson. *Matrix Analysis*. Cambridge University Press, Cambridge UK, 1999. doi: 10.1002/zamm.19920721231.
- [189] L.-H. Zhang. On optimizing the sum of the rayleigh quotient and the generalized rayleigh quotient on the unit sphere. *Comput. Optim. Appl.*, 54:111, 2013.
- [190] Carl W. Helstrom. *Quantum detection and estimation theory / Carl W. Helstrom*. Academic Press New York, 1976. ISBN 0123400503.